Nonlinear Crystal Based Efficient Terahertz Generation and Development of Prototype RADAR System for Defense & Food Processing Applications

A thesis submitted to the
University of Hyderabad

Towards partial fulfilment for the degree of
Doctor of Philosophy
in
Physics
By

Chandan Ghorui

(19ACPP05)

Under the guidance of

Prof. Anil Kumar Chaudhary

School of Physics

Advanced Centre of Research in High Energy Materials
ACRHEM (DIA-CoE)
University of Hyderabad, Hyderabad 500046,
Telangana, India

August, 2024

Dedicated to Maa-Baba

&

Late Murari Mohan Bag (Dadu)

&

Prof. Abani Mohan Rudra
(Academic Father)

Head, Professor in Physics

Burdwan Raj College, Burdwan University

"The highest education is that which does not merely gives us the information but makes our life in harmony with all existence."

Rabindranath Tagore

"Take up one idea. Make that one idea your life - think of it, dream of it, and live on that idea. Let the brain, muscles, nerves, every part of your body, be full of that idea, and just leave every other idea alone. This is the way to success and the way great spiritual giants are produced."

Swami Vivekananda

UNIVERSITY OF HYDERABAD
Advanced Centre of Research in High Energy Materials
DIA CoE (ACRHEM), School of Physics

Dr. A.K. Chaudhary
Professor (Physics)
Email Id: anilphys@yahoo.com, akcphys@gmail.com, akcsp@uohyd.ac.in
Phones : +91-040-23138807, 9490747623

Certificate

This is to certify that the thesis entitled **"Nonlinear Crystal Based Efficient Terahertz Generation and Development of Prototype RADAR System for Defense & Food Processing Applications"**, being submitted to the University of Hyderabad by PMRF Scholar Chandan Ghorui (Reg. No 19ACPP05), for the award of the degree of Doctor of Philosophy in Physics, is a record of bonafide work carried out by him under my supervision and is free of plagiarism.

The thesis has not been submitted previously in part or in full of this or any other University or Institution for award of any degree or diploma.

20.08.2024
Prof. Anil Kumar Chaudhary
(Supervisor)

Dr. Anil Kr. Chaudhary
Professor (Physics)
Advanced Centre of Research in High Energy Materials (ACRHEM),
UNIVERSITY OF HYDERABAD
HYDERABAD-500 046. T.S. INDIA.

S C Bhattacharyya 20/8/24
Director
DIA-CoE, ACRHEM
University of Hyderabad,
Director
DIA-CoE, UoH

Dean 20/8/24
School of Physics,
University of Hyderabad.
DEAN
School of Physics
University of Hyderabad
HYDERABAD - 500 046

Certificate

This is to certify that the thesis entitled **"Nonlinear Crystal Based Efficient Terahertz Generation and Development of Prototype RADAR System for Defense & Food Processing Applications"**, being submitted to the University of Hyderabad by PMRF Scholar Chandan Ghorui (Reg. No 19ACPP05), for the award of the degree of Doctor of Philosophy in Physics, is a record of bonafide work carried out by him under my supervision and is free of plagiarism.

The thesis has not been submitted previously in part or in full of this or any other University or Institution for award of any degree or diploma.

Further, the student has the following publications before submission of the thesis for adjudication:

Peer Reviewed Journal:

1) Chandan Ghorui, A. M. Rudra, Udit Chatterjee, A. K. Chaudhary, and D. Ganesh, "Efficient second-harmonic and terahertz generation from single BiB_3O_6 crystal using nanosecond and femtosecond lasers", Appl. Opt. **60**, 5643-5651 (2021).
2) Chandan Ghorui and Arjun V Kidavu and P Naveen Kumar and S Das and A K Chaudhary and Yu M Andreev, "Comparative studies of terahertz-based optical properties in transmission/reflection modes of GaSe: S and measurement of its scattering losses due to surface roughness for efficient terahertz generation", Physica Scripta, **98**,2, 025508, 2023.
3) Chandan Ghorui and A. K. Chaudhary, "Linear and nonlinear optical characterization of tellurium dioxide (α-TeO_2) for generation of terahertz radiation using time-domain spectroscopy", Appl. Opt. **62**, 4831-4835 (2023).
4) Chandan Ghorui, P. Naveen Kumar, Anil Kumar Chaudhary, "Measurement of surface roughness of painted & rusted metallic objects using THz profilometer", **(Manuscript Under Review).**
5) Chandan Ghorui, Kummari Venkata Sreenivasulu, Anil Kumar Chaudhary and vadali Venkata satya sai Srikanth, "Ultra-thin Sheets of α-MoO_3 /β-PVDF Composites for THz Shielding by transmission and reflection Spectroscopy", **(Manuscript Under Review).**
6) Chandan Ghorui, Anil Kumar Chaudhary, "Study of 300 GHz Silicon Radar based Cross-Sections of Canonical Objects using Integrating Physical Optics and Numerical Simulation Techniques for Security Applications", **(Communicated).**
7) Chandan Ghorui, Tejas Kannampuzha, Anil Kumar Chaudhary, "AI based Identification of different types of Explosives and Metals in Concealed and Non-Concealed Conditions Using a 0.3 THz Radar System for Defense Applications," **(Communicate)**

Patents:

1) A. K. Chaudhary & Chandan Ghorui "A Tunable Incident Angle and Frequency Based 3d Terahertz Profilometer System" Indian Patent, Application No.: 202441040603 (24/05/2024).

2) A. K. Chaudhary, Chandan Ghorui and Tejas Kannampuzha "Artificial Intelligence coupled Tera Sensor for non-contact Meat Freshness Tester", Indian Patent, Provisional accepted.

Conference proceedings:

1) Chandan Ghorui and Anil Kumar Chaudhary, SPIE, DOI: 10.1117/12.3025308 (2024).
2) Chandan Ghorui, A.K.Chaudhary, Naveen Periketi, Koalla Rajesh, IEEE, 1-2, (2022), DOI:10.1109/WRAP54064.2022.9758310.
3) Chandan Ghorui, A.M. Rudra, U. Chatterjee, A.K. Chaudhary, and D. Ganesh, Technical Report, THz Technology, OSA.

Participation in conferences/workshops:

1) Presented work on " Study of Optical Properties of Different Grades Indian Cement Samples Using Terahertz Spectroscopy" at Proceedings of 28th National Conference on Condensed Matter Physics. Springer Proceedings in Physics, vol 269. Springer, Singapore, NIT Silchar, Aasam, November, 2021.
2) Presented work on " Study of THz time domain spectroscopy based optical properties and detection of minerals and explosives from soil samples of different origins" at IEEE Workshop on Recent Advances in Photonics (WRAP), 2022, organised by IEE Photonics Society, Mumbai. IIT Bombay, 4th-6th March, 2022.
3) Presented work on "Development of THz profilometer for the study of surface roughness of metallic and high-energy materials for homeland and defense applications," organised by in Mahindra University, Hyderabad, from April 20th to April 22nd, 2023
4) Presented work on " Efficient Second Harmonic and Terahertz generation from BIBO crystal using ultrashort laser pulses", organised by BARC, Mumbai, 19th-20th January, 2022.
5) Presented work on, "Real time imaging and measurement of surface roughness effect of metallic and high energy materials for homeland and defense applications" at NLS-31, organised by DAE-BRNS, IIT Kharagpur, 2nd-6th December, 2022.
6) Highlighted Poster Presentation in PMRF annual Symposium, IIT Indore, 3-4th March, 2024.
7) Presented Work on "Optoelectronic Characterisation and synthesis of MgO nanoparticle for antibacterials activities", Amity University, Kolkata, India. **(Awarded ACS Applied Nano Materials Best Poster)**

The following Courses have taken as a part of the course work

COURSE NO	TITLE OF THE COURSE	CREDITS	RESULTS
PY801	RESEARCH METHODOLOGY	4	PASS
PY802	ADVANCED QUANTUM MECHANICS	4	PASS
PY803	ADVANCED EXPERIMENTAL TECHNIQUES	4	PASS
PY819	NON-EQUILIBRIUM STATISTICAL MECHANICS	4	PASS

20.08.2024

Prof. Anil Kumar Chaudhary
(Supervisor)
Professor in Physics, DIA CoE
University of Hyderabad

Dr. Anil Kr. Chaudhary
Professor (Physics)
Advanced Centre of Research in High Energy Materials (ACRHEM),
UNIVERSITY OF HYDERABAD
HYDERABAD-500 046. T.S. INDIA.

20/8/24

Director
DIA CoE (ACRHEM)
University of Hyderabad

Director
DIA-CoE, UoH

20/8/24

Dean
School of Physics
University of Hyderabad

DEAN
School of Physics
University of Hyderabad
HYDERABAD - 500 046

Declaration

I, Chandan Ghorui, (Reg.No: 19ACPP05), hereby declare that research work reported in this thesis entitled **"Nonlinear Crystal Based Efficient Terahertz Generation and Development of Prototype RADAR System for Defense & Food Processing Applications"**, is original and has been carried out by me under the supervision of Prof. Anil Kumar Chaudhary, Professor in Physics, DIA-CoE, ACRHEM, School of Physics, University of Hyderabad, Hyderabad-500046, Telangana, India, as per the Doctor of Philosophy (Ph.D) in Physics ordinance of the University, which is also free from plagiarism. I further declare that this work has not submitted for the award of research degree of any other University. I hereby agree that my thesis can be deposited in Shodhganga/INFLIBNEST.

A report on plagiarism statistics from University Librarian is enclosed.

Chandan Ghorui

Chandan Ghorui

(19ACPP05)

20.08.2024

Prof. Anil Kumar Chaudhary

(Supervisor)

Professor in Physics,

DIA-CoE, ACRHEM, School of Physics,

University of Hyderabad, Hyderabad-500046

Telangana, India.

Dr. Anil Kr. Chaudhary
Professor (Physics)
Advanced Centre of Research in
High Energy Materials (ACRHEM),
UNIVERSITY OF HYDERABAD
HYDERABAD-500 046. T.S. INDIA.

A word of Gratitude

First and foremost, I would like to express my deepest gratitude and sincere thanks to my thesis supervisor Prof. A. K. Chaudhary, ACRHEM (DIA-CoE), School of Physics, Hyderabad University for providing his valuable guidance, scholarly inputs, and consistent encouragement throughout the research work and giving me an opportunity to join his research group. I am truly thankful for the time and effort he invested in my development as a research scholar. His insights and feedback have been invaluable in shaping my research skills and academic understanding. He has not only helped me become a better researcher but also inspired me to pursue excellence in my field. I am writing to express my profound gratitude for his exceptional guidance and unwavering support, which have been instrumental in my transformation from a regular junior research scholar to a Prime Minister's Research Fellow, one of the most prestigious and highest-paid fellowships in India. The path to this fellowship was challenging, but his consistent support and providing all instrumental and logistic support for developing a THz radar, Surface roughness, and AI based diary and agro product testing systems. I learned invaluable lessons under his supervision which made all the difference. His commitment to my development has inspired me to pursue excellence in my research and has set a benchmark for the kind of mentor I aspire to be in the future. Thanking him once again for everything he has done for me.

I would not have completed my research work and written this thesis without the kind moral and technical support and help received from many academic scholars.

I would like to take this opportunity to thank my doctoral review committee members Prof. Soma Venugopal Rao, ACRHEM (DIA-CoE), School of Physics & Dr. N. Sri Ram Gopal, School of Physics for their valuable suggestions and insightful questions during the D.C. meeting.

I am so delighted to express my deep gratitude to Dr. S. Bhattacharya, Director of ACRHEM (DIA-CoE) and Dr. V.K. Rao, Ex. Director, ACRHEM for providing needful experimental facilities and conducive research atmosphere.

I wanted to take a moment to express my deepest gratitude to Dr. Abani Mohan Rudra, Professor and Head, Raj College, Burdwan University for his guidance and support throughout my academic journey. Thanks, his academic mentorship, I feel confident in my capabilities and am excited about my future academic endeavors. Also, I extend my gratitude to Prof. Udit Chatterjee, Burdwan University, India, for the valuable academic discussions, suggestions and various aspect of nonlinear optics (NLO). I am express to my sincere gratitude to Prof,

Sourangshu Mukharjee, Dr. Hema Dutta, Dr. Apala Bhattacharya, and Dr. Partha Sarathi Ghosh for their valuable guidance in B. Sc and M.Sc. I take this opportunity to thank Dr. Subhasis Das, Department of Physics, The University of Burdwan, for providing GaSe crystal. I also thank Dr. G. Manoj Kumar, Prof. Sivakumar, Prof. Jayeeta Lahiri, Prof. J. Goutam and Prof. V.V.S Srikanth for his support.

I wish to thank my seniors Dr. D. Ganesh, Dr. C. Abinash Bhuyan, Rajesh Koalla, P. Naveen Kumar, N. Menchu, Dr. Mahendra & Arjun for their support in labs. I would like to extend thank to, Dr. Samuel Nalam and Dr. Linga Murthy Narlagiri, for their guidance and help in writing MATLAB program. It is my pleasure to thank my batch mates Karthik Jain, Eesam Vishnu, Nitish Kumar, Shriniketan Acharya, Kanaka Ravi Kumar, Lavudya Praveen Kumar, Bishnupriya Sahu, Bratati Das, Priyanka Kumari, Upasana Baishya, Gummadi Arun Prakesh, Rathod Jagannath, Supratik Mukharjee, Subhasree Ghosh, Subhadeep Saha, Akash Chowhan, Chinna Kandula, Mukulika Mondal, Sumi Rana, R. Saradar, Papiya Panda & Priya Misra for their constant help, motivation and support during my Ph. D life. In this context, I would like to thank my juniors from DIA CoE (ACRHEM) and colleagues from the School of Physics for their great cooperation and support.

I have to mention my special thanks to my roommates Dr. Subrata Mondal and Dipanjan Banerjee for their encouragement and moral support. I express my sincere thanks to my brother Saikat Das, Soumok Nag, Kamakhya Narayan Dutta for their constant, support, encouragement and motivation.

I would like to special thanks to Tejas K & Dhanish for their constant support.

I feel it is a pleasant duty to express my regards to non-teaching staffs Sri Sai Gaud anna, Nagaraju anna, Balraju anna, Bharat anna, of ACRHEM (DIA-CoE), B. Shashikala, K. Arjun, K. Sudarshan, Mahesh, Venket of School of Physics, workshop, IGM Library and University of Hyderabad administration. I also acknowledge DRDO, IoE, PMRF Govt. of India for providing me fellowship throughout my PhD period.

In the last but not least, I am indebted to my father Mr. Krishna Chandra Ghorui, my mother Srimati Monika Ghorui, my sister Bijoya Santra and her daughters Anjana & Aradhya for everything I have now. With their unconditional love, secrecies and support, I have become what I am today.

Your Sincerely,

Date:25/08/2024

Chandan Ghorui

Prime Minister Research Fellow

Abbreviations

Abbreviations	Descriptions
AC	Alternating Current
ADAS	Advanced Driver-Assistance Systems
AFM	Atomic Force Microscopy
ANN	Artificial Neural Network
AOM	Acousto-Optic Modulators
ASK	Amplitude Shift Keying
AN	Ammonium Nitrate
ATP	Adenosine Triphosphate
BBO	β-Barium Borate
BIBO	Bismuth triborate
BNA	N-benzyl-2-methyl-4-nitroaniline
BPD	Balanced Photo Diodes
BS	Beam Spillier
CdTe	Cadmium Telluride
CE	N-Methyl-N-2,4,6-tetranitroaniline
CPA	Chirped Pulse Amplification
CMOS	Complementary Metal-Oxide-Semiconductor
CV	Cross Validation
CW	Continuous Wave
CL-20	Hexanitrohexaazaisowurtzitane
DAST	4-N, N- Dimethylamino -4′ - N′-methyl-stilbazolium toyslate
DC	Direct Current
dB	Decibel
DCF	Dispersion-Compensating Fibers
DDS	Direct Digital Synthesis
DFM	Difference Frequency Mixing
DMF	Dimethylformamide
EF	Electric Field

EM	Electromagnic
EMI	Electromagnetic Interface
EO	Electro Optic
EOS	Electrooptic Optic Sampling
EVM	Error Vector Magnitude
eWLBs	embedded Wafer Level Ball Grid Array
Fs/fs	Femtosecond
FS EOS	Free Space Electro Optic Sampling
FFT	Fast Fourier Transform
FD	Frequency Domain
FDTD	Finite Difference Time Domain
FIR	Far Infrared Radiation
FOM	Figure of Merit
FMCW	Frequency Modulated Continuous Wave
FNN	Feedforward Neural Network
FWHM	Full Width at Half Maximum
GaAs	Gallium Arsenide
GaP	Gallium Phosphide
GaN	Gallium Nitride
GaSe	Gallium Selenide
GHz	Gigahertz
GPS	Global Positioning System
GVD	Group Velocity Dispersion
Hz	Hertz
HAZ	Heat-Affected Zone
HEMs	High Energy Materials
HMX	1, 3, 5, 7-Tetranitro-1, 3, 5, 7-Tetrazocane
IC	Integrated Circuit
IF	Intermediate Frequency
IMPACT	Ionization-Mode Planar Avalanche-CMOS Transistor
IMPATT	Impact Avalanche and Transit Time
ISM	Industrial, Scientific, and Medical

InAlAs	Indium Aluminium Arsenide
InAs	Indium Arsenide
InGaAs	Indium Gallium Arsenide
InP	Indium Phosphate
InSb	Indium Antimonide
kNN	k-Nearest Neighbour
LASER	Light Amplification by Stimulated Emission of Radiation
LBO	Lithium Triborate
LO	Local Oscillator
LCP	Liquid Crystal Polymer
LT	Low Temperature
LNA	Low Noise Amplifier
$LiNbO_3$	Lithium Niobate
$LiTaO_3$	Lithium Tantalate
LTCC	Low-Temperature Cofired Ceramic
MHz	Megahertz
MIMO	Multiple-Input/Multiple-Output
MMIC	Monolithic Microwave Integrated Circuit
MoO_3	Molybdenum Trioxide
Ns/ns	Nanosecond
NFC	Near Field Communication
NH_4NO_3	Ammonium Nitrate
NLO	Non-Linear Crystal
OAPM	Off-Axis Parabolic Mirror
OPO	Optical Parametric Oscillation
OR	Optical Rectification
OLS	Ordinary Least Square
OLR	Ordinary Linear Regression
PA	Power Amplifier
PAR	Phased-Array Radar
PC	PhotoConductive
PCA	Photoconductive Antennas

PCB	Printed Circuit Board
PCS	Photoconductive Sampling
PETN	2,2-bis[(nitrooxy)methyl]-1,3-propanediol dinitrate
PFM	Piezo Response Force Microscopy
PLL	Phase Lock Loop
PM	Polarization-Maintaining
PO	Physical Optics
Ps/ps	Picosecond
PVDF	Polyvinylidene Fluoride
QFN	Quad Flat No-Lead
QPSK	Quadrature Phase Shift Keying
RADAR	Radio Detection and Ranging
RCS	Radar Cross Section
RDX	1, 3, 5-Trinitroperhydro-1, 3, 5-Triazine
RF	Radio Frequency
RMSE	Root Mean Square Error
SiGe	Silicon Germanium
SiP	System in Package
SoC	System on Chip
SDG	Synchronization and Delay Generator
SE	Shielding Effectiveness
SSE	Specific Shielding Effectiveness
SHG	Second Harmonic Generation
SHM	Sub Harmonic Mixture
SEM	Scanning Electron Microscopy
SLM	Spatial Light Modulators
SM	Single-Mode
SNR	Signal to Noise Ratio
TDS	Time Domain Spectroscopy
TE	Transverse Electric
TeO_2	Tellurium Oxide
THz	Terahertz

THz TDS	Terahertz Time-Domain Spectroscopy
TRTS	Time Resolved THz Spectroscopy
TRCS	THz Radar Cross Section
TM	Transverse Magnetic
TNT	2-Methyl-1, 3, 5-Trinitrobenzene
Urea	Carbamide
VCO	Voltage Control Oscillator
WPANs	Wireless Personal Area Networks
ZnTe	Zinc Telluride

Table of Contents

Chapter 1: Introduction and Thesis Overview 1

1. Introduction and Motivation: 2

1.1 Generation and detection of terahertz waves from optical and electronic source: 5

1.1.1 Optical terahertz sources: 5

1.1.1 (a) Photoconductive switching techniques: 5

1.1.1 (b) Optical rectification techniques in nonlinear crystals: 6

1.1.2 Two terminal solid-state devices: 10

1.1.2 (a) (i) Gunn diodes: 11

1.1.2 (b) (ii) IMPACT diodes: 11

1.1.2 (c) Frequency multipliers: 12

1.1.3 Detectors for detection of THz signal: 13

1.1.3 (a) Photoconductive sampling: 14

1.1.3 (b) Free space electro-optic sampling: 15

1.1.3 (c) Pyro detector: 18

1.2 Generation and detection of THz frequency (at University of Hyderabad): 18

1.3 Advantage of an electronic source over optical source: 20

References: 25

Chapter 2: Experimental details for THz and second harmonic generation, theoretical consideration and data processing 30

2.1 Laser background: 31

2.2 Ultrafast lasers background and sources: 31

2.3 Femtosecond coherent chameleon ultra-II (oscillator): 36

2.3.1 THz time-domain spectroscopy (TDS) using femtosecond laser oscillator: 36

2.4. Femtosecond coherent amplified ultrafast Ti: Sapphire laser system (LIBRA): 37

2.4.1 Efficient SHG and THz generation using femtosecond laser amplifier: 38

2.5 TeraFlash Pro: versatile terahertz time domain platform: 39

2.5.1 THz time-domain reflection spectroscopy using femtosecond laser: 41

2.6 Silicon radar: 41

2.7 For measuring UV generation and detection using Nd: YAG nanosecond laser: 51

2.8 Theoretical consideration and data processing: 52

2.8.1 THz transmission geometry: 52
2.8.2 THz reflection geometry: 53
2.8.3 THz based Surface roughness, optical impedance and reflection coefficients in transverse electric (TE) and transverse magnetic (TM) mode: 54
2.8.4 Data analysis for proto-type silicon radar system: 55
Reference: 56
Chapter 3: Evalution of BIBO, S- doped GaSe, α-TeO_2 nonlinear crystals for efficient SHG and terahertz generation: 59
3.1 Nonlinear effects in nonlinear crystals: 60
3.1.1 Efficient THz generation from nonlinear ZnTe crystals using optical rectification process 60
3.2 BIBO (BiB_3O_6): 64
3.3 S-doped GaSe: 65
3.4 α-TeO_2: 67
3.5 Result and Discussion: 69
3.5.1 Efficient UV & second harmonic generation of BIBO crystal using Nd: YAG 1064 nm, 10 ns laser pulse: 69
3.5.2 THz transmission & efficiency from BIBO crystal using femto second Ti: sapphire oscillator laser: 76
3.5.3 Efficient THz generation & optoelectronic characterisation of S (sulfur) doped GaSe nonlinear crystal using both THz TDS transmission and reflection geometry: 81
3.5.4 Second harmonic generation, theoretical predication of DFG & Type -I phase matching angle of α-TeO_2 semimetal semiconductor crystal 88
3.5.5 Optoelectronic characterisation of using broadband THz time domain spectroscopy: 90
References: 96
Chapter 4: Designing aspects of newly developed THz profilometer for measuring the surface roughness of remote metallic and explosive targets 102
4.1 Introduction: 103
4.2 Existing state of art: 110
4.2.1 Atomic Force Microscopy: 112
4.3 Advantage of 3D Profilometer over 1D Profilometer: 114
4.4 Theoretical Consideration: 115

4.5 Results and Discussion: 115
4.5.1 Terahertz time/frequency domain reflected signal & optical property of old metallic target 116
4.5.2 2D THz imaging, 3D surfaces profiling, surface roughness effects, and reflection coefficients in TE mode for painted and unpainted/rusted metallic targets 117
4.5.3 Q factor depending the signal strength: 120
4.6 Real time metallic object detection and surface roughness effects: 122
4.7 Surface roughness effect on explosive materials: 123
4.8 Surface roughness effect on high energy fertilizer materials: 127
Reference: 133
Chapter 5: Calibration of Silicon Germanium 0.3 THz horizontal radar system for homeland, defense and food processing applications 137
5.1 Introduction: 138
5.2. FMCW (frequency-modulated continuous wave) radar operating principles 139
5.3 Design and performance of fully integrated 122 and 60 GHz SiGe transceiver for industrial radar applications: 140
5.4 Calibration & performance evaluation of 300 GHz (0.3 THz) FMCW radar source 145
5.4.1 Antenna working mechanism and Joule heat effect on silicon microlens antenna: 147
5.5 Physical optical methods for measuring radar cross section (RCS) of two canonical objects 150
A. circular flat plate: 150
B. Rigid circular cylinder: 153
5.6 Experimentally verification of modelled TRCS of brass cylindrical object: 155
5.6.1 Data collection of 300 GHz radar source and data processing: 155
5.7 Direct and concealed detection of metallic object using prototype THz radar system 157
5.8 AI based classification of different types of metallic objects using THz radar source 158
5.9 Using the calibrated system for freshness detection in meat – A unique utility: 162
5.10 Existing work – THz for meat freshness 163
5.11 Preliminary data collection – biological correlations: 164

5.11.1 Collection of polutry data for training AI model – primary data collection: 165
5.11.2 Analysis, interpretation and model making: 166
5.11.3 Linear model to predict freshness: 170
5.12 Feed forward artificial neural network-introduction and architecture:.....171
5.12.1 Backpropagation: 172
5.12.2 Cross validation: 173
5.12.3 Optimizing backpropagation.....173
5.12.4 Prediction and accuracy: 174
5.13 Conclusion: 178
References:.....181
Chapter 6: Study of ultra-thin & free-standing α-MoO_3/β-PVDF composites for radar shielding applications.....187
6.1 Introduction:.....188
6.2 Experimental methods and sample preparation: 190
6.2.1 Starting materials & preparation of the thin sheets of β-PVDF and α-MoO_3/β-PVDF composites: 190
6.2.2 Experimental techniques of measurement of THz electromagnetic shielding values of α-PVDF composites: 191
6.3 Measurement of concealed metallic target using 300 GHz radar source.....192
6.4 Results and Discussion: 193
6.4.1 Crystallographic information & Raman spectroscopy:.....193
6.4.2 Electromagnetic shielding interface of α-MoO_3/β-PVDF composites in THz range: ..198
6.4.3 Radar shielding application: 203
Reference: 206
Chapter 7: Conclusion and future scope: 212
7.1 Conclusion: 212
7.2 Future Scope: 214
Appendix A Radar Code Flowchat.....215
Appendix B THz Radar Cross Section Simulation using MATLAB Software.....217

List of Figures

Figure 1.1 Electromagnetic spectrum……2
Figure.1.2: Schematic diagram of THz generation from photoconductive antenna……...5
Figure 1.3: Schematic diagram of THz generation from nonlinear crystal by optical rectification process……8
Figure 1.4: Schematic diagram of optical rectification process……...9
Figure 1.5: IMPACT diode in CMOS process……...12
Figure 1.6: Schematic diagram of THz detection using photoconductive antenna……14
Figure 1.7. Schematic diagram of THz detection using electro-optic sampling……16
Figure.1.8 The direction of the polarization of THz and probe laser beams……16
Figure 1.9 Pyroelectric detector…….……...18
Figure.1.10 Structure of Photoconductive Antenna……...……...19
Figure 2.1: The development of pulsed laser technology and significant achievements in the field of laser research are discussed in the article "High-Power Lasers" available at the link provided(https://www.americanscientist.org/article/high-power-lasers) 34
Figure.2.2: The experimental setup schematic for THz generation and transmission/absorption measurements……...……37
Figure.2.3: Experimental set-up for efficient second harmonic generation using femtosecond laser amplifier. The spectrum is recorded using Maya 2000 pro-ocean optics spectrometer…39
Figure. 2.4: Diagram of the design of the experiment for employing a pyro-electric detector to evaluate the power of the terahertz signal from nonlinear crystals……39
Figure.2.5 Schematic experimental set up for THz reflection geometry…….….41
Figure 2.6 Base board of 300 GHz (0.3 THz) silicon radar……...….43
Figure.2.7 Schematic diagram of the 300 GHz signal ……44
Figure.2.8 Schematic of the 300 GHz transceiver……45
Figure 2.9 Design for a monostatic, single-channel TRx device operating at 300 GHz……...47
Figure.2.10 Schematic Experimental setup for 0.3 THz radar……...48
Figure 2.11 (a) Pins 18 (5V) as well as 20 (GND) within the CN7 connector of the F303RE Nucleo board provide the power connection (5V, GND) on the bottom side of the Easy. (b) Power Connection on the 300 GHz front end (5V, GND) …….……...49
Figure.2.12 Flowchat of 300 GHz silicon radar code……50
Figure. 2.13: Experimental setup was designed for tunable second harmonic generation within the range of 325-340 nm using nanosecond lasers, with components including (1) Nd: YAG

laser; (2) 532 nm pump beam for dye laser; (3) Dye laser; (4) Vertically polarized fundamental dye radiation; (5) Plano convex lens with f = 50 cm; (6) Plano concave lens with f = - 25 cm; (7) crystal; (8) Fundamental and its SHG radiations, (9) CaF_2 prism, (10) Horizontally polarized generated UV radiation (SHG), (11) Power/energy meter, (12) Unconverted vertically polarized fundamental radiation and (13) Beam dumper……...…...51
Figure. 3.1: Refractive index v/s Incident wavelength of Bismuth triborate (BIBO) crystal in YZ plane (Type –I o e e interaction) obtained from the Sellmeier relation (3.22), (3.23) & (3.24) respectively…….....…….69
Figure 3.2 The figure displays the variation of the input dye laser energy (E_1) at different dye laser wavelengths (λ_1) during the interaction, maintaining a constant energy for the dye pump beam. The blue dots in the graph correspond to our measured values……70

Figure.3.3: The angle tuning characteristics for second harmonic generation (SHG) in Bismuth triborate crystal are depicted in the figure. The black smooth curve represents the theoretical prediction obtained from the Sellmeier coefficients of the inorganic Bismuth triborate (BIBO) Crystal, while the blue dots correspond to our measured values……71
Figure. 3.4: Angular acceptance bandwidth of SHG in 1.29 mm thick Bismuth triborate. The smooth curve is theoretically predicted while the dots are experimental points...…….71
Figure.3.5: Spectral acceptance bandwidth of SHG in 1.29 mm thick inorganic BiB_3O_6 crystal. The smooth curve is theoretically predicted while the dots are experimental points……72
Figure.3.6 Illustrates Nonlinear coefficient (d_{eff}) with incident wavelength (λ_1) and Phase Matching Angle (θ) of inorganic Bismuth triborate Crystal. The black dots are theoretical points whereas blue dots are experimental point…….……...73
Figure. 3.7 Variation of energy E_1 of dye SHG in 1.29 mm thick BIBO.The black dots are experimental points where as red smooth curve are theoretical value……...74
Figure.3.8 Variation of energy E_1 of dye SHG in 1.29 mm thick BIBO.The blue dots are experimental points where as black smooth curve are theoretical value……74
Figure 3.9: (a) Spectral profile distributions of the fundamental (1ω) laser pulse at 800 nm and the second harmonic (2ω) pulse at 400 nm. (b) and (c) show the peak profiles at 400 nm and 800 nm wavelengths, respectively. The fitting was performed after collecting data points from the Maya 2000 Pro Ocean Optics spectrometer (India) and confirms the Gaussian nature of the incident and generated radiation. The blue dots represent experimental values, while the black smooth curves are Gauss Amp fitted values…….75
Figure 3.10:(a) Temporal Profile of (a) Bismuth triborate Crystal (b) air…….77

Figure. 3.11 Spectral Profile of BIBO Crystal with respect to air. The black curve represents the spectral amplitude for air & blue one for BIBO crystal……77
Figure. 3.12: (a) Refractive Index and (b) Extinction Coefficient of biaxial inorganic BIBO crystal. The refractive index & absorption coefficient are calculated using equations (2.2) & (2.3) in the Chapter 2……...……...……...77
Figure. 3.13 (a) Transmittance (b) Absorbance of Bismuth triborate Crystal in THz domain……...…...78
Figure. 3.14 (a) Relative Permittivity (b) Reflectivity of BIBO Crystal in THz domain……...79
Figure. 3.15 Optical Conductivity of BIBO Crystal. The values are calculated by the equation (2.9) in the chapter 2……...…...79
Figure. 3.16: Coherent length of biaxial BIBO Crystal in THz domain……80
Figure.3.17 THz SHG efficiency with the variation of incident femtosecond laser power…...80
Figure. 3.18 (a) Time domain spectra and (b) Generated THz frequency range of GaSe: S in transmission mode……81
Figure. 3.19 (a) Refractive Index (b) Absorption coefficient semiconductor semimetal rough GaSe: S crystal……...…...81
Figure. 3.20 (a) Time domain (b) Frequency domain signal from GaSe: S with respect to gold coated mirror surface as a reference…….……82
Figure.3.21 (a) Refractive Index (b) Absorption Coefficient of semi metal & semiconductor GaSe: S crystal in THz domain……83
Figure.3.22 Coherence length of S doped GaSe crystal. The values are calculated by equation (2.7) in Chapter 2……...…...84
Figure.3.23: THz power generated from S doped GaSe crystal with the variation of incident laser power. The generated power was measured by using pyroelectric detector…….84
Figure.3.24: (a) GaSe: S crystal and (b) 2D Surface image. The 2D Surface image is captured by the optical profilometer (Model No: Bruker-Contour GT) ……..…85
Figure.3.25(a) g value & (b) ρ value of S-doped GaSe crystal at 25-degree angle of incidence……...86
Figure. 3.26. Reflection Coefficients of S doped GaSe crystal with respect to angle of refraction at 0.7 THz. The black curve represents the reflection in transverse magnetic mode whereas the red curve represents the transverse electric mode…….……87
Figure.3.27: Optical impedance of S doped semiconductor semimetal rough crystal…….…87

Figure.3.28. Theoretical calculation for ordinary & extraordinary refractive index of α-TeO_2 Calculated by equations (3.29) & (3.30) respectively. The black smooth curve represents ordinary refractive index whereas pink one represents the extra ordinary refractive index….88
Figure. 3.29. Group velocity (b) Coherence length of α-TeO_2 crystal in THz domain……...89
Figure.3.30. Type-I Phase matching angle with respect to generated second harmonic wavelength of α-TeO_2 crystal……89
Figure.3.31. Pump wavelength vs generated wavelength α-TeO_2 crystal in THz domain……90
Figure.3.32 (a) Temporal (b) Spectral profile of semimetal semiconductor α-TeO_2 Crystal. The blue dotted line in the spectral profile is represented as high SNR (~10^6) ……90
Figure. 3.33. (a) Refractive Index (b) Absorption Coefficient of α-TeO_2……91
Figure.3.34 (a) Permittivity of semimetal semiconductor α-TeO_2 Crystal & (b) imaginary part of dielectric constant of α-TeO_2 Crystal shown as a function of broadband high THz frequency at 30^0 C……..……..……...92
Figure.3.35 Comparative study of Figure of Merits of α-TeO_2 in Optical and THz domain. FOM values are calculated by using equation (3.31) ……93
Figure 4.1: Lateral resolution of THz frequency for metallic and explosive targets……107
Figure 4.2 A 2D rough surface scattered by THz wave with incidence and scattering angles of θi and θs, respectively. The formula for calculating surface height is z = h(x) = cosθ = cosθi (r = 1), where d is the distance between any two points on the rough material's surface……....108
Figure.4.3 Schematic diagram of (a) AFM at HCU & (b) stylus profilometer……...111
Figure.4.4 Schematic diagram of an Interferometric Profilometer ……111
Figure.4.5 Schematic diagram of atomic force microscopy setup……...113
Figure 4.6: (a) Optical images of (i) a painted metallic object and (ii) an unpainted metallic object. (iii) Time-domain waveforms from the reference (gold-coated mirror) and both types of objects. (iv) Frequency-domain waveform of the reference and both test samples. (b) Refractive index and (c) absorption coefficients of the test samples with respect to THz frequency…….…...116
Figure 4.7: (a) 2D-THz images of a painted old metallic object at frequencies of 0.5, 1.0, 1.5, and 2.0 THz, respectively. (b) 3D surface images of the same object at frequencies of 0.5, 1.0, 1.5, and 2.0 THz, respectively. (c) Effect of surface roughness on the effective reflectivity of the painted surface at given THz frequencies. (d) Reflection coefficients versus THz frequency for different levels of roughness in TE mode……...118

Figure 4.8: (a) 2D-THz images of a rusted old metallic object at frequencies of 0.5, 1.0, 1.5, and 2.0 THz, respectively (b) 3D surface images of the same object at frequencies of 0.5, 1.0, 1.5, and 2.0 THz, respectively. (c) Effect of surface roughness on the effective reflectivity of the rusted surface at given THz frequencies. (d) Reflection coefficients versus THz frequency for different levels of roughness in TE mode.....119
Figure 4.9: Quality factor of coated and uncoated old metallic objects as a function of THz frequency……...…….121
Figure 4.10: Influence of surface roughness on optical and THz imaging of a coin….……123
Figure 4.11: THz 2D imaging of NH_4NO_3 at frequencies (a) 0.5 THz, (b) 1.0 THz, and (c) 1.5 THz, with corresponding 3D surface profiles at (d) 0.5 THz, (e) 1.0 THz, and (f) 1.5 THz.……124
Figure.4.12 Surface roughness effect on NH_4NO_3……...……...125
Figure.4.13(a) AFM image (b) surface analysis of NH_4NO_3……..…126
Figure.4.14 Reflection Coefficient of NH_4NO_3……...……...127
Figure.4.15 THz 2D imagining of Urea at (a) 0.5 THz (b) 1.0 THz (c) 1.5 THz corresponding the 3D Surface Profile at (d) 0.5 THz (e) 1.0 THz & (f) 1.5 THz……128
Figure.4.16 Surface roughness effect on Urea……129
Figure.4.17 (a) AFM image (b) surface analysis of Urea……129
Figure.4.18 Reflection Coefficient of Urea in TE mode……130
Figure 5.1 Block diagram of a single-channel, bistatic TRx chip for 122-GHz radar operation (PLL-Phase Locked Loop, TRx-Transceiver) ……...142
Figure 5.2 Block diagram of a single-channel, monostatic TRx chip, for 60-GHz operation……144
Figure 5.3 Block diagram of a single channel, monostatic TRx chip, for 300 GHz (0.3 THz) operation……...……...…...145
Figure 5.4 (a) Photograph of Silicon microlens antenna (b) Geometry of Silicon microlens antenna copywrite [Ref. 31] ……....……147
Figure 5.5. Silicon lens affected by varying temperature.....149
Figure.5.6 Circular flat plate and radar position…….....….150
Figure.5.7 Radar cross-section simulation for circular flat plate.....151
Figure.5.8 Back scattered TRCS for a flat circular plate w.r.t (a) THz frequency (b) aspect angle.....152
Figure.5.9 Rigid cylinder cross-section simulation.....153

Figure. 5.10 (a) Circular cylindrical configuration and radar position (b) Finite length cylinder cross section with respect to THz frequency……...154
Figure.5.11 Back scattered TRCS for a circular cylindrical target with respect to (a) aspect angle (b) THz frequency…….……..……..…154
Figure. 5.12 Measurement of range of brass cylindrical object using 0.3 THz SiGe radar source.....155
Figure.5.13 (a) Finite length circular brass cylinder configuration (b) experimentally verifies THz RCS for a circular rigid cylinder.....156
Figure 5.14 Direct detection of metallic target using 0.3 THz radar source……157
Figure 5.15 (a) Metallic object inside the cardboard (b) Detection response from metallic object at 1.0 m distance using 0.3 THz Silicon radar source.....157
Figure 5.16 Response of bandwidth to achieve maximum target distance using 0.3 THz radar source.....158
Figure 5.17 Detection of radar signal of different types metallic objects (a) direct and (b) concealed condition.....160
Figure 5.18 Average peak power of different types of metallic targets in concealed and non-concealed conditions.....160
Figure 5.19 Detection of radar signal of different types of explosive materials (a) Direct and (b) concealed condition.....161
Figure 5.20 Average peak power of different types of explosive targets in concealed and non-concealed conditions.....161
Figure 5.21 k-NN algorithm classification of object samples into various metals, with accuracy of 87.5% in metals.....162
Figure 5.22 k-NN algorithm classification of explosive substances into Tetryl (CE), TEX, TNT and CL-20 with accuracy of 92.3%.....162
Figure 5.23 Trend in reflectivity signals observed over time duration in a single day for a biological sample.....165
Figure 5.24 Prototype 0.3 THz Radar system with all components.....166
Figure. 5.25: System with analysis system with analysis in smartphone via a remote server. Another embodiment of the same idea is as in same figure no. used.....167
Figure 5.26. Flowchat of THz meat freshness detection system.....167

Figure. 5.27 Trending data of the 0.3 THz radar source (a) average reflected power signal with respect to time (b) average reflected power vs average density (c) average time vs average density (d) average pH with average time.....168
Figure 5.28 (a) Local non-linear corelation with pH (b) Trend of density with power.....170
Figure 5.29 (a) Actual vs Predicted values for a typical untrained day (Time and pH) 171
Figure 5.30 (top to bot Feedforward ANN architecture used in our system. Modular ANN for prediction of (a) pH and (b) time respectively. (c) The density module is trained separately using weight and volume as parameters alongside Temperature, humidity and signal.....174
Figure.5.31 Feed forward ANN based model for prediction of (a) time & (b) pH.....175
Figure.5.32 A flowchart summarising the model creation process is as attached adjacent....176
Figure.5.33 Freshness score with respect to the time of the day.....176
Figure 6.1 (a) Sample preparation process of ultra-thin α-MoO_3/β-PVDF composites (b) optical image of PVDF-F, M1, M2, M3, M5, and M7 samples by prepared 1 wt%, 3 wt%, 5 wt% & 7 wt% of α-MoO_3 respectively……..…191
Figure 6.2. X-ray diffractograms of PVDF-O, MP, PVDF-F, and different free-standing α-MoO_3/PVDF composite films (M1, M3, M5, and M7). The X-ray diffractograms are recorded using Copper Kα radiation……..…193
Figure 6.3**.** X-ray diffractograms of PVDF-O, MP, PVDF-F, and different free-standing α-MoO_3/β-PVDF composite films (M1, M3, M5, and M7) in the 2θ range of 16°-29°. The crystallographic planes in α and β phases of PVDF are indicated……194
Figure 6.4. Raman spectra of PVDF-O, MP, PVDF-F, and different free-standing α-MoO_3/β-PVDF composite films (M1, M3, M5, and M7). 532 nm LASER was used to record these spectra……195
Figure 6.5: Raman optical Micrographs of PVDF (M0) and its α-MoO_3 composites at 1 wt% (M1), 3 wt % (M3) and 7 wt % (M7) ……196
Figure 6.6: Scanning Electron Micrographs of PVDF (M0) and its α-MoO_3 composites at 1wt% (M1), 3 Wt % (M3) and 7 wt % (M7) ……197
Figure 6.7. Graphical representation of THz EMI shielding for α-MoO_3/β-PVDF composites.....198
Figure 6.8. (a) transmission (b) reflection (c) absorption and (b) effective absorption for α-MoO_3 in the composites with different weight percentage of MoO_3 sample.....200

Figure 6.9**.** (a) EMI shielding by transmission, (b) EMI shielding by reflection, (c) EMI shielding by absorption, and (d) total shielding of PVDF-F and α-MoO_3/β-PVDF composite films (M1, M3, M5, and M7) as a function of THz frequencies…….201
Figure 6.10 Absolute Shielding values of 100 μm thick PVDF-F, M1, M3, M5, and M7 at 205, 840, 841, 842 and 888 $dBcm^2g^{-1}$, respectively. The calculations are done by considering twenty measurements for each sample……...202
Figure 6.11. (a) The real part (i.e., permittivity) and (b) imaginary part of the dielectric constants (ε″) of the 100 μm ultra-thin free-standing M7, M5, M3, M1 and PVDF-F samples as a function of the considered THz frequencies…….203
Figure 6.12. EMI Shielding by reflection of α-MoO_3/β-PVDF composite films for radar applications……...……..203
Figure 6.13. (a) Radar signal of direct metal & concealed metal with wrap of α-MoO_3/β-PVDF composites ……..……...204

List of Tables

Table -3.1 Comparision of three nonlinear crystals for their properties.....68

Table -3.2 Summary of THz generation for three nonlinear crystals carried out in this thesis chapter 3.....94

Table-4.1 Values of Q-factor and signal to noise ratio of painted and unpainted/rusted objects.....122

Table 4.2 Comparision of surface roughness of different types of materials using AFM, optical profilometer & THz profilometer.....131

Table 5.1: Results from analysis methods used for determining Time and pH.....177

Table 6.1. THz electromagnetic shielding of nanomaterial/polymer composites with optimal characteristics……...…….....188

Table 6.2: Vibrational mode wavenumbers (cm^{-1}) of undoped PVDF……195

Table 6.3: Energy dispersive x-ray spectrum (EDX) analysis of PVDF and its α-MoO_3 composites……..…197

Chapter 1

Introduction and Thesis Overview

Abstract

In this chapter, we briefly discussed the fundamentals of THz radiation and its excellent properties. We described the THz sources and detectors used in this thesis. This chapter also covers the fundamental mechanisms responsible for efficient THz generation and detection from PC antennas and non-linear crystals. A short description of electronic source used for THz generation and detection techniques, such as Gunn diodes, IMPATT diodes, and frequency multipliers was also included. Furthermore, we discussed the advantages of electronic sources over optical sources. Finally, summary and organization of thesis is presented.

1. Introduction and Motivation:

The understanding of the interaction of light with metals have paved way for a wealth of new applications across diverse fields revolutionising our daily lives. The ongoing research and development in the field of terahertz science and technology is now matured enough and finds potential applications in the various fields such as defense, chemical and biological, food industries etc. THz band lie between the infrared and microwave region of electromagnetic spectrum having frequency range of 100 GHz (1 GHz = 10^9 Hz) - 10 THz (1 THz = 1 x 10^{12} Hz) which corresponds to wavelengths ranging from 30 µm to 3 mm [1]. It has unique features such as high absorption in water, highly reflected from metal surfaces, and transmit through packing materials such as cardboard, cloths, plastic, leather, wood etc., as compared to the other electromagnetic radiation. In addition, it has wide range of spectral features associated with vibration of bonds in organic and inorganic molecules, semiconductor intra-band transitions, vibrational and rotational transitions of organic molecules [1-4]. Furthermore, it is a non-ionizing and non-destructive in nature because of low photon energy (order of meV) [4-5].

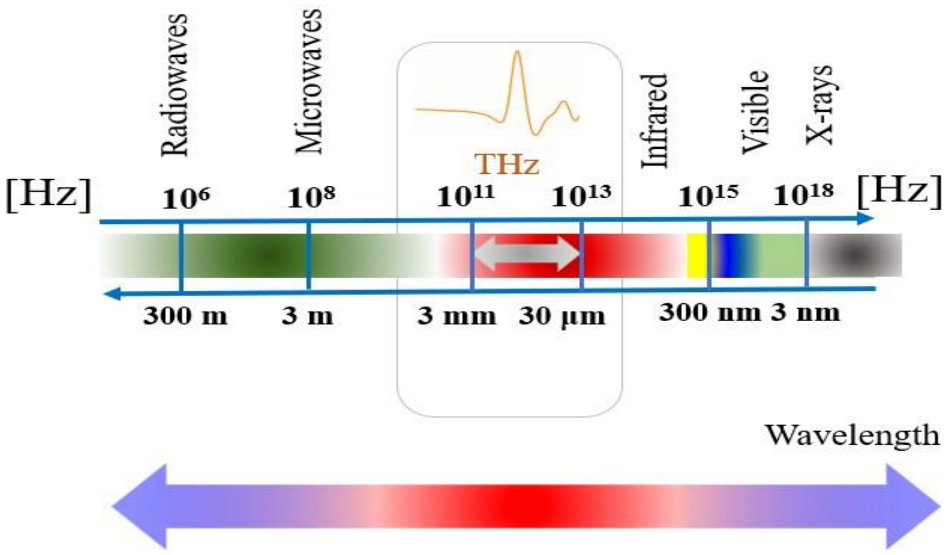

Figure 1.1 Electromagnetic spectrum

Figure1.1 shows the electromagnetic spectrum of THz and its neighbouring radiation range which is extended up to far-infrared region. THz spectroscopy is an efficient technique for identification and characterisation of material's polymorphic structures as compared to X-ray diffraction and Raman spectroscopy techniques [6]. X-ray diffraction is limited to large crystalline structures and destructive in nature whereas Raman spectroscopy induces phase change in material during measurements. THz spectroscopy is a potential solution to these

limitations. Terahertz time domain spectroscopy (THz-TDS) is a powerful and versatile techniques used for investigating the optoelectronics properties and silent spectroscopic features of organic materials in the transmission/ reflection. The interaction between the terahertz pulses and the sample leads to absorption, reflection or transmission of the radiation depending on the material's properties. THz time resolved spectroscopy (TRTS) is useful in studying the dynamic properties of different types of materials including water molecules [7]. TRTS has several advantages over other known techniques such as time-resolved luminescence, transient absorption, pump-probe and four wave mixing in determination of material's dynamical properties which can be extended to study the carrier dynamics of direct and indirect bandgap semiconducting materials, while luminescence technique is restricted to only direct band gap materials [8]. It can also probe material properties evolving with frequencies whereas four wave mixing and transient grating are unable to determine the frequency dependent properties. Moreover, it can be used to study the intraband relaxation as well as interband recombination dynamics of excited carriers in materials on ultrafast time scales [9].

As compared to X-ray imaging, THz imaging has several advantages such as increased in image contrast, chemical identification, and reduced risk of radiation exposure from high energy materials [10]. The advancement in the nonlinear crystal growth technology attracted many optics group to explore their potential as a THz source using optical frequency mixing techniques. In continuation of same, we have also selected three numbers of well crystals for the efficient THz generation. There are several challenges associated with the detection of THz radiation in real time measurements in standoff mode. One of the most common reasons is the absorption due to presence of water molecules in the atmosphere that restricts the use of THz radiation in detection, spectroscopy and imaging to shorter and longer distances [11-13]. This limitation can be overcome by increasing the sensitivity of THz detector, selection of frequency (where no water absorption peak is available) in air windows and increasing the emission efficiency (or using powerful THz sources). Hence, there is need to develop high power sources and sensitive detectors in THz domain.

Recently, several groups have shown that standard silicon technology can be used as a potential candidate for terahertz generation and detection. The semiconductor THz source enabling easy integration with on-chip readout and control electronics. The motivation for designing and calibrating THz silicon radar systems lies in their potential advantages across various applications. These systems offer high-resolution, high accuracy imaging and spectroscopic capabilities at THz frequencies, enabled by silicon technology's superior performance in this

range compared to lower frequencies. Additionally, THz radar systems penetrate diverse materials and detect molecular signatures, making them valuable for security, non-destructive testing, and medical imaging. Leveraging silicon's attributes like high-speed electronics and integrated circuit design, THz radar achieves high bandwidth and data rates, enabling real-time communication and imaging. Electronic sources have more advantage over the optical source. Electronic sources for terahertz generation, such as Gunn diodes and IMPACT diodes, offer broad frequency coverage, making them ideal for broadband THz applications. Additionally, electronic THz sources are cost effective, simpler to operate and maintain, and easily integrate with electronic systems, enabling diverse applications like THz radar, THz communications, sensing, and imaging for different types of materials such as hidden metal, explosives, drugs, organic and inorganic materials.

Our main objective is to generate efficient THz radiation using optical rectification techniques in three selected semiconductor, semimetal and inorganic crystals. THz radiation can be generated and detected using different types of electronic and optical techniques. Among all of them, optical rectification, photoconductive switching, and focusing of ultra-short pulses in air and semiconductor surfaces are some of the widely used generation techniques. The photoconductive and electro optic sampling are also treated as prominent coherent detection techniques. Whereas, micro-bolometer, pyrometer and Golay cells are employed as an incoherent detection device. In this thesis, we have employed ultra-short pulses based optical techniques for generation, detection of THz radiation from three selected nonlinear crystals such as BIBO, S-doped GaSe and α-TeO_2 crystals [14-16]. In certain instances, the intensity of light is diminished and scattered in various directions due to the rough surface of the target material. Consequently, while attempting standoff detection of targets, we encounter challenges due to reduction in signal strength. To address this issue and mitigate the impact of water absorption in the free space medium, along with the presence of rough surfaces on the targets, we have developed a modality to convert 2D imaging system into a 3D THz profilometer. This device enables us to measure the surface roughness of different types of surfaces like metallic, painted and rusted naval vessel and explosive war head targets accurately. The nonlinear optics-based THz system is pumped by femtosecond laser pulses and its detection systems are coherent and incoherent in nature. Therefore, this system is suitable for short distance measurement like transmission and reflection modes. However, for long range detection a heterodyne type of detection system requires which needs a lot of optics and kinematics mounts, stages etc. The best demonstration of long-range application in form of horizontal radar system, we have selected single frequency 0.3 THz electronic source which is clubbed

with facility of source and detector aligned at very short or acute angle (2°). Finally, we have calibrated the prototype 0.3 THz silicon radar system for short range upto 3 meters for different types of target materials such as explosive, metal and dairy product. In addition, we have also tested the same system for evaluating the shielding effect of α-MoO_3 materials for EMI radar applications.

1.1 Generation and detection of terahertz waves from optical and electronic source:

1.1.1 Optical terahertz sources:

Many optical sources, including ultrafast photoconductive antenna switching, optical rectification in nonlinear crystals, CO_2 lasers, semiconductor substrates, free electron lasers, optically and electrically pumped lasers, etc., are the source of terahertz radiation. Surge currents and nonlinear processes on the semiconductor surface can produce THz radiation [17-27]. Based on key factors like laser power, spectral bandwidth, and pulse duration, we chose PC antennas and crystals for THz source and detector. On the other hand, the electronic based such as resonant tunnelling diode, backward wave oscillator, nonlinear mixing, photo mixing techniques, two terminal solid-state device (IMPACT diode and Gunn diode), and frequency modulation techniques also responsible for THz generation. We have described all types of aforesaid techniques for the efficient generation of THz radiation.

1.1.1 (a) Photoconductive switching techniques:

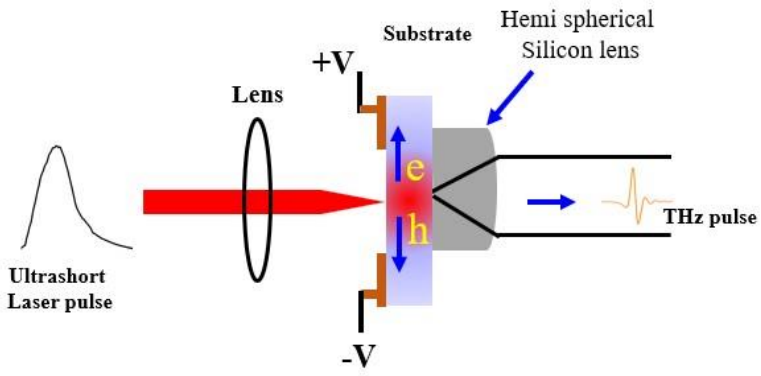

Figure. 1.2: Schematic diagram of THz generation from photoconductive antenna.

In this technique, photoconductive antennas (PCAs) fabricated on a semiconductor substrate (such as GaAs, InAlAs, InGaAs etc.) are employed for efficient terahertz (THz) generation. Ultrashort laser pulses are directed onto the semiconductor substrate to induce photo excitation, leading to the generation of ultrashort lifetime free charge carriers within the semiconductor.

These charge carriers undergo acceleration by an applied bias field across the antenna, thereby inducing a transient current within the substrate, which in turn is responsible for THz generation. Ultrafast pulsed broadband THz radiation was initially produced and observed in the 1980s using optically pumped PCAs by research teams under THz innovators David Auston [28-31] and Daniel Grischkowsky [32-34]. The idea is depicted in Figure 1.2. An ultra-short optical pulse interacts with a biased metal dipole antenna on a photoconductive substrate, generating high-frequency THz pulse through acceleration of photocarriers. Carriers are made in the photoconductor as the pulse is absorbed, accelerating along the bias field to produce a transient photocurrent proportional to the pulse intensity. Photoconductors with short carrier lifetimes like low temperature (LT) GaAs are used to prevent pulse broadening. Laser pulses for photo excitation must have enough energy to exceed the semiconductor band gap. The semiconductor material switches between non-conductive and conductive states based on the laser pulse width and carrier lifetime. PCAs are classified by gap size into (i) small, (ii) semi-large, and (iii) large groups. The loosely defined antenna gap values for these categories are 5-50 μm (<100 μm), 0.1-2 mm, and 1-5 mm (> 1 mm), respectively. Semi-large and large gap antennas have the capability to generate high-power THz radiation compared to narrow gap antennas. However, they necessitate large biasing voltages and high-power lasers for operation, unlike small gap antennas. Moreover, the bandwidths generated by semi-large and large gap antennas tend to be narrower than those of small gap antennas. Therefore, small gap antennas are more suitable for the generation of broadband THz radiation.

1.1.1 (b) Optical rectification techniques in nonlinear crystals:

We present an overview of the underlying the physics involved in the THz generation process through optical rectification utilizing ultra short laser pulse. To facilitate a comprehensive understanding needed for accurate system modelling, we initially employ models based on the undepleted pump approximation. Given that experimentally observed optical-to-THz conversion efficiencies typically remain below 10%, invoking this approximation appears reasonable initially. It will be demonstrated in this section that such models adequately explain many fundamental aspects of THz generation by optical rectification, particularly in a qualitative sense. Although, THz generation via ultra short-pulse constitutes a non-collinear process and is ideally modelled in two dimensions (2D) [35], our analysis commences with a treatment employing an effective 1D equation, as outlined in previous works. Let the electric field of THz radiation with angular frequency ω moving in the z-direction be represented as E_{THz}, (n,z). With regard to the THz pulse, the optical pump pulse

travels at an angle γ, where γ is the angle of the ultra-fast pulse. It is observed that the optical field spans a distance z/cosγ when the THz electric field propagates a distance of z, simplifying the scenario to one dimension. As an alternative, the effective wave number of the optical field can be decreased by cosγ. Although this method may be considered phenomenological, it successfully elucidates several elements of optical rectification by using ultra-short, high-power laser pulses. For the THz electric field at each angular frequency ω driven by, we have developed the 1-D wave equation at each angular frequency ω driven by the nonlinear polarization term P_{THz} (ω,z)

$$\frac{d^2E_{THz}(\omega,z)}{dz^2} + k^2(\omega)E_{THz}(\omega,z) = -\frac{\omega^2}{\varepsilon_0 c^2}P_{THz}(\omega,z) \tag{1.1}$$

The nonlinear polarization term for optical rectification involves various difference frequency processes within the bandwidth of the optical pump pulse spectrum. Optical rectification is a second-order nonlinear process activated by strong laser light on optical materials to induce direct current polarization. As a result, it may be expressed as in (1.2), where $\chi_{eff}^{(2)}$ represents the nonlinear materials' effective second-order nonlinearity.

$$P(\omega,z) = \varepsilon_0 \chi_{eff}^{(2)} \int_0^{\infty} E_{opt}(\omega'+\omega)E_{opt}^*(\omega')e^{-j\left(k(\omega+\omega'')-k(\omega'')\right).z}d\omega'' \tag{1.2}$$

The envelope of the optical pump probe's electric field at angular frequency (ω") is denoted by E_{opt}(ω"). The exponent k(ω+ω")'s factor, after removing the effects of group velocity dispersion, -k(ω") =$(\cos\gamma)^{-1}\omega n_g(\omega)/c$. It depicts the ultra-short laser pulse phenomenologically. The formula in (1.2) simplifies to that in (1.3) for a transform-limited Gaussian pulse centered at co.

$$P_{THz}(\omega) = \varepsilon_0 \chi_{eff}^{(2)} \frac{E_0^2\tau}{2\sqrt{2\pi}} e^{\frac{-\omega^2\tau^2}{8}} \tag{1.3a}$$

$$E_{opt}(\omega) = \frac{E_0\tau}{2\sqrt{\pi}} e^{\frac{\tau^2(\omega-\omega_0)^2}{4}} \tag{1.3b}$$

The THz peak electric field amplitude, E_0, and the e^2 pulse width, τ/√2, are shown in (1.3). The ratio τFWHM/√(2ln2) = τ may be used to link it to the full width at half maximum (FWHM) pulse width. In the case that group velocity dispersion (GVD) of the optical pulse is omitted, a general analytic solution to (1.1) is attainable. Examining this expression is interesting because it sheds light on important characteristics of THz radiation produced by optical rectification. Generally speaking, the answer to (1.1) is the product of the forced and homogeneous solutions. This is stated in (1.4) below. It is assumed that there is no THz wave moving backward. In

sufficiently thick crystals, this is a plausible approximation where the backward propagating THz wave would be absorbed by the material.

$$E_{THz}(\omega, z) = Ce^{-jk(\omega)z} - \frac{\omega^2 \chi_{eff}^{(2)} {E_0}^2 \tau}{c^2 2\sqrt{2\pi}} e^{-\frac{\omega^2\tau^2}{8}} e^{-\frac{j\omega n_g(\omega_0).\, z}{c}} \quad (1.4)$$

The boundary condition $E_{THz}(\omega, 0) = 0$ is used to determine the constant C. This indicates that the THz field is zero at the crystal's commencement. With these justifications included, the analytical expression for the THz field in (1.5) is as follows.

$$E_{THz}(\omega, z) = -j\frac{\omega^2 \chi_{eff}^{(2)} E^2 \tau}{c^2 2\sqrt{2\pi}} \frac{e^{-\frac{j}{2}\left(\frac{\omega n(\omega)}{c} + \frac{\omega n_g(\omega)}{c\cos\gamma}\right).\, z}}{\left(k(\omega) + \frac{\omega n_g(\omega_0)}{c}\right)} \mathrm{Sinc}\left(\frac{\omega[n(\omega) - n_g(\omega_0)/\cos\gamma]z}{c}\right).z \quad (1.5)$$

There are similarities between equation (1.5) and other nonlinear optical generating techniques [27]. The characteristic sinc function, which is maximal for an argument of zero, describes its fluctuation with propagation. The phase-matching condition is determined by this criterion. As a result, we can obtain the matching phase-matching condition in (1.6) by setting the argument of the sinc function in (1.5) to zero

$$n(\omega)\cos\gamma = n_g(\omega_o) \quad (1.6)$$

This suggests that in order to satisfy equation (1.6), the pulse-front-tilt angle γ needs to be modified. Phase-matching angle is approximately 63 degrees in materials such as lithium niobate, where the group refractive index at optical wavelengths is about 2.25 and the THz refractive index is about 5. The THz electric field grows linearly with distance if the phase-matching requirement is satisfied. From a time-domain point of view, this means that the optical field propagates at an angle γ to the created THz radiation as it is generated, and the subsequently generated THz radiation coherently adds to the previously generated THz radiation. A highly broad THz pulse is produced in lithium niobate due to the material's very low refractive index dispersion in the lower THz region. This is indicative of the main feature of THz generation using ultrafast laser pulses.

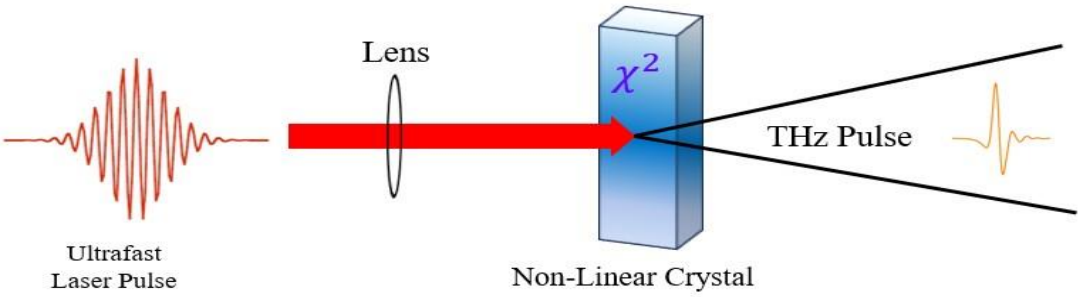

Figure 1.3: Schematic diagram of THz generation from nonlinear crystal by optical rectification process.

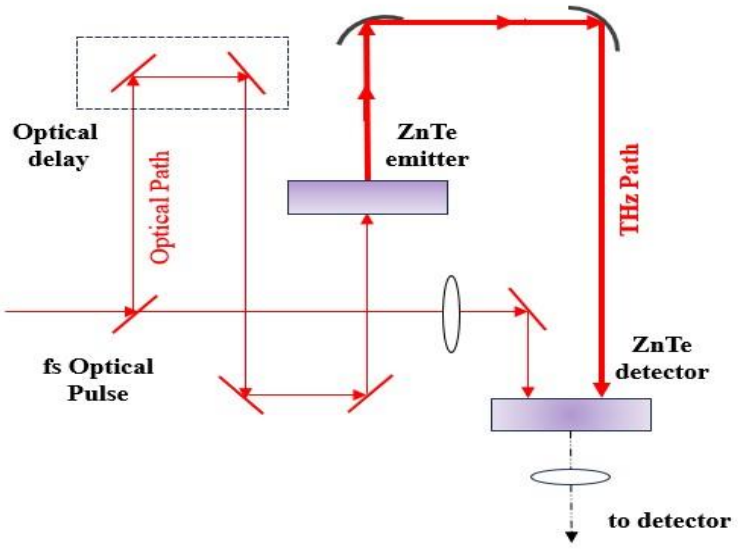

Figure 1.4: Schematic diagram of optical rectification process

The widely used optical rectification method (shown in figure 1.4) has a very wide bandwidth and a high signal-to-noise ratio. This process induces a transitory polarization, which results in terahertz radiation. When a femtosecond laser passes through a transparent crystalline material like InP, CdTe, GaAs, or ZnTe, it generates a short electrical pulse in the THz frequency band without the requirement for applied voltage. Sub-picoseconds are the duration of dc polarization under ultrashort laser pulses in nonlinear crystals. THz electromagnetic field is created as a result. For THz generation, a variety of non-linear crystals are used, including GaAs, InSb, InAs, and others. Figure. 1.3 illustrates how optical rectification in nonlinear crystal effectively generates THz. The non-linear crystals such as GaAs, InSb, InAs, $LiNbO_3$, $LiTaO_3$, ZnTe, DAST, BNA, BIBO, S doped GaSe, α-TeO_2 etc., are used for THz generation [23,36-47]. The dc polarization in the crystal caused by the laser electric field is expressed by equation no. (1.7).

$$P(\omega, t) = \varepsilon_0 \chi^{(2)}(\omega = \omega_2 - \omega_1) E^*_{\omega_1}(t) E_{\omega_2}(t) \tag{1.7}$$

where ω is the frequency of the electromagnetic radiation generated and $\chi^{(2)}$ is the second order non-linear susceptibility. The following is the equation for THz emission from nonlinear crystals: [46, 47].

$$E_{THz}(t, \omega) \propto \frac{\partial^2 P(t,\omega)}{\partial t^2} \propto \omega_x I(\omega_x) \tag{1.8}$$

According to equation (1.8), the bandwidth of THz radiation produced is proportional to the product of the incident laser pulse's central frequency [ω_x] and frequency bandwidth [$I(\omega_x)$]. The bandwidth of THz radiation in the case of PC switching is [46]. Within the crystal's coherence length, the THz signal strength and detection sensitivity increase with crystal

thickness while the bandwidth of THz radiation detected and emitted decreases [4,46]. For THz investigations, we employed ZnTe, BIBO, S doped GaSe, and α-TeO_2 crystals. According to equations (1.8) and (1.9), THz radiation produced by optical rectification on crystals has a bandwidth ωx times larger than THz radiation produced via PC switching. The formation of THz in the optical rectification process is dependent on the nonlinear features of the material, rather than the generation of free charge carriers. As a result, even with laser pulses that have photon energies lower than the band gap of the material being used, this method produces THz radiation. However, by using laser pulses with energy above the bandgap, which can provide more THz power, the nonlinear properties of the material are improved [2,48-50]. Because nonlinear crystals are easy to align, can operate at high laser strengths, and produce broadband THz pulses, they are widely employed in THz generation. However, these values have not been supported by experimental results. The discrepancy between theoretical and experimental results forces an assessment of current models in order to identify any possible shortcomings. The spectral bending of the optical pump pulse caused by THz production was not taken into consideration by earlier models. Nevertheless, these impacts need to be taken into account in order to clarify the significant frequency decrease and spectrum broadening of the optical pump pulse that are found in experiments using both 1 μm and 800 nm pump sources. When THz photons are generated, the optical pump frequency undergoes a cascaded down-shift, which causes the spectrum broadening known as "cascading effects". The substantial spectrum widening brought about by THz production makes phase mismatch worse because of dispersive effects. Consequently, the conversion efficiency drops with propagation length more quickly than other limiting variables such as self-phase modulation (SPM). Since the material dispersion at optical frequencies (<1000 fs^2/mm) is much smaller than the group velocity dispersion (GVD) parameter, the latter appears to represent the main dispersive effect in lithium niobate. To obtain conversion efficiencies at the 1% level, cascade effects require optical-to-THz photon conversion levels larger than 100%. However, dispersive effects are made worse by cascading-related spectrum broadening, severely limiting any increase in conversion efficiency.

1.1.2 Two terminal solid-state devices:

Sub-THz radiation is typically produced using Gunn and IMPACT diodes. Due to the tendency of both diode types to function in the regions of negative differential resistance, oscillations will arise when a slight voltage variation is amplified and feedback is applied appropriately. The composition and degree of doping of the material have a major impact on how frequently the system operates. Simulations reported by A. Reklaitis and L. Reggiani

suggest that GaN IMPATT diodes may have applications up to 0.7 THz [51]. Using 0.25 μm CMOS technology, Talal Al-Attar [52] was able to build and test IMPACT diodes towards the end of 2005. In Figure 1.5, their design is depicted. Different methods allow Gunn diodes and IMPATT (Impact Avalanche and Transit Time) diodes to produce terahertz radiation (THz).

1.1.2 (a) (i) Gunn diodes:

Gunn diodes exploit the transferred electron effect in semiconductors. When a high electric field is applied across certain semiconductor materials, such as gallium arsenide (GaAs), electrons can transfer between energy valleys in the conduction band. This transfer results in a negative differential resistance (NDR) region in the current-voltage characteristic of the diode. Within the NDR region, electrons undergo transit-time oscillations, where they move ballistically through the device at high velocities. These oscillations result in the generation of microwave and millimeter-wave radiation, including frequencies in the THz range. In addition to fundamental frequency oscillations, Gunn diodes can also generate higher harmonics of the fundamental frequency. By selecting appropriate device parameters and operating conditions, THz radiation can be efficiently generated as a harmonic of the fundamental frequency.

1.1.2 (b) (ii) IMPACT diodes:

The IMPACT (Ionization-Mode Planar Avalanche-CMOS Transistor) diode source is a device utilized for THz generation. This diode source operates based on the principle of Impact Ionization, where carriers are generated via collision with high-energy electrons. In the IMPACT diode, a high electric field is applied across the diode structure, leading to carrier acceleration. When carriers gain sufficient energy from the electric field, they undergo Impact Ionization, producing additional carriers. This process results in an avalanche multiplication effect, where a large number of carriers are generated in a short period. The IMPACT diode source typically consists of a semiconductor structure, such as silicon or gallium arsenide, with appropriate doping profiles to achieve the desired electric field distribution. When biased appropriately, the electric field within the diode reaches a critical value, leading to impact ionization and the generation of THz radiation. The emitted THz radiation is a result of the ultrafast current transient induced by the avalanche process. The advantage of the IMPACT diode source lies in its compactness, high efficiency, and potential for integration with complementary metal-oxide-semiconductor (CMOS) technology. Additionally, its operation does not require ultrafast laser systems, making it attractive for various THz applications, including imaging, spectroscopy, and communication.

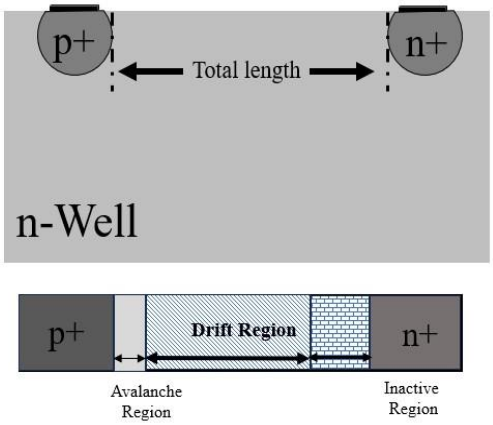

Figure 1.5: IMPACT diode in CMOS process

Both Gunn and IMPACT diodes offer compact and efficient THz radiation sources, with potential applications in spectroscopy, imaging, and communications. However, optimizing device performance and stability remains an ongoing challenge in THz technology based on diode sources.

1.1.2 (c) Frequency multipliers:

Frequency multipliers serve as a means to enhance the frequency of sub-THz emitters originating from sources like IMPACT, Gunn, and BWO through radiation coupling into nonlinear devices like Schottky diodes. The concept of frequency multiplication holds promise for THz generation, yet it comes with certain limitations, the diminishing output power with each multiplication phase. This decrease in power constrains the overall output power due to the source's limitations and the thermal capacity of the multiplier. These devices, known as frequency multipliers, function as nonlinear entities that produce harmonic frequencies of an initial signal. Typically constructed with nonlinear transmission lines or semiconductor components showcasing nonlinear traits, they respond to lower frequency inputs, such as microwave or millimeter-wave signals, by generating harmonics of the input frequency. Tailored to specific frequency ranges, frequency multipliers exhibit proficiency in producing harmonics several times higher than the input frequency. Within the realm of THz generation, frequency multipliers play a vital role in producing higher harmonics of signals within the microwave or millimeter-wave spectrum. Through the cascading of multiple frequency multiplier stages, it becomes feasible to achieve harmonic amplification reaching the THz frequency domain. Each stage of the frequency multiplier system amplifies the higher harmonics of the preceding stage, resulting in progressively elevated frequencies. The effectiveness and power output of THz radiation stemming from frequency multipliers hinge on diverse factors, encompassing the device's nonlinear characteristics, input signal potency,

and the layout of the frequency multiplier setup. Noteworthy advantages of frequency multipliers include their compact nature, simplicity in design, and broad bandwidth, rendering them suitable for a range of THz applications like spectroscopy, imaging, and communication purposes.

1.1.3 Detectors for detection of THz signal:

The detection of THz radiation involves the utilization of various types of detectors that operate based on distinct mechanisms. Given the weak nature of emitted THz signal powers, detecting THz signals poses inherent challenges. Assessing the performance of each detector is typically done by evaluating its responsivity and sensitivity characteristics. Responsivity is a parameter that establishes a relationship between the output signal of the detector and the incident power it receives. Consequently, detectors with higher responsivity levels exhibit greater output signals for a given incident power. On the other hand, sensitivity in a detector denotes the minimum level of incident power that can be detected, and this aspect is intricately linked to the output noise produced by the device. The signal noise-ratio (SNR) assumes a pivotal role in determining the effectiveness of a detector, with higher SNR values indicating superior detector performance. In field of optics, sub-THz detection, three distinct approaches are commonly employed. The first approach involves detecting ultra-short pulses, which can be achieved through two main methods. One method utilizes photoconductive sampling with a photoconductive antenna, as depicted in Figure 1.6. Alternatively, free-space-electro-optic-sampling (FS-EOS) can be employed for this purpose. FS-EOS functions by detecting the polarization alteration of the probe beam induced by the THz electric field using the electro-optic (EO) effect present in the sensor crystal. Particularly in compound semiconductors, the EO effect occurs almost instantaneously on the THz time scale, enabling FS-EOS to generate a signal that is directly proportional to the THz electric field, as cited in reference [51]. Figure 1.7 provides an illustration of FS-EOS THz detection methodologies. Both photoconductive sampling and electro-optic sampling are extensively utilized coherent techniques for THz detection. The electro-optic sampling technique relies on the pockels effect observed in nonlinear crystals. In contrast, the mechanism underpinning THz detection in the photoconductive sampling method mirrors the generation process seen in PC antennas.

1.1.3 (a) Photoconductive sampling:

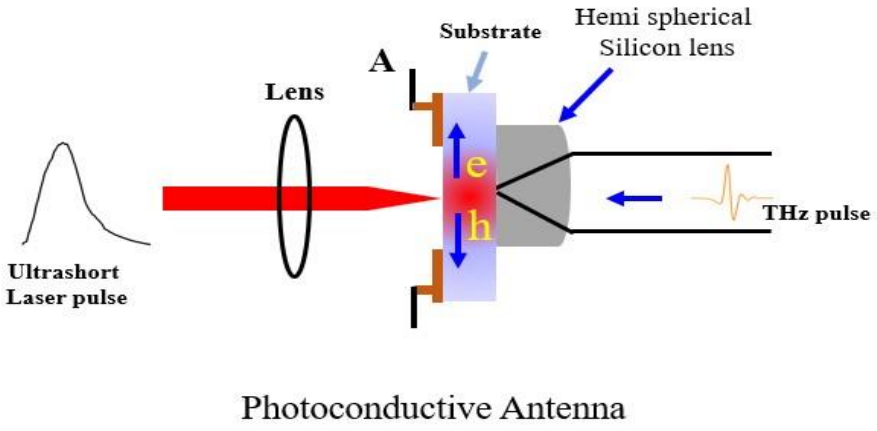

Figure 1.6: Schematic diagram of THz detection using photoconductive antenna (A-Ammeter).

In the photoconductive sampling (PCS) technique, both the generated terahertz (THz) pulses and ultrashort laser pulses are focused within the gap of an antenna. The focused laser pulses initiate the creation of free charge carriers, which are subsequently accelerated by the electric field of the focused THz radiation. This acceleration of charge carriers results in the generation of a photocurrent. The magnitude of the induced current is directly proportional to the amplitude of the focused THz radiation on the detector (i.e., antenna) and the transient carrier density [44]. To measure the induced photocurrent, a current meter, typically comprising a picoammeter and lock-in amplifier, is employed. By varying the delay time between the THz and laser pulses, the temporal profile of the THz radiation can be obtained by monitoring the induced current. Subsequently, the spectral amplitude and bandwidth of the THz radiation are determined by performing a fourier transform on the measured THz temporal profile. The schematic diagram of THz detection using PC antennas is schematically depicted in Figure 1.7. The induced photocurrent in the detector at a given delay time (t) is mathematically described by the following equation no (1.16) [4].

$$J(t) \propto \int_{-\infty}^{t} \sigma(t - t')E_{THz}(t')dt' \tag{1.16}$$

where $\sigma(t)$ is transient conductivity and $E_{THz}(t)$ is electric field of focused THz radiation on to the detector. From equation (1.13), the measured current exactly reflects the THz electric field when surface conductivity has Dirac delta function. The transient surface conductivity is written as

$$\sigma(t) \propto \int_{-\infty}^{t} \mu(t)n(t)I_{opt}(t)dt \tag{1.17}$$

Where, $\mu(t) = 1 - e^{-t/t_s}$, $I(t) = e^{-t/t_p}$ and $n(t) = e^{-t/t_c}$ are mobility, Intensity of laser pulse and transient current density of the detector. The t_p , t_c and t_n are laser pulse duration, carrier life time and momentum relaxation time. Substituting $\mu(t)$, $I(t)$ and $n(t)$in equation (1.14), then equation becomes [57]

$$\sigma(t) \propto \int_{-\infty}^{t} e^{-t/t_p^2} e^{-t/t_c} \left[1 - e^{-t/t_s}\right] dt \quad (1.18)$$

From equation (1.15), the surface conductivity is restricted by laser pulse duration and carrier lifetime of detector. Hence, detector lifetime and incident laser duration are crucial for detecting the THz radiation [54]. In addition, the detector antenna structure also affects the efficiency of collected THz signal [55,56]. The collection efficiency depends on overlap between THz beam waist and antenna gap.

1.1.3 (b) Free space electro-optic sampling:

Free space electro-optic sampling (EOS) is another popular technique employed for detection of efficient THz radiation which is first demonstrated by Valdmanis et al. in 1982 [57]. It uses electro-optic (Pockels) phenomenon of the crystal for THz detection. By applying electric field, the optical properties of electro-optic (EO) crystals can be changed. The applied electric field induces birefringence in crystals, which changes the polarization state of beam propagating through crystal. The EO crystals such as GaSe, ZnTe, DAST, GaAs, GaP, EO polymer films etc., are used for THz detection [39, 58-62]. Among them, ZnTe crystal is most popular and widely used crystal for THz generation and detection due to its excellent phase matching at Ti: sapphire laser wavelengths, high EO coefficient, and high transparency at optical and THz frequencies. The schematic of EO detection for THz radiation is illustrated in Fig. 1.7. The EO crystal, λ/4 plate, Wollaston prism and photo-detectors are some of essential optics used in EO detection setup. THz pulse and laser pulses are focused on the EO crystal. The polarization state of laser pulses remain same until the propagated THz field and linearly polarized laser pulses are not overlapped both temporally and spatially in EO crystal. The combination of λ/4 plate and Wollaston prism converts the linear polarized pulses into circular and circular to two orthogonal polarized beams having same intensity. These polarization components were focused onto the balanced photo-diodes, which measures the intensity difference between inputs. The output of photo-diodes was zero in the absence of THz radiation.

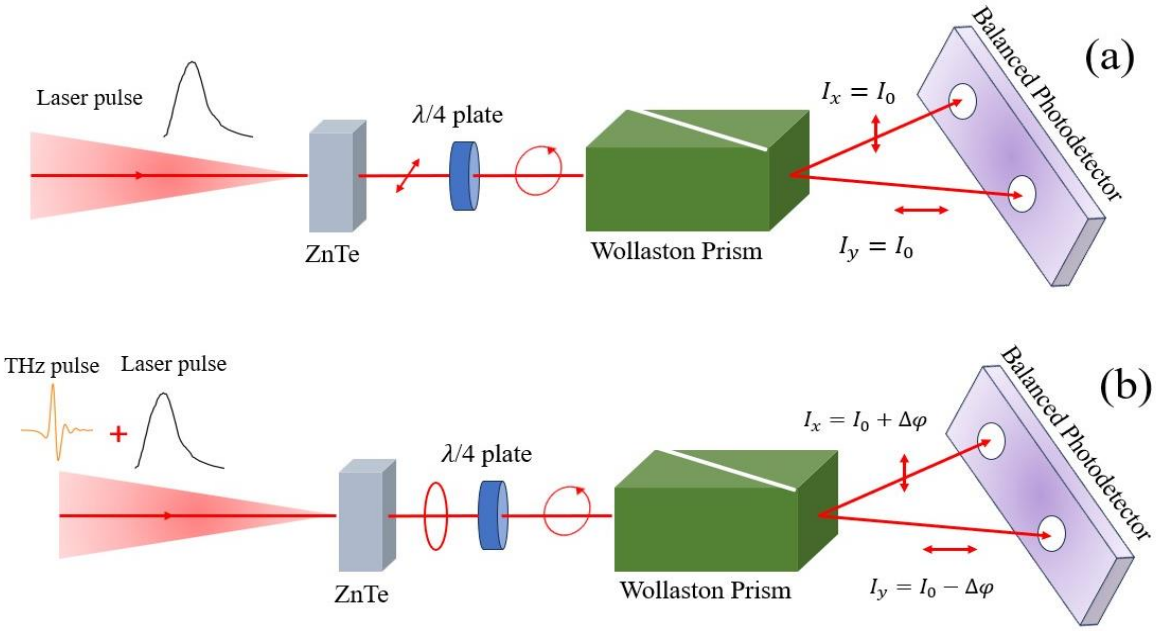

Figure 1.7. Schematic diagram of THz detection using electro-optic sampling.

In the presence of THz field, polarization state of linear polarized pulse is changed to elliptically polarized pulse due to field-induced birefringence in EO crystal. The λ/4 plate induces π/2 phase retardation in elliptically polarized laser pulses, which reduces signal distortion. The Wollaston prism splits the probe beam into two orthogonal polarization components i.e., I_x and I_y having different intensity. The intensity difference is measured by balanced photo-diodes that is proportional to field amplitude of THz radiation. This condition is depicted as in Figure. 1.7 (b).

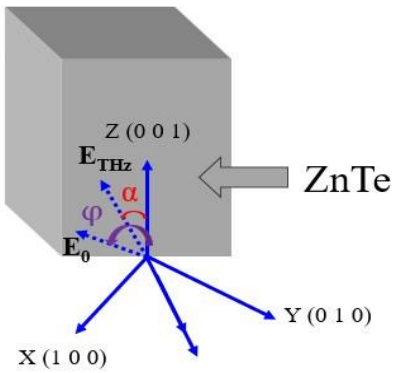

Figure. 1.8 The direction of the polarization of THz and probe laser beams

Given the ZnTe cubic structure and point group $\bar{4}3m$, Equation (1.19) explained the ellipsoid's refractive index

$$\frac{1}{n_0^2}(x^2+y^2+z^2)+2E_{THz,1}\,r_{41}yz+2E_{THz,2}\,r_{41}zx+2E_{THz,3}\,r_{41}xy=1 \quad (1.19)$$

Here, x, y, and z are defined as crystal axes (100), (010), and (001), respectively. $E_{THz,1}$, $E_{THz,2}$, and $E_{THz,3}$ are the components of THz electric field along x, y, and z directions, respectively.

After several coordinate transformations, we can obtain in Equation (1.20)

$$x'^2\left(\frac{1}{n_0^2}+E_{THz,}r_{41}\cos\alpha\right)+y'^2\left(\frac{1}{n_0^2}-E_{THz,}r_{41}[\cos\alpha\sin^2\theta+\cos(\alpha+2\theta)]\right)+z'^2\left(\frac{1}{n_0^2}-E_{THz,}\ r_{41}[\cos\alpha\cos^2\theta+\cos(\alpha+2\theta)]\right)=1 \quad (1.20)$$

Where, $2\theta=\tan^{-1}(\tan(2\tan\alpha))-n\pi$. Now y' and z' are on the plane of the electro optic ZnTe crystal. For small E_{THz} field, the refractive indices along y' and z' axes are

$$n_y'\approx n_0+\frac{n_0^3}{2}E_{THz}r_{41}[\cos\alpha\sin^2\theta+\cos(\alpha+2\theta)] \quad (1.21)$$

$$n_z'\approx n_0+\frac{n_0^3}{2}E_{THz}r_{41}[\cos\alpha\sin^2\theta+\cos(\alpha+2\theta)] \quad (1.22)$$

The probe beam then encounters various diffraction indices and acquires elliptical polarization. The differential detector's measurement of the intensity difference is explained by,

$$\Delta I(\alpha,\varphi)=I_0\sin[2(\varphi-\theta)]\sin\left\{\frac{\omega}{c}[n_y(\alpha)-n_z(\alpha)]L\right\} \quad (1.23)$$

Here, L is the crystal length and I_0 is the probe intensity. Substituting eq. (1.20), (1.21) and (1.22), we can obtain, the output (i.e. laser light intensity difference) of balance photodiodes can be written as [4]

$$\Delta I(\alpha,\varphi)=I_x-I_y=I_0\Delta\varphi$$

$$=\frac{I_0\omega L n_0^3\,r_{41}E_{THz}}{2c}\times(\cos\alpha\sin2\varphi+2\sin\alpha\cos2\varphi) \quad (1.24)$$

From equation (1.24), it is evident that the disparity in intensity detected by the differential detector shows a direct correlation with the THz electric field. This relationship highlights the significance of the THz electric field in influencing the measured intensity difference. Additionally, when $\varphi=\alpha+90^0$ or $\varphi=\alpha$, the greatest intensity difference can be obtained.

$$\Delta I_{max}(\alpha,\varphi)=I_x-I_y=I_0\Delta\varphi=\frac{I_0\omega L n_0^3\,r_{41}E_{THz}}{2c} \quad (1.25)$$

where, I_0 is incident laser beam intensity on Wollaston prism, $\Delta\varphi$ is phase retardation of laser beam and n_0^3 is group refractive index of electro optic ZnTe crystal at optical frequency (ω). The L, r_{41} and E_{THz} are ZnTe crystal length, electro optic coefficient and THz electric field, respectively. From equation (1.24) & (1.25), the $I(\alpha,\varphi)$ is proportional to crystal thickness and electro optic coefficient that indicates thicker crystals with high electro optic coefficient is good for detection of THz signal. The actual resolution of this technique is limited by optical pulse

duration, susceptibility dispersion and velocity mismatch between laser pulse and THz radiation [4, 63, 64].

1.1.3 (c) Pyro detector:

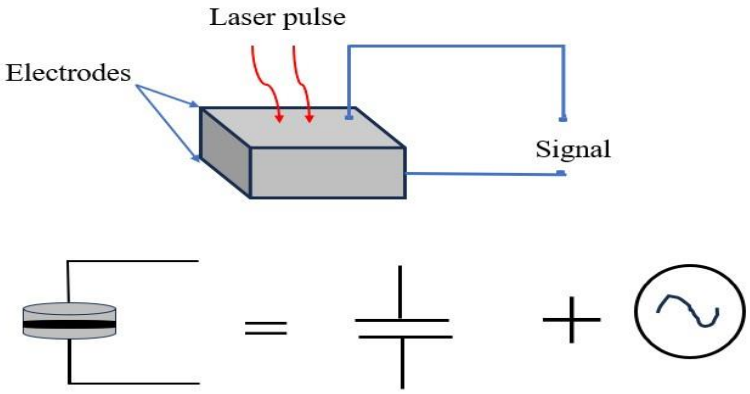

Figure 1.9 Pyroelectric detector

Despite having different mechanics, pyroelectric devices work in the same way, as seen in Figure 1.9. Temperature is monitored using either small voltage changes across the device or current flow to balance out changes in the pyroelectric charge. Although pyroelectric detectors respond more slowly than Golay cells and bolometers, they are nonetheless faster than other detectors, their response times are still in the millisecond range. One type of semiconductor THz detector is the Schottky diode, which responds to THz radiation by rectifying the incident radiation. Schottky diodes were developed utilizing 0.13 µm CMOS technology, according to R. Han et al. They were defined in terms of photo-detection where the radiation power that had been measured to be 28 mW [65].

1.2 Generation and detection of THz frequency (at University of Hyderabad):

The photoconductive antenna in our lab is composed of semiconductors called GaAs/LT-GaAs. It is made up of two parallel metal electrodes on a semiconductor substrate spaced just 5–10 microns apart. Ultrafast time-domain spectroscopy benefits from PCA. An external voltage of around 10 V is used to bias the two metal electrodes, producing an extremely strong electric field. The photoconductive materials produce a broadband terahertz pulse with picosecond or even femtosecond time durations when they are illuminated by an ultrafast laser pulse. Time-resolved terahertz measurements are thus possible. In semiconductor materials, ultrafast laser pulses with a duration of 140 femtoseconds or less often contain energy close to the bandgap and incident in the gap, which helps to produce photo charge carriers. These freely generated photo charge carriers accelerate when subjected to the biasing

field, producing transient photocurrent J(t). This time-dependent current, which is created as charge carriers accelerate, releases radiation in the Terahertz band, which is determined by the following equation (1.26).

$$\vec{E}(r,t) = \frac{1}{4\pi c^3 r^3}\vec{r} \times \left(\vec{r} \times \frac{d\vec{j}}{dt}\right) \quad (1.26)$$

Emission of THz radiation is limited in its bandwidth and power by material breakdown limitations, effective mass, and carrier lifetime. The spacing gap between metal electrodes or plates and the type and shape of electrodes are important design factors in semiconductor materials that greatly impact THz emission. Many designs have been used, including the dipole, bow-tie, and strapline. Larger gaps in antennas require higher bias voltages, which limits the amount of bandwidth that can be generated; hence, smaller gaps are better for reaching high bandwidth, and vice versa for power considerations. In this experiment, an inter-digital photoconductive antenna (BATTOP iPCA-21-05-300-800-h) with an array of antennas and multiple strips with continuous spacing was used. An incident laser beam with a diameter of around 1 mm was able to fall on the iPCA thanks to the use of a micro lens array to concentrate the laser beam into the electrode array's gaps. This allowed for the maximal usage of the laser energy landing on the antenna surface [37]. Usually, photolithography and semiconductor fabrication methods are used to make PCA.

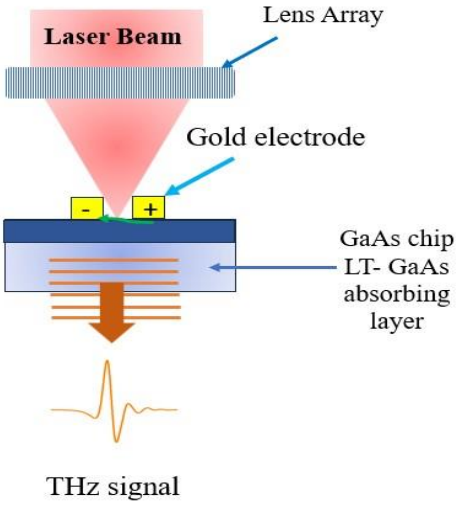

Figure.1.10 Structure of Photoconductive Antenna

In order to prevent thermal noise, the photoconductive materials are frequently placed on a substrate that is not heated. Applications for photoconductive antennas can be found in many

different domains, such as material characterisation, terahertz imaging communication, and terahertz spectroscopy. Their ability to generate and detect terahertz waves with ultrafast response makes them invaluable for studying various materials and biological samples. Despite their usefulness PCAs also have some limited power handling capabilities and the need for cooling in certain cases due to the high-power laser sources used to drive them. Overall, photoconductive antennas are essential components in advancing terahertz science and technology and have facilitated numerous scientific and technological advancements in recent year. Optical rectification or differential frequency mixing in second-order nonlinear optical materials like ZnTe can produce effective THz radiation. In chapter 3, the generation method was briefly outlined.

1.3 Advantage of an electronic source over optical source:

The electronic sources are more compact and portable than optical equivalents, allowing for easy integration into both field applications and laboratory setups. They are also cost-effective, with lower manufacturing and operational costs, and simpler to operate and maintain due to less complex biasing and control circuits. Moreover, electronic THz sources can be directly integrated with electronic circuits, enhancing applications in THz communications, sensing, and imaging. Although they cannot be used in high power applications owing to lower power output, the compactness enables new possibilities for use in defence, consumer products, food industry, biomedical applications and as tools for research in other domains of science. Hence, we believe that work in this direction is crucial and has potential for great impact in many aspects of humanity's future. Our aims were to identify and show proof of concept for a wide variety of applications possible with a THz radar. Radar systems based on silicon operating at terahertz frequencies present a viable and cost-effective option for high-frequency radar applications. The utilization of 0.3 terahertz radar holds promise for various practical uses. Its elevated frequency facilitates precise spatial resolution, rendering it suitable for the detection and imaging of minute objects. The employment of silicon-based radar at terahertz frequencies can contribute to advanced driver-assistance systems (ADAS) aimed at augmenting automotive safety. Particularly in urban settings where heightened spatial resolution is essential, it could enhance collision detection and avoidance. The potential applications of 0.3 terahertz silicon radar extend to gesture recognition systems. Its high frequency enables the detection of subtle gestures, making it beneficial for touchless interfaces and interactions between humans and machines. Terahertz silicon radar could be harnessed for indoor positioning and tracking purposes, furnishing accurate location data in environments where conventional positioning systems like GPS exhibit reduced efficacy. Silicon-based radar

operating in the terahertz range offers non-destructive testing capabilities for industrial uses, enabling material inspection, defect detection, and structural integrity assessment. For short-range applications such as near field communication (NFC) and wireless personal area networks (WPANs), terahertz (THz) communications represent a promising avenue for high-speed data transmission. The naturally wide bandwidth of the THz band allows significant data speeds to be achieved even with simple modulation techniques. Amplitude shift keying (ASK) and quadrature phase shift keying (QPSK) modulation techniques have expanded on this idea by successfully demonstrating high-data-rate transmission at 0.3 THz. Silicon CMOS (SCMOS) and silicon Germanium BiCMOS technologies are lauded for their compactness and compatibility with CMOS processes. III-V semiconductors, including those based on Indium Phosphide (InP), offer elevated operating frequencies due to extreme parametric effects, with select devices reaching up to 1.5 THz and achieving throughputs of 20 GHz. Photonic applications targeting high data transmission rates and information capacity strive for frequencies surpassing 0.3 THz. Nevertheless, challenges persist in integrating and segregating phases in optical monadic conversion systems and quantum cascade lasers. The convergence of electronic and photonic systems has brought about significant changes in traditional device-oriented technology. Microelectromechanical systems (MEMS) are capable of performing electronic functions such as beam steering, polarization, and frequency control, which are unattainable with conventional semiconductor and optical technologies. Our aim was to utilize a 0.3 THz radar for material detection. Samples of various materials were collected for defense institute, India. Metals and explosives were identified using the radar with specific samples gathered. A machine learning algorithm was developed to predict material identity based on peak reflected signal and density value. An innovative system for efficient meat freshness detection in markets was proposed. Diverse raw data is crucial for reliable model development. Artificial intelligence models are vital for effective trend interpretation in meat quality assurance. The system uses silicon radar-like technology for non-contact meat inspection. Its key feature is the non-contact nature, appealing to various establishments. The study confirms the link between factors affecting meat freshness and potential system commercialization. Results promote the integration of the proposed solution into quality assurance frameworks.

The thesis comprises seven chapters, each detailing the aforementioned studies. The organization of the thesis is as follows:

Chapter 1 (Introduction and Thesis Overview)

In this chapter, we briefly discussed the fundamentals of THz radiation and its excellent properties. We described the THz sources and detectors used in this thesis. This chapter also

covers the fundamental mechanisms responsible for efficient THz generation and detection from PC antennas and non-linear crystals. A short description of electronic source used for THz generation and detection techniques, such as Gunn diodes, IMPATT diodes, and frequency multipliers was also included. Furthermore, we discussed the advantages of electronic sources over optical sources. Finally, summary and organization of thesis is presented.

Chapter 2: THz experimental techniques, theoretical consideration and data processing.

This chapter describes the many optoelectronics experimental methods used to generate THz radiation and assess optical materials in the same frequency range encompassing both transmission and reflection modes. In the second part of the chapter, related theoretical consideration and data processing are discussed. Nanosecond and picosecond lasers have longer pulse durations, narrower spectral bandwidths, and lower peak powers, making them less efficient for generating THz radiation through nonlinear optical processes. Therefore, femtosecond lasers are the preferred choice for generating THz radiation from crystals. The advantages of femtosecond laser for the generation of THz signal from NLO crystal are also explained. A comprehensive discussion on the mechanisms of THz generation, detection, and associated artefacts is well documented. Furthermore, an in-depth exploration of the incoherent technique for THz detection using a pyroelectric detector is also covered. In the concluding part of the chapter, we introduced a compact and economically viable fully-integrated solution designed for short-range communication systems operating at 0.3 THz frequency range. Since silicon radar source is a newly developed technology therefore, it is currently undergoing through testing. The intricate details of the silicon radar source mechanism, along with all the theoretical considerations for each experimental technique are thoroughly discussed.

Chapter 3: Evalution of BIBO, S-doped GaSe, α-TeO_2 nonlinear crystals for efficient SHG and terahertz generation

This chapter deals with the investigation of efficient THz generation and optoelectronic characterization of three nonlinear crystals from different categories such as uniaxial and biaxial belong to semiconductor, semimetal and inorganic groups. The optoelectronic characterization was performed using femtosecond laser based coherent and incoherent techniques. We have selected BIBO, S-doped GaSe, and α-TeO_2 crystals for our studies. Efficient SHG and THz radiation were generated using nanosecond (1064nm,10ns) and femtosecond (800 nm, 140 fs & 50 fs) laser systems respectively. The absorption coefficients, refractive indices, surface roughness, reflection coefficients in both TE and TM modes, and dielectric properties of the NLO crystals were evaluated to assess their performance as THz

devices. In addition, effect of doping of sulfur (S) was also studied in cased GaSe. Chalcopyrite crystal, particularly S-doped GaSe, was selected due to its excellent linear and nonlinear optical properties such as transmission in visible to FIR range, high anisotropy and second order nonlinearity and high damage threshold. S-doped GaSe demonstrates superior THz conversion efficiency as compared to α-TeO_2 and BIBO crystals, attributed to its above mentioned linear and nonlinear properties. The optimized experimental conditions for THz generation were ascertained for these crystals and obtained results are compared with existing reported works in terms of their THz conversion efficiency.

Chapter 4: Designing aspects of newly developed THz profilometer for measuring the surface roughness of remote metallic and explosive targets

In this chapter, we explore the cutting-edge advancements in terahertz (THz) frequency domain 3D profilometry, specifically designed for standoff detection of surface roughness in metallic and explosive targets. By employing reflection geometry, we optimize signal strength by carefully selecting incident angles and frequency modalities, particularly crucial for surfaces with paint and rust/unpainted layers. Our focus lies on understanding surface scattering properties, directly influencing the quality of THz signals recorded within the frequency range of 0.5 to 2.0 THz. Our system, surpassing existing technologies in complexity, utilizes an interferometric arrangement, enabling precise measurement of penetration depth with exceptional resolution. Unlike traditional methods like optical profilometers and AFMs, our THz profiler excels in assessing surface roughness beneath paint layers, providing significant improvements in detection capabilities. Moreover, our innovative system can accurately measure small sample quantities (50 mg to 500 mg) and penetration depths ranging from 500μm to 30 mm. Furthermore, while existing systems are limited to 2D THz surface imaging, we have developed MATLAB code for generating comprehensive 3D surface profiles, enhancing our ability to characterize surface roughness across diverse targets. Our system's ability to penetrate paint layers facilitates the detection of corrosion effects on metallic surfaces. Additionally, our profiler can measure surface profiles of hydraulic pressed pellet materials without relying on interferometric designs, thereby offering a versatile solution for various applications. Surface roughness significantly influences the absorption and reflection characteristics, impacting the spectroscopic signatures of explosive substances. We have selected NH_4NO_3, for distinctive fingerprint absorption spectra in the THz range, aiding in their identification. Surface roughness alters reflective properties, affecting the strength and quality of THz signals.

Chapter 5: Calibration of Silicon Germanium 0.3 THz horizontal radar system for homeland, defense and food processing applications

This chapter describes the calibration of a prototype THz horizontal radar system for several real-world applications such as classification of various metallic, explosive targets and food processing industry. In addition, an artificial intelligence model was developed for the assessment of the freshness of meat. We also explained the working principle of 0.3 THz SiGe radar system. For the first time, we have made an attempt to explain the joule's effect on silicon micro lens which is responsible for excessive heating of the radar system. In additions, we have experimentally and theoretically verified the THz radar cross section (TRCS) of canonical objects. We have also classified the metallic and explosive targets using artificial intelligence-based machine learning tools.

Chapter 6: Study of ultra-thin and free-standing α-MoO_3/β-PVDF composites for radar shielding applications

In this chapter, free-standing thin sheets (~100 μm thick) of α-MoO_3/β-polyvinylidene fluoride (PVDF) composites prepared by our collaborators Prof. V.V.S.S Srikanth and Dr. Venkata Sreenivasulu Kummari, SEST, University of Hyderabad, using a simple solution casting-coagulation method. These composites, chosen for their scientifically rational constituents, exhibit electromagnetic shielding (SE) by absorptions from 30.10 to 42.38 dB in the 0.2-1.6 THz range, with SE by absorption well-correlated to their dielectric behavior. These materials show great potential in THz-based communication, medical imaging, military, and defense applications by reducing the detectability of aircraft, ships, and vehicles through minimized radar cross-section (RCS). They are used in aerospace and maritime industries to enhance stealth, in automotive vehicles for safety features, and to protect critical infrastructure from hostile radar targeting. Additionally, they find civilian uses in telecommunications, meteorology, and environmental monitoring by minimizing radar interference and improving signal quality. Overall, α-MoO_3/β-PVDF composites are essential for applications requiring reduced radar signature for improved operational effectiveness, safety, security, and stealth technology.

Chapter 7: Conclusions and Future scope

This chapter provides a summary of all previous chapters, conclusions, and potential future directions for this work.

Appendix A Radar Code Flowchat

Appendix B THz Radar Cross Section Simulation using MATLAB

References:

[1]. Debayle, L. Gremillet, L. Bergé, C. Köhler, R. M. Woodward, and T. Elsaesser, "Analytical model for THz emissions induced by laser-gas interaction & quot; Strong terahertz pulse generation by chirped laser pulses in tenuous gases," New J. Phys. Opt. Express, **22**, 13691-13709 (2014).

[2]. X. C. Zhang and J. Xu, "Chapter 2 - Generation and detection of terahertz waves," in Introduction to THz Wave Photonics (2010).

[3]. B. Ferguson and X. C. Zhang, "Materials for terahertz science and technology," Nat. Mater. (2002).

[4]. Y. S. Lee, Principles of Terahertz Science and Technology (2009).

[5]. H. Park, J.H. Son, and C.B. Ahn, "Enhancement of terahertz reflection tomographic imaging by interference cancellation between layers," Opt. Express, **24**, 7028-7036 (2016).

[6]. P. F. Taday, I. V. Bradley, D. D. Arnone, and M. Pepper, "Using Terahertz pulse spectroscopy to study the crystalline structure of a drug: A case study of the polymorphs of ranitidine hydrochloride," J. Pharm. Sci, **92**(4), 831-8 (2003).

[7]. J. H. Strait, P. A. George, M. Levendorf, M. Blood-Forsythe, R. Rana, and J. Park, "Measurements of the Carrier Dynamics and Terahertz Response of Oriented Germanium Nanowires," Nano Lett, **9**, 8, 2967–2972 (2009).

[8]. Y. C. Shen, P. C. Upadhya, E. H. Linfield, and A. G. Davies, "Temperature-dependent low-frequency vibrational spectra of purine and adenine," Appl. Phys. Lett. **82**, 2350–2352 (2003).

[9]. M. C. Beard, G. M. Turner, and C. A. Schmuttenmaer, "Transient photoconductivity in GaAs as measured by time-resolved terahertz spectroscopy," Phys. Rev. **B** Condens. Matter Mater. Phys., **62**, 15764 (2000).

[10]. M. Jazbinsek, U. Puc, A. Abina, and A. Zidansek, "Organic crystals for THz photonics," Appl. Sci., **9** (5), 882 (2019).

[11]. X. C. Zhang, "Air photonics: Tera - Mid infrared radiation," NATO Sci. Peace Secur. Ser. B Phys. Biophys. (2011).

[12]. M. R. Leahy-Hoppa, J. Miragliotta, R. Osiander, J. Burnett, Y. Dikmelik, C. McEnnis, and J. B. Spicer, "Ultrafast laser-based spectroscopy and sensing: Applications in LIBS, CARS, and THz spectroscopy," Sensors, **10** (5), 4342-72 (2010).

[13]. H. B. Liu, H. Zhong, N. Karpowicz, Y. Chen, and X. C. Zhang, "Terahertz spectroscopy and imaging for defense and security applications," in Proceedings of the IEEE, **95**, 1514 - 1527 (2007).

[14]. Chandan Ghorui, A.M. Rudra, U. Chatterjee, A.K. Chaudhary, D. Ganesh, "Efficient Second-Harmonic and Terahertz Generation from Single BiB_3O_6 Crystal Using Nanosecond and Femtosecond Lasers", Appl. Opt., **60** (19), 5643–5651, (2021).

[15]. Chandan Ghorui, Arjun V. Kidavu, P.N. Kumar, S. Das, A.K. Chaudhary and Yu M Andreev, "Comparative studies of terahertz-based optical properties in transmission/reflection modes of GaSe: S and measurement of its scattering losses due to surface roughness for efficient terahertz generation", Physica Scripta, **98**,1-12, 025508 (2023).

[16]. Chandan Ghorui, A.K. Chaudhary, "Linear and nonlinear optical characterization of Tellurium dioxide (α-TeO_2) for generation of terahertz radiation using time-domain spectroscopy", Appl. Opt. **62**,18, 4831-4835 (2023).

[17]. X.C. Zhang, D. Auston, "Optoelectronic measurement of semiconductor surfaces and interfaces with femtosecond optics," J.Appl.Phys. **71**, 326 (1992).

[18]. L. Ozyuzer, A. Koshelev, C. Kurter, N. Gopalsami, Q. Li, M. Tachiki, K. Kadowaki, T. Yamamoto, H. Minami, H. Yamaguchi, "Emission of Coherent THz Radiation from Superconductors," Science **318**, 1291 (2007).

[19]. D. Cook, R. Hochstrasser, "Intense terahertz pulses by four-wave rectification in air," Opt. Lett. **25**, 1210 (2000).

[20]. C. Waschke, H.G. Roskos, R. Schwedler, K. Leo, H. Kurz, K. Köhler, "Coherent submillimeter-wave emission from Bloch oscillations in a semiconductor superlattice," Phys. Rev. Lett. **70**, 3319 (1993).

[21]. M.C. Beard, G.M. Turner, C.A. Schmuttenmaer, "Measuring Intramolecular Charge Transfer via Coherent Generation of THz Radiation," J. Phys. Chem. A **106**, 878 (2002).

[22]. D.J. Hilton, R. Averitt, C. Meserole, G.L. Fisher, D.J. Funk, J.D. Thompson, A.J. Taylor, "Terahertz emission via ultrashort-pulse excitation of magnetic metal films," Opt. Lett. **29**, 1805 (2004).

[23]. A. Rice, Y. Jin, X. Ma, X.C. Zhang, D. Bliss, J. Larkin, M. Alexander, "Terahertz optical rectification from < 110 > zinc-blende crystals," Appl. Phys. Lett. **64**, 1324 (1994).

[24]. P.C. Planken, M.C. Nuss, I. Brener, K.W. Goossen, M.S. Luo, S.L. Chuang, "Terahertz emission in single quantum wells after coherent optical excitation of light hole and heavy hole excitons," Phys. Rev. Lett. (1992).

[25]. P.R. Smith, D.H. Auston, M.C. Nuss, "Sub picosecond photoconducting dipole antennas" IEEE J. Quant. Electron. **24**, 255 (1988).

[26]. J. Shen, X. Fan, Z. Chen, M.F. DeCamp, H. Zhang, J.Q. Xiao, "Damping modulated terahertz emission of ferromagnetic films excited by ultrafast laser pulses," Appl. Phys. Lett. **101**, 072401 (2012).

[27]. G.H. Welsh, N.T. Hunt, K. Wynne, "Terahertz-Pulse Emission Through Laser Excitation of Surface Plasmons in a Metal Grating," Phys. Rev. Lett. **98**, 026803 (2007).

[28]. D. H. Auston, "Sub picosecond electro-optic shock waves," Appl. Phys. Lett. **43**, 713–715 (1983).

[29]. D. H. Auston, K. P. Cheung, and P. R. Smith, "Picosecond photoconducting Hertzian dipoles," Appl. Phys. Lett. **45**, 284–286 (1984).

[30]. D. H. Auston et al., "Cherenkov radiation from femtosecond optical pulses in electro-optic media," Phys. Rev. Lett. **53**, 1555–1558 (1984).

[31]. P. R. Smith, D. H. Auston, and M. C. Nuss, "Sub picosecond photoconducting dipole antennas," IEEE J. Quantum Electron. **24**, 255–260 (1988).

[32]. C. Fattinger and D. Grischkowsky, "Terahertz beams," Appl. Phys. Lett. **54**, 490–492 (1989).

[33]. M. B. Ketchen et al., "Generation of sub picosecond electrical pulses on coplanar transmission-lines," Appl. Phys. Lett. **48**, 751–753 (1986).

[34]. C. Fattinger and D. Grischkowsky, "Point source terahertz optics," Appl. Phys. Lett. **53,** 1480–1482 (1988).

[35]. K. Vodopyanov, "Optical generation of narrow-band terahertz packets in periodically-inverted electro-optic crystals: conversion efficiency and optimal laser format," Optics Express, **14**, 6, 2263-2276 (2006).

[36]. Venkatesh, M., Thirupugalmani, K., Rao, K.S. et al. Generation of efficient THz radiation by optical rectification in DAST crystal using tunable femtosecond laser pulses., Indian J Phys, **91**, 319–326 (2017).

[37]. T.J. Carrig, G. Rodriguez, T.S. Clement, A. Taylor, K.R. Stewart, "Scaling of terahertz radiation via optical rectification in electro-optic crystals," Appl. Phys. Lett. **66**, 121 (1995).

[38]. Wilke, S. Sengupta, "Terahertz Spectroscopy: Principles and Applications", Optical Science and Engineering, **131**, 41 (2008).

[39]. A. Nahata, A.S. Weling, T.F. Heinz, "A wideband coherent terahertz spectroscopy system using optical rectification and electro-optic sampling," Appl. Phys. Lett. **69**, 2321 (1996).

[40]. A. Schneider, I. Biaggio, P. Günter, "Optimized generation of THz pulses via optical rectification in the organic salt DAST", Opt. Commun. **224**, 337 (2003).

[41]. P. Gu, M. Tani, S. Kono, K. Sakai, X.-C. Zhang, "Study of terahertz radiation from InAs and InSb," J.Appl.Phys. **91**, 5533 (2002).

[42]. X. Zheng, C.V. McLaughlin, P. Cunningham, L.M. Hayden, "Organic Broadband TeraHertz Sources and Sensors," J. Nanoelectron. Optoelectron. **2**, 58 (2007).

[43]. S. Karthick, D. Ganesh, K. Thirupugalmani, A.K. Chaudhary, S. Brahadeeswaran, "Terahertz generation and optical properties of N-benzyl-2-methyl-4-nitroaniline single crystals in 0.1–2.0 THz range for photonic applications", Materials Letters, **246**,95-98 2019,

[44]. K. Arjun, D. Ganesh, S. Karthick, A. Santha, M. Venkatesh, S. Ganesamoorthy, S. Brahadeeswaran, A.K. Chaudhary, "Investigations on aqueous solution grown L- Arginine Phosphate monohydrate (LAP) single crystals for efficient THz generation", Journal of crystal growth, **575**, 1, 126337,1-5, (2021).

[45]. M. Mahendar, R. N. V. Krishna, and A. K. Chaudhary, "Femtoseconds laser based efficient THz generation from different temperature annealed CdTe thin films," Indian J. Pure Appl. Phys. **60,** 401–406 (2022).

[46]. Sakai, K., Tani, M. Introduction to Terahertz Pulses. In: Sakai, K. (eds) "Terahertz Optoelectronics", Topics in Applied Physics, **97**. Springer, Berlin, Heidelberg.

[47]. K. Radhanpura, "All-optical terahertz generation from semiconductors: materials and mechanisms", 2012

[48]. D. Dragoman, M. Dragoman, "Terahertz fields and applications," Prog. Quantum Electron. **28**, 1 (2004).

[49]. J.B. Khurgin, "Optical rectification and terahertz emission in semiconductors excited above the band gap," J. Opt. Soc. Am. B **11**, 2492 (1994).

[50]. M. Xiaodong, I.B. Zotova, Y.J. Ding, "Power Scaling on Efficient Generation of Ultrafast Terahertz Pulses," IEEE J. Sel. Top. Quantum Electron. **14**, 315 (2008).

[51]. A. Reklaitis, L. Reggiani, "Monte Carlo Study of Hot-Carrier Transport in Bulk Gan and Modelling of a Near Terahertz Impact Avalanche Transit Time Diode," Journal of Applied Physics, **95**, 12, 7925-7935, (2004).

[52]. T. Al-Attar, T. H. Lee, "Monolithic Integrated Millimeter-Wave IMPATT Transmitter in Standard CMOS Technology," IEEE Transactions on Microwave Theory and Techniques, **53**, 11, 3557-3561 (2005).

[53]. S. G. Park, M. R. Melloch, A. M. Weiner, "Analysis of Terahertz Waveforms Measured by Photoconductive and Electro Optic Sampling," IEEE Journal of Quantum Electronics, **35**, 5, 810-815,1999.

[54]. A. Singh, S. Pal, H. Surdi, S.S. Prabhu, S. Mathimalar, V. Nanal, R.G. Pillay, G.H. Döhler, "Carbon irradiated semi-insulating GaAs for photoconductive terahertz pulse detection," Opt. Express **23**, 6656 (2015).

[55]. P.U. Jepsen, R.H. Jacobsen, S. Keiding, "Generation and detection of terahertz pulses from biased semiconductor antennas," J. Opt. Soc. Am. B **13**, 2424 (1996).

[56]. S. Kono, M. Tani, K. Sakai, "Ultrabroadband photoconductive detection: Comparison with free-space electro-optic sampling," Appl. Phys. Lett. **79**, 898 (2001).

[57]. J.A. Valdmanis, G. Mourou, C.W. Gabel, "Picosecond electro-optic sampling system," Appl. Phys. Lett. **41**, 211 (1982).

[58]. A. Kübler, R. Huber, S. Tübel, A. Leitenstorfer, "Ultrabroadband detection of multi-terahertz field transients with GaSe electro-optic sensors: Approaching the near infrared," Appl. Phys. Lett. **85**, 3360 (2004).

[59]. Q. Wu, X.-C. Zhang, "7 terahertz broadband GaP electro-optic sensor," Appl. Phys. Lett. **70**, 1784 (1997).

[60]. M. Vossebürger, M. Brucherseifer, G.C. Cho, H.G. Roskos, H. Kurz, "Propagation effects in electro-optic sampling of terahertz pulses in GaAs," Appl.Opt. **37**, 3368 (1998).

[61]. A.M. Sinyukov, L.M. Hayden, "Generation and detection of terahertz radiation with multilayered electro-optic polymer films," Opt. Lett. **27**, 55 (2002).

[62]. P. Han, M. Tani, F. Pan, X.-C. Zhang, "Use of the organic crystal DAST for terahertz beam applications," Opt. Lett. **25**, 675 (2000).

[63]. G. Gallot, D. Grischkowsky, "Electro-optic detection of terahertz radiation," J. Opt. Soc. Am. B **16**, 1204 (1999).

[64]. G. Gallot, J. Zhang, R. McGowan, T.-I. Jeon, D. Grischkowsky, "Measurements of the THz absorption and dispersion of ZnTe and their relevance to the electro-optic detection of THz radiation," Appl. Phys.Lett. **74**, 3450 (1999).

[65]. R. Han, Y. Zhang, D. Coquillat, H. Videlier, W. Knap, E. Brown, K. O. Kenneth, "A 280-GHz Schottky Diode Detector in 130-nm Digital CMOS," IEEE Journal of Solid-State Circuits, **46,** 11, 2602-2612, (2011).

Chapter 2

2. Experimental details for THz and second harmonic generation, theoretical consideration and data processing

Abstract

This chapter describes the many optoelectronics experimental methods used to generate THz radiation and assess optical materials in the same frequency range encompassing both transmission and reflection modes. In the second part of the chapter, related theoretical consideration and data processing are discussed. Nanosecond and picosecond lasers have longer pulse durations, narrower spectral bandwidths, and lower peak powers, making them less efficient for generating THz radiation through nonlinear optical processes. Therefore, femtosecond lasers are the preferred choice for generating THz radiation from crystals. The advantages of femtosecond laser for the generation of THz signal from NLO crystal are also explained. A comprehensive discussion on the mechanisms of THz generation, detection, and associated artefacts is well documented. Furthermore, an in-depth exploration of the incoherent technique for THz detection using a pyroelectric detector is also covered. In the concluding part of the chapter, we introduced a compact and economically viable fully-integrated solution designed for short-range communication systems operating at 0.3 THz frequency range. Since silicon radar source is a newly developed technology therefore, it is currently undergoing through testing. The intricate details of the silicon radar source mechanism, along with all the theoretical considerations for each experimental technique are thoroughly discussed.

2.1 Laser background:

Throughout much of history, the primary function of light has been to illuminate and observe. The word LASER stands for **"**Light Amplification by Stimulated Emission of Radiation**"** marked a pivotal moment in 1961, ushering in a new era of exploration and applications characterized by coherent light [1]. Optical and laser-based gadgets are becoming commonplace in both home and industrial settings in modern civilization [2, 3]. Research with lasers has revolutionized a variety of industries, including communication, micro-structuring, surgery, ultrafast studies, and remote sensing [4-10]. Laser technology has not only expanded our imaging capabilities and dynamic studies to a molecular level but has also demonstrated the capacity to sustain and deposit high powers [11-13]. With the advent of high-power lasers, applications including remote sensing and micro-structuring have advanced significantly [14,15]. Accurate spatial and temporal localization of energy is essential for micro-structuring, and long-range propagation without dissipation and mode distortion improves remote sensing, particularly when accompanied by qualitative and quantitative spectroscopic investigations. High power levels can be produced by both pulsed and continuous wave lasers, each with a different amplification method. In instance, temporally localizing energy is an advantage of pulsed lasers. This facilitates energy conversion while achieving high peak powers and offers instruments for ultrafast spectroscopy and imaging [16]. Despite the considerable progress in pulsed laser applications and research, it appears that development will persist into the foreseeable future, driven by the ever-growing demand and expanding scope of these ultrafast lasers.

2.2 Ultrafast lasers background and sources:

Due to the requirement for increased precision and less thermal effects in a variety of applications, laser technology has advanced significantly from nanosecond lasers to picosecond and femtosecond lasers. Pulses with durations ranging from 1 to 1000 nanoseconds (ns) are produced by nanosecond lasers. These lasers are frequently employed in fields where the longer pulse duration is adequate for efficient energy delivery, such as laser cutting, welding, and marking. The relatively longer pulse duration leads to significant heat diffusion into the surrounding material, causing thermal damage and less precise machining. Picosecond lasers have pulse durations ranging from 1 to 1000 picoseconds (ps), which is three orders of magnitude shorter than nanosecond lasers. The shorter pulse duration significantly reduces the heat-affected zone (HAZ), allowing for more precise material processing with minimal thermal damage. Picosecond lasers are used in applications requiring high precision, such as

micromachining, medical device fabrication, and microelectronics. Femtosecond lasers emit pulse durations ranging from 1 to 1000 femtoseconds (fs), which is another three orders of magnitude shorter than picosecond lasers. The ultra-short pulse duration leads to an even more precise energy delivery, often resulting in "cold" ablation where the material is removed with negligible heat transfer to the surrounding area. This enables extremely high precision and the ability to machine very delicate structures. Femtosecond lasers are used in applications such as precision surgery (e.g., LASIK eye surgery), nanoscale fabrication, and in the study of ultrafast processes in materials science. The development of mode-locking techniques has been crucial in generating ultra-short laser pulses. Picosecond and femtosecond pulses are achieved primarily through the employment of electro-optic modulators for active mode-locking and saturable absorbers for passive mode-locking. Chirped pulse amplification (CPA) technology has enabled the amplification of ultra-short pulses without damaging the laser gain medium. This involves stretching the pulse in time to lower its peak power, amplifying it, and then compressing it back to its original duration. Femtosecond pulse creation and manipulation heavily relies on nonlinear optical phenomena. The self-phase modulation effect is the result of light intensity changing the medium's refractive index, which broadens the pulse spectrum. This broadening is essential for generating shorter pulses. Four wave mixing is a nonlinear process where two or more wavelengths interact within a medium to produce new wavelengths. This can be used to compress pulses and generate new frequencies. A form of passive mode-locking that exploits the intensity-dependent refractive index (Kerr effect) in the gain medium to achieve ultra-short pulses. Pulse broadening is the result of group velocity dispersion (GVD), which causes the various frequency components of a pulse to travel at different speeds. Dispersion-compensating mirrors and prisms are used to counteract this effect. Special optical fibers designed with alternating sections of positive and negative dispersion help manage and control the dispersion over long distances, maintaining the pulse integrity. Pulse shaping techniques are used to tailor the temporal profile of the laser pulses. This can involve adjusting the phase and amplitude of various frequency components inside the pulse using acousto-optic modulators (AOMs) or spatial light modulators (SLMs) [17]. Improvements in the caliber and accuracy of optical parts like diffraction gratings, lenses, and mirrors are essential. High reflectivity mirrors, low-loss optical coatings, and precise alignment are all essential for maintaining the integrity of ultra-short pulses. The development of new laser gain media with broad gain bandwidths, such as titanium-sapphire (Ti: sapphire), has been instrumental in achieving femtosecond pulses. These media support a wide range of wavelengths, allowing for

the generation of very short pulses. The inception of pulsed laser generation marked a significant breakthrough with the development of Q-switching [18, 19]. This method involved the discovery of mode locking, wherein multiple resonator cavity modes are synchronized to produce ultrashort pulses in the femtosecond range. These pulses could be further amplified using the chirped amplification technique, generating intense ultrashort pulses. The pulses, lasting less than one picosecond, are considered ultrashort, facilitating the study of ultrafast phenomena. In the initial phases, femtosecond lasers made use of different dyes as active gain mediums. The extensive fluorescence (> 100 nm) and broad bandwidth adjustability of these dyes rendered them attractive for incorporation in the development of high-speed lasers. Nevertheless, challenges arose during the operation of dye lasers, such as issues pertaining to dye circulation (maintenance of cells and plumbing) and the durability of dye molecules (photo-bleaching) for prolonged usage [17]. The invention of chirped pulse amplification (CPA), followed by the realization that Ti: Sapphire is a useful gain medium were essential to overcoming these challenges. By applying CPA, the pulse is stretched and then compressed before it is released. This allows high-power femtosecond laser pulses to be produced, which have short pulse lengths (of the order of femtoseconds) and very high-power outputs (in Gigawatts). In other words, they compress millijoules of energy into a few femtoseconds. Figure 2.1 illustrates the evolution of lasers, highlighting the advancements enabled by CPA. Femtosecond pulses, initially the fastest man-made events, facilitate the study of molecular dynamics, they can inhibit chemistry occurring in the femtosecond range. Femtosecond lasers' short temporal range makes them useful for microfabrication and microscopic imaging. Ultrashort pulses provide substantially smaller interaction zones in multiphoton fluorescence experiments [19]. Femtosecond pulses having a period of 100 femtoseconds have a bandwidth of 10 THz because of Heisenberg's uncertainty, which relates spectral and temporal widths inversely. Even shorter ultrashort pulses (< 2 fs) exist, characterized by bandwidths that span an entire octave, leading to their classification as white light lasers [20]. The concentration of millijoule energy within femtosecond timescales results in a significant increase in peak power to the scale of terawatts. Presently, femtosecond lasers have the capability to produce Petawatt (10^{15} W) powers and achieve remarkable intensities (10^{20} W/cm^2) [21,22].

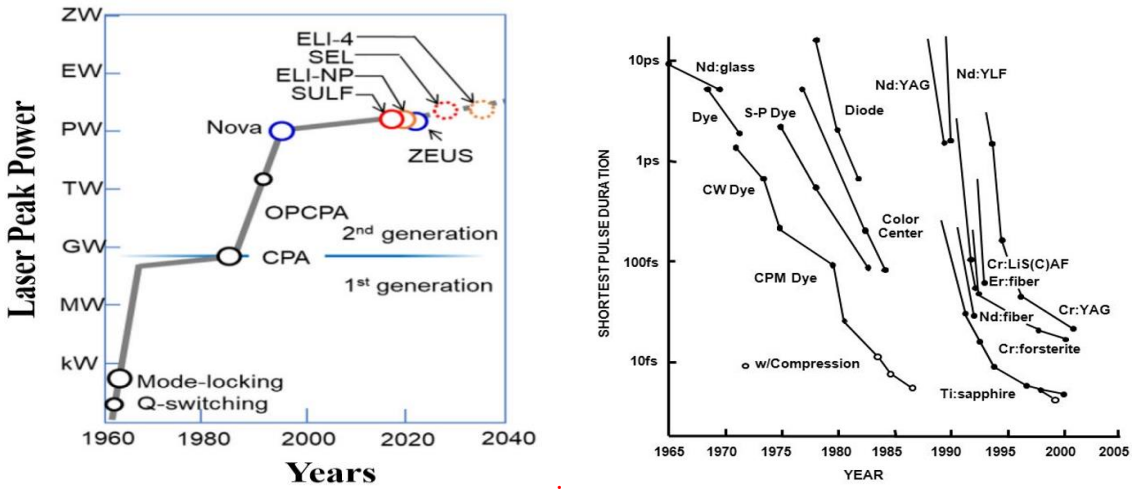

Figure 2.1: The development of pulsed laser technology and significant achievements in the field of laser research are discussed in the article "High-Power Lasers" available at the link provided (https://www.americanscientist.org/article/high-power-lasers).

The classification of the femtosecond lasers used in the experiment is given below,

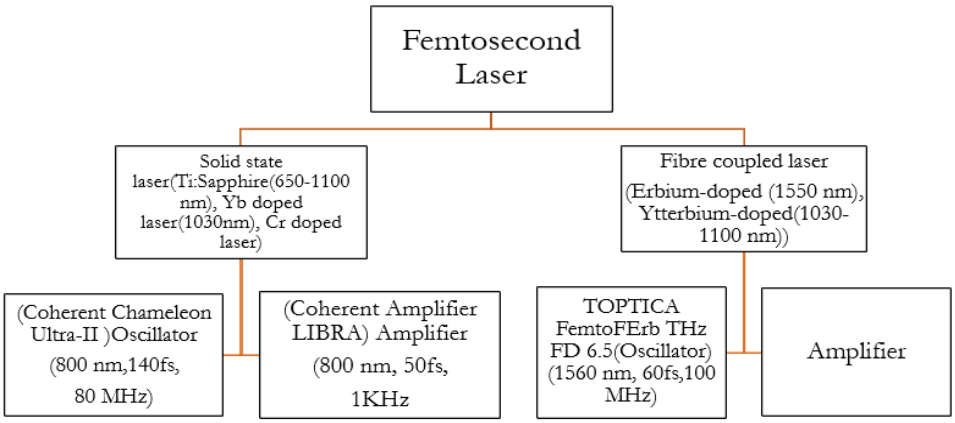

Nanosecond and picosecond lasers, with their longer pulse durations, narrower spectral bandwidths, and lower peak powers, are less efficient for generating THz radiation through nonlinear optical rectification processes. However, femtosecond lasers have extremely short pulse durations (in the order of 10 to 100 femtoseconds), resulting in a broad spectral bandwidth and high peak power and ideal for process of optical rectification and photoconductive switching, which are commonly used to generate THz radiation. The broad spectrum of femtosecond pulses is ideal for generating broadband THz radiation, which is desirable for many applications in spectroscopy and imaging. The high peak power induces strong nonlinear polarization in the crystal, enhancing THz generation efficiency. Additionally, the short pulse durations minimize thermal effects within the crystal. Longer pulses from

nanosecond or picosecond lasers deposit more energy over a longer period, leading to significant heating and potential damage to the crystal. In addition, femtosecond pulses deliver energy so quickly that thermal diffusion is minimal, preserving the integrity of the crystal. Femtosecond lasers also provide excellent temporal resolution, which is important for time-domain spectroscopy. The ability to generate and measure THz pulses with precise timing enables detailed investigation of fast dynamic processes in materials. In nonlinear optical processes, phase matching is critical for efficient THz generation. Femtosecond pulses can achieve better phase matching conditions in nonlinear crystals, enhancing the conversion efficiency from optical to THz frequencies. Many nonlinear optical processes used for THz generation, such as optical rectification, benefit from the ultrafast electric field variation in femtosecond pulses. These processes are more efficient when driven by the rapid changes in the electric field associated with femtosecond pulses compared to the slower variations of nanosecond or picosecond pulses. All the experiments carried out were performed on following ultrafast laser sources

2.3 Femtosecond Coherent Chameleon Ultra-II (Oscillator)

2.4 Femtosecond Coherent Amplifier Ti: Sapphire Laser (LIBRA)

2.3 TeraFlash Pro: Versatile Terahertz Time domain Platform

2.4 Silicon Radar

In addition, we have employed electronic sources for terahertz (THz) generation in form of Si Radar system which offers notable advantages over photonic or optical sources. Some other well-known semiconductor-based devices like Gunn and IMPACT diodes provide broad frequency coverage, making them ideal for applications needing broadband THz sources. These electronic sources are more compact and portable than optical equivalents, allowing for easy integration into both field applications and laboratory setups. They are also cost-effective, with lower manufacturing and operational costs, and simpler to operate and maintain due to less complex biasing and control circuits. Moreover, electronic THz sources can be directly integrated with electronic circuits, enhancing applications in THz communications, sensing, and imaging. Although they cannot be used in high power applications, the compactness enables new possibilities for use in defence, consumer products, food industry, biomedical applications and as tools for research in other domains of science. Hence, we believe that 300

GHz electronic source is crucial and has potential for great impact in many aspects of humanity's future.

2.7. For generating tunable UV radiation dye laser coupled with using Nd: YAG nanosecond laser was used.

2.3 Femtosecond coherent chameleon ultra-II (oscillator):

The Chameleon Ultra-II laser source, operating in the 680 – 1080 nm range (visible to Near Infrared) of the electromagnetic spectrum, is a compact and tunable device that produces femtosecond coherent laser pulses. These pulses, with a duration of approximately 140 fs and a repetition rate of 80 MHz, yield an average power of 4 mW at 800 nm as measured by a power meter. The laser system comprises key components such as the laser head, power supply, chiller, and miniature-recirculating unit (MRU). The thermal regulation of the baseplate within the ultrafast pulsed ultrafast (UPUF) system is meticulously maintained at 200°C through the circulation of a pre-mixed solution, orchestrated by an external chiller. Employed as the active gain medium in this system is Ti: Sapphire, renowned for its emission of ultrashort femtosecond pulses. This emission is achieved through the application of the Kerr lens mode locking technique, leveraging Kerr lensing a phenomenon in which the refractive index of the medium undergoes variation in response to the characteristic intensity of light. Within the Chameleon laser system, tunability is accomplished by manipulating the cavity length, a factor contributing to the generation of ultrashort femtosecond pulses characteristic of Ti: Sapphire as the active gain medium. Extending the utility of this femtosecond laser oscillator, the application now includes terahertz generation and detection techniques. The specific methodologies involved in terahertz generation and detection utilizing the femtosecond laser oscillator are contingent upon the intricacies of the experimental setup and configurations. The Chameleon laser, capable of producing femtosecond pulses, offers a versatile platform for exploring and utilizing terahertz frequencies, enabling a wide range of applications across various scientific and technological fields.

2.3.1 THz time-domain spectroscopy (TDS) using femtosecond laser oscillator:

Analyses of transmission and absorption spectra in the THz range were carried out through the utilization of a THz spectrophotometer that was designed indigenously. In the following experimental stage, a crystal utilized as a generator of THz waves was used in a setup based on the time domain. Figure 2.2 provides a schematic depiction of the experimental layout for THz generation and transmission/absorption measurements. This configuration facilitated

a thorough exploration of the interaction dynamics of materials and Terahertz radiation, allowing for precise characterization of their transmission and absorption characteristics in the THz frequency range.

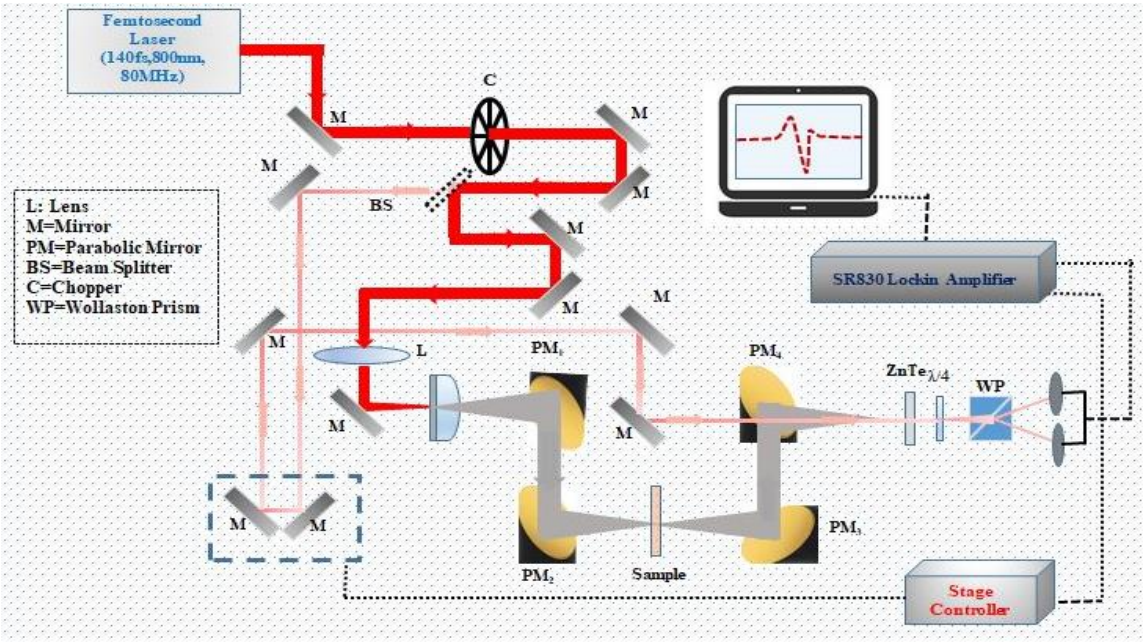

Figure.2.2: The experimental setup schematic for THz generation and transmission/absorption measurements.

A Ti: sapphire laser (Coherent Chameleon Ultra-II) running at an 80 MHz repetition rate provided the 800 nm wavelength and 140 fs pulse duration needed for the transmission measurement. This laser produced tunable THz radiation in the 0.1-3.5 THz range. A 90:10 beam splitter (BS) was used to divided the laser pulse into two parts. To produce effective THz radiation, the reflected portion was directed toward a low-temperature (LT) GaAs-based photoconductive antenna (PC antenna). Using an off-axis parabolic mirror (OAPM) arrangement, the generated THz radiation was directed towards the crystals for the purpose of transmission measurement. Using an additional pair of OAPM sets, the transmitted radiation was collimated and focussed on an electro-optic ZnTe crystal. Therefore, the resultant THz signal was evaluated through the utilization of an electro-optic (E-O) sampling methodology consisting of a ZnTe crystal, quarter-wave (λ/4) plates, a Wollaston prism, and a set of balanced PIN photodiodes. This complex experimental arrangement facilitated accurate and effective assessment of the THz radiation that was propagated, thus permitting an elaborate examination of its characteristics.

2.4. Femtosecond coherent amplified ultrafast Ti: Sapphire laser system (LIBRA):

We employed a Class IV amplified Ti: Sapphire laser system in our experimental arrangement. This laser system functions at a central wavelength of 800 nm and generates femtosecond pulses with a duration of approximately 50 fs. It produces an average power of up to 4.0 Watts, equivalent to 4.0 mJ per pulse, at a repetition rate of 1.0 kHz. The amplification of the mode-locked femtosecond pulse sequence is accomplished through a regenerative amplifier utilizing the chirped pulse amplification method, ensuring the production of powerful femtosecond pulses [23]. The specific laser system utilized is the Coherent LIBRA, a compact oscillator combined with a regenerative amplifier laser system. The primary constituents include the optical bench assembly, the synchronization and delay generator (SDG), the power supply for Vitesse and Evolution, and the chiller. The all-in-one amplified laser system Coherent Libra's optical bench consists of 4 distinct modules: (i) Coherent Vitesse seed laser (oscillator), (ii) Regenerative amplifier, (iii) Coherent Evolution 25 pump laser (for regenerative amplification), and (iv) The compressor and stretcher modules [24].

2.4.1 Efficient SHG and THz generation using femtosecond laser amplifier:

The experimental configuration aimed to investigate the second harmonic generation properties of the crystals, providing intricate insights into the nonlinear optical processes induced by ultrashort laser pulses within the crystal medium. A dichroic mirror was used to filter out the unconverted portion of 800 nm, while a λ/4 wave plate and polarizer-based attenuator were used to adjust the incident power of 800 nm. However, we have used a fiber linked spectrometer (Maya 2000 pro Ocean Optics, India) to detect the generated and unconverted component of 800 nm. To assess the efficiency of the THz power generated from the crystal, which was depicted in Figure 2.3, the pyrometer was used instead of the fiber detector. In the subsequent experimental phase, the crystals were specifically utilized for the generation of the second harmonic of the 800 nm wavelength. This process involved employing 50 fs pulses through the Ti: Sapphire amplifier, operating at a frequency of 1 kHz. For efficient Terahertz (THz) generation, we replaced the photoconductive (PC) antenna with a crystal, as depicted in Figure 2.4, to record the time-domain THz signal emanating from the crystal. To eliminate the unconverted portion of the 800 nm femtosecond laser beam, a silicon plate was employed as a filter. This silicon plate acted as an effective filter, selectively allowing the observation of the focused THz signal generated by the crystal.

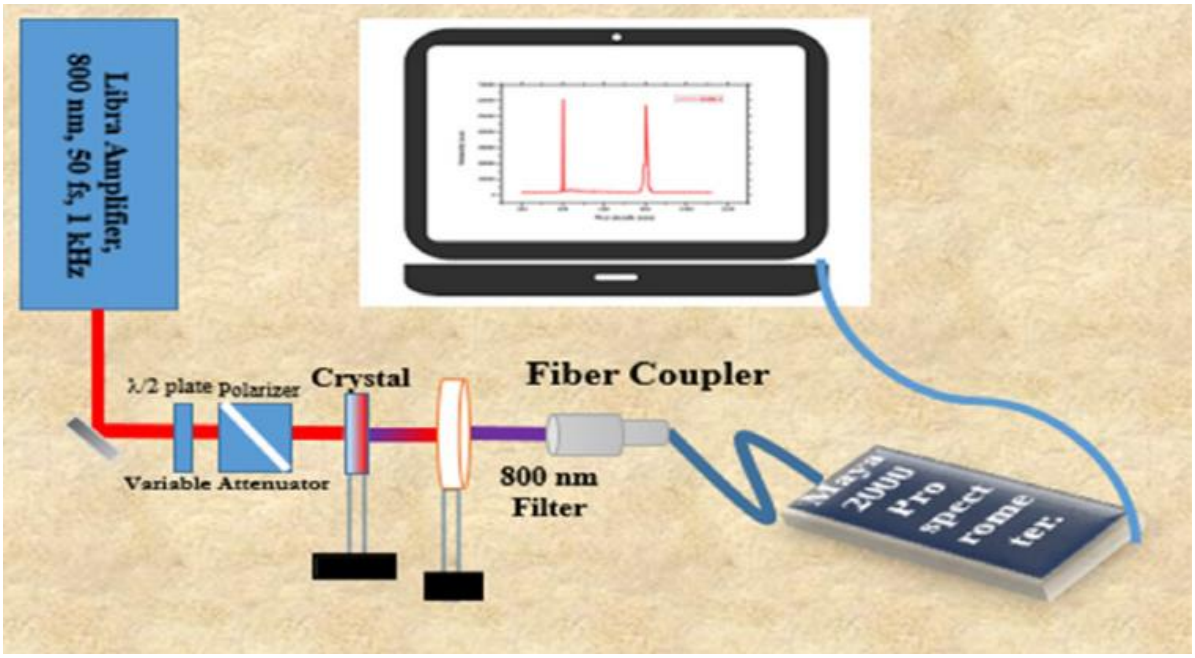

Figure.2.3: Experimental set-up for efficient second harmonic generation using femtosecond laser amplifier. The spectrum is recorded using Maya 2000 pro-ocean optics spectrometer.

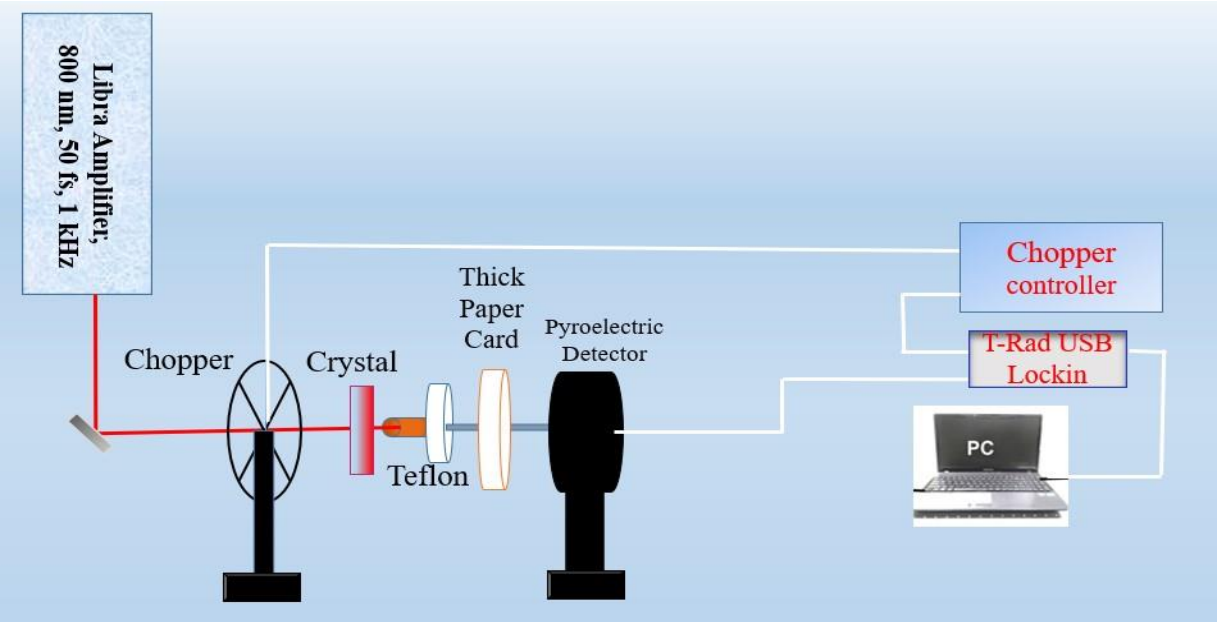

Figure. 2.4: Diagram of the design of the experiment for employing a pyro-electric detector to evaluate the power of the terahertz signal from nonlinear crystals.

2.5 TeraFlash Pro: versatile terahertz time domain platform:

Developed by TOPTICA in Germany, the TERAFLASH system is a compact table-top terahertz platform that combines direct bandgap semiconductor-based InAlAs/InGaAs photoconductive switches with proven femtosecond laser technology in a unique way. With a measurement time of less than one minute, this system has achieved an impressive bandwidth

exceeding 5.0 THz, mostly due to the use of an extremely accurate mechanical delay stage that guarantees a peak dynamic range of over 90 dB. Significantly, the entire system is powered by advanced 1560 nm technology, and antenna modules are carefully outfitted with single-mode, polarization-maintaining (SM/PM) fiber pigtails to maximize efficiency. The use of femtosecond lasers in this system allows for the production of pulsed terahertz radiation. Using a 50:50 beam splitter, the ultra-short laser pulse is divided into two pieces in this operation. One of these components is aimed at the InAlAs/InGaAs photoconductive antenna-based terahertz emitter, and the other component is aimed at the detector following its interaction with a sample. The system's two optical routes each have extremely accurate mechanical delay stages that are connected by fiber. While the reception path is built with a slower, longer-travel delay system, the path that emits THz radiation has a quick, scanning delay mechanism. The ultra-short laser pulses within the terahertz emitter are used to create free charge carriers, which are then accelerated by an externally applied 100-volt biasing field. This results in the creation of a transient current that generates the terahertz pulse, which is then radiated into free space. Conversely, the detector functions as a "pump and probe" device. In this setup, the incident terahertz pulse accelerates charge carriers generated by the "probe" laser pulse, simultaneously creating a voltage across the receiving photoconductive antenna. The photocurrent which is generated has a direct relationship with the terahertz electric field. A prominent feature of the THz time-domain spectroscopic (THz-TDS) system is the pulse width mismatch between the probing laser pulse (60 fs) and the generated terahertz pulse (~1 ps). Because of this difference in pulse width, each time the laser pulse contacts with the two InAlAs/InGaAs photoconductive detectors, just a portion of the terahertz pulse is recorded. Using the much shorter "probe" pulse, a variable delay stage is used to scan the terahertz wave packet in order to reassemble the entire pulse shape. The terahertz frequency domain spectrum is produced by performing a fast fourier transform on the terahertz amplitude. An ethernet link is built into the tabletop system to enable LabVIEW-based software control. Because of its fiber-pigtailed design, it can be positioned freely in transmission or reflection geometry. Using a robust all-fiber-based femtosecond laser system (TOPTICA FemtoFErb THz FD 6.5) with a typical pulse width of 60 fs and a wavelength of 1560 nm and a repetition rate of 100 MHz. At the fiber output that maintains polarization, the laser has an output power of about 80 mW. Dispersion-compensating fibers (DCF) are incorporated into the fiber-optic beam route in order to reduce the effects of dispersion in the fiber delivery. In addition, a motor-driven corner-cube mirror with a 4-fold optical path and a long-travel delay line are included to establish a constant

temporal offset and compensate for changes in the terahertz path, resulting in a delay of up to 4000 ps. Measuring the time delay value, the resolution of 1.3 fs is remarkable.

2.5.1 THz time-domain reflection spectroscopy using femtosecond laser:

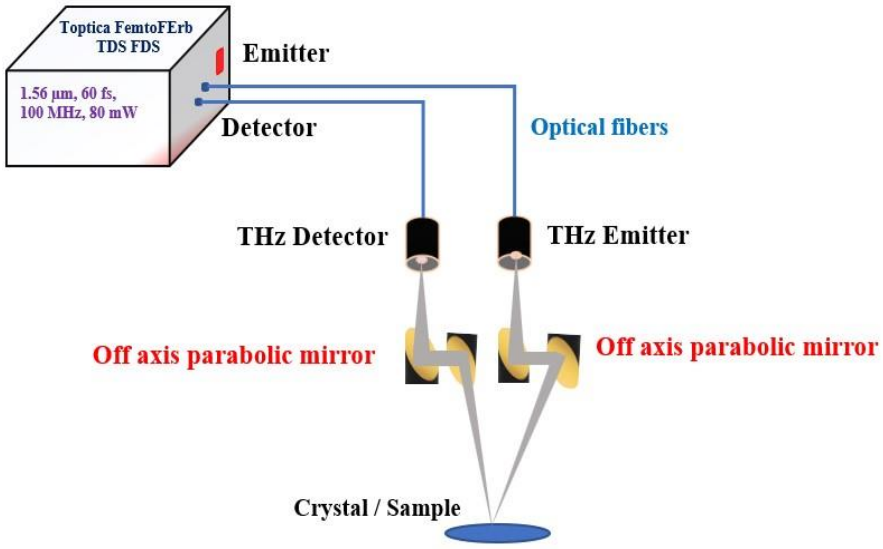

Figure.2.5 Schematic experimental set up for THz reflection geometry

Our experimental setup is shown in Figure 2.5 for determined the optical characterisation of the samples such as refractive index, absorption coefficient, real and imaginary dielectric constants in THz domain.

2.6 Silicon radar:

A compact, economically viable, fully integrated solution has been innovatively engineered for short range communication systems operating at a frequency of 300 GHz. Capitalizing on the sophisticated attributes of low-temperature cofired ceramic (LTCC) technology, this advancement incorporates an integrated reflector for the on-chip antenna, alongside high-data-rate signal interconnections featuring a flip-chip and via transition, all impeccably embedded within a meticulously designed package. Within the confines of the package cavity, a diminutive silicon lens antenna coexists with a flip-chip bonded receiver IC, complete with an on-chip antenna. Notably, the overall dimensions of the front-end receiver are confined to a mere 10 × 10 × 4 mm^3, encompassing the 6 mm diameter silicon lens. Upon integration onto an evaluation board, this compact terahertz receiver demonstrated wireless links, showcasing commendable data rates of up to 27 Gb/s. Thanks to the significant advancements in CMOS and BiCMOS technology, millimeter-wave applications are possible to be affordably mass

produced, leading to greater market penetration in consumer electronics. Signal frequencies within the D-band are immensely appealing due to their exceptional spatial resolution capabilities, leading to the development of compact chip sizes and diminutive antenna dimensions. The utilization of handheld devices, such as mobile phones and tablet PCs, has witnessed a notable increase, enabling individuals to access vast amounts of digital data. This surge in demand for extensive data transfers, particularly through multimedia servers, has been a driving force behind the escalation of wireless data rates to unprecedented levels. Radio frequency (RF) systems intricately interact with customized radiating elements, particularly antennas, based on the specific application requirements. The integration of antennas and an RF integrated circuit (IC) within a unified package eliminates the necessity to transmit high-frequency RF signals through the package lead frame onto a printed circuit board (PCB) substrate characterized by a coarse feature size and pitch. The development of a robust and efficient package at millimeter-wave frequencies presents a myriad of challenges that need to be addressed. First and foremost, establishing a thermal pathway between the IC and the package is crucial to dissipate the heat generated by the active IC, thereby preventing circuit malfunctions or potential damage. Secondly, achieving a high-performance IC to antenna connection poses inherent difficulties at millimeter-wave frequencies, necessitating thorough analysis and design considerations. Lastly, the limited substrate area amplifies the effects of unwanted electromagnetic interference among various package components, potentially leading to degradation of the far-field radiation pattern of antennas and negatively impacting overall package performance. As a result, the intricate design requirements of both passive and active circuits within a millimeter-wave package demand a profound level of radio frequency (RF) expertise, supported by rigorous electromagnetic simulations. The deployment of a miniaturized 0.3 THz industrial, scientific and medical (ISM) band frequency-modulated continuous wave (FMCW) radar system, which includes a SiGe single-chip radar sensor and liquid crystal polymer (LCP) off-chip antennas integrated into a quad flat no-lead (QFN) package, has enabled the system to achieve an unparalleled level of millimeter-level distance accuracy. Evaluation kits equipped with a user-friendly graphical interface (Web-GUI) empower users to fine-tune baseboard parameters, visualize radar data, and make real-time adjustments, enhancing the usability and functionality of the radar system. Two primary methodologies are employed for establishing the IC to antenna connection, namely system-on-chip (SoC) and system-in-package (SiP) approaches. In the SiP framework, an off-chip antenna is utilized, avoiding the use of semiconductor technology for its implementation. The flexibility

in selecting the substrate for antenna design presents the opportunity to achieve increased antenna bandwidth and efficiency. However, this methodology is not exempt from limitations, as it is constrained by manufacturing precision and resolution, dependent on the chosen technology, and requires a high-bandwidth millimeter-wave interconnect. Conversely, the SoC approach represents the epitome of circuit integration, eliminating the need for millimeter-wave interconnections while ensuring the highest level of integration and addressing the challenges associated with high-frequency interconnections.

A. Circuit physics of silicon radar

The circuit gets an input voltage of around 5V and this is then transformed into near 30V which is then used to generate THz frequency rays. This process involves several steps that are written as follows: Transforming a 5V voltage to 30V in a silicon radar system that uses microcontrollers to generate terahertz (THz) frequencies involves several stages of electronic components and principles of electronic circuit design. Here's a simplified explanation of the physics and electronics involved:

1. **DC-DC boost converter:**

To increase the voltage from 5V to 30V, a DC-DC boost converter is typically used. This converter operates based on the principles of electromagnetic induction and energy conservation. A boost converter's fundamental parts are an inductor, a diode, a switch (often a transistor), and a capacitor.

Figure 2.6 Base board of 300 GHz (0.3 THz) silicon radar

2. **Switching operation:**

The microcontroller generates a control signal that turns the switching transistor on and off at a high frequency (THz). The inductor stores energy in its magnetic field when current passes through it when the transistor is turned on.

3. **Inductive energy storage:**

The magnetic field collapses when the transistor is turned off, creating a voltage across the inductor that is applied in the opposite direction. A higher output voltage is obtained by adding this value to the input voltage.

4. **Diode and capacitor:**

A diode is placed in parallel with the load to prevent reverse current flow, and a capacitor is used to filter and stabilize the output voltage.

5. **Control loop:**

A feedback control loop is commonly utilized to modify the output voltage to the intended level. The microprocessor adjusts the duty cycle and switching frequency of the transistor in order to maintain a constant 30V voltage.

6. **Efficiency:**

A few examples of the variables that affect this voltage transformation's efficiency are the control method, switching frequency, and component quality. When properly designed, boost converters can attain a pretty high efficiency.

7. **THz frequency generation:**

The microcontroller also plays a critical role in generating THz frequencies. This typically involves using direct digital synthesis (DDS) or phase-locked loop (PLL) techniques to generate high-frequency signals.

Figure.2.7 Schematic diagram of the 300 GHz signal

Figure 2.7 shows the schematic diagram of 300 GHz signal, which consists of a 75 GHz colpitts structure voltage-controlled oscillator (VCO) with an output power greater than 5 dBm and a tuning range of over 10 GHz. An oscillator's primary wave output port incorporates a frequency

divider by two to facilitate the construction of the phase-locked loop (PLL). The signal source also includes a power amplifier operating at 150 GHz, a 300 GHz doubler, and a 150 GHz doubler. The design goal is to provide an output signal at 300 GHz that is greater than 0 dBm. The highest oscillation frequency (f_{max}) of the process is 329 GHz, and the cut-off frequency (f_{cut}) is 300 GHz. FMCW radar begins with a signal generator, often employing a voltage-controlled oscillator (VCO), to create a radio frequency (RF) signal. Crucially, this RF signal is subject to continuous frequency modulation, achieved by applying a voltage (5V DC) that smoothly varies the output frequency of the VCO over time, creating what's known as a frequency ramp. This ramping signal is then sent to the radar's transmit antenna, which emits it into the surrounding space. As the transmitted signal travels, it encounters objects in its path. Some of this signal is reflected in the radar system as echoes, and these echoes carry essential information. The radar employs a mixing process through a component called a mixer, to combine the transmitted signal with the received echoes. This combination results in an intermediate frequency (IF) signal whose frequency is directly related to the difference between the transmitted and received frequencies. Signal processing techniques are then employed to analyse this IF signal. By measuring the frequency difference, the radar can determine the round-trip time for the signal to travel to the object and back, allowing for precise distance measurements. FMCW radar is widely recognized for its ability to measure both distance and velocity with high accuracy. This capability makes it invaluable in various applications, including automotive collision avoidance systems, industrial sensing, and remote sensing for weather and environmental monitoring.

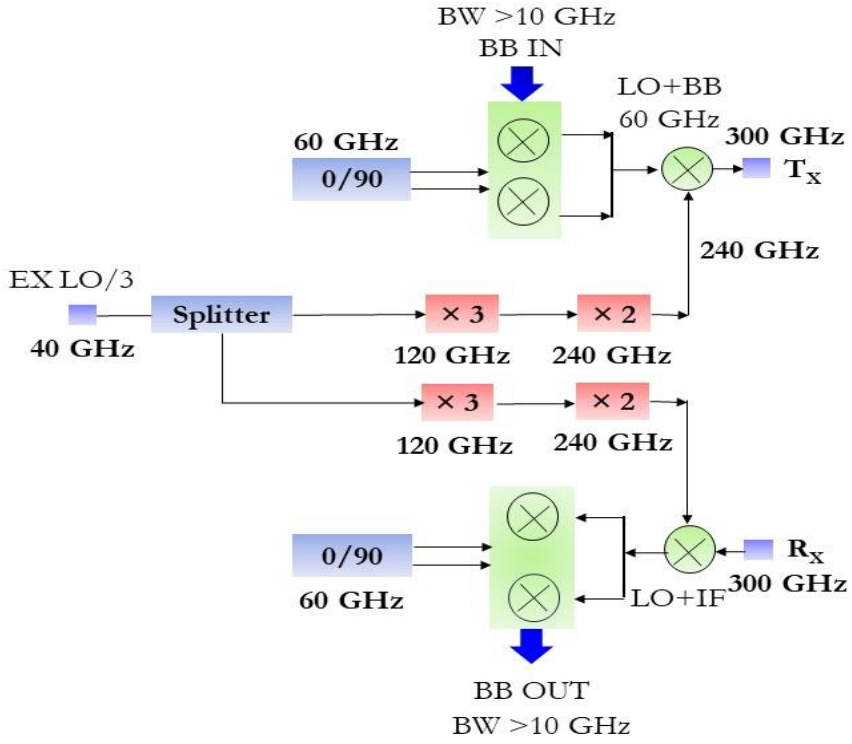

Figure.2.8 Schematic of the 300 GHz transceiver

The schematic of a 300 GHz silicon radar transceiver is shown in Figure 2.8. Three components make up the transmitter: a 240 GHz frequency multiplier-by-6 chain, a 300 GHz up-converter, and a 60 GHz zero IF IQ up-converter. The system includes a LO (Local Oscillator) frequency multiplication chain, despite chip area loss, because the current signal source's low output power exceeds 200 GHz. When measuring the transmitter's performance, it reaches a maximum output power of 4.1 dBm at 300 GHz and continues to exceed 10 dBm between 270 and 315 GHz. The generating THz frequencies involves sophisticated and specialized components and techniques due to the extremely high frequencies involved. Silicon-based radar systems may require special semiconductor technology such as GaN or SiGe, to handle high-frequency operations efficiently. A baseband (BB) input signal with a bandwidth greater than 10 GHz is introduced at the top. This signal was combined with a local oscillator (LO) signal at 60 GHz. The LO signal, after passing through a 0/90-degree phase shifter, is mixed with the BB signal using a mixer. It produces an intermediate frequency (IF) signal at 240 GHz. The 240 GHz signal was further multiplied by 2 using a frequency multiplier, resulting in a 300 GHz signal. The 300 GHz signal, corresponding to the terahertz range, was transmitted as the final output signal. On the receiving side, the 300 GHz THz signal was received and fed into a mixer, where it was mixed with a 240 GHz LO signal to down-convert the THz signal. The LO signal,

obtained from the same frequency multiplication chain as used for THz generation, was combined with the received signal. The mixer down-converts the 300 GHz signal back to an intermediate frequency (IF) that can be processed. The output was a baseband (BB) signal with a bandwidth greater than 10 GHz, which corresponds to the original input signal before THz transmission. The LO signal starts at 40 GHz and is split into two paths. Each path undergoes a multiplication process: first by 3 (in 120 GHz) and then by 2 (in 240 GHz). This multiplied signal was used in both the transmitter and receiver sides to generate and detect the 300 GHz THz signal.

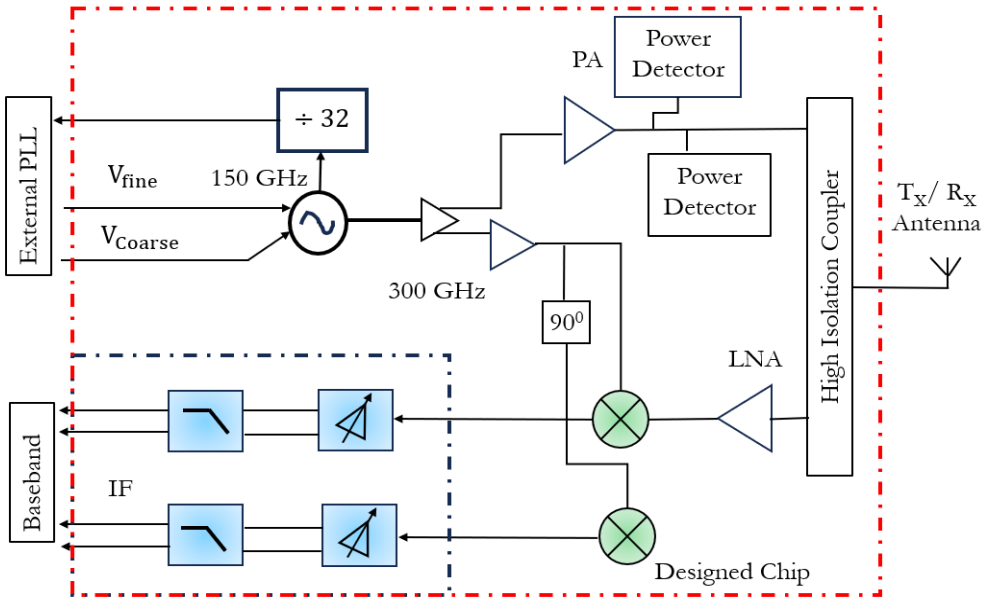

Figure 2.9 Design for a monostatic, single-channel TRx device operating at 300 GHz

A schematic of a very flexible single-channel transceiver (TRx) is shown in Figure 2.9. A low-noise amplifier (LNA) is integrated in the receiver (Rx) portion to maximize the incoming signal and reduce noise interference. A passive power splitter divides the amplified signal into two separate signals that are meant for the in-phase and quadrature (I/Q) mixer cores, which are located in the transconductance stages. After that, these I/Q signals pass through one more passive structure and enter the switching phases. There are several advantages to using I/Q processing, including phase information facilitation, IF amplification, and picture frequency cancellation. The differential IF outputs resulting from the I/Q processing are then internally and externally refined using filters and variable-gain amplifiers (VGAs). The voltage-controlled oscillator (VCO) of the transmitter (Tx) component operates in a certain frequency range, mainly between 150 GHz and 300 GHz. The frequencies generated by the circuit cores

are 150 GHz and 300 GHz, respectively. To achieve the appropriate center frequencies, these frequencies are internally doubled. Depending on the particular chip architecture, a power amplifier (PA) is built into the VCO, usually in the driving stage, to guarantee the creation of strong output power. In order to incorporate external phase-locked-loop (PLL) capability, an integrated frequency-tuning mechanism is used. This mechanism offers possibilities for both fine and coarse sweeps through multi-bit operation, which is usually carried out by means of a stack of parallel variable capacitors inside the VCO core. Additionally, for TRxs running at 300 GHz, an integrated frequency divider with a 32:1 ratio produces an output with an estimated bandwidth of 40 GHz. The VCO's output is then split into the receiver (Rx) and transmitter (Tx) channels, with the Tx channel going via the primary PA to increase the output power even more. The schematic experimental setup for a 300 GHz radar and the flowchart of the silicon radar data visualization code are shown in Figures 2.10 and 2.12, respectively.

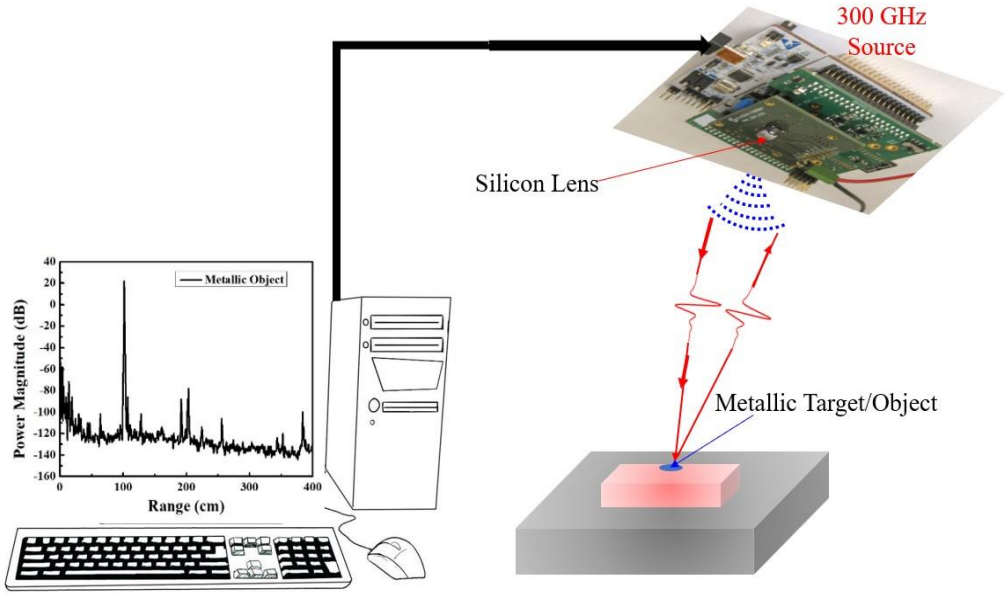

Figure.2.10 Schematic Experimental setup for 0.3 THz radar

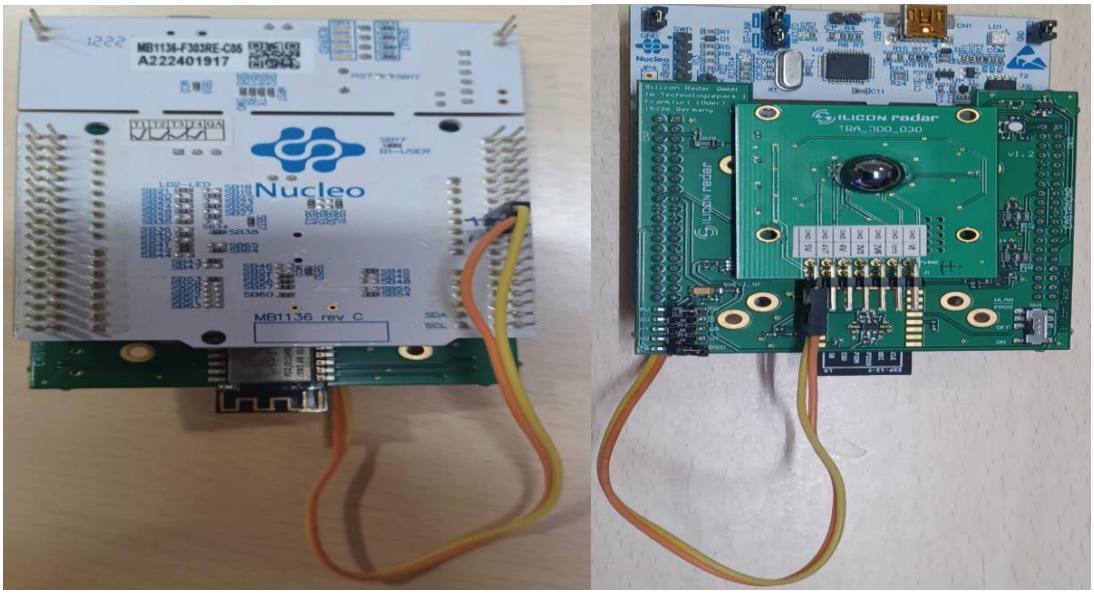

Figure 2.11 (a) Pins 18 (5V) as well as 20 (GND) within the CN7 connector of the F303RE Nucleo board provide the power connection (5V, GND) on the bottom side of the Easy. (b) Power Connection on the 300 GHz front end (5V, GND)

To supply power to the front end, a separate connection is necessary as illustrated in Figure 2.11(a) and (b) of the Easy kit. The front end should be connected to +5V and GND on pin 18 and pin 20 of the CN7 connector on the Nucleo board MB1136-F303RE, avoiding the 5V pin of the header bar on the Easy. An alternative is to use an external power source with a typical supply current of 270mA, connecting the front end to the power source before powering it on and potentially utilizing corner connectors CN11 or CN12 for GND connection.

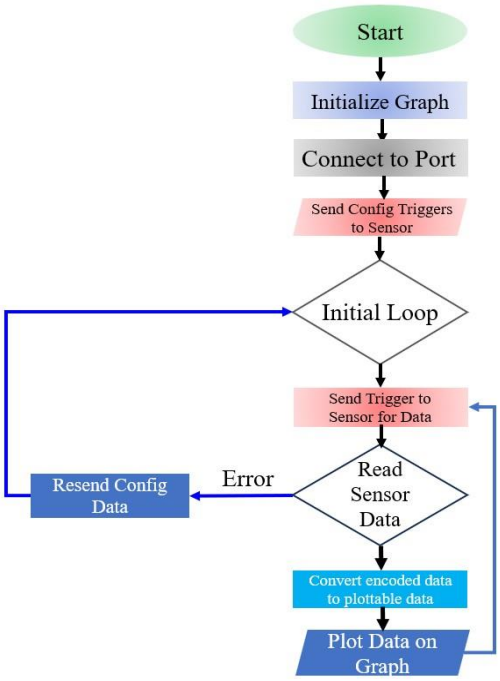

Figure.2.12 Flowchat of 300 GHz silicon radar code

The flowchart describes the process of configuring and reading data from a sensor which is part of a radar system, and plotting the data on a graph. Here is a detailed explanation of each step in the flowchart:

Start:

The process begins here.

Initialize Graph:

The system initializes the graph that will be used to plot the sensor data.

Connect to Port:

The system establishes a connection to the sensor through a specific port.

Send Config Triggers to Sensor:

Configuration triggers are sent to the sensor to set it up for data collection.

Initial Loop:

The system enters an initial loop to start the data collection process.

Send Trigger to Sensor for Data:

A trigger was sent to the sensor to prompt it to start sending data.

Read Sensor Data:

The system reads the data sent by the sensor.

Error Check:

The system checks if there was an error in reading the sensor data. If an error is detected, the process goes to the "Resend Config Data" step. If no error is detected, the process moves to the next step.

Convert Encoded Data to Plottable Data:

The encoded data received from the sensor is converted into a format that can be plotted on the graph.

Plot Data on Graph:

The converted data was plotted on the graph.

Loop Back:

After plotting the data, the process loops back to the "Send Trigger to Sensor for Data" step to continuously collect and plot new data.

Resend Config Data:

If an error occurs, the configuration data is resent to the sensor, and the process loops back to the "Initial Loop" step to reinitialize and restart the data collection.

This flowchart effectively outlines the steps involved in initializing a graph, setting up a sensor, continuously collecting and plotting data, and handling errors by reconfiguring the sensor.

2.7 For measuring UV generation and detection using Nd: YAG nanosecond laser:

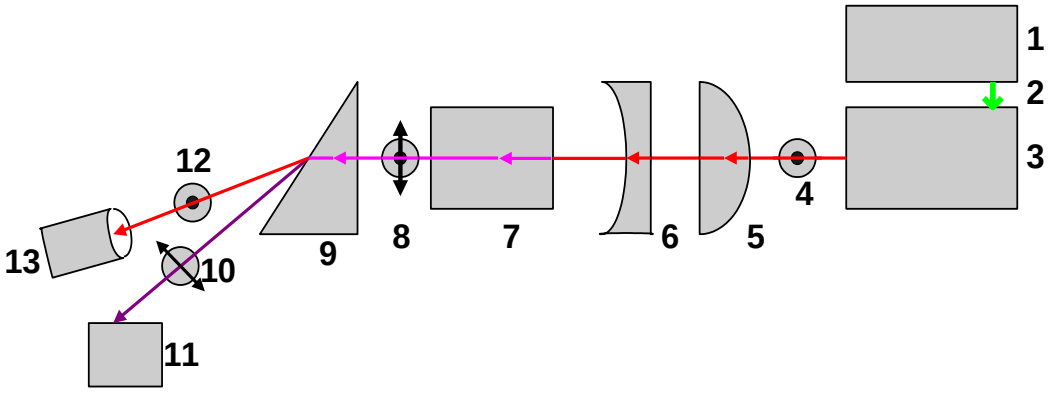

Figure. 2.13: Experimental setup was designed for tunable second harmonic generation within the range of 325-340 nm using nanosecond lasers, with components including (1) Nd: YAG laser; (2) 532 nm pump beam for dye laser; (3) Dye laser; (4) Vertically polarized fundamental dye radiation; (5) Plano convex lens with f = 50 cm; (6) Plano concave lens with f = - 25 cm; (7) crystal; (8) Fundamental and its SHG radiations, (9) CaF_2 prism, (10) Horizontally polarized generated UV radiation (SHG), (11) Power/energy meter, (12) Unconverted vertically polarized fundamental radiation and (13) Beam dumper.

A Q-switched Nd: YAG laser (LAB-170, spectra physics, USA) with a pulse length of 10 ns and a repetition rate of 10 Hz was used to pump 532 nm from SHG of 1064 nm light to

the dye laser (PDL-2, spectra physics, USA). The dye laser beam had an adjustable wavelength of 650–700 nm and was vertically polarized. To refine and control the laser beam properties, the dye laser output underwent a telescopic arrangement featuring a plano convex-concave lens combination, as illustrated in Figure. 2.13. This arrangement not only reduced the beam diameter to 1.0 mm but also maintained its parallelism over a considerable distance. With the LDS-698 dye laser, the crystal's ability to produce variable UV light between 325 and 340 nm was assessed after it was added to the system. Figure 2.13 shows the schematic representation of this experimental setup. The goal of this setup was to examine and utilize the tunable UV radiation characteristics made possible by the crystal medium's interaction with the dye laser.

2.8 Theoretical consideration and data processing:

2.8.1 THz transmission geometry:

The equations presented are utilized to measure transmission and optoelectronics parameters of materials/crystals in the THz spectrum. Equation (2.1) defines the magnitude of transmitted THz electric field T, considering the amplitudes of THz electric field radiation passing through the crystal/sample and air, $E_{Crystal}$ and E_{Ref}.

$$T = \frac{E_{Crystal}}{E_{Ref}} \tag{2.1}$$

$$\text{Absorption coefficient } (\alpha_{Crystal}) = -\frac{1}{d_{Crystal/Sample}} \ln \frac{T_{Crystal/Sample}}{T_{Air}} \tag{2.2}$$

In equation 2.2, $T_{Crystal}$ and T_{Air} are THz electric field intensity from crystal and air (reference), respectively. The refractive index of the crystal is found with equation no. (2.3),

$$n_{Crystal/Sample} = 1 + \frac{\Delta\phi \times c}{2\pi\nu \times d_{Crystal/Sample}} \tag{2.3}$$

where, $\Delta\phi$ is phase difference between crystal and air, ν is corresponding THz frequency, $d_{Crystal}$ is the thickness of the crystal and c is the speed of light in vacuum respectively.

Equation (2.4) can be used to determine the imaginary refractive index (k) of the crystal

$$k = \frac{c}{2\pi\nu \times d_{Crystal}} \ln\left(\frac{4n_{Crystal}}{T(n+1)^2}\right) \tag{2.4}$$

The real part of the dielectric constant and THz reflectivity of the crystal are calculated by equations nos. (2.5) and (2.6) as,

$$|\varepsilon_r| = n_{Crystal/Sample}{}^2 + k_{Crystal/Sample}{}^2 \tag{2.5}$$

$$R_{Crystal} = \frac{(n_{Crystal}-1)^2}{(n_{Crystal}+1)^2} \quad (2.6)$$

The coherent length of the NLO crystal is given by Eq (2.7),

$$L_c = \frac{\lambda_{THz}}{2(n_{gr}-n_{THz})} \quad (2.7)$$

Where, λ_{THz} is the terahertz wavelength (1 THz = 300 μm), n_{gr} and n_{THz} are the refractive indices of optical and THz region. Additionally, the terahertz transmittance of the crystal is evaluated using Eq. (2.8).

$$T = e^{-\alpha_{Crystal} d_{Crystal/Sample}}\left(1 - R_{Crystal}\right)^2 \quad (2.8)$$

The optical conductivity of the crystal can be calculated by using the equation no. (2.9)

$$\sigma = \frac{n_{Crystal}+1}{Z_0 \times d_{Crystal}}\left(\frac{1}{T} - 1\right) \quad (2.9)$$

Here, $Z_0 = 377\Omega$ is the wave impedance in vacuum. The group velocity of the nonlinear crystal can be calculated using eq. no (2.10)

$$v_g = \frac{c}{n_g} \quad (2.10)$$

2.8.2 THz reflection geometry:

For the measurement of reflectance and optoelectronic characterisation of the crystals using the following equations in the THz domain: The magnitude of reflected THz electric field R is given by equation no. (2.11)

$$R_{Crystal} = \frac{E_{Crystal}}{E_{Ref}} \quad (2.11)$$

The absorption coefficients (α) & refractive index (n) of the NLO crystals were ascertained by using equation nos. (2.12) and (2.13), respectively in THz reflection mode,

$$\alpha_{Crystal} = -\frac{4\pi\nu}{c}\frac{2R\sin\phi}{1+R^2-2R\cos\phi} \quad (2.12)$$

$$n_{Crystal} = \frac{1-R^2}{1+R^2-2R\cos\phi} \quad (2.13)$$

The THz spectra for nonlinear crystals were measurable at room temperature (300K). Equation 2.14 gives the complex refractive index,

$$N(\omega) = n_{Crystal/Sample}(\omega) + ik_{Crystal/Sample}(\omega) \quad (2.14)$$

The real and imaginary dielectric constant are calculated by using equation nos. (2.15) & equation (2.16) respectively.

$$\varepsilon' = n_{Crystal/Sample}{}^2 - k_{Crystal/Sample}{}^2 \quad (2.15)$$

$$\varepsilon'' = 2n_{Crystal/Sample}k_{Crystal/Sample} \quad (2.16)$$

2.8.3 THz based Surface roughness, optical impedance and reflection coefficients in transverse electric (TE) and transverse magnetic (TM) mode:

The approximation of the Kirchhoff theory of electromagnetic (EM) scattering is the idea that a smooth surface devoid of corners or sharp edges will minimize shadowing and multiple scattering, resulting in the best possible outcomes with a gaussian surface height distribution profile. The determination of the rayleigh factor is an essential step in evaluating the surface roughness of materials or crystals. The modified reflection coefficients are significantly impacted by the exponent factor σ, which denotes the standard deviation of the surface height of the crystal. With the use of the modified Fresnel equations, impedance, modified reflection coefficient, and surface roughness factor, equation no. (2.18) may be used to calculate the real scattering loss in a given direction [25-26].

$$\rho_{Crystal} = e^{-g/2} \quad (2.17)$$

$$g_{Crystal} = \left(\frac{4\pi.\sigma.\cos\theta_i}{\lambda}\right)^2 \quad (2.18)$$

The parameters θ_i, λ, σ, and Z are utilized to describe the angle of incidence, incident wavelength, standard deviation of surface roughness, and impedance of crystals/materials of THz electric field radiation, respectively, with Z determined through equation no. (2.19).

$$Z = \sqrt{\frac{\mu_0}{\varepsilon_0\left(n_{Crystal/Sample}{}^2 - \left(\frac{\alpha_{Crystal}c}{4\pi f}\right)^{\frac{1}{2}}\right)}} \quad (2.19)$$

Where f denotes the incident THz frequency of the NLO crystals, ε_0 is the permittivity, and μ_0 is the free space permeability. The modified reflection coefficients based on surface roughness which show the decline in THz signal power in the specular direction are

$$r'_{TE} = \rho_{Crystal}.r_{TE} \quad (2.20)$$

$$r'_{TM} = \rho_{Crystal}.r_{TM} \quad (2.21)$$

When the TE or TM polarized waves from the smooth surface of the crystals or materials are represented by the Fresnel reflection coefficients, r_{TE} and r_{TM}. The THz reflection coefficient of the nonlinear crystal in both TE and TM modes has been determined through the use of modified Fresnel equations (2.20) and (2.21), respectively. Usually, Fresnel equations no. 2.22 and 2.23 are used to compute reflection from the surface.

$$r_{TE} = \frac{Z\cos\theta_i - Z_0\cos\theta_t}{Z\cos\theta_i + Z_0\cos\theta_t} \tag{2.22}$$

and

$$r_{TM} = \frac{Z\cos\theta_t - Z_0\cos\theta_i}{Z\cos\theta_t + Z_0\cos\theta_i} \tag{2.23}$$

Where, $\theta_t = \sin^{-1}\sin\left(\sin\theta_i \times \frac{Z}{Z_0}\right)$ represents the angle of refraction

2.8.4 Data analysis for proto-type silicon radar system:

For data collection, a reference measurement was first recorded using a material with properties similar to those of the sample being tested. Then the sample was subjected to the THz radiation and the reflected radiation was recorded for calculation purposes. The net amplitude of the transmitted electric field (EF) was recorded as an E_{sample} and that of the initial reference as an $E_{reference}$. To calculate the distance, the time it took for the transmitted ray to be reflected was measured. Fourier transformation provides temporal information to frequency amplitude together with phase and intensity information when electric fields are observed in the THz time domain of spectroscopy. After that, the data collection was subjected to the fast fourier transform (FFT). The fast fourier-transform (FFT) computation requires equal separation of the recorded time domain data points. The Fourier transformed signal can be represented as in equation (2.24)

$$E(\nu) = \int_{-\infty}^{\infty} E(t)e^{-ti\nu}\,dt \tag{2.24}$$

The transmission signal is given by equation (2.25)

$$H(\nu) = \frac{E_{Sample}(\nu)}{E_{Reference}(\nu)} \tag{2.25}$$

Reference:

[1]. T.H. Maiman, "Stimulated Optical radiation in Ruby", Nature, **187**, 493-494 (1960).

[2]. Celebrating 60 years of laser, Commun Phys, **3**, 96 (2020).

[3]. W. Sibbett, A. A. Lagatsky, and C. T. A. Brown, "The development and application of femtosecond laser systems", Opt. Exp **20**, 6989-7001 (2012).

[4]. Luc G. Legres, Christophe Chamot, Mariana Varna and Anne Janin, "The Laser Technology: New Trends in Biology and Medicine", J. Mod Phys **5**, 267-279 (2014).

[5]. M. Toyoshima et al., "Ground-to-satellite laser communication experiments", in IEEE Aerospace and Electronic Systems Magazine, **23(8)**, 10-18 (2008).

[6]. R. Martínez Vázquez, G. Trotta, A. Volpe, G. Bernava, V. Basile, M. Paturzo, P. Ferraro, A. Ancona, I. Fassi, and R. Osellame, "Rapid Prototyping of Plastic Lab-on-a-Chip by Femtosecond Laser Micromachining and Removable Insert Microinjection Molding", Micromachines, **8 (11)**, 328 (2017).

[7]. X. Liu, D. Du and G. Mourou, "Laser ablation and micromachining with ultrashort laser pulses", IEEE J. Quantum Electronics, **33 (10)**, 1706-1716 (1997).

[8]. Jerome Lapointe, Yannick Ledemi, Sébastien Loranger, Victor Lambin Iezzi, Elton Soares de Lima Filho, Francois Parent, Steeve Morency, Younes Messaddeq, and Raman Kashyap, "Fabrication of ultrafast laser written low-loss waveguides in flexible As2S3 chalcogenide glass tape", Opt. Lett. **41**, 203-206 (2016).

[9]. Kamil Stelmaszczyk and Philipp Rohwetter, "Long-distance remote laser-induced breakdown spectroscopy using filamentation in air", Appl. Phys. Lett. **85**, 3977 (2004).

[10]. R. Berera, R. Van Grondelle, and J. T. M. Kennis, "Ultrafast transient absorption spectroscopy: principles and application to photosynthetic systems", Photosynth Res, **101**, 105–118 (2009).

[11]. S. Ameer-Beg, W. Perrie, S. Rathbone, J. Wright, W. Weaver, and H. Champoux, "Femtosecond laser micro structuring of materials", App. surface science **127**, 875-880 (1998).

[12]. W. J. Whitman, "The CO_2 laser", Springer **53** (2013).

[13]. H. Wille, M. Rodríguez, J. Kasparian, D. Mondelain, J. Yu, A. Mysyrowicz, R. Sauerbrey, J-P. Wolf, and L. Woeste, "Teramobile: a mobile femtosecond-terawatt laser and detection system", The European Physical Journal Applied Physics, **20(3),** 183-190 (2002).

[14]. M. Deubel, G. Freymann, M. Wegener, S. Pereira, K. Busch and C. M. Soukoulis, "Direct laser writing of three-dimensional photonic-crystal templates for telecommunications", Nature Materials, **3**, 444–447 (2004).

[15]. G. Méjean, J. Kasparian, J. Yu, S. Frey, E. Salmon, and J-P. Wolf, "Remote detection and identification of biological aerosols using a femtosecond terawatt lidar system", App. Phys. B, **78 (5)**, 535-537 (2004).

[16]. Feng Liu, K. M. Yoo, and R. R. Alfano, "Ultrafast laser-pulse transmission and imaging through biological tissues", Appl. Opt. **32**, 554-558 (1993).

[17]. M. E. Fermann, A. Galvanauskas and G. Sucha (eds.), "Ultrafast lasers: technology and applications", CRC Press, **80** (2002).

[18]. D. Strickland and G. Mourou, "Compression of amplified chirped optical pulses", Optics Communications, **55(6)**, 447-449 (1985).

[19]. K. König, A. Ehlers, F. Stracke, and I. Riemann, "In vivo drug screening in human skin using femtosecond laser multiphoton tomography", Skin Pharmacol Physiol, **19(2)**, 78-88 (2006).

[20]. N. Granzow, "Supercontinuum white light lasers: a review on technology and applications", Photonics and Education in Measurement Science, **11144**, 1114408 (2019).

[21]. M. D. Perry, D. Pennington, B. C. Stuart, G. Tietbohl, J. A. Britten, C. Brown, S. Herman, B. Golick, M. Kartz, J. Miller, H. T. Powell, M. Vergino, and V. Yanovsky, "Petawatt laser pulses", Opt. Lett. **24**, 160-162 (1999).

[22]. X. Zeng, K. Zhou, Y. Zuo, Q. Zhu, J. Su, X. Wang, X. Wang, X. Huang, X. Jiang, D. Jiang, Yi Guo, N. Xie, S. Zhou, Z. Wu, J. Mu, H. Peng and F. Jing, "Multi-petawatt laser facility fully based on optical parametric chirped-pulse amplification", Opt. Lett. **42**, 2014-2017 (2017).

[23]. D. Strickland and G. Mourou, "Compression of amplified chirped optical pulses", Optics Communications, **55 (6)**, 447-449 (1985).

[24]. R. Paschotta, "Field Guide to Laser Pulse Generation", SPIE press Bellingham, **14 (**2008).

[25]. R. Piesiewicz, T. Kleine-Ostmann, N. Krumbholz, D. Mittleman, M. Koch, and T. Kürner, "Terahertz Characterisation of bulding materials", Electron. Lett. **41** (18), 1002-1004, (2005).

[26]. R. Piesiewicz, C. Jansen, D. Mittleman, T. Kleine-Ostmann, M. Koch, and T. Kurner, "Scattering Analysis for the Modeling of THz Communication Systems", IEEE Trans. Antennas Propag. **55** (11), 3002-3009 (2007).

Chapter 3

3. Evalution of BIBO, S- doped GaSe, α-TeO_2 nonlinear crystals for efficient SHG and terahertz generation:

Abstract

This chapter deals with the investigation of efficient THz generation and optoelectronic characterization of three nonlinear crystals from different categories such as uniaxial and biaxial belong to semiconductor, semimetal and inorganic groups. The optoelectronic characterization was performed using femtosecond laser based coherent and incoherent techniques. We have selected BIBO, S-doped GaSe, and α-TeO_2 crystals for our studies. Efficient SHG and THz radiation were generated using nanosecond (1064nm,10ns) and femtosecond (800 nm, 140 fs & 50 fs) laser systems respectively. The absorption coefficients, refractive indices, surface roughness, reflection coefficients in both TE and TM modes, and dielectric properties of the NLO crystals were evaluated to assess their performance as THz devices. In addition, effect of doping of sulfur (S) was also studied in cased GaSe. Chalcopyrite crystal, particularly S-doped GaSe, was selected due to its excellent linear and nonlinear optical properties such as transmission in visible to FIR range, high anisotropy and second order nonlinearity and high damage threshold. S-doped GaSe demonstrates superior THz conversion efficiency as compared to α-TeO_2 and BIBO crystals, attributed to its above mentioned linear and nonlinear properties. The optimized experimental conditions for THz generation were ascertained for these crystals and obtained results are compared with existing reported works in terms of their THz conversion efficiency.

A part of the research work presented in this chapter has published in the following scientific peer reviewed journals

a) ***Chandan Ghorui***, *A. M. Rudra, Udit Chatterjee, A. K. Chaudhary, and D. Ganesh, "Efficient second-harmonic and terahertz generation from single BiB_3O_6 crystal using nanosecond and femtosecond lasers", Appl. Opt.* ***60****, 5643-5651 (2021).*
b) ***Chandan Ghorui*** *and Arjun V Kidavu and P Naveen Kumar and S Das and A K Chaudhary and Yu M Andreev, "Comparative studies of terahertz-based optical properties in transmission/reflection modes of GaSe: S and measurement of its scattering losses due to surface roughness for efficient terahertz generation", Physica Scripta,* ***98****,2, 025508, 2023.*
c) ***Chandan Ghorui*** *and A. K. Chaudhary, "Linear and nonlinear optical characterization of tellurium dioxide (α-TeO_2) for generation of terahertz radiation using time-domain spectroscopy", Appl. Opt.* ***62****, 4831-4835 (2023).*

3.1 Nonlinear effects in nonlinear crystals:

Nonlinear crystals have got wide attention from the scientists working in the field of optics and materials science over the past two decades. It is mainly due to their moderate generation efficiency between UV to THz range and the capability to produce broad bandwidths tunable EM spectra. It has also overcome the limitations of photoconductive antennas used for THz generation. Because it needs incident radiation energy of the order of the semiconductor material's bandgap. In contrast, THz generation from nonlinear crystals do not have such type of stringent requirements. It is attributed to the availability of nonlinear frequency mixing techniques such as optical rectification (OR) and difference frequency mixing (DFM). Due to excellent nonlinear quality of and wide transmission range enable them to generate new frequencies or modify the phase of incident light efficiently. In classical electronics circuit the process of rectification used for converting alternating current (AC) to direct current (DC). Similarly, in the field of optics, optical rectification occurs when a changing electric field component of an optical signal is transformed into a DC field along with polarized wave by the crystal. To generate THz from nonlinear crystals using optical rectification process, certain requirements must be met, such as a laser pulse must be in the femtosecond domain, a thin crystal (thinness ~1 mm for offset the group dispersion effect) with moderate second-order nonlinearity, and high transmission in the optical and THz domains.

3.1.1 Efficient THz generation from nonlinear ZnTe crystals using optical rectification process:

In this section, we have selected ZnTe crystal which is an ideal and commercially used for the THz pulses generation using mechanism of OR induced by femtosecond laser pulses. The applied electric field ($\vec{E}$) and induced polarization ($\vec{P}$) are linearly connected in dielectric medium, however, which requires electric field strength of the order of 10^5 to 10^8 V/m. The Taylor series expansion of the polarization, as indicated by Equation. 3.1, introduces the higher-order nonlinear elements into the picture is represented

$$\vec{P_i} = \varepsilon_0 \vec{E} \, (1 + \chi^{(1)}\vec{E} + \chi^{(2)}\vec{E}^2 + \chi^{(3)}\vec{E}^3 + ..) \qquad (3.1)$$

In the electro-optic effect, the nonlinear terms $\chi^{(1)}$, $\chi^{(2)}$, $\chi^{(3)}$are the higher orders. Since the higher terms $\chi^{(2)}$ in the crystal of Centro Symmetry must be identically equal to zero, $\chi^{(1)}$, $\chi^{(1)}\vec{E}\,(\omega_1)$ =-$\chi^{(3)}\vec{E}\,(\omega_2)$. As a result, we can only write nonlinearity due to the first term nonlinear $\chi^{(3)}$.

$$\vec{P_i} = 2d\vec{E}^2 \tag{3.2}$$

Now, the equation of linear polarization for the forward standing wave represents as equations (3.3) & (3.4) respectively.

$$\vec{E}_1(z,t) = \vec{E}_1 \mathrm{Cos}\,(\omega_1 t + \vec{k}_1 z) \tag{3.3}$$

$$\vec{E}_2(z,t) = \vec{E}_2 \mathrm{Cos}\,(\omega_2 t + \vec{k}_2 z) \tag{3.4}$$

Now, the linear polarization written as equation (3.5)

$$\vec{P_i} = 2d\left[\vec{E_1}^2 \mathrm{Cos}^2(\omega_1 t + \vec{k}_1 z) + \vec{E_2}^2 \mathrm{Cos}^2(\omega_2 t + \vec{k}_2 z) + 2\vec{E}_1\vec{E}_2\,\mathrm{Cos}\,(\omega_1 t + \vec{k}_1 z)\,\mathrm{Cos}\,(\omega_2 t + \vec{k}_2 z)\right] \tag{3.5}$$

$$\vec{P}_{2\omega_1} = 2d[\vec{E_1}^2(\omega_1)\mathrm{Cos}\,\{2(\omega_1 t + \vec{k}_1 z)\}]$$

$$\vec{P}_{2\omega_2} = 2d[\vec{E_2}^2(\omega_2)\mathrm{Cos}\,\{2(\omega_2 t + \vec{k}_2 z)\}]$$

$$\vec{P}_{(\omega_1+\omega_2)} = 2d\vec{E}_1(\omega_1)\vec{E}_2(\omega_2)\mathrm{Cos}\,\{2(\omega_1+\omega_2)t + (\vec{k}_1+\vec{k}_2)z)\}$$

$$\vec{P}_{(\omega_1-\omega_2)} = 2d\vec{E}_1(\omega_1)\vec{E}_2(\omega_2)\mathrm{Cos}\,\{2(\omega_1-\omega_2)t + (\vec{k}_1-\vec{k}_2)z)\} \tag{3.6}$$

and a study term $\vec{P}_{\mathrm{direct}} = 2d\{\vec{E_1}^2 + \vec{E_2}^2\}$. After that, the nonlinear polarization has a stable term, a sum and difference frequency, and what are typically referred to as the second harmonics, the first overtone of both input frequencies. The second harmonic, sum frequency $\vec{E}\,(\omega_1+\omega_2)$ (SFG), and difference frequency $\vec{E}\,(\omega_1-\omega_2)$ (DFG) of $\vec{E}_1$ and $\vec{E}_2$ are among the resulting frequency components of the polarization. When ultrafast pulses are used to leave the optical rectification, a matching electric field $\vec{E}\,(\omega_1-\omega_2)$ produces DC polarized waves with a duration of sub picoseconds. This is a special case of difference frequency generation (DFG).

$$\vec{E}_{\mathrm{THz}} \propto \frac{\partial^2\vec{P}^2}{\partial t^2} \tag{3.7}$$

Consequently, there exists a correlation between the second order derivative of the pulse and the THz signal that is produced. The THz radiation, encompassing all spectral elements of the laser pulse, can be conceptualized as difference frequency generation (DFG). Specifically, the electric fields $\vec{E}_1(\omega_1)$ and $\vec{E}_2(\omega_2)$ must exhibit oscillations at closely spaced frequencies denoted as ω_1 and ω_2, so as to ensure that their frequency disparity, $\omega_3 = \omega_{THz} = \omega_1 - \omega_2$, aligns with the THz domain. Consequently, a polarization oscillating at a THz frequency ω_{THz} is

generated through the process of difference frequency generation (DFG). The ensuing discussion outlines the requisite phase matching criteria for the wave vectors:

$$\Delta k = \vec{k}_{THz} - (\vec{k}_1 - \vec{k}_2) \quad (3.8)$$

where $\vec{k}_{THz}$ is the wave vector of the THz-wave is defined as $\vec{k}_{THz} = 2\pi n_{THz}/\lambda_{THz}$ and $\vec{k}_1$ and $\vec{k}_2$ are the wave vectors of optical fields and defined as $\vec{k}_i = \frac{2\pi n_i}{\lambda_i}$, where n_{THz} is the refractive index of NLO crystals in terahertz range, while n_i (i = 1, 2) are the refractive indices of the crystal at the optical wavelengths λ_i (i =1, 2) of the interacting fields $\vec{E}_1(\omega_1)$ and $\vec{E}_2(\omega_2)$ respectively. We can describe the nonlinear polarization induced by optical rectification as [1, 15] in equation no (3.9)

$$P_i^{(2)}(\omega_{THz}) = \sum_{j,k} \varepsilon_0 \chi_{ijk}^{(2)}(\omega_{THz}, \omega + \omega_{THz}, -\omega) E_j(\omega + \omega_{THz}) E_j^*(\omega) \quad (3.9)$$

where the THz electric fields' cartesian components are represented by the indices i, j, and k, and the second-order nonlinear susceptibility tensor element is denoted by $\chi_{ijk}^{(2)}$ Equation no. (3.10) can be used to simplify the second-order nonlinear susceptibility tensor element when the indices are permutable.

$$d_{il} = \frac{1}{2}\chi_{ijk}^{(2)} \quad (3.10)$$

Here,

l =	1	2	3	4	5	6
jk =	11	22	33	23,32	31,13	12, 21

We can rewrite the equation (3.1) as the matrix equation form

$$\begin{pmatrix} P_x(2\omega) \\ P_y(2\omega) \\ P_z(2\omega) \end{pmatrix} = 2\varepsilon_0 \begin{pmatrix} d_{11} & d_{12} & d_{13} & d_{14} & d_{15} & d_{16} \\ d_{21} & d_{22} & d_{23} & d_{24} & d_{25} & d_{26} \\ d_{31} & d_{32} & d_{33} & d_{34} & d_{35} & d_{36} \end{pmatrix} \begin{pmatrix} E_x^2 \\ E_y^2 \\ E_z^2 \\ 2E_yE_z \\ 2E_zE_x \\ 2E_xE_y \end{pmatrix} \quad (3.11)$$

Due to the cubic crystallographic nature of the ZnTe crystal with point group $\bar{4}3m$, the nonvanishing tensor elements would be $\chi_{xyz} = \chi_{xzy} = \chi_{yzx} = = \chi_{yxz} == \chi_{zxy} == \chi_{zyx}$ in the equation no (3.9). The nonlinear susceptibility tensor can thus be simplified as shown in equation (3.12).

$$d_{il} = \begin{bmatrix} 0 & 0 & 0 & d_{14} & 0 & 0 \\ 0 & 0 & 0 & 0 & d_{25} & 0 \\ 0 & 0 & 0 & 0 & 0 & d_{36} \end{bmatrix} \quad (3.12)$$

Here, $d_{14} = d_{25} = d_{36}$. The arbitrary electrical field of femtosecond laser beam can be written as equation no (3.13)

$$\vec{E}_0 = E_0 \begin{pmatrix} \sin\theta\cos\varphi \\ \sin\theta\sin\varphi \\ \cos\theta \end{pmatrix} \tag{3.13}$$

where θ is the polar angle and φ is the azimuthal angle which shows in chapter 1, figure 1.12. Substituting equations (3.12) and (3.13) into equation (3.11), we obtain the nonlinear polarization equation in (3.14)

$$\begin{pmatrix} P_x \\ P_y \\ P_z \end{pmatrix} = 2\varepsilon_0 \begin{pmatrix} 0 & 0 & 0 & 1 & 0 & 0 \\ 0 & 0 & 0 & 0 & 1 & 0 \\ 0 & 0 & 0 & 0 & 0 & 1 \end{pmatrix} \begin{pmatrix} \sin^2\theta\cos\varphi \\ \sin^2\theta\sin\varphi \\ \mathrm{Cos}^2\theta \\ \sin 2\theta\sin\varphi \\ \sin 2\theta\cos\varphi \\ \sin^2\theta\sin 2\theta \end{pmatrix} \tag{3.14}$$

$$= 2\varepsilon_0 d_{14} E_0^2 \begin{pmatrix} \sin 2\theta\sin\varphi \\ \sin 2\theta\cos\varphi \\ \sin^2\theta\sin 2\theta \end{pmatrix}$$

$$= 4\varepsilon_0 d_{14} E_0^2 \sin\theta \begin{pmatrix} \cos\theta\sin\varphi \\ \cos\theta\cos\varphi \\ \sin\theta\cos\varphi\sin\varphi \end{pmatrix} \tag{3.15}$$

The nonlinear polarization of the materials and the polarization of THz radiation produced are parallel. Equation (3.16) can be used to express the THz radiation intensity.

$$I_{THz}(\theta,\varphi) \propto |P|^2 = 4\varepsilon_0 d_{14} E_0^2 \sin^2\theta\,(4\cos^2\theta + \sin^2\theta\sin^2 2\varphi) \tag{3.16}$$

Equation (3.16) postulates that the maximum THz intensity occurs at $\sin^2 2\varphi = 1$, specifically when φ equals π/4 or 3π/4. The THz intensity reaches its peak when the optical polarization aligns with the {110} plane of the electro-optic ZnTe crystal. Equation (3.17) provides a means to represent the THz intensity when the optical electric field lies within the plane of the ZnTe {110} crystal.

$$I_{THz}(\theta,\varphi) \propto 4\varepsilon_0 d_{14} E_0^2 \sin^2\theta\,(4 - 3\sin^2\theta) \tag{3.17}$$

It can be seen that the maximum THz intensity is obtained at $\theta = \sin^{-1}\sqrt{\frac{2}{3}}$

From equation (3.15), the THz field when optical field lies on the {110} plane of the ZnTe crystal can be express as in equation (3.18)

$$\vec{E}_{THz}(\theta) \propto \vec{P}(\omega) \tag{3.18}$$

The different polarization directions of THz electric field corresponding to the different polarization directions of optical electric field are listed as follows in equation no's (3.19) & (3.20) respectively.

$$= 2\varepsilon_0 d_{14} E_0^2 \sin\theta \begin{pmatrix} \sqrt{2}\cos\theta \\ \sqrt{2}\cos\theta \\ \sin\theta \end{pmatrix} \quad (3.19)$$

$$\vec{E}_{THz} = 0 \quad \text{when} \quad \vec{E}_0 \,//\, [0\ 0\ 1] \quad (3.20)$$

$$\vec{E}_{THz} \propto \begin{pmatrix} 0 \\ 0 \\ 1 \end{pmatrix} \perp \vec{E}_0 \quad \text{when,} \quad \vec{E}_0 // [0\ 0\ 1] \quad (3.21)$$

Chapter 2, Figure 2.4 illustrates the experimental setup for generating THz radiation using a ZnTe crystal. The pump beam and the probe beam are the two separate laser beams produced by a regeneratively amplified Ti: sapphire laser system. The system produces pulses of about 50 fs at a wavelength of 800 nm and operates at a repetition rate of 1 kHz. The principal purpose of the pump beam was to excite a ZnTe crystal orientated at 1 mm, which resulted in the generation of THz radiation through optical rectification. A silicon wafer was deliberately used to block all other beams so that only the THz beam could pass through in order to isolate it. Then, the THz beam and the probe beam were aimed to light the same spot on the ZnTe crystal that was orientated 1 mm inward. The free space electro-optic sampling method was used to detect the THz waves.

Nonlinear crystals used for THz generation are classified into three significant categories

1. Inorganic Crystals: BIBO, $LiTaO_3$, BBO, KTP, KTA, $LiNbO_3$ etc.
2. Organic Crystals: P-B1, DAST, OH_1, BNA, DSTMS, HMQ-TMS etc.
3. Semiconductor Crystals: ZnTe, GaAs, S-doped GaSe, α-TeO_2, CdTe, GAP, etc.

In this chapter, we mainly focused on the efficient THz generation from three nonlinear crystals such as BIBO, S-doped GaSe, α-TeO_2 etc. using femto second amplifier by optical rectification techniques. We also characterized the optoelectronic properties of these NLO crystals using 800 nm femtosecond laser oscillator and first time attempt the surface roughness-based characterisation of nonlinear crystal in terms of scattering factor, optical impedance, reflection coefficient in both TE & TM mode.

3.2 BIBO (BiB_3O_6):

Bismuth triborate (BiB_3O_6 or BIBO) emerges as a consequential nonlinear optical (NLO) crystal, demonstrating applicability in second harmonic generation (SHG), optical parametric oscillation (OPO), and electro optic domains. This crystal exhibits notable

characteristics, including a substantial effective SHG coefficient, elevated damage threshold, extensive temperature bandwidth, and resistance to moisture. Originating from the monoclinic group C_2, BIBO was introduced by Hellwig et al. in 1998 [1-4]. Beyond its inherent nonlinear optical prowess and superior laser damage threshold, BIBO manifests as a non-hygroscopic entity. Its optical transparency spans the 160 nm to 2.7 µm region, featuring a UV transmission cut-off at a wavelength surpassing that of Beta Barium Borate (BBO). The crystal presents a noteworthy effective nonlinearity (d_{eff} = 3.2 pm/V), exceeding the nonlinear coefficients of Lithium Triborate (LBO) and BBO by factors of 3.5-4 and 1.5-2, respectively. Recent investigations have harnessed these compelling attributes to showcase BIBO's efficacy in SHG processes, employing diverse laser sources, including continuous-wave [5-6], long-pulse, nanosecond, picosecond [7-8], and femtosecond pulsed lasers [9-13]. Observed conversion efficiencies in pulsed regimes span from 11% [14] with nanosecond pulses to 67.7% with picosecond pulses, illustrating the crystal's versatility. Noteworthy achievements include the generation of tunable SHG between 375-435 nm from a femtosecond oscillator, yielding a 50% conversion efficiency [15]. In our current investigation, the BIBO crystal exhibited a THz conversion efficiency on the order of 1.85 x 10^{-5} %, peaking at 100 mW. Concurrently, comprehensive optoelectronic characterization of the crystal in the THz regime was undertaken.

3.3 S-doped GaSe:

Gallium Selenide (GaSe) has been a subject of scientific interest since its recognition in 1934 due to its exceptional optical frequency conversion and detection capabilities across a broad spectrum of wavelengths [16]. This polytype crystal, exhibiting remarkable physical attributes and belonging to the point group symmetry, offers excellent transparency for non-polarized light, extending beyond wavelengths of ≥ 50 µm [17,18]. Its unique features include extraordinary birefringence (β = 0.375 at λ = 10.6 µm [19] and 0.79 in the terahertz (THz) range [20], an extremely high second-order nonlinear susceptibility (d_{22} = 54 pm/V at 10 µm and 24.3 pm/V in the THz band [21], and the second-highest optical damage threshold [22]. A comprehensive overview of its physical properties has been thoroughly documented elsewhere [20, 23]. GaSe, as one of the oldest nonlinear single crystals, has garnered attention for enhancing its optical and surface hardness properties through the introduction of various dopants. Research efforts by S. Das, Vodopyanov et al. have reported efficient Mid-IR generation from GaSe through difference frequency mixing of CO_2 wavelengths [24]. Additionally, AC Das et al. carried out a comparative examination of undoped and doped GaSe crystals, focusing on parameters such as hardness, frequency range, and the identification of

distinct phonon frequencies manifested as absorption peaks [25]. Despite the extensive body of research, there is a scarcity of literature concerning thin GaSe crystals fabricated as wafers, exhibiting superior generation efficiency in comparison to thicker crystals. GaSe belongs to chalcogenides, a group III–VI semiconductor, characterized as a non-isotropic, negatively uniaxial crystal, available in wafer format, and falling under the specified point group [26]. This crystal boasts the second-highest optical damage threshold, standing at around 30 MW/cm² at 1.064 μm with a 10 ns pulse width. Various research teams have recognized the potential of GaSe in the infrared (IR) and THz spectral regions. Doping GaSe crystals not only improves surface hardness but also broadens the range of THz radiation generation and enhances conversion efficiency [27-30]. Studies by Wei Shi et al. showcased THz frequency generation spanning from 0.57 to 3.57 THz via difference frequency mixing (DFM) from a composite GaSe crystal with an energy of 9.75 nJ [31]. Huang et al. presented emission between 0.57 and 3.57 THz using collinear difference frequency generation from $GaSe_{0.91}$ $S_{0.09}$, achieving a conversion efficiency of 45% with a generated power output of 21.8 W [32]. Wei Chen Chu et al. documented wideband THz generation from GaSe: Te crystal employing femtosecond pulses, with the highest power output capped at 1.3 μW [33]. Jialin Mei et al. explored optical parametric oscillation (OPO) based on KTP crystals, tunable between 0.41 and 3.71 THz from GaSe, achieving a conversion efficiency of 7.8 x 10^{-7} [34]. J. Guo et al. investigated the effects of Al doping in GaAs, resulting in significantly lower absorption by 2 to 3 times and notably reinforced structural and optical characteristics. They also delved into S doping in GaSe, amplifying the damage threshold by 5 times and yielding a signal spectrum ranging from Mid-IR to millimeter wavelengths [35]. While optical spectroscopy offers valuable insights into material properties, THz time domain spectroscopy (TDS) distinguishes itself by directly measuring the temporal profile of the associated electric field. The fast fourier transform (FFT) of the time-domain signal furnishes critical details about the phase and amplitude of the pulse, facilitating the determination of the real and imaginary components of dielectric constants in a crystalline substance without reliance on the Kramers-Kronig relation. Furthermore, precise evaluations of the refractive index and absorption coefficients provide clues regarding the various phonon modes of the wafer within the THz regime [25,26,31]. Correcting surface roughness holds significance in this study, uncovering Mie scattering losses and the consequent reduction in the power of the generated signal. Notably, Mittleman et al. detailed non-contact assessments of surface roughness scattering characteristics and optical impedance utilizing THz radiation [36,37]. Additionally, the dielectric characteristics of

GaSe:S were probed through time-domain THz spectroscopy [25,26]. GaSe:S emerges as a promising substitute for $LiNbO_3$ and ZnTe crystals in laboratory settings for THz radiation generation [38,39]. $LiNbO_3$, known for strong THz generation, exhibits a large difference between optical and THz refractive indices, significantly reducing the coherence length, making it less suitable for detection. In contrast, ZnTe exhibits a small difference between optical and THz refractive indices, resulting in a long coherence length, making it the preferred material for both THz generation and detection. Modern methods have been developed to achieve a large coherence length in a Lithium Niobate crystal and high conversion efficiency [38]. The present study delves into GaSe:S, a doped iteration of GaSe, with a focus on efficient THz generation and optoelectronic characterization in both transmission and reflection modes. Surface roughness properties have been systematically measured to assess reflection, optical impedance, and corresponding losses from the crystal surface. These factors play a pivotal role in influencing the efficiency of the generated THz signal. GaSe:S, exhibiting minimal differences in refractive indices in both optical and THz spectral ranges, emerges as a promising candidate for achieving high conversion efficiency in the THz domain through the optical rectification technique. Remarkably, the attained THz conversion efficiency in this study, approximately **η ~2.2 x 10^{-3} %,** is found to be equivalent to that of a 20 mm thick GaSe crystal employed in the difference frequency mixing (DFM) technique [23,40-41].

3.4 α-TeO_2:

Tellurium oxide (TeO_2) is a highly appealing semiconductor, also classified as a semimetal, existing in both crystalline and amorphous phases. Within the crystalline phase, specifically as Tellurium dioxide (TeO_2), two distinct phases, paratellurite with tetragonal phases featuring orthorhombic symmetry, are observed [42]. In its paratellurite form, TeO_2 belongs to the point group D4 (422), boasting significant symmetry and valuable elastic and piezoelectric properties [43-44]. Numerous studies have highlighted the applications of TeO_2 single crystals as acousto-optic devices in the visible region [45-47]. The acousto-optic figure of merit for a single-crystal paratellurite (1.2 × s3 g" for transverse acoustic waves) surpasses that of existing optically transparent materials, showcasing high chemical stability, mechanical durability, a wide bandgap, and a high dielectric constant. Consequently, it finds extensive use in the fabrication of active optical devices such as deflectors, modulators, tunable filters, and as a dielectric medium in capacitors. Broadband THz radiation is typically generated through various methods, including ultrashort laser-pumped photoconductive switches (PCS), optical rectification (OR) in nonlinear crystals, and difference frequency mixing (DFM) [47-50].

Notable progress has been made in developing new THz sources like quantum cascade lasers, Gunn diode lasers, IMPACT diodes, semiconductor films, and semimetal films. Nonlinear optics (NLO)-based sources are particularly intriguing due to their coverage of the complete THz frequency band (ranging from 0.1 THz to beyond 10 THz). The generated broadband THz pulses on a picosecond time scale offer advantages in phase-coherent detection, providing a time resolution as short as a few tens of femtoseconds. In the quest for new materials, α-TeO_2 emerges as an ideal colorless compound for investigating the role of THz radiation. In contrast to optically opaque pure Te and InSb, which act as broad-band semiconductors and behave like insulators, α-TeO_2 exhibits transparency between 0.33 μm to 6.5 μm. Consequently, no photo charge carriers are generated by femtosecond laser pulses with an 800 nm wavelength. α-TeO_2, with its colorless tetragonal structure within the point group D4 (422), lacks space inversion symmetry at room temperature, resulting in piezoelectricity. Its large acoustic-optic effect makes it suitable for optical modulation and deflection devices in the visible frequency range. However, its application in the THz frequency range at a 300 K temperature is limited due to the high absorption of generated radiation. Additionally, the second-order nonlinear optical coefficient of α-TeO_2 exhibits a moderate value of ~ 0.69 ± 0.08 pm/V at 1.064 μm. Moreover, α-TeO_2 demonstrates optical activity, influencing the orientation of incident laser pulse. The important parameters such as Crystallographic information, transparency range, d_{eff} and Crystal damage threshold value shown in Table 1. In this present study, we have measured the optoelectronics characterisation of semimetal semiconducting α-TeO_2 crystal. We have theoretically calculated TYPE-I phase matching angle θ~21.15° for DFG process whereas phase matching angle for second harmonic generation (SHG) is θ ~35.5^0 (using 800 nm wavelength).

Table -3.1 Comparision of three nonlinear crystals for their properties

Name of Crystal	Crystallographic Information	Transparency Range	d_{eff} (pm/V)	Crystal Damage Threshold	Ref.
BIBO	Monoclinic, point group C2	160nm-2.7μm	3.0±0.2 @1064nm	0.3 GW/cm^2 @1064nm	[5-6]
GaSe:S	Hexagonal, point group $\bar{6}2m$	0.62-20μm	54 @10μm	30 MW/cm^2 @1064nm	[19-21]
α-TeO_2	Tetragonal Orthorhombic, point group, D4-422	0.33-5μm	0.69±0.08 @1064nm	327 @1-3μm	[43-44]

3.5 Result and Discussion:

3.5.1 Efficient UV & second harmonic generation of BIBO crystal using Nd: YAG 1064 nm, 10 ns laser pulse:

The Sellmeier relation of Bismuth triborate (BIBO) inorganic crystal is given by the following equations: $n_i^2 = A+B/(\lambda^2-C)-D\lambda^2$ [51,52] which is valid in 0.32-3.09 µm region.

$$n_x^2 = 3.074 + \frac{0.0323}{(\lambda^2-0.0316)} - 0.01337\lambda^2 \quad (3.22)$$

$$n_y^2 = 3.1685 + \frac{0.0373}{(\lambda^2-0.0346)} - 0.0175\lambda^2 \quad (3.23)$$

$$n_z^2 = 3.6545 + \frac{0.05116}{(\lambda^2-0.0371)} - 0.0226\lambda^2 \quad (3.24)$$

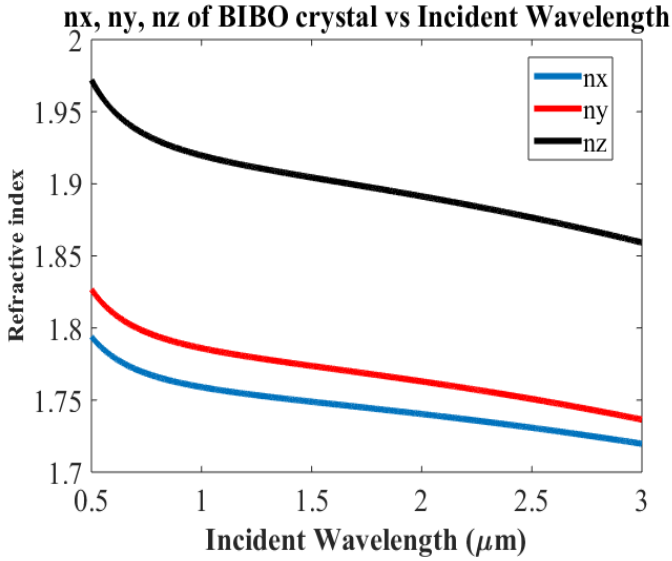

Figure. 3.1: Refractive index v/s Incident wavelength of Bismuth triborate (BIBO) crystal in YZ plane (Type –I o e e interaction) obtained from the Sellmeier relation (3.22), (3.23) & (3.24) respectively

The graph illustrates the relationship between the refractive indices (n_x, n_y, and n_z) of a BIBO crystal and the incident wavelength measured in micrometer. The refractive index n_x starts around 1.76 at 0.5 µm and gradually decreases to about 1.73 at 3 µm. The refractive index n_y begins at approximately 1.82 at 0.5 µm and decreases to about 1.79 at 3 µm. Similarly, the refractive index n_z starts at around 1.96 at 0.5 µm and decreases to approximately 1.91 at 3 µm. All three refractive indices (n_x, n_y, and n_z) show a decreasing trend as the incident wavelength increases. This indicates a dispersive behavior of the Bismuth triborate crystal, where the refractive index is higher at shorter wavelengths and lower at longer wavelengths. Understanding the optical properties of Bismuth triborate crystals, particularly how the refractive indices vary with wavelength, is crucial for applications involving laser systems, nonlinear optics, and other photonics applications. Precise knowledge of refractive indices at different wavelengths is essential for optimizing these applications. An intriguing outcome of

the study is the potential utilization of the dispersion properties in the UV-visible range. Figure. 3.1 illustrates the dispersion properties of BIBO in both the visible and UV ranges. A Bismuth triborate crystal was subjected to LDS-698 dye laser radiation tunable within the 650-700 nm range, served as the source for second harmonic generation (SHG) spanning from 325 to 350 nm. This dye laser, in turn, was stimulated by SHG (532 nm) radiation originating from an electro optically Q-switched Nd: YAG laser with a pulse repetition rate of 10 Hz and a pulse width of 10 ns. Achieving a conversion efficiency of 4.01%, UV at 343.5 nm was successfully generated. The optoelectronic characterization of the BIBO crystal was conducted to produce SHG through a nanosecond-pulsed DCM dye laser, which was pumped by 532 nm wavelength derived from a nanosecond Q-switched Nd: YAG laser.

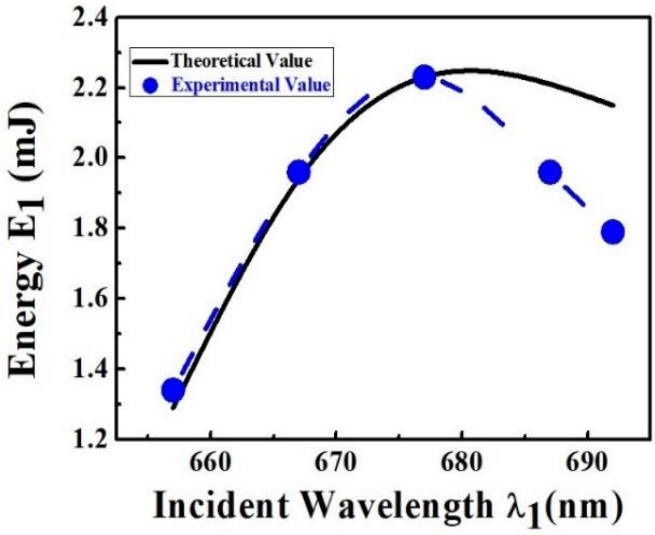

Figure 3.2 The figure displays the variation of the input dye laser energy (E_1) at different dye laser wavelengths (λ_1) during the interaction, maintaining a constant energy for the dye pump beam. The blue dots in the graph correspond to our measured values.

Figure. 3.3 illustrates the angle tuning characteristic for phase-matched second harmonic generation (SHG) in Bismuth triborate. The black curve represents the theoretical prediction based on reported Sellmeier coefficients, while the blue dot curve depicts the experimental results. Our experimentally measured values exhibit a high level of agreement with the theoretical prediction.

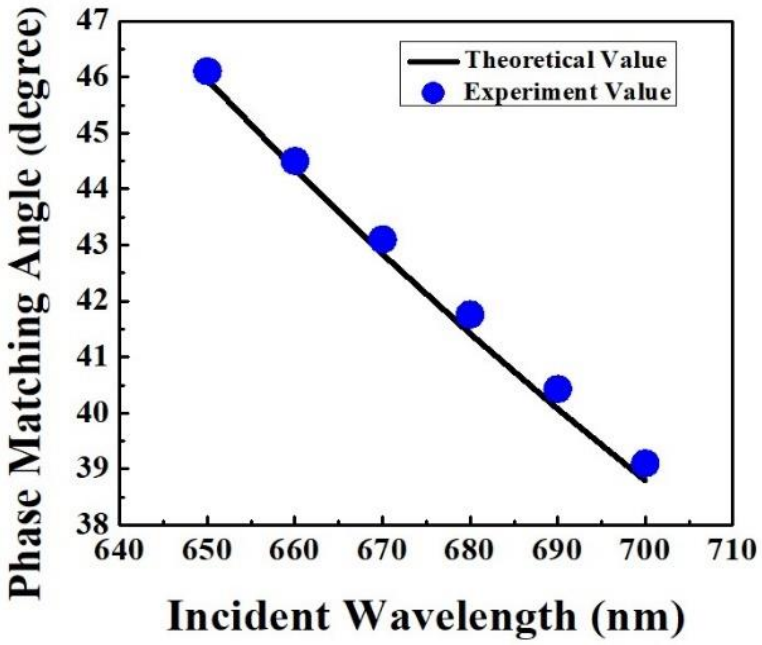

Figure.3.3: The angle tuning characteristics for second harmonic generation (SHG) in Bismuth triborate crystal are depicted in the figure. The black smooth curve represents the theoretical prediction obtained from the Sellmeier coefficients of the inorganic Bismuth triborate (BIBO) Crystal, while the blue dots correspond to our measured values.

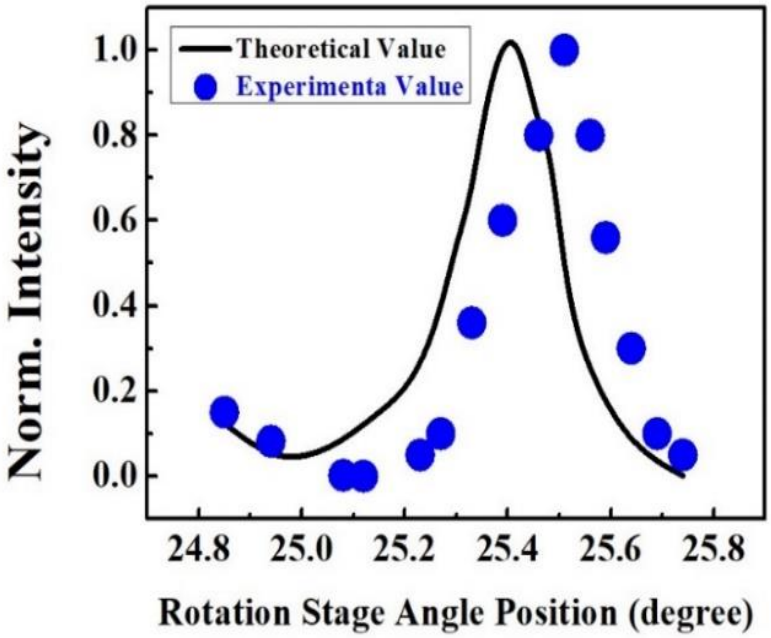

Figure. 3.4: Angular acceptance bandwidth of SHG in 1.29 mm thick Bismuth triborate. The smooth curve is theoretically predicted while the dots are experimental points.

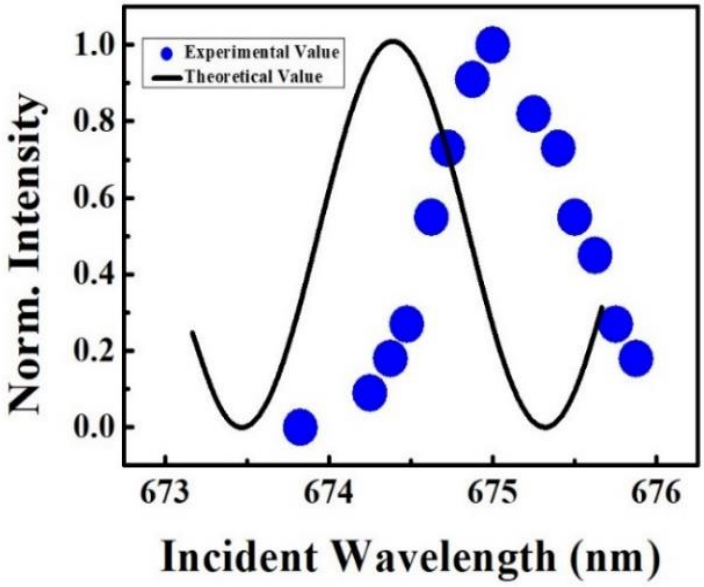

Figure.3.5: Spectral acceptance bandwidth of SHG in 1.29 mm thick inorganic BiB_3O_6 crystal. The smooth curve is theoretically predicted while the dots are experimental points.

In all subsequent calculations related to phase-matching properties, consistent Sellmeier coefficients were employed. The angular acceptance in this crystal was measured and is illustrated in Figure. 3.4. The measured value of Δθ (at full width half maximum) was found to be 3.84 mrad, while the theoretical value is 4.01 mrad. Additionally, we measured the spectral acceptance bandwidth, depicted in Figure. 3.5. The measured value of Δλ (at full width half maximum) was determined to be 0.90 nm, compared to the theoretical value of 0.913 nm. Apart from these measurements, the energy conversion efficiency for the SHG was assessed. Figure. 3.7 presents the measured variation of energy for the tunable SHG wavelengths. The smooth curve represents the theoretical prediction, while the dots depict the measured values. Since the crystal is relatively thin, neglecting crystal absorption and considering no change in beam diameter, the SHG energy was estimated using the formula,

$$E_2 = 8\pi d_{eff}^2 d^2 E_1^2 / [\lambda_1^2 (n_1^o)^3 c\varepsilon_o \tau r^2] \quad (3.25)$$

and

$$d_{eff} = d_{12}\cos^2\theta + d_{13}\sin^2\theta + d_{14}\sin(2\theta) \quad (3.26)$$

Where, E_1 and E_2 are the energies of the fundamental dye beam and its SHG (λ_2), d is the crystal's thickness in meters, n_1^o is the SHG crystal's ordinary (o) refractive index, which is 1.7766, c is the light's velocity, which is 3×10^8 meters per second, and ε_o is the vacuum's permittivity, which is 8.854×10^{-12} Farads/meter. The wavelengths must be measured in meters. The radius of the fundamental beam, r, is 0.50×10^{-3} meters, and is the laser pulse width, which is 10 ns for all interacting beams.

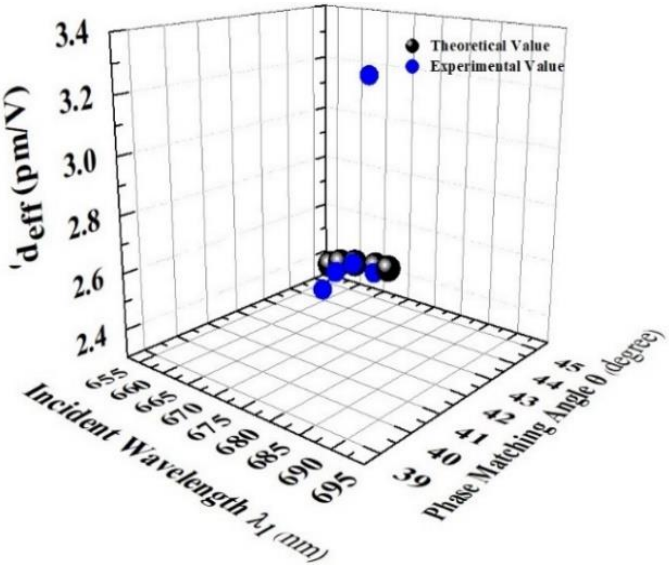

Figure.3.6 Illustrates Nonlinear coefficient (d_{eff}) with incident wavelength (λ_1) and Phase Matching Angle (θ) of inorganic Bismuth triborate Crystal. The black dots are theoretical points whereas blue dots are experimental point.

Figure 3.6 shows the variation in the nonlinear coefficients with respect to the incident wavelength and phase matching angle. The figure indicates that both theoretical and experimental values of the effective nonlinear coefficient (d_{eff}) are being compared over a range of incident wavelengths tunable from 655-695 nm and phase matching angles. The black spheres (theoretical values) and the blue spheres (experimental values) are close to each other, suggesting that the experimental data aligns well with the theoretical predictions. The values of d_{eff} are relatively consistent across the range of incident wavelengths and phase matching angles shown, with slight variations. At the peak dye fluorescent region (687nm), a typical energy conversion efficiency E_2/E_1 of 4.01% was obtained for an input energy (E_1) of ~ 2.23 mJ.

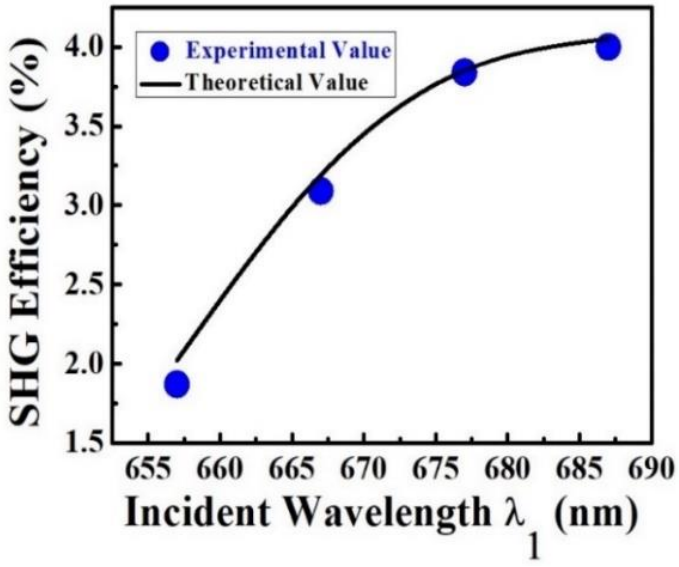

Figure. 3.7 Variation of energy E_1 of dye SHG in 1.29 mm thick BIBO.The black dots are experimental points where as red smooth curve are theoretical value.

Our experimentally measured values exhibit strong agreement with the theoretical predictions depicted in Figure. 3.7 and 3.8 concerning incident wavelength and dye energy, respectively. The efficiency parameter is influenced by various factors, including crystal cut, input laser energy, effective nonlinear coefficient of the crystal, and beam diameter. At 687 nm, the measured efficiency reaches its peak at 4.01 %, slightly below the corresponding theoretical value of 4.09 %.

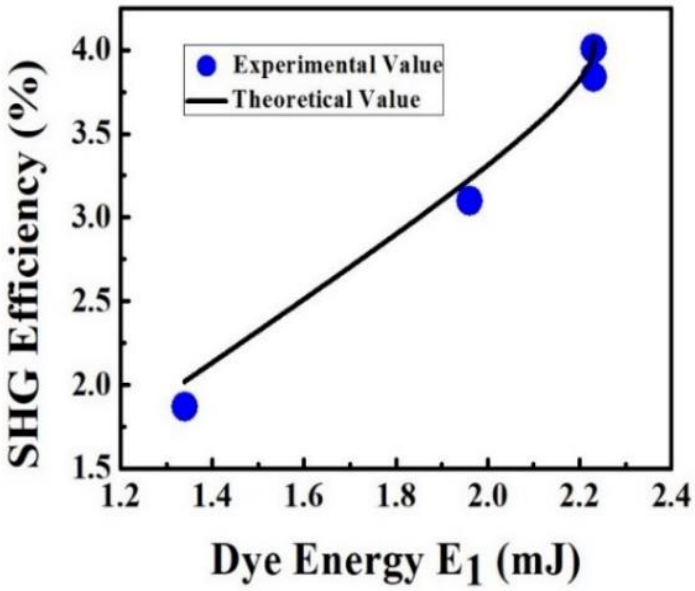

Figure.3.8 Variation of energy E_1 of dye SHG in 1.29 mm thick BIBO.The blue dots are experimental points where as black smooth curve are theoretical value.

Second harmonic generation (SHG) from a Beta Barium Borate (BIBO) crystal using an 800 nm femtosecond laser amplifier can be explained through a nonlinear optical process. When a high intensity femtosecond laser beam (800 nm wavelength, power 4 Watt) interacts with a nonlinear crystal BIBO, it induces a nonlinear polarization in the crystal.

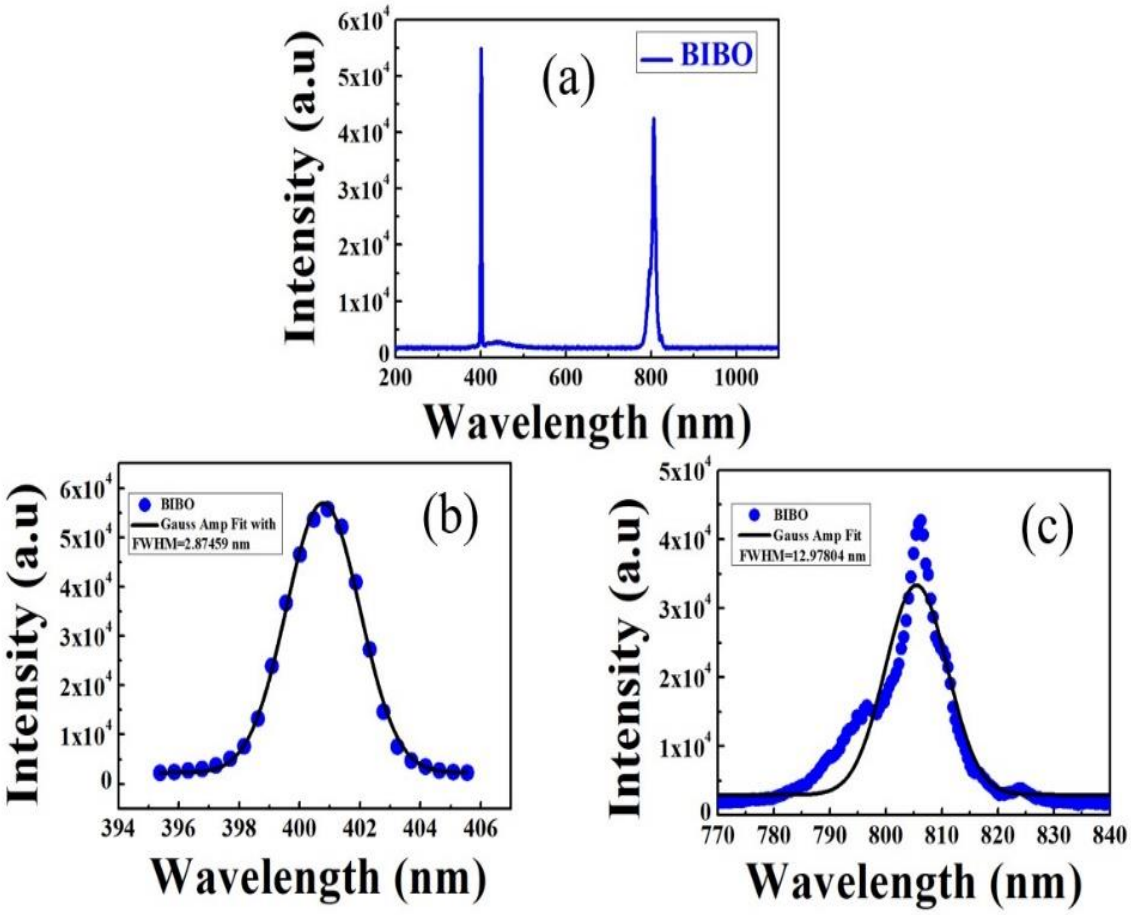

Figure 3.9: (a) Spectral profile distributions of the fundamental (1ω) laser pulse at 800 nm and the second harmonic (2ω) pulse at 400 nm. (b) and (c) show the peak profiles at 400 nm and 800 nm wavelengths, respectively. The fitting was performed after collecting data points from the Maya 2000 Pro Ocean Optics spectrometer (India) and confirms the Gaussian nature of the incident and generated radiation. The blue dots represent experimental values, while the black smooth curves are Gauss Amp fitted values.

Figure. 3.9 (a) shows that the spectral distribution of fundamental and second harmonic pulse using 800 nm femtosecond laser pulses. In second harmonic generation (SHG), the incident laser beam at 800 nm was characterised by a fundamental frequency (1ω) and the nonlinear BIBO crystal responds by the newly generating frequency which was exactly twice of the fundamental frequency (2ω). This process occurs due to high second order nonlinear susceptibility of the crystal. In BIBO crystal, the arrangement of Bi, B and O atoms and the

lattice structure contribute to its second order nonlinear optical properties. The BIBO crystal was responds to that oscillates at twice the frequency of the incident laser, leading to the generation of the second harmonic signal at 400 nm. The spectral was recorded though fiber coupled spectrometer (Maya 2000 pro Ocean Optics, India). In this graph, Y-axis represent the intensity in arbitrary unit and X axis represent the corresponding tunable wavelength. The fitting is performed after collecting data points from the Maya spectrometer, confirming the Gaussian nature of both the incident and generated signals. This has very crucial applications such as frequency doubling in laser sources, nonlinear optics and generation of coherent detection at shorter wavelengths. To understanding the principles behind SHG in BIBO crystals helps in optimization of our experimental setup and harnessing the unique properties of nonlinear crystals for spectroscopic, imaging, homeland security and defense applications. The study demonstrated the use of a Type I, $\theta = 28.9^{\circ}$ cut nonlinear BIBO crystal for producing UV to broadband THz radiation with nanosecond and femtosecond laser pulses. Laser pulses of 800 nm wavelength and varying durations were used from Ti: sapphire laser amplifier and oscillator. Conversion efficiency for SHG and THz generation was observed to be around 50% and 1.85×10^{-5} %, respectively. Tunable UV radiation was generated through SHG of a nanosecond dye laser with an efficiency of about 4.01 %. The phase-matching angle in the Y-Z plane for Type I condition was measured along with angular and spectral bandwidths of the signal. Properties of the BIBO crystal in THz domain were determined for the first time, including coherence length, refractive index, absorption coefficients, and conductivity.

3.5.2 THz transmission & efficiency from BIBO crystal using femto second Ti: sapphire oscillator laser:

Figures 3.10 and 3.11 present the temporal and spectral profiles of BIBO concerning its interaction with air. The received time-domain THz signal, subsequent to its passage through the BIBO crystal, underwent transformation into frequency domain spectra through the implementation of the fast fourier transformation (FFT) technique. The observed dynamic range distinctly illustrates the crystal's capacity for efficient radiation generation, extending up to 2.5 THz. The maximum THz generation is realized at ~1.2 THz.

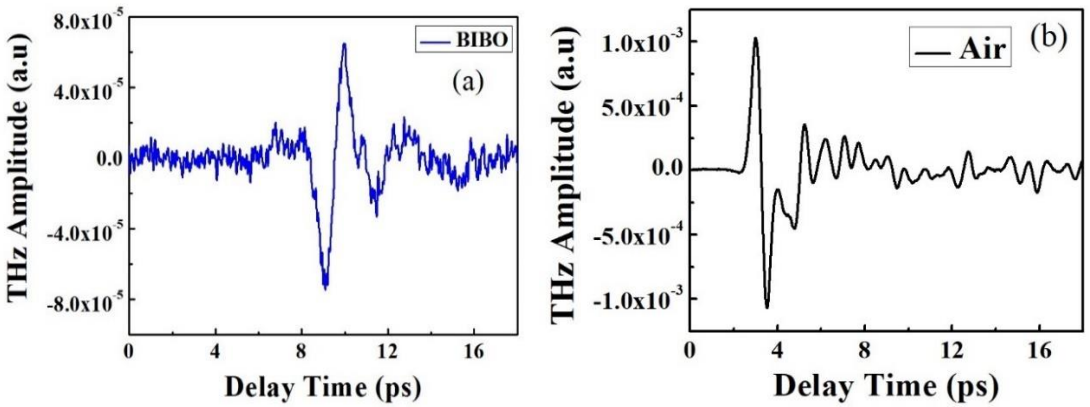

Figure 3.10:(a) Temporal Profile of (a) Bismuth triborate Crystal (b) air

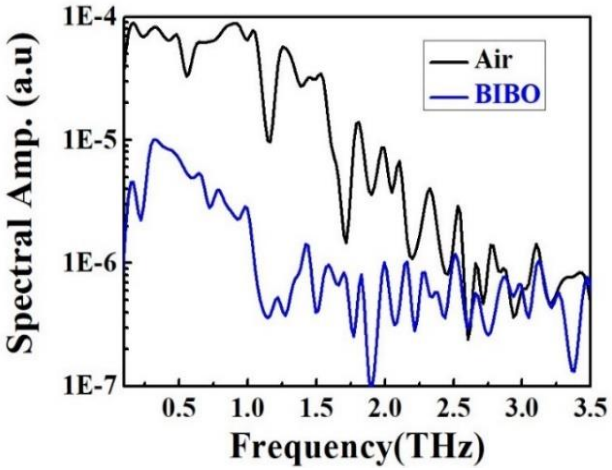

Figure. 3.11 Spectral Profile of BIBO Crystal with respect to air. The black curve represents the spectral amplitude for air & blue one for BIBO crystal.

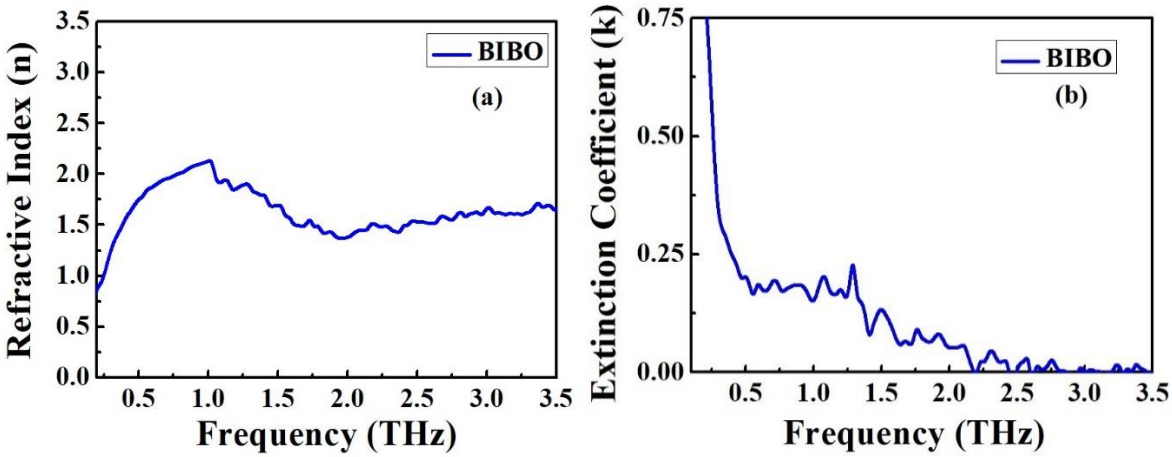

Figure. 3.12: (a) Refractive Index and (b) Extinction Coefficient of biaxial inorganic BIBO crystal. The refractive index & absorption coefficient are calculated using equations (2.2) & (2.3) in the Chapter 2.

Figure. 3.12 (a & b) illustrates the refractive index and extinction coefficient in relation to THz frequencies within the range of 0.1-3.5 THz. The refractive index exhibits variability from 1.9 to 2.2 at the 1.0 THz range, with a noticeable decline between 1 to 1.5 THz, followed by stabilization within the 2-3.5 THz range. On average, the refractive index maintains a value of approximately 1.75 in the THz domain, aligning with the extraordinary refractive index in the optical domain as derived from the Sellmeier equation. Conversely, the extinction coefficient for this crystal experiences an exponential decrease, reaching a constant level between 2.25-3.5 THz.

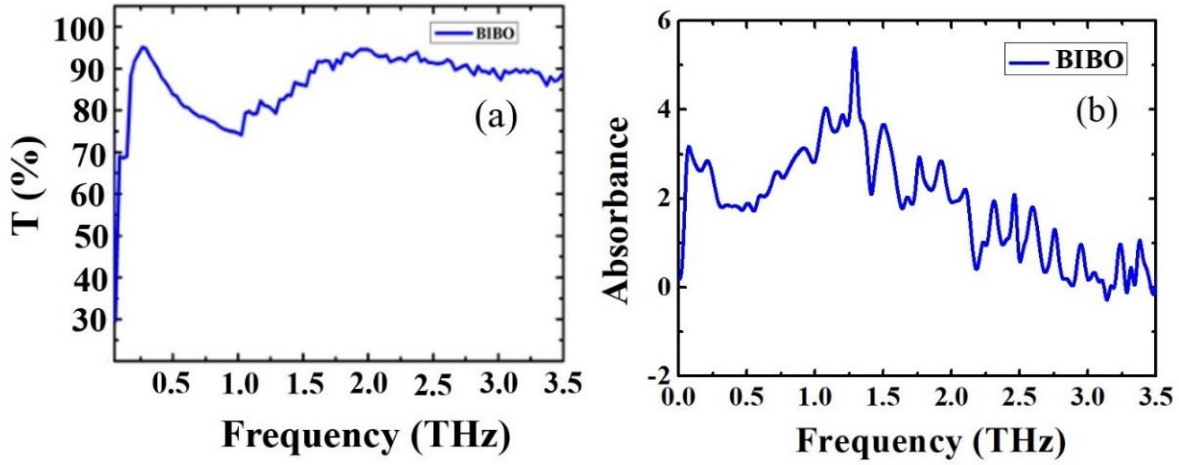

Figure. 3.13 (a) Transmittance (b) Absorbance of Bismuth triborate Crystal in THz domain

Figure 3.13 (a) depicts the transmittance characteristics of the BIBO crystal within the frequency range of 0.1-3.5 THz. A reduction in transmittance was observed at the 1 THz region, reaching 75%. However, it exhibits a gradual increase to 90% within the 1.75-3.5 THz range, underscoring the exceptional transmittance capabilities of BIBO across a broad spectrum, from deep 160 nm to the higher THz range. This property positions BIBO as a pivotal component for the development of a versatile frequency-generating device. Figure 3.14 (b) illustrates the absorbance of the BIBO crystal in the THz region. BIBO exhibits the lowest absorption coefficient values in the THz domain. Specific absorbance bands at 1.93, 2.1, 2.3, 2.6, and 2.75 are identified and align with findings in the existing literature review.

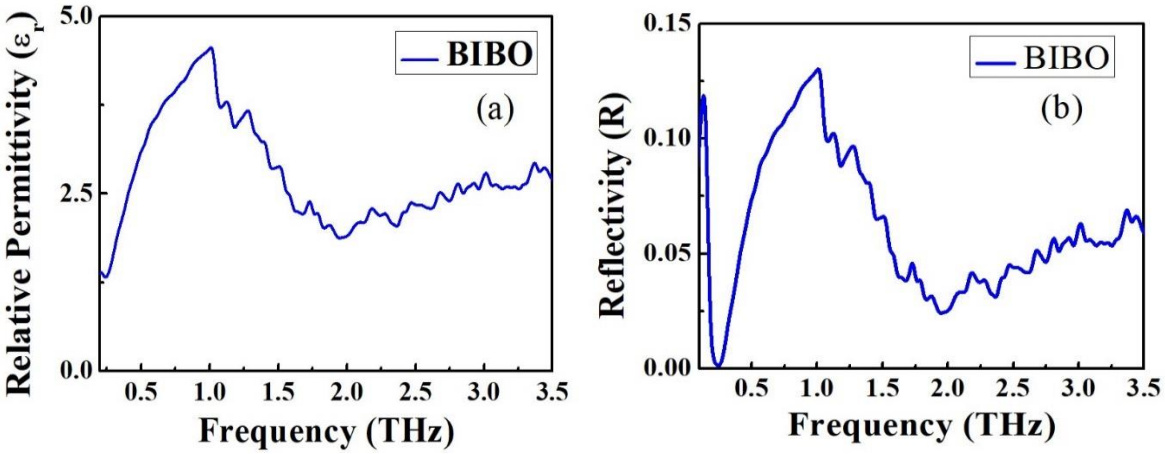

Figure. 3.14 (a) Relative Permittivity (b) Reflectivity of BIBO Crystal in THz domain

Figure. 3.14 (a) and (b) illustrate the relative permittivity and reflectivity of the BIBO crystal in the THz domain using data obtained from THz time-domain spectroscopy. The relative permittivity is determined through equation (2.5) in Chapter 2, with the maximum value observed in the 1.0 THz range, gradually decreasing up to 2.0 THz. Simultaneously, the reflectivity maintains a constant value in the 2.5 to 3.25 THz range. The reflectivity curve peaks at 1.0 THz and remains constant at higher THz ranges.

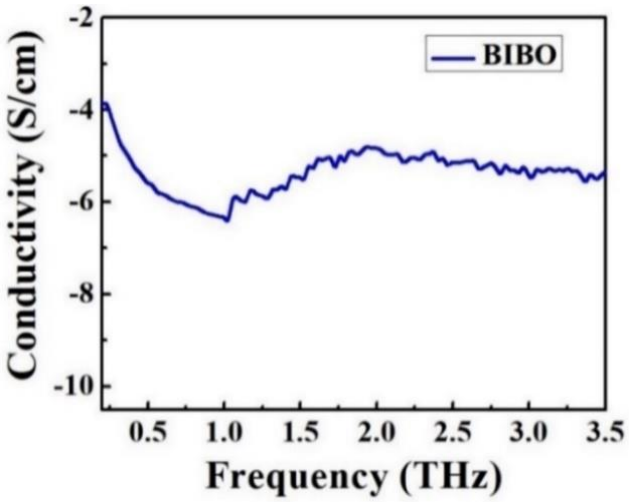

Figure. 3.15 Optical Conductivity of BIBO Crystal. The values are calculated by the equation (2.9) in the chapter 2.

Figure. 3.15 represents the negative conductivity observed in a nonlinear BIBO crystal, demonstrating a reduction in response to specific external energy exposure. BIBO crystals are recognized for their photorefractive effect, wherein changes in the distribution of charge carriers within the crystal lattice are associated with alterations in the refractive index. Upon exposure to laser light, the nonlinear BIBO crystal can generate a spatially varying, time-

dependent electric field, causing the redistribution of charge carriers. This redistribution accounts for the decrease in conductivity. Figure.3.16 represent the coherent length of bi-axial BIBO crystal.

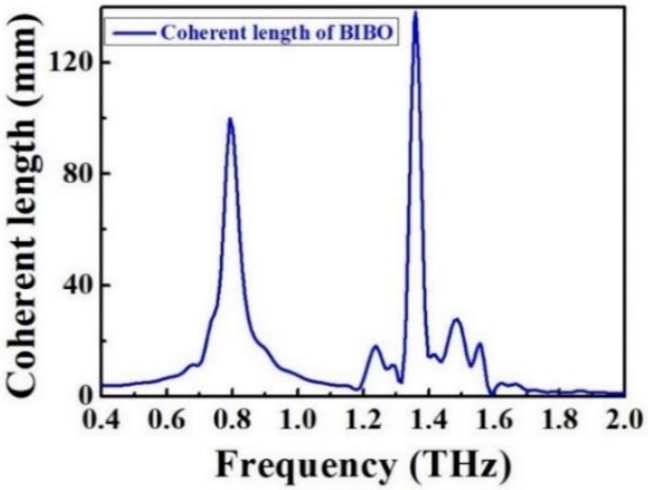

Figure. 3.16: Coherent length of biaxial BIBO Crystal in THz domain

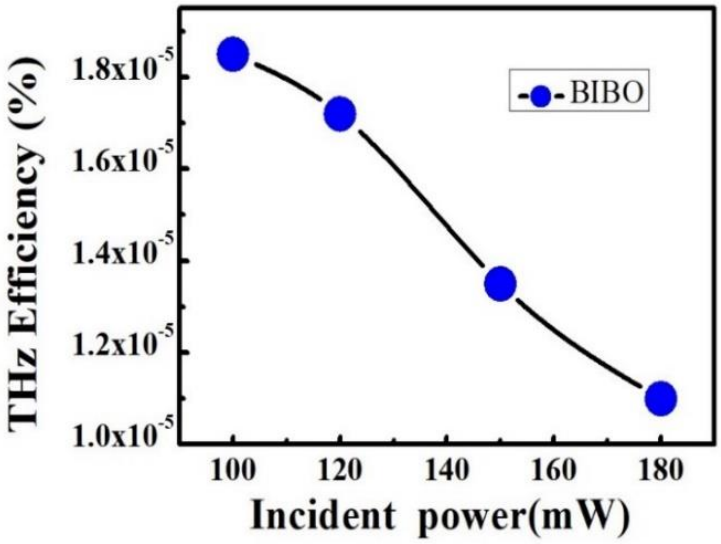

Figure.3.17 THz SHG efficiency with the variation of incident femtosecond laser power

It is evident that over 50 % of 800 nm wavelength photons undergo conversion into 400 nm UV radiation, consistent with previous findings. Nevertheless, the THz conversion efficiency is approximately 1.85 x 10^{-5} %, reaching its peak at 100 mW. The decline in conversion efficiency at higher power levels can be attributed to various factors, including changes in coherence length due to variations in refractive index (R.I.) with respect to temperature. Figure.3.17 illustrate the THz efficiency generated from BIBO crystal.

3.5.3 Efficient THz generation & optoelectronic characterisation of S (sulfur) doped GaSe nonlinear crystal using both THz TDS transmission and reflection geometry:

Figures 3.18 (a) and (b) depict the THz spectra of GaSe: S in both time and frequency domains in comparison to air. The frequency domain spectra of the crystal were derived through the fast fourier transform (FFT) of the time domain terahertz signal transmitted through the sample. The substantial dynamic range evident in the figures highlights the crystal's capability to efficiently generate radiation in the range of up to 2.5 THz.

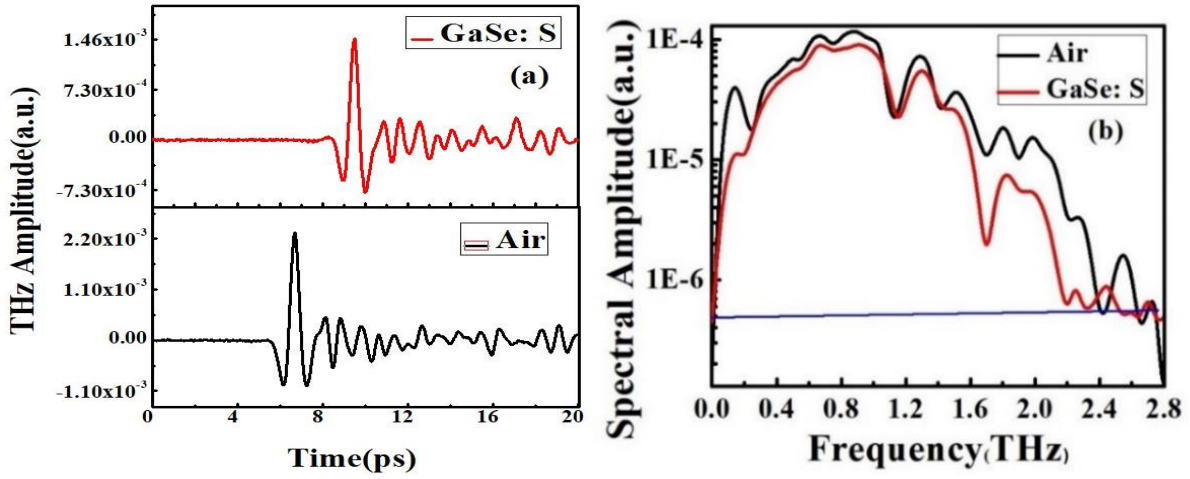

Figure. 3.18 (a) Time domain spectra and (b) Generated THz frequency range of GaSe: S in transmission mode

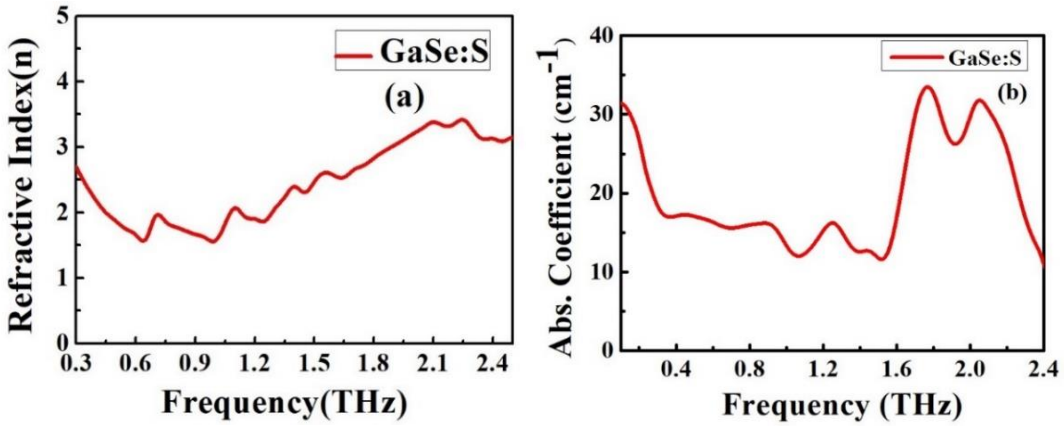

Figure. 3.19 (a) Refractive Index (b) Absorption coefficient semiconductor semimetal rough GaSe: S crystal

The refractive index and absorption coefficients of GaSe: S in the 0.1-2.4 THz range are shown in Figures 3.19 (a) and (b). The crystal's surface roughness is probably the cause of the absorption coefficient curve's abrupt fringe pattern variation across a narrow range [36, 37].

The absorption curves of semiconductor GaSe crystal and S doped semimetal have been found to exhibit the influence of optical phonon modes, with absorption peaks centered at 1.28, 1.78, 1.84, and 2.28 THz, respectively [25]. In the refractive index data, the crystal demonstrates a slightly elevated value between 0.1 and 0.2 THz, gradually decreasing up to the 2.4 THz range. The average real refractive index is ~ 2.0, consistent with the extraordinary refractive index value measured in the optical domain by J.F. Molloy et al [53,54]. However, the imaginary part exhibits an exponential drop with increasing frequency, confirming that a significant portion of the incident and generated radiation is utilized to compensate for various inherent absorption losses.

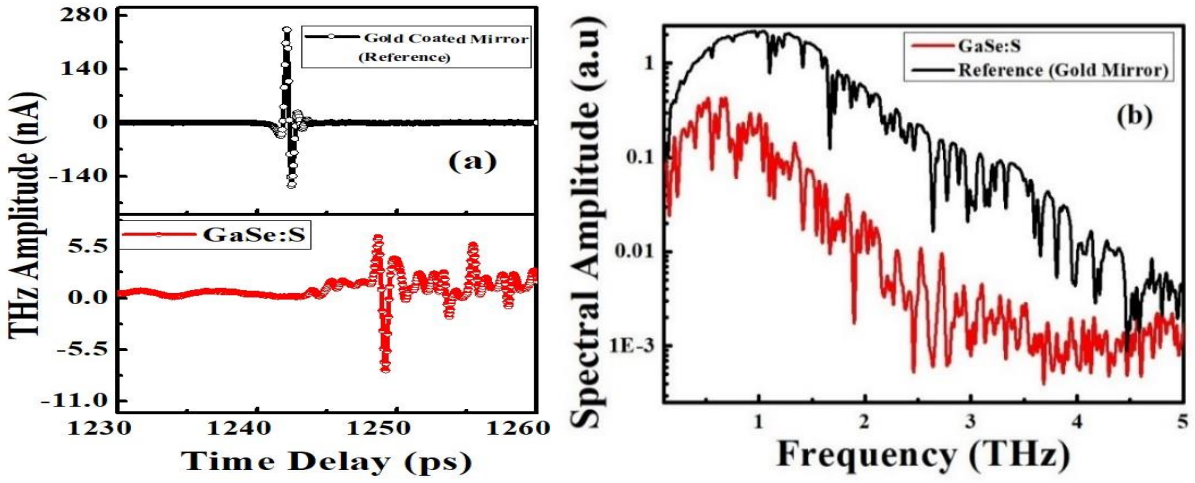

Figure. 3.20 (a) Time domain (b) Frequency domain signal from GaSe: S with respect to gold coated mirror surface as a reference.

The GaSe: S crystal underwent examination using a commercially available optical fiber-coupled broadband THz time-domain spectroscopy (TDS) system (Toptica Photonics AG, TeraFlash Pro, Germany). The system is capable of generating THz pulses with a duration of 0.3 ps at a 100 MHz repetition rate, and data recording was conducted in reflection mode. Using a beam splitter, the laser component divides into two parts, one of which is supplied to the detector and the other to the emitter photo conductive antenna (PCA). With the help of an external 100 V DC bias applied to the antenna, photo charge carriers (produced by the fs optical pulse) are accelerated at the emitter PCA to generate THz radiation. Figure 3.20 (a) and (b) show the THz spectra in the time and frequency domains, respectively. Reference time and frequency domain signals were acquired in relation to the gold-coated mirror, since the measurements were carried out in reflection mode in a dry air purge atmosphere.

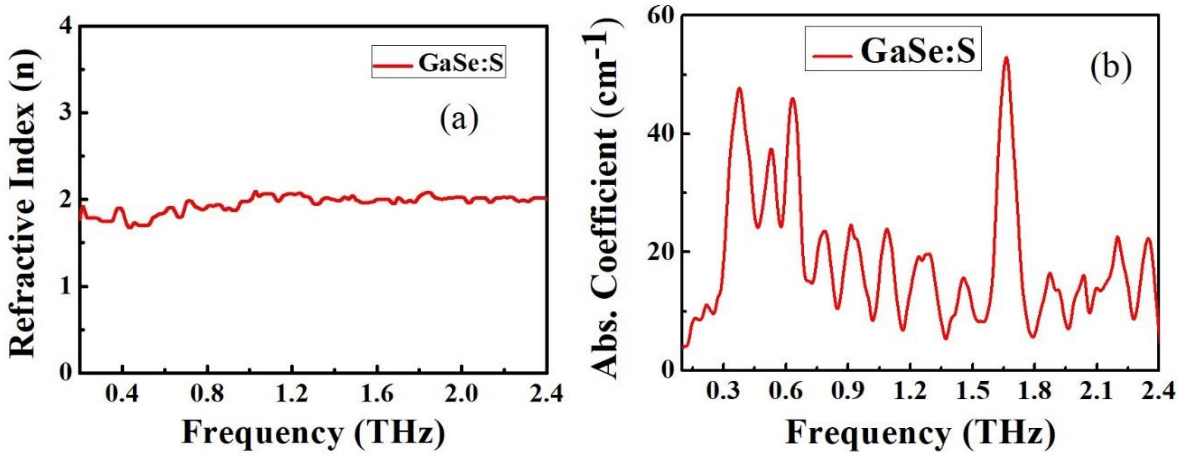

Figure.3.21 (a) Refractive Index (b) Absorption Coefficient of semi metal & semiconductor GaSe: S crystal in THz domain

Figures 3.21 (a) and (b) depict the refractive index and absorption coefficients of GaSe: S. Within the 0.3-0.7 THz range in reflection mode, there is a slight elevation in the refractive index values. The equations (3.19) and (3.20) are utilized to calculate the ordinary and extraordinary refractive indices. While the spectra are well distinguished, the absorption coefficients show slightly higher values ranging from 0.3-0.6 THz. The absorption coefficient reaches its peak value at 1.7 THz in reflection mode. The values in transmission and reflection modes, outside of this range, are relatively similar. Molloy et al have emphasized the possibility of observing multiple phonon absorption peaks at 0.59, 1.0, and 2.5 THz due to the higher sulfur content (11% mass). The peak at 1.8 THz, moving towards a higher frequency, is linked to the increased sulfur content. The appearance of minor peaks is associated with reflections from various crystal layers. Despite these fluctuations, the average absorption coefficient values fall within the 20-50 cm^{-1} range, in line with data from transmission mode. The Sellmeier equations for GaSe crystals are represented by equations (3.27) and (3.28).

$$n_0^2 = 7.39 + \frac{0.405}{\lambda^2} + \frac{0.0184}{\lambda^4} + \frac{0.0061}{\lambda^6} + \frac{3.1436\lambda^2}{\lambda^2 - 2193.8} + \frac{0.017\lambda^2}{\lambda^2 - 262177.5577} \quad (3.27)$$

$$n_e^2 = 5.76 + \frac{0.3879}{\lambda^2} - \frac{0.2288}{\lambda^4} + \frac{0.1223}{\lambda^6} + \frac{0.4206\lambda^2}{\lambda^2 - 1780.3} \quad (3.28)$$

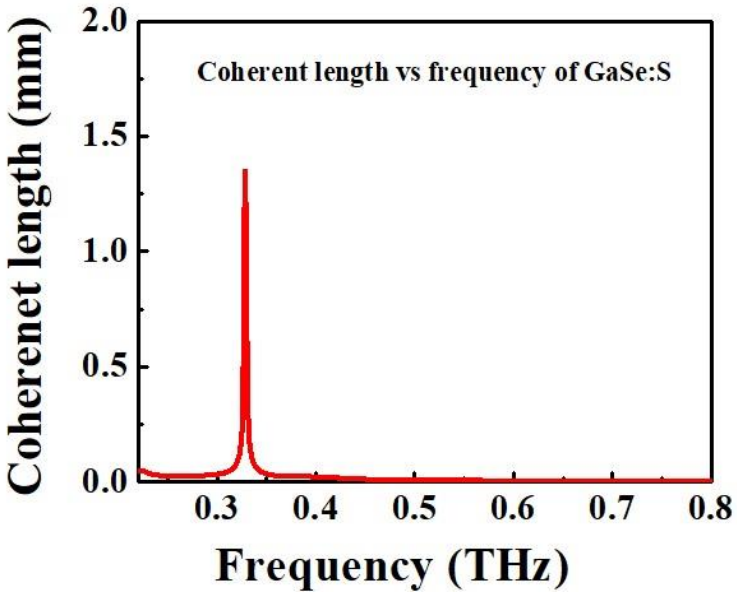

Figure.3.22 Coherence length of S doped GaSe crystal. The values are calculated by equation (2.7) in Chapter 2.

Equation no. (10) was utilized to measure the coherence length of GaSe: S, as depicted in Figure 3.22. The coherence length of the sample is around 1.37 mm at 0.33 THz, which is adequate to produce strong THz radiation.

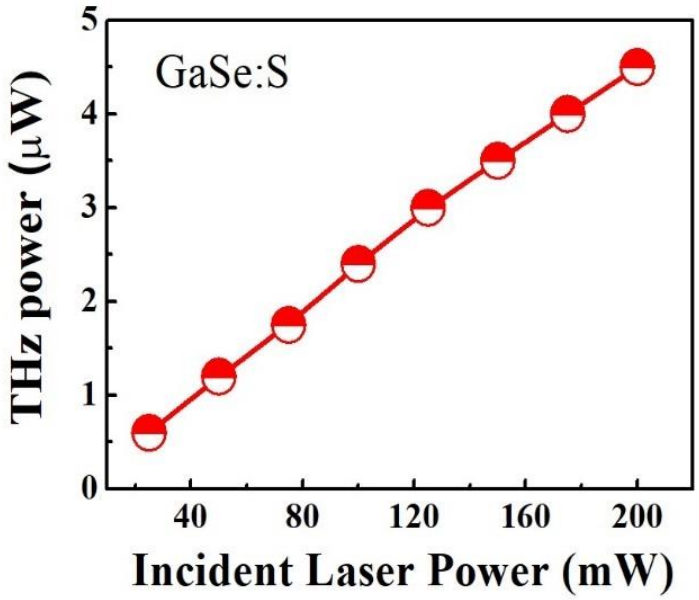

Figure.3.23: THz power generated from S doped GaSe crystal with the variation of incident laser power. The generated power was measured by using pyroelectric detector.

Figure 3.23 depicts the measurement of generated THz power versus pump laser power. The graph trend unmistakably indicates a continuous growth in the generated signal. The maximum generated power reached ~4.5 μW, a significant achievement enabling a wide range of

spectroscopic studies. The experimental setup was modified, as illustrated in Chapter 2, Figure. 2.4. The maximum output terahertz power was recorded at 200 mW incident power, surpassing levels reported in previous works involving other nonlinear crystals [5]. The corresponding conversion efficiency of GaSe: S was calculated as 2.2 × 10^{-3} %, a notably high value comparable to the 20 mm thick GaSe crystal used by Yujie J. Ding [51,55].

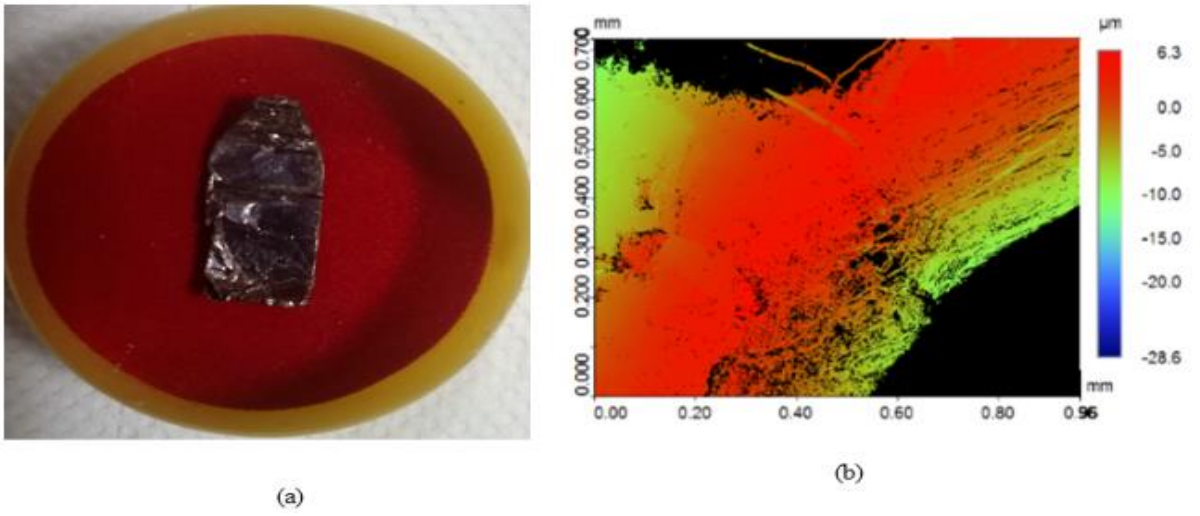

Figure.3.24: (a) GaSe: S crystal and (b) 2D Surface image. The 2D Surface image is captured by the optical profilometer (Model No: Bruker-Contour GT)

Figure. 3.24 (a) displays an image of GaSe: S, while (b) provides a 2D surface image of the same crystal obtained using a profilometer. In Figure. 3.25 (a), the g value of the GaSe: S sample is depicted, showcasing a rapid increase in the g value up to 2.4 THz, is determined through equation (2.18) in Chapter 2 (Raleigh roughness factor of the crystal), which gradually decreases up to 2.4 THz. This determination is achieved by solving the underlying Maxwell boundary value problems and incorporating experimental values of surface roughness [36,37,56]. The purpose is to understand the surface scattering effect and optical impedance of GaSe: S, while numerical simulation approaches based on differential equations are complex, we opted for an analytical approximation approach due to the availability of refractive index (R.I), absorption coefficients (α), and surface roughness data for the crystal. The present work aligns with the Kirchhoff scattering theory from rough surfaces.

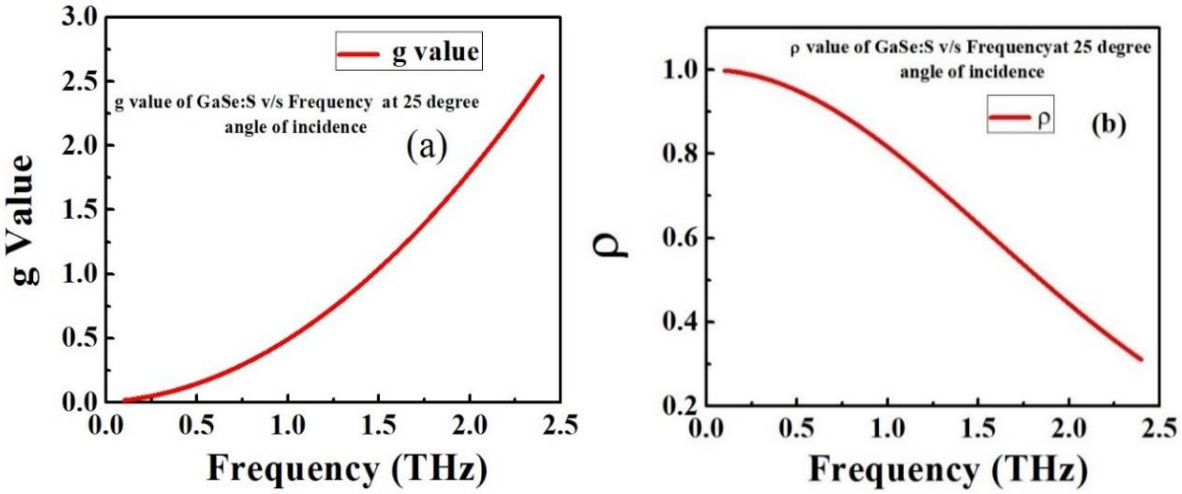

Figure. 3.25 (a) g value & (b) ρ value of S-doped GaSe crystal at 25-degree angle of incidence.

In Figure. 3.26, the reflection coefficients of transverse magnetic (TM) and transverse electric (TE) modes are presented, confirming the Brewster's angle. The intensity of the TM mode exhibits a drastic increase in reflectivity after 60 degrees. Similarly, Figure. 3.27 displays the optical impedance curve, showcasing exponential growth behavior between 0.1 to 2.4 THz ranges. The average value of optical impedance is on the order of 200 Ohms, which is lower than the impedance of air. The significance of the g value in predicting the strength of the generated THz frequency range is evident in Figure. 3.25 (a). For instance, a g value much smaller than 1 indicates a relatively smooth surface, leading to appreciably reduced generated power in the specular direction. Conversely, a g value near 1 suggests a moderately rough surface, resulting in high reflection in the non-specular direction. Finally, when the g value is greater than 1, the surface is considered very rough, and diffuse scattering losses dominate the reflection losses. The g value is less than 1 up to 1.4 THz, indicating smoother surface characteristics, but at 2.4 THz, it rises to 2.5, indicating higher losses and corresponding strength and range of the generated signal.

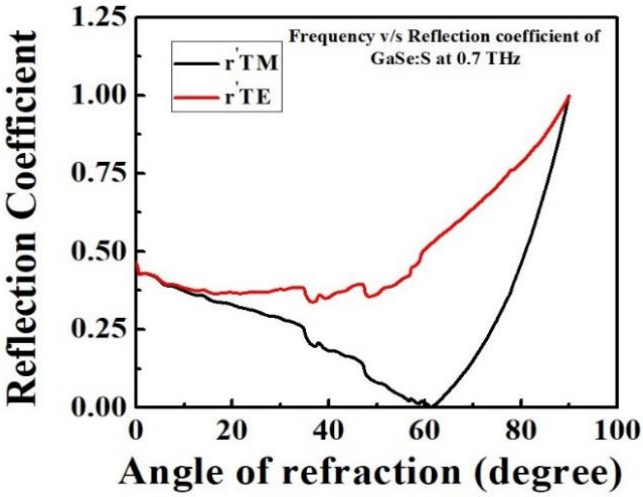

Figure. 3.26. Reflection Coefficients of S doped GaSe crystal with respect to angle of refraction at 0.7 THz. The black curve represents the reflection in transverse magnetic mode whereas the red curve represents the transverse electric mode

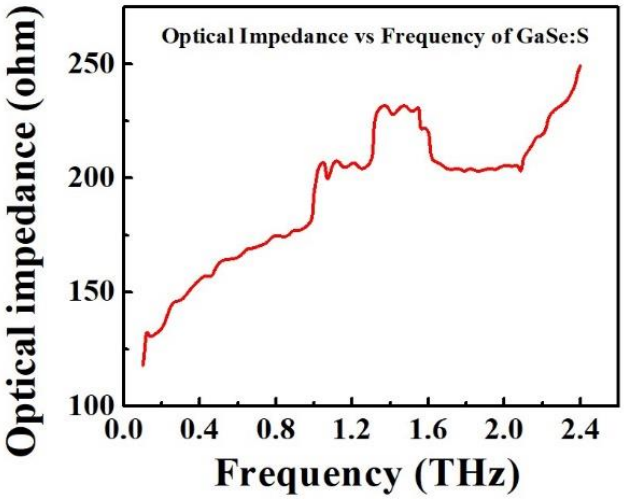

Figure. 3. 27: Optical impedance of S doped semiconductor semimetal rough crystal.

In our investigation, we conducted a systematic analysis of the surface roughness characteristics, particularly focusing on reflection loss. The significance of the surface roughness factor was pivotal in the assessment of optical impedance, conductivity, and permeability of the crystal, thereby offering novel insights into these properties. Our primary objective was to comprehend the constraints on efficiency exhibited by S-doped GaSe crystals by establishing correlations between transmission/absorption data and surface loss data derived from the principles of Fresnel law of reflection and the surface roughness of the crystal. An interesting observation was made regarding the efficiency of radiation generation at 0.7 THz, which peaked when the g value was below 1. However, with an increase in frequency to 1.0 THz, the g value escalated to 2.5, resulting in a decline in signal strength. We effectively

assessed the 1.0 mm thin GaSe: S crystal for the purpose of generating THz radiation efficiently, whereby we quantified the real and imaginary refractive index, as well as absorption coefficients in transmission/reflection modes. The measured power of THz radiation produced, amounting to 4.5 μW through the process of optical rectification, showcased a conversion efficiency of approximately η ~2.2 × 10-3 %, comparable to the efficiency of a 20 mm thick GaSe crystal utilized in the difference frequency mixing method. Our analyses conducted in reflection mode, employing a commercially available rapid THz system with pulses of 0.3 ps at a repetition rate of 100 MHz, revealed satisfactory agreements over a broad spectrum of THz frequencies. In addition, our exploration into the surface roughness characteristics yielded valuable insights, with the application of the surface roughness factor in the assessment of optical impedance, conductivity, and permeability of the crystal representing a novel advancement. This holistic approach contributes significantly to enhancing our comprehension of the limitations in performance and possible utilities of S-doped GaSe crystals within the THz frequency domain.

3.5.4 Second harmonic generation, theoretical predication of DFG & Type -I phase matching angle of α-TeO_2 semimetal semiconductor crystal

The Sellmeier equations of α-TeO_2 crystals are equation (3.29) & (3.30) respectively.

$$n_0^2 = 1 + \frac{2.584\lambda^2}{\lambda^2 - 0.1342^2} + \frac{1.157\lambda^2}{\lambda^2 - 0.2638^2} \quad (3.29)$$

$$n_e^2 = 1 + \frac{2.823\lambda^2}{\lambda^2 - 0.1342^2} + \frac{1.542\lambda^2}{\lambda^2 - 0.2631^2} \quad (3.30)$$

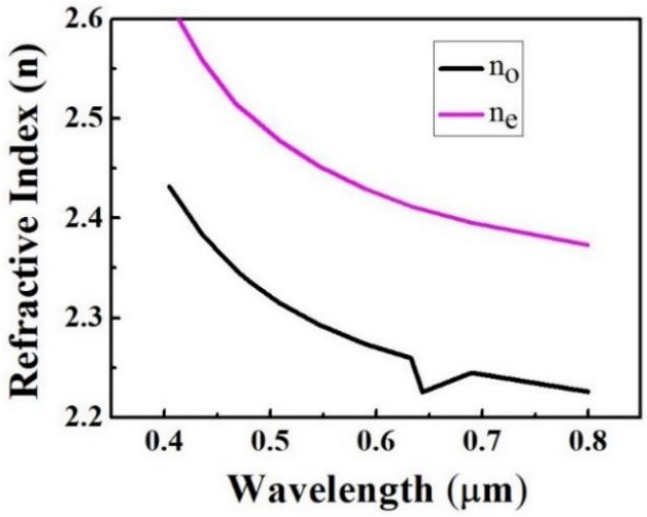

Figure.3.28. Theoretical calculation for ordinary & extraordinary refractive index of α-TeO_2 Calculated by equations (3.29) & (3.30) respectively. The black smooth curve represents ordinary refractive index whereas pink one represents the extra ordinary refractive index.

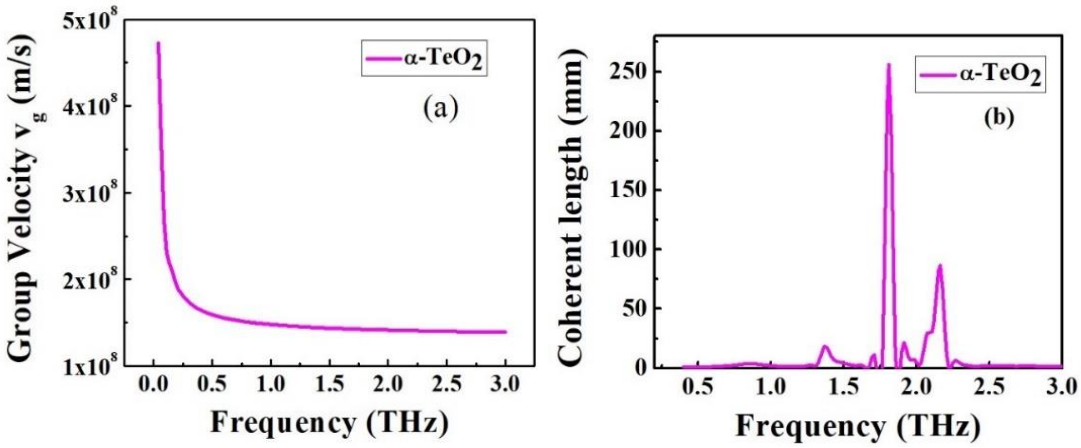

Figure. 3.29. Group velocity (b) Coherence length of α-TeO_2 crystal in THz domain

In the generation of efficient THz radiation using optical rectification or the DFM (Difference Frequency Mixing) process with ultrashort pulses, having prior knowledge of group velocity dispersion and coherent length is crucial. This information guides us in understanding the role of a given material as an efficient emitter of a particular frequency. The values of group velocity and coherent length for terahertz radiation are calculated using equations (2.10) and (2.7), respectively, as detailed in Chapter 2. The group velocity and coherent length of this crystal in the THz domain are depicted in Figure. 3.29.

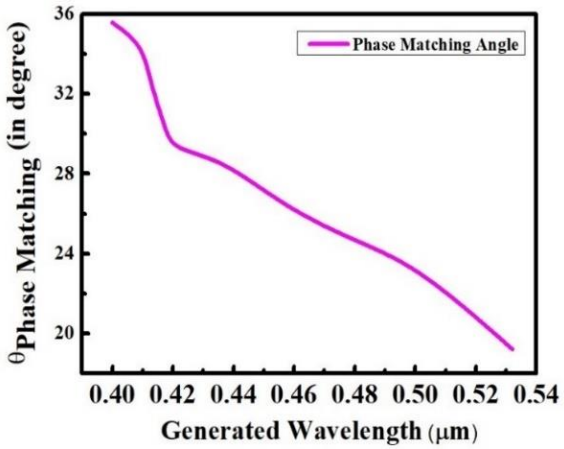

Figure.3.30. Type-I Phase matching angle with respect to generated second harmonic wavelength of α-TeO_2 crystal

We propose a Type-I difference frequency mixing (DFM) scheme for THz generation using a tunable range of 0.799-0.796 μm as the pump and 800 nm as the signal to generate tunable THz radiation within the 0.1-1.9 THz range. The calculated phase matching for TYPE-I angles θ~21.15° (DFG process) whereas phase matching angle for second harmonic generation (SHG) is θ ~35.5^0 (using 800 nm wavelength). Figure.3.30 illustrates the theoretical calculations for

the Type-I phase matching angle concerning incident and generated wavelengths for second harmonic generation. The nature of phase-matching angles exhibits an exponential trend.

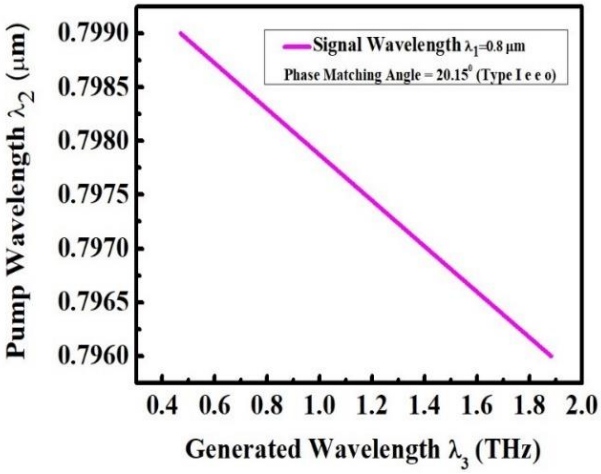

Figure.3.31. Pump wavelength vs generated wavelength α-TeO_2 crystal in THz domain

Figure. 3.31 illustrates how the pump wavelength changes concerning the generated wavelength at a constant phase matching angle of 20.15^0 and a signal wavelength of 800 nm.

3.5.5 Optoelectronic characterisation of using broadband THz time domain spectroscopy:

The α-TeO_2 crystal, obtained from BIOTAIN CRYSTAL CO., LIMITED, China, has a thickness of 1 mm and a 110 orientation. For the recording of temporal and spectral profiles of α-TeO_2 in the transmission mode with respect to air, we utilized our indigenously designed time-domain THz spectrometer. Figure. 3.28 (a and b) showcases the temporal and spectral spectra of α-TeO_2, respectively. Figure. 3.28 (b) provides confirmation of the dynamical cutoff range of this crystal at 2.5 THz.

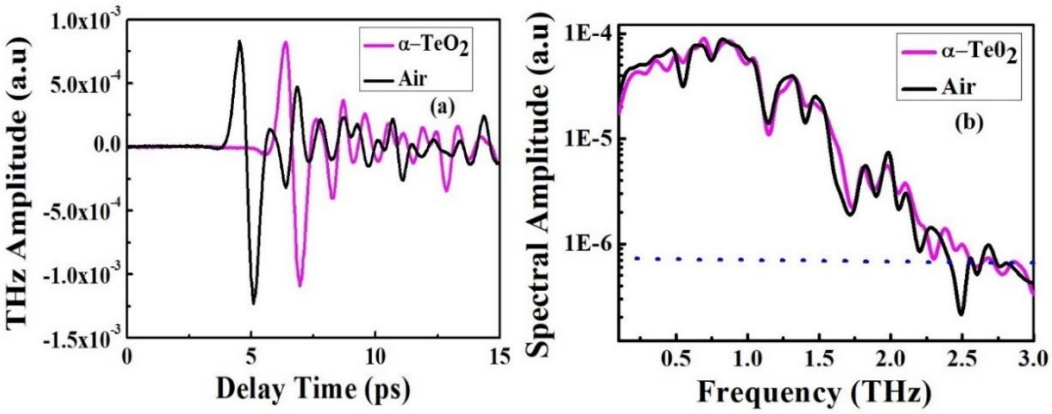

Figure.3.32 (a) Temporal (b) Spectral profile of semimetal semiconductor α-TeO_2 Crystal. The blue dotted line in the spectral profile is represented as high SNR (~10^6)

Figure. 3.32 (a and b) displays the time domain and frequency domain spectra of α-TeO2 concerning air. The power spectrum exhibits an intensity fringe pattern with peak structures at approximately 1.6 and 2.0 THz, extending up to around 3.0 THz, as illustrated in Figure. 3.32(b). The frequency domain data are utilized for the measurements of refractive index (R.I.) and absorption coefficients in the THz domain.

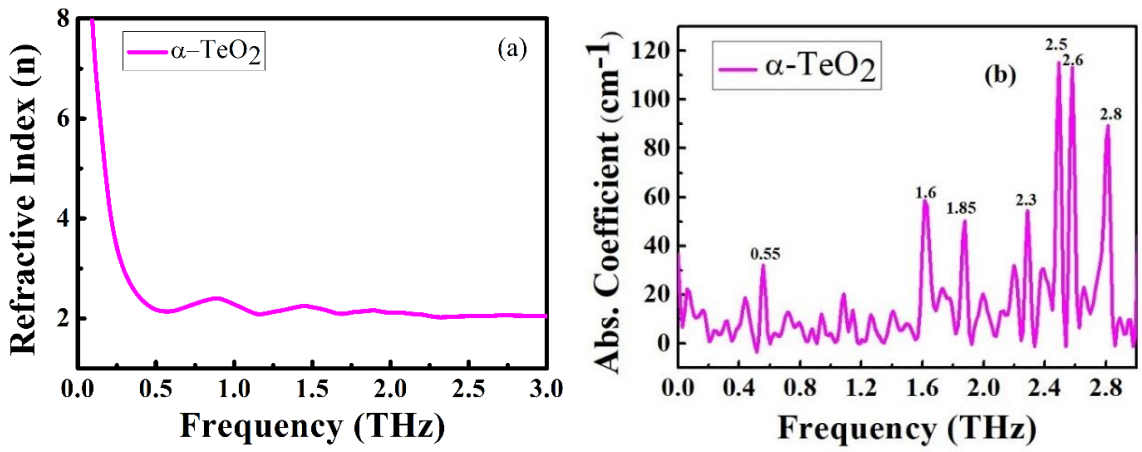

Figure. 3.33. (a) Refractive Index (b) Absorption Coefficient of α-TeO2

Figure. 3.33 (a) presents the values of real refractive indices concerning THz frequencies within the 0.1-3.0 THz range. The graph illustrates an exponential drop between 0.1-0.5 THz, stabilizing up to 3.0 THz. The average refractive index value across the entire THz domain is approximately 2.25, aligning with the ordinary refractive index in the optical domain derived from the Sellmeier equation using a two-oscillating model [58]. The substantial variation in the refractive index below 0.5 THz can be attributed to several factors. The use of fast fourier transform (FFT)-based data in the Kramers-Kronig relationship for calculating the refractive index in the THz domain is not straightforward. The high brightness of ultrashort pulses, compared to continuous-wave sources, necessitates recording transmission at high intensity, leading to increased absorption coefficients and a loss of phase information. This phenomenon is associated with time-domain THz-based coherent measurement techniques, where terahertz time-domain spectroscopy (TDS) exhibits a high SNR ($> 10^6$) of power. The refractive index is ascertained using equation number (2.3) in chapter 2. Figure.3.33 (b), the absorption coefficient of the α-TeO2 crystal is depicted. α-TeO2 single crystal exhibits the lowest values of absorption coefficients in the THz domain. The absorption bands of α-TeO2 are identified at 0.55, 1.6, 1.85, 2.3, 2.5, 2.6, and 2.8 THz, respectively, which aligns with findings from the literature survey [57-61].

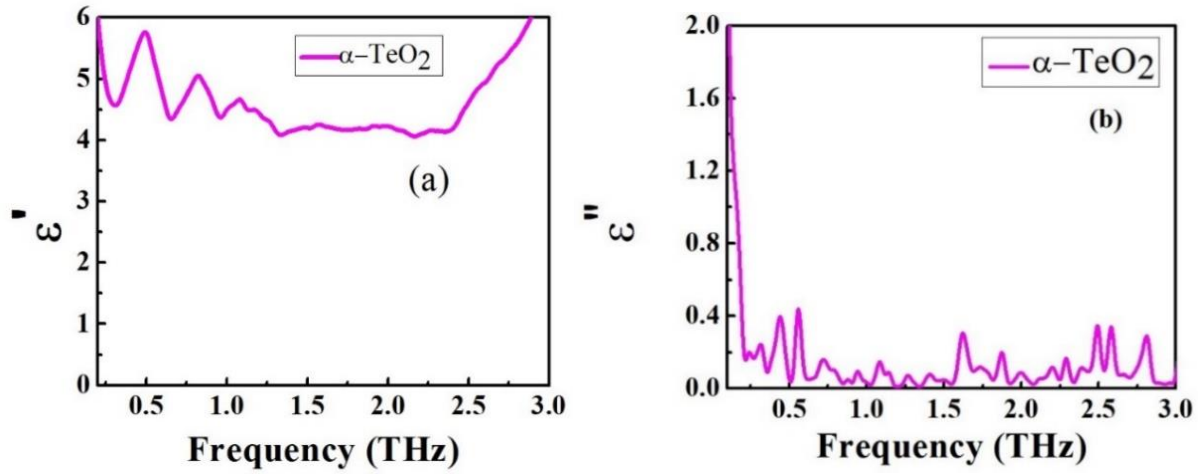

Figure.3.34 (a) Permittivity of semimetal semiconductor α-TeO_2 Crystal & (b) imaginary part of dielectric constant of α-TeO_2 Crystal shown as a function of broadband high THz frequency at 30^0 C.

The dielectric behavior of the α-TeO_2 crystal in the THz domain is depicted in Figures 3.34(a) and (b). The imaginary part of the dielectric constant indicates the crystal's capacity to permanently absorb energy from a time-varying THz electric field, whereas the dielectric constant defines the crystal's ability to interact with a THz electric field without absorbing energy. When the frequency is increased, the actual part of the dielectric constant reduces up to 1.3 THz, stays constant up to 2.5 THz, and then increases up to 3.0 THz. Simultaneously, the imaginary part of the dielectric constant exponentially decays within the 3.0 THz range. The values of the real and imaginary dielectric constants are calculated using equations (2.15) and (2.16), respectively, in Chapter 2. For the evaluation of the optical and commercial values of the crystal for optical devices, the figure of merit (FOM) is considered. Given that TeO_2 is not widely recognized for second harmonic generation (SHG) and terahertz (THz) applications, and the lack of available phase matching and other optical & dielectric parameters in the THz domain, we have made the first attempt to compare its FOM in both optical and THz domains. Figure. 3.35 illustrates the figure of merit (FOM) in the optical pump range, exceeding 0.02 x 10^{-24} $(pm/V)^2$. In the case of THz, the FOM oscillates in the range of 0.015 to 0.01 x 10^{-24} $(pm/V)^2$. Figure. 3.35 (a and b) presents the FOM in both optical and THz domains. The values of the figure of merit for α-TeO_2 single crystal are calculated using equation,

$$\text{figure of merit} = \frac{d_{eff}^2 \sin^2\theta}{n_0^3} \tag{3.31}$$

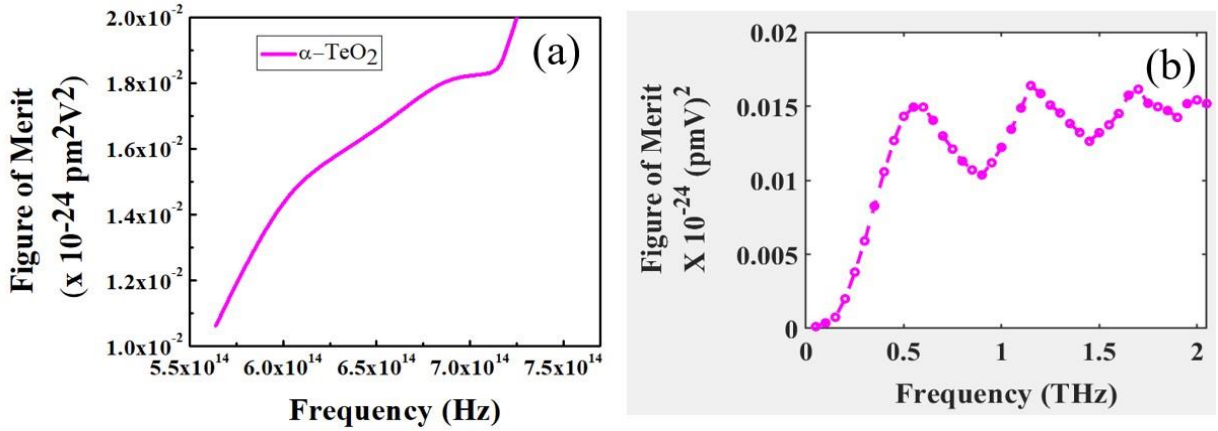

Figure.3.35 Comparative study of Figure of Merits of α-TeO_2 in Optical and THz domain. FOM values are calculated by using equation (3.31)

Figure. 3.35 presents the figure of merit of the crystal in both optical and THz domains with respect to frequency, demonstrating a similar trend in both domains. The figure of merit is higher in the optical domain compared to the THz domain. However, γ-TeO_2 crystal is considered more suitable for THz generation, as its effective non-linear coefficient is 10 times greater than that of α-TeO_2. In conclusion, we have assessed the potential role of α-TeO_2 single crystals for the efficient generation of THz radiation using two prominent optical techniques: (i) optical rectification (OR) and (ii) difference frequency mixing (DFM), based on experimental and theoretically generated data from optical and THz spectroscopy for the first time. The phase matching angle under Type-I DFM conditions for the generation of tunable radiation between 0.1-1.9 THz range is $\theta=21.15^0$. The figure of merits (FOM) in optical and THz domains ranges between 0.02 and 0.015. The generated spectral range lies between 0.1 and 3.0 THz. Lastly, we compare the THz generation efficiency of three Nonlinear Optical (NLO) crystals, namely BIBO, S-doped GaSe, and α-TeO_2, with DAST, BNA, CdTe, and LAP crystals for efficient THz Generation. Their THz efficiency is in the order of 10^{-5} to 10^{-3}, with the materials arranged as BNA > GaSe:S > DAST > TeO_2 > BIBO > LAP.

Table -3.2 Summary of THz generation for three nonlinear crystals carried out in this thesis chapter 3.

Sl. No	Crystal Name	Crystal nature	$n_{optical}$ (800nm)	n_{THz}	Coherence length (mm)	Conversion Efficiency (η)	Reference
1	BNA	biaxial	1.66	~1.65	0.85 @ 2.2 THz	26. $1x10^{-4}$	[56,65]
2	DAST	positive biaxial	2.07	~2.20	0.5 mm @0.1-5 THz	16. 1 x 10^{-4}	[5, 66]
3	LAP	biaxial	~1.55	~1.52	800 @ 1.0 THz; 200 @2.3 THz	6.2 x 10^{-5}	[67]
4	CdTe	negative uniaxial	2.95	~2.8	5 @1.1 THz	2.3 x 10^{-6}	[68,69]
5	BIBO	biaxial	~1.72	~1.75	100.3 @0.79 THz; 138 @ 1.36 THz	1.85×10^{-5}	Present Work [62]
6	GaSe:S	negative uniaxial	2.84	~2.0	1.37 @ 0.33 THz	~2.2 x 10^{-3}	Present Work [63]
7	α -TeO_2	positive uniaxial	2.20	~2.20	256 @ 1.65 THz; 86.6 @ 2.0 THz	2.6 x 10^{-4}	Present Work & [64,70]

Intentional Blank Page

References:

[1]. H. Hellwig, J. Liebertz, and L. Bohaty, "Exceptional large nonlinear optical coefficients in the monoclinic Bismuth borate BiB_3O_6 (BIBO)," Solid State Commun, **109**,249–251 (1999).

[2]. H. Hellwig, J. Liebertz, and L. Bohaty, "Linear optical properties of the monoclinic bismuth borate BiB_3O_6," J. Appl. Phys. **88**, 240–244 (2000).

[3]. Y. Li, J. Huang, Z. Huang, N. Nikolaev, G. Lanskii, A. Mamrashev, and Y. Andreev, "Optical properties of BiB_3O_6 in the terahertz range," Results Phys. **16**, 1–3 (2020).

[4]. S. C. Luciano and F. C. Cruz, "External power-enhancement cavity versus intra cavity frequency doubling of Ti: sapphire lasers using BIBO," Opt. Express **15**, 11913–11921 (2007).

[5]. V. Mottamchetty, T. Karunanithi, S. Brahadeeswaran, and A. K. Chaudhary, "Generation of efficient THz radiation by optical rectification in DAST crystal using tunable femtosecond laser pulses," Indian. Journal Phys. **91**, 319–326, (2016).

[6]. Y. Takida, T. Ohira, S. Maeda, and H. Kumagai, "High-efficiency second harmonic generation of mode-locked picosecond Ti: sapphire laser using BiB3 O6 crystal with external enhancement cavity," J. Laser Micro/Nanoeng. **6,** 231–234 (2011).

[7]. Z. Wang, B. Teng, K. Fu, X. Xu, R. Song, C. Du, H. Jiang, J. Wang, Y. Liu, and Z. Shao, "Efficient second harmonic generation of pulsed laser radiation in BiB_3O_6 (BIBO) crystal with different phase matching directions," Opt. Commun. **202**, 217–220 (2002).

[8]. M. Ghotbi and M. Ebrahim-Zadeh, "Optical second harmonic generation properties of BiB_3O_6," Opt. Express **12**, 6002–6019 (2004).

[9]. A. J. Antonczak, J. Z. Sotor, M. Matysiak, and K. M. Abramski, "Blue473-nm solid state diode pumped Nd: YAG/BiBO microchip laser," Opto-Electron. Rev. **18**, 71–74 (2010).

[10]. V. Petrov, M. Ghotbi, O. Kokabee, A. Esteban-Martin, F. Noack, A. Gaydardzhiev, I. Nikolov, P. Tzankov, I. Buchvarov, K. Iyata, A. Majchrowski, I. V. Kityk, F. Rotermund, E. Michalski, and M. Brahim-Zadeh, "Femtosecond nonlinear frequency conversion based on BiB_3O_6," Laser Photonics Rev. **4**, 53–98 (2010).

[11]. M. Thorhauge, J. L. Mortensen, P. Tidemand-Lichtenberg, and P. Buchhave, "Tunable intra-cavity SHG of CW Ti: Sapphire lasers around 785 nm and 810 nm in BIBO-crystals," Opt. Express **14,**2283–2288 (2006).

[12]. Z. Hong, S. A. Rezvani, Q. Zhang, and P. Lu, "Ultrafast mid-IR laser pulses generation via chirp manipulated optical parametric amplification," Appl. Sci. **8,** 744 (2018).

[13]. M. Baudisch, M. Hemmer, H. Pires, and J. Biegert, "Performance of MgO: PPLN, KTA, and KNbO3 for mid-wave infrared broadband parametric amplification at high average power," Opt. Lett. **39**,5802–5805 (2014).

[14]. Y. Yin, J. Li, X. Ren, K. Zhao, Y. Wu, E. Cunningham, and Z. Chang, "High-efficiency optical parametric chirped-pulse amplifier in BiB_3O_6 for generation of 3 mJ, two-cycle, carrier-envelope-phase-stable pulses at 1.7μm," Opt. Lett. **41**, 1142–1145 (2016).

[15]. M. E. Zadeh, "Efficient ultrafast frequency conversion sources for the visible and ultraviolet based on BiB_3O_6," IEEE J. Sel. Top. Quantum Electron. **13**, 679–691 (2007).

[16]. Andreev YM, Apollonov VV, Shakir YA, Verozubova GA, Gribenyukov AI. "Submillimeter waves generation with $ZnGeP_2$ crystals", J Korean Phys Soc, **33**, 356–361, (1998).

[17]. Chen CW, Tang TT, Lin SH, Huang JY, Chang CS et al. Optical properties and potential applications of ε-GaSe at terahertz frequencies. JOSA B,**26**, A58–A65, (2009).

[18]. Nazarov MM, Shkurinov AP, Angeluts AA, Sapozhnikov DA. On the choice of nonlinear optical and semiconductor converters of femtosecond laser into terahertz range. Radio phys Quant Electron, **52**, 536–545, (2009).

[19]. Dmitriev VG, Gurzadyan GG, Nikogosyan DN. Handbook for Nonlinear Optical Crystals, Springer Series in Optical Sciences, **64**, 3rd ed. Berlin: Springer, 1999.

[20]. Tochitsky SY, Sung CE, Trubnick SE, Joshi C, Vodopyanov KL. High-power tunable, 0.5-3 THz radiation source based on nonlinear difference frequency mixing of CO_2 laser lines. J Opt Soc Am B, **24**, 2509–2516, (2007).

[21]. Vodopyanov KL, Mirov SB, Voevodin VG, Schunemann PG. Two-photon absorption in GaSe and $CdGeAs_2$. Opt Comm, **155**, 47–50, (1998).

[22]. Guo J, Li DJ, Xie JJ, Zhang LM, Feng ZS et al. "Limit pump intensity of Ti: sapphire laser systems for $GaSe_{12x}S_x$". Laser Phys Lett, **11**, 055401, (2014).

[23]. Fernelius NC. "Properties of gallium selenide single crystal". Prog Cryst Growth Charact 1994, **28,** 275–353, (1994).

[24]. S. Das, C. Ghosh, S. Gangopadhyay, U. Chatterjee, G. C. Bhar, V. G. Voevodin, and O. G. Voevodina, "Tunable coherent infrared source from 5 –16 μm based on difference-frequency mixing in an indium-doped GaSe crystal," JOSA B, **23** (2), 282-288 (2006).

[25]. A. C. Das, S. Bhattacharya, M. Jewariya, S. S. Prabhu, K. C. Mandal, T. Ozaki, and P. K. Datta, "Identification of Combination Phonon Modes in Pure and Doped GaSe Crystals by THz Spectroscopy", IEEE J. Sel. Top. Quantum Electron. **23,** 1-7 (2017).

[26]. K. C. Mandal, S. H. Kang, M. Choi, J. Chen, X.-C. Zhang, J. M. Schleicher, C. A. Schmuttenmaer, and N. C. Fernelius, "III–VI Chalcogenide Semiconductor Crystals for Broadband Tunable THz Sources and Sensors" IEEE J. Sel. Top. Quantum Electron.**14**, 284-288 (2008).

[27]. J. Guo, J.J. Xie, D.J. Li, G.L. Yang, F. Chen, C.-R. Wang, L.-M. Zhang, Y. M. Andreev, K. A. Kokh, G. V Lanskii, and others, "Doped GaSe crystals for laser frequency conversion", Light Sci. Appl. **4**, e362, 1-12 (2015).

[28]. S. A. Ku, W.C. Chu, C. W. Luo, Y. M. Andreev, G. Lanskii, A. Shaidukoi, T. Izaak, V. Svetlichnyi, K. H. Wu, and T. Kobayashi, Opt. Express, **20**, 5029-5038 (2012).

[29]. V. V Atuchin, Y. M. Andreev, K. A. Kokh, G. V Lanskii, A. V Shaiduko, T. I. Izaak, and V. A. Svetlichnyi, in Nonlinear Opt. Appl. VII p. 87721Q, 1-9 (2013).

[30]. Ch-Wei Chen, Yu-Kuei Hsu, Jung Y. Huang, and Chen Shiung Chang, "Generation properties of coherent infrared radiation in the optical absorption region of GaSe crystal", Opt. Exp. **14** (22), 10636-10644 (2006).

[31]. W. Shi, Y. J. Ding, N. Fernelius, and F. Ken Hopkins, "Observation of difference-frequency generation by mixing of terahertz and near-infrared laser beams in a GaSe crystal", Appl. Phys. Lett. **88**, 101101-101103 (2006).

[32]. Jingguo Huang, Zhiming Huang, Jingchao Tong, Cheng Ouyang, Junhao Chu, Yury Andreev, Konstantin Kokh, Grigory Lanskii and Anna Shaiduko, "Intensive terahertz emission from $GaSe_{0.91}S_{0.09}$ under collinear difference frequency generation", Appl. Phys. Lett. **103**, 081104-1-4, (2013).

[33]. W.C. Chu, S. A. Ku, H. J. Wang, C. W. Luo, Y. M. Andreev, G. Lanskii, and T. Kobayashi, "Widely linear and non-phase-matched optical-to-terahertz conversion on GaSe: Te crystals", Opt. Lett. **37,** 945-947 (2012).

[34]. J. Mei, K. Zhong, M. Wang, Y. Liu, D. Xu, W. Shi, Y. Wang, J. Yao, R. A. Norwood, and N. Peyghambarian, "Widely-tunable high-repetition-rate terahertz generation in GaSe with a compact dual-wavelength KTP OPO around 2 μm", Opt. Express **24,** 23368-23375 (2016).

[35]. J. Guo, J.J. Xie, L.M. Zhang, K. Kokh, Y. Andreev, T. Izaak, G. Lanskii, A. Shaiduko, and V. Svetlichnyi, "Characterization of optical quality of GaSe: Al crystals by exciton absorption peak parameters", J. Mater. Sci. Mater. Electron. **25**, 1757-1760 (2014).

[36]. R. Piesiewicz, T. Kleine-Ostmann, N. Krumbholz, D. Mittleman, M. Koch, and T. Kürner, "Terahertz Characterisation of bulding materials", Electron. Lett. **41** (18), 1002-1004 (2005).

[37]. R. Piesiewicz, C. Jansen, D. Mittleman, T. Kleine-Ostmann, M. Koch, and T. Kurner, "Scattering Analysis for the Modeling of THz Communication Systems", IEEE Trans. Antennas Propag. **55** (11), 3002-3009 (2007).

[38]. S. Vidal, J. Degert, M. Tondusson, E. Freysz, and J. Oberlé, J. Opt. Soc. Am. B, **31,**149-152 (2014).

[39]. Baolong Zhang, Zhenzhe Ma, Jinglong Ma, Xiaojun Wu, Chen Ouyang, Deyin Kong, Tianshu Hong, Xuan Wang, Peidi Yang, Liming Chen, Yutong Li, and Jie Zhang, Laser Photonics Rev., **15**,1-11 (2021).

[40]. B. L. Yu, F. Zeng, V. Kartazayev, R. R. Alfano, and K. C. Mandal, "Terahertz studies of the dielectric response and second-order phonons in a GaSe crystal," Appl. Phys. Lett., **87** 182104, 1-4 (2005).

[41]. Dong-wen Zhang, Zhi-hui Lv, Lin Sun, and Jian-min Yuan, "Dielectric properties of GaSe crystal measured by Terahertz time-domain spectroscopy", Joint 32nd International Conference on Infrared and Millimetre Waves and the IEEE Xplore International Conference on Terahertz Electronics, 239-240, (2007).

[42]. T. Siciliano, M. Di Giulio, M. Tepore, E. Filippo, G. Micocci and A. Tepore, Vacuum "Effect of thermal annealing time on optical and structural properties of TeO_2 thin films" Vaccum, **84**, 935 (2010).

[43]. M F Al-Kuhaili, S M A Durrani, E Khawaja and Shirokoff, "Effects of preparation conditions on the optical properties of thin films of tellurium oxide", J. Appl. Phys. 35, 910-915 (2002).

[44]. Shiv Kumar and Abhai Mansingh, "Annealing-induced structural changes in tellurium dioxide thin films", J. Appl. Phys. **23**, 1252-1255, (1990).

[45]. Namrata Dewan, K. Sreenivas, Vinay Gupta, "Properties of crystalline γ-TeO_2 thin film", J. Cryst. Growth. 305, 237-241, (2007).

[46]. Ranu Nayak, Vinay Gupta, A.L. Dawar, K. Sreemivas, "Optical waveguiding in amorphous tellurium oxide thin films", Thin Solid Films, **445**, 118-126 (2003).

[47]. M. Venkatesh, K.S. Rao, T.S. Abhilash, S.P. Tewari, and A.K. Chaudhary, "Optical characterization of GaAs photoconductive antennas for efficient generation and detection of Terahertz radiation", Opt. Mater. **36,** 596-601 (2014).

[48]. M. Venkatesh and A. K. Chaudhary, "Generation of THz radiation from Low temperature Gallium Arsenide (LT-GaAs) photoconductive (PC) antennas using tunable femtosecond oscillator", 12th International Conference on Fiber Optics and Photonics, OSA Technical Digest (online) (Optical Society of America, pp. S5 A. 33 (2014).

[49]. M. Venkatesh and A. K. Chaudhary, "Study of terahertz intensity dependence on time resolved dynamic fringes in the interferometric autocorrelation setup", Optics 2014, AIP Conference Proceedings 1620, 616-621 (2014).

[50]. D. M. Lubenko, G. V. Lansky, N. A. Nikolaev, E. A. Sandabkin, V. F. Losev, and Y. M. Andreev, "Generation of THz emission in nonlinear BBO crystal at room temperature", Proc. SPIE 11322, Tomsk, Russian Federation, 113222C (2019).

[51]. Shi, W. and Ding, Y.J., "A monochromatic and high-power terahertz source tunable in the ranges of 2.7–38.4 and 58.2–3540 μm for variety of potential applications", Applied Physics Letters, **84** (10), 1635-1637 (2004).

[52]. A. Shirakawa, I. Sakane, M. Takasaka, and T. Kobayashi, "Sub 5 fs visible pulse generation by pulse-front-matched non collinear optical parametric amplification," Appl. Phys. Lett. **74**, 2268 (1999).

[53]. J. F. Molloy, M. Naftaly, Y. M. Andreev, K. Kokh, G. V Lanskii, and V. A. Svetlichnyi, in 2015 40th Int. Conf. Infrared, Millimeter, Terahertz Waves, 1–2 (2015).

[54]. Ching-Wei Chen, Tsung-Ta Tang, Sung-Hui Lin, Jung Y. Huang, Chen-Shiung Chang, Pei Kang Chung, Shun-Tung Yen, and Ci-Ling Pan, "Optical properties and potential applications of ε-GaSe at terahertz frequencies", J. Opt. Soc. Am. B. 26 (9) 58-65 (2009).

[55]. Dominik Bänninger and Hannes Flühler, "Modeling light scattering at soil surfaces", IEEE Transactions on Geoscience and Remote Sensing, **42** (7) 1462-1471, (2004).

[56]. S. Karthick, D. Ganesh, K. Thirupugalmani, A. K. Chaudhary, and S. Brahadeeswaran, "Terahertz generation and optical properties of N-benzyl-2-methyl-4-nitroaniline single crystals in 0.1–2.0 THz range for photonic applications", Mater. Lett. **246**, 95-98 (2019).

[57]. M. Sotome, N. Kida, R. Takeda, and H. Okamoto, "Terahertz radiation induced by coherent phonon generation via impulsive stimulated Raman scattering in paratellurite", Physical Review A, **90**, 033842, 1-15 (2014).

[58]. N. Uchida., "Optical Properties of Single-Crystal Paratellurite (TeO_2)", Phys. Rev.B **4**, 3736-3745 (1971).

[59]. Yanlu Li, Weiliu Fan, Honggang Sun, Xiufeng Cheng, Pan Li, and Xian Zhao, "Structural, electronic, and optical properties of α, B, and γ -TeO_2," Journal of Applied Physics, **107**, 093506,1-8, (2010).

[60]. Márta Unferdorben, Andrea Buzády, János Hebling, Krisztián Kiss, Ivett Hajdara, László Kovács & Ágnes Péter & László Pálfalv, "Index of Refraction and Absorption Coefficient Spectra of Paratellurite in the Terahertz Region", J Infrared Milli Terahertz Waves, **37**, 703–709 (2016).

[61]. Gennadiy Komandin, Vadim Nozdrin, Sergey Chuchupal, Vladimir Lomonov, Yurii Pisarevskii, Oleg Provodnikov and Igor Spektor, "Dielectric permittivity of organ silicate glass thin films on a sapphire substrate determined using time-domain THz and Fourier IR spectroscopy", J. Phys. D: Appl. Phys. **53**, 495102,1-4, (2020).

[62]. Chandan Ghorui, A.M. Rudra, U. Chatterjee, A.K. Chaudhary, D. Ganesh, "Efficient second-harmonic and terahertz generation from single BiB_3O_6 crystal using nanosecond and femtosecond lasers", Appl. Opt., **60** (19), 5643–5651 (2021).

[63]. Chandan Ghorui, Arjun V Kidavu, P Naveen Kumar, S Das, A K Chaudhary and Yu M Andreev, "Comparative studies of terahertz-based optical properties in transmission/ reflection modes of GaSe: S and measurement of its scattering losses due to surface roughness for efficient terahertz generation", Phys. Scr. **98**, 025508,1-12 (2023).

[64]. M. Mahendar, R.N. Vamsi Krishna and A.K. Chaudhary, "Effect of the annealing temperature on structural, morphological, and nonlinear optical properties Of TeO_2 thin films used for efficient THz generation", Appl. Opt. **62** ,2394-2402 (2023).

[65]. K. Miyamoto, S. Ohno, M. Fujiwara, H. Minamide, H. Hashimoto, and H. Ito, "Optimum Phase-matched Terahertz-wave Generation of BNA-DFG," Optics Express, **14832**, 1-7,2009.

[66]. C. Vicario, M. Jazbinsek, A. Ovchinnikov, O. Chefonov, S. Ashitkov, M. Agranat, and C. Hauri, "High efficiency THz generation in DSTMS, DAST and OH1 pumped by Cr: forsterite laser," Opt. Express **23**, 4573-4580 (2015).

[67]. K. Arjun, D. Ganesh, S. Karthick, A. Santha, M. Venkatesh, S. Ganesamoorthy, S. Brahadeeswaran, A.K. Chaudhary, "Investigations on aqueous solution grown L- Arginine Phosphate monohydrate (LAP) single crystals for efficient THz generation", Journal of crystal growth, **575**, 1, 126337,1-5, (2021).

[68]. M. Mahendar, R. N. V. Krishna, and A. K. Chaudhary, "Femtoseconds laser based efficient THz generation from different temperature annealed CdTe thin films," Indian J. Pure Appl. Phys. **60**, 401–406 (2022).

[69]. Minwoo Yi, Kanghee Lee and Jaewook Ahn, Optimal Molar Fractions of Ternary Zinc-Blende Terahertz Emitters, J. Korean Phys. Soc. **51**(2), 475 - 479 (2007).

[70]. Chandan Ghorui, A.K. Chaudhary, Linear and nonlinear optical characterization of Tellurium dioxide (α-TeO_2) for generation of terahertz radiation using time-domain spectroscopy, Appl. Opt. **62**,18, 4831-4835 (2023).

Chapter 4

4. Designing aspects of newly developed THz profilometer for measuring the surface roughness of remote metallic and explosive targets

Abstract

In this chapter, we explore the cutting-edge advancements in Terahertz (THz) frequency domain 3D profilometry, specifically designed for standoff detection of surface roughness in metallic and explosive targets. By employing reflection geometry, we optimize signal strength by carefully selecting incident angles and frequency modalities, particularly crucial for surfaces with paint and rust/unpaint layers. Our focus lies on understanding surface scattering properties, directly influencing the quality of THz signals recorded within the frequency range of 0.5 to 2.0 THz.Our system, surpassing existing technologies in complexity, utilizes an interferometric arrangement, enabling precise measurement of penetration depth with exceptional resolution. Unlike traditional methods like optical profilometers and AFMs, our THz profiler excels in assessing surface roughness beneath paint layers, providing significant improvements in detection capabilities. Moreover, our innovative system can accurately measure small sample quantities (50 mg to 500 mg) and penetration depths ranging from 500µm to 30 mm. Furthermore, while existing systems are limited to 2D THz surface imaging, we have developed MATLAB code for generating comprehensive 3D surface profiles, enhancing our ability to characterize surface roughness across diverse targets. Moreover, our system's ability to penetrate paint layers facilitates the detection of corrosion effects on metallic surfaces. Additionally, our profiler can measure surface profiles of hydraulic pressed pellet materials without relying on interferometric designs, thereby offering a versatile solution for various applications.

A part of the research work presented in this chapter has been filling an Indian Patent and communicated to the journal

a) *A.K. Chaudhary,* ***Chandan Ghorui****, "A Tunable Incident Angle and Frequency Based 3d Terahertz Profilometer System" Indian Patent, Application No.: 202441040603 (24/05/2024)*
b) ***Chandan Ghorui****, P. Naveen Kumar and A.K. Chaudhary,* "Q- *factor based measurements of surface roughness of painted & rusted metallic objects using THz profilometer*", *(Communicated)*

4.1 Introduction:

The roughness refers to the texture of a material's surface and is a key indicator of its quality and performance in various applications. It quantifies the deviations of the surface from an ideal, perfectly smooth plane. These deviations can include peaks, valleys, and other irregularities that are inherent to the material or introduced during manufacturing processes. Accurate measurement and control of surface roughness are essential in ensuring the desired properties and performance of manufactured products. Surface roughness affects friction, wear, lubrication, and the interaction of the surface with other materials. For instance, a smoother surface generally has lower friction and wear. The surface texture can influence the mechanical properties of a material, including its fatigue strength and corrosion resistance. For coatings, paints, or adhesives, the surface roughness can impact the bonding strength and durability of the applied layers. In applications where appearance is important, such as in consumer electronics or automotive parts, surface roughness contributes to the visual and tactile appeal. 1D optical profile measurement typically involves capturing the height information of a surface along a single line. The main equations used in 1D profilometry are related to the reflection of light and triangulation methods. The equation is given by (4.1)

$$Z = \frac{d \tan\theta}{1+\tan\theta^2} \tag{4.1}$$

Where, Z is the height of the surface, 'd' the distance from source to detector, and θ is the angle of the reflected laser beam, respectively. Scientists are also used the equation (4.2) to intensity-based measure the surface roughness of the materials/any kind of objects.

$$I(z) = I_0 \exp^{\left(-\frac{4\pi z}{\lambda}\right)} \tag{4.2}$$

Where, I(z) is the intensity of reflected laser at height z, I_0 is the initial intensity of the laser beam and λ is the wavelength of laser used.

3D optical profilometry is a highly useful technique for measuring the surface roughness of materials by capturing a full three-dimensional profile of the surface. The surface roughness is quantified by using two important parameters derived from the height data obtained from the test surface. One of the most common parameters is the arithmetic mean of roughness, R_a. Here is the equation (4.3) used in 3D optical profilometry to measure R_a,

$$R_a = \frac{1}{N}\sum_{i=1}^{N}|z_i - \bar{z}| \tag{4.3}$$

Where, R_a is the arithmetic mean roughness, N is the total no of measurement points on the surface, Z_i is the height of the surface at point i, $\bar{z}$ is the mean height of the surface, calculated as equation no (4.4),

$$\bar{z} = \frac{1}{N}\sum_{i=1}^{N}|z_i| \tag{4.4}$$

While a 1D optical profilometer is useful for certain applications, it has several drawbacks when compared to a 3D optical profilometer. In a 1D profilometer, height information is measured along a single line, providing limited data about the surface topography. In contrast, a 3D profilometer captures comprehensive surface information over an area, offering a full 3D representation. To obtain a full surface profile with a 1D profilometer, multiple scans along different lines are required, which can be time-consuming and may introduce errors due to misalignment. On the other hand, a 3D profilometer acquires complete surface data in a single scan, significantly reducing the time required for measurement. The resolution of a 1D profilometer is limited to the number of points along the scan line, which may not capture fine surface details accurately. In contrast, a 3D profilometer provides high-resolution data across the entire surface, ensuring accurate and detailed measurements. A 1D profilometer struggles with complex surfaces that have varying topographies, as it cannot provide a holistic view. However, a 3D profilometer easily handles complex and irregular surfaces, offering detailed and precise topographical maps. In addition, a 1D profilometer requires manual interpretation and stitching of multiple line profiles to understand the full surface. In contrast, a 3D profilometer provides immediate and intuitive 3D visualizations, making data interpretation straightforward and reliable.

In the last ten years, surface roughness has been measured with optical profilometers. The benefit of optical profilometers over mechanical ones is contactless scanning, which shields soft surfaces from potential damage and deformation. Moreover, optical profilometers are capable of scanning surfaces that are not reachable by mechanical tools. For example, it can measure the background of a metallic, rusty plate or determine the roughness texture of a surface that comes into contact with water or air by recording the surface profile via a painted layer. This feature is especially helpful for analyzing how roughness textures change with different loads. The performance of mechanical, electrical, and optical systems is greatly impacted by surface roughness [1]. There are currently many different optical measurement instruments available, each based on a distinct concept. For example, the TOPO measurement system by WYKO Company in the USA and the FOCODYN optical probe from Feinpruf

Company in Germany [2–3] are popular choices. Optical measurements are in great demand for noncontact measurements both in research and production. Although these noncontact measurement instruments can offer very high accuracy, they are very sensitive to mechanical vibrations, air turbulence, and temperature variations. Q. Li et al. used a Stokes and Muller matrix-based technique to make optical measurements. The polarization of light coming from the Nomarski prism is expressed by Stokes vectors, as shown in equation (4.5) [4].

$$S = \begin{bmatrix} S_1 \\ S_2 \\ S_3 \\ S_4 \end{bmatrix} = \begin{bmatrix} E_x^2 + E_y^2 \\ E_x^2 - E_y^2 \\ 2E_xE_y\cos\phi \\ 2E_xE_y\sin\phi \end{bmatrix} \quad (4.5)$$

Where, E_x and E_y denote the electric field amplitudes of polarized light beam along the x and y axes, respectively, with ϕ denoting the phase difference between the two polarised beams. Physically, S_1 corresponds to the intensity of the polarized light beam (which is expressed as $I = \frac{1}{2}c\varepsilon_0 E.E^*$). When polarized light passes through polarizing components, its polarization shifts. The relation between the polarizing element and the polarized light is the same as that between a Mueller matrix and vector.

This interaction can be described mathematically by adopting the analogy of Mueller matrix. The wave plate and the detector, both are serving as polarizers and analyzer, having their respective components of Mueller matrices given by [5] equations (4.6) & (4.7), respectively.

$$M(\alpha,\delta) = \begin{bmatrix} 1 & 0 & 0 & 0 \\ 0 & \cos^2 2\alpha + \sin^2 2\alpha\cos\delta & \sin 2\alpha\cos 2\alpha(1-\cos\alpha) & -\sin 2\alpha\sin\delta \\ 0 & \sin 2\alpha\cos 2\alpha(1-\cos\delta) & \sin^2 2\alpha + \cos^2 2\alpha\cos\delta & \cos 2\alpha\sin\delta \\ 0 & \sin 2\alpha\sin\delta & -\cos 2\alpha\cos\delta & \cos\delta \end{bmatrix} (4.6)$$

$$M(\theta) = \frac{1}{2}\begin{bmatrix} 1 & \cos 2\theta & \sin 2\theta & 0 \\ \cos 2\theta & \cos^2 2\theta & \sin 2\theta\cos 2\theta & 0 \\ \sin 2\theta & \sin 2\theta\cos 2\theta & \sin^2 2\theta & 0 \\ 0 & 0 & 0 & 0 \end{bmatrix} \quad (4.7)$$

Here, δ denotes the wave plate's phase delay, θ the angle between the detector's axis and the x axis, and α the angle between the wave plate's axis and the x axis. During the sampling of the interference fringes obtained by means of raster scanning in the optical profilometer, the

contrast of the interference field must not be changed & the directional incident angle of the antenna must vary in terms of θ those changes in each step after completion of a scanning frame of the sample. Assuming that, the number of steps in one period is equal to an integer N, So the total laser beam intensity can be expressed as in equation no (4.8),

$$I(x, y, \theta) = a_0 + a_1 \sin 2\theta_i + b_1 \cos 2\theta_i \tag{4.8}$$

where, $\theta_i = {}^{i\pi}/_{N}, i = 1, 2, \ldots\ldots\ldots\ldots N$

Using trigonometric function, we can get from equation (4.8)

$$a_1 = \frac{2}{N}\sum_{i=1}^{N} I_i\,(x, y, \theta) \cos 2\theta_i \tag{4.8.1}$$

$$b_1 = \frac{2}{N}\sum_{i=1}^{N} I_i\,(x, y, \theta) \sin 2\theta_i \tag{4.8.2}$$

The phase is written as $\phi\,(x, y) = \tan^{-1}\frac{b_1}{a_1} = \tan^{-1}\frac{\sum_{i=1}^{N} I_i(x,y,\theta)\sin 2\theta_i}{\sum_{i=1}^{N} I_i(x,y,\theta)\cos 2\theta_i}$ (4.9)

Equation (4.9) shows that the phase distribution $\phi\,(x, y)$ which can be calculated from the N numbers of measurements of the laser beam intensity collected from the different portion of the surface at the relevant directional angles of the PCA antenna. Once the value of $\phi\,(x, y)$is ascertained by lock-in-amplifier, that helps to determine the partial derivative of the surface topography in the direction x using equation (4.10)

$$\frac{\partial H(x,y)}{\partial x} = \frac{\lambda}{4\pi} \times \frac{\phi(x,y)}{\Delta x} \tag{4.10}$$

Where, λ is the wavelength, and Δx is the offset between the two orthogonally polarized beams. In the same way, we get the partial derivative in the y direction. The surface topography H (x, y) is then calculated using equation (4.11)

$$H(x, y) = \int_{(0,0)}^{(x,y)} \frac{\partial H(x,y)}{\partial x} dx + \frac{\partial H(x,y)}{\partial y} dy \tag{4.11}$$

From equation (4.11) it is clearly evident that, the surface topography is determined by integrating the measured data in the x-y plane. Consequently, the optical profilometer can measure surface topography with micro fluctuations greater than half the laser wavelength, minimizing the impact of random measurement errors. The developed profilometer in the THz range has an offset (Δx) of 5 mm between the two orthogonally polarized beams and a scan speed of 5 mm/s along both the x and y axes. We calculated the phase information using FFT data from the time-domain spectra. The surface roughness of old metallic objects was found to

be in the range of 30-150 µm, which is much greater than the wavelength of the laser light used. In contrast, for explosive and high-energy materials, the surface roughness ranged from 0.05-0.15 µm, which is less than the wavelength of the laser beam. The lateral resolution is determined by the size of the laser beams focus spot, which is not limited by diffraction effects. The dimension of a diffraction-spot size can be defined by the so-called 50 % irradiance width ($d_{0.5}$), which is the diameter of the circle where the irradiance is 50 % of the maximum irradiance. The lateral resolution can be expressed by equation (4.12)

$$d_{0.5} = \frac{c}{2\,\nu \times NA} \tag{4.12}$$

Where, c is velocity of light, ν is the THz frequency and NA is the numerical aperture of the rough metallic or explosive object (NA=$n \times \sin\theta_i$) , n is refractive index of rough painted metallic or explosive surfaces and θ_i is the angle of incident of PCA, respectively.

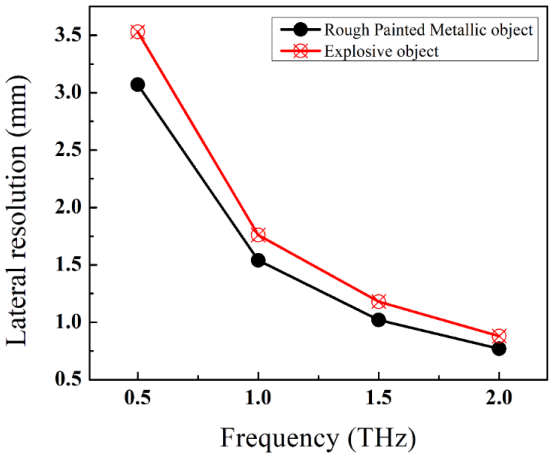

Figure 4.1: Lateral resolution of THz frequency for metallic and explosive targets

THz profilometer's combination of non-contact operation, penetration capabilities, and high precision positions it as a versatile and advantageous tool for surface roughness measurements, especially when compared to AFM and Optical Profilometers in specific applications and material contexts. This non-invasive nature ensures minimal impact on delicate or sensitive surfaces, preserving their integrity. Complexity level is more of the existing system which involves the interferometric arrangement of the system. Optical profilometer and AFM may face difficulties in accurately measuring the depth of features, especially in structures with complex geometries, but our developed system is able to measure the penetration depth of the samples. Resolution capability is very high compare to the existing systems. Existing systems

can't measure the surface roughness of the metallic objects painted layer, because they are mostly visible range profilometer which can't penetrate through the paint layer. If the materials surface roughness in the order of mm, we can't utilize the available technology which is based on visible light. The motivation for studying the surface roughness of both painted and unpainted metallic targets and explosive materials is rooted in the need to enhance security technologies, optimize material characterization techniques, improve sensitivity in detection systems, increase the material integrity, improving the quality of metallic target and ensure the reliability of non-destructive testing methods.

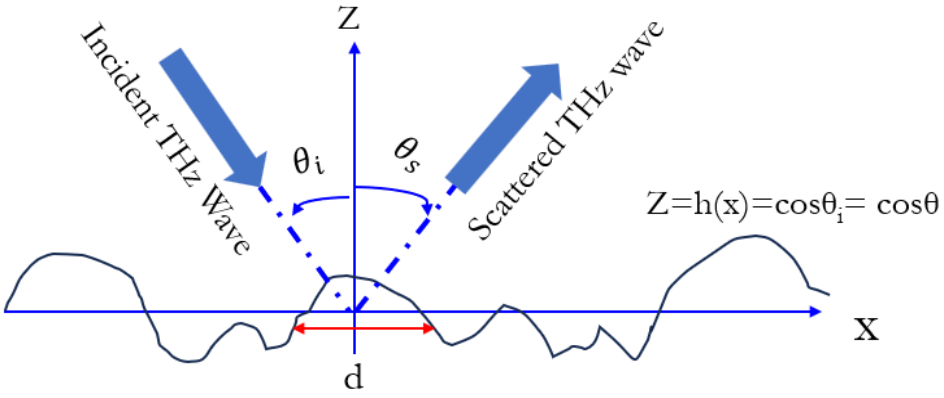

Figure 4.2 A 2D rough surface scattered by THz wave with incidence and scattering angles of θi and θs, respectively. The formula for calculating surface height is z = h(x) = cosθ = cosθi (r = 1), where d is the distance between any two points on the rough material's surface.

By measuring the scattered light, particularly the angle of scattering θs and the intensity of the scattered light, the profilometer can deduce the surface profile z=h(x). The variation in the scattering angle and intensity provides information about the surface roughness and other characteristics of the materials. The angle of incidence θi is a known parameter that helps in the calculations of the surface profile.

In equation (4.2), we re have replaced the z value by z = cosθ, Now, the Kirchhoff modified version of the equation is specular direction in terms of reflectivity can be written as,

$$R_{rough} = R_{smooth} e^{-\left(\frac{4\pi\sigma f \cos\theta}{c}\right)} \quad (4.13)$$

Where, R_{smooth} is the reflectance of a perfectly smooth surface (σ=0), f represents the THz wave frequency and θ is the incident angle respectively. Due to optical polishing, the smooth surface of gold-coated mirror was selected as a reference and incident angle of THz beam was fixed at 4^0. As per equation (4.1) we have followed three assumptions (i) surface roughness is random in nature and normally distributed (ii) contours of the

roughness is much greater than the incident wavelength (iii) no multiple scattering was allowed between exist surface points [6-9]. We have directly measured R_{rough} of both painted/unpainted old metallic and explosive targets with 4^0 angles of incidence and value of R_{smooth} as a reference from the gold coated mirror.

In our designed profilometer, the incident angle is fixed of the order of 4^0. We have measured the p-polarised reflectivity signal from smooth surface and rough surface. The surface roughness of the p-polarised light beam measured by the modified ($\cos 4^0 = 1$) following equation (4.14)

$$\sigma = \begin{matrix} 1 \\ 2 \\ 3 \\ \vdots \\ m \end{matrix}\begin{bmatrix} \sigma_{11} & \sigma_{12} & \cdots & \sigma_{1n} \\ \sigma_{21} & \sigma_{22} & \cdots & \sigma_{2n} \\ \sigma_{31} & \sigma_{23} & \cdots & \sigma_{3n} \\ \vdots & \vdots & \vdots & \vdots \\ \sigma_{m1} & \sigma_{m2} & \cdots & \sigma_{mn} \end{bmatrix} = \frac{c}{4\pi f} \ln \begin{bmatrix} R_{11} & R_{12} & \cdots & R_{1n} \\ R_{21} & R_{22} & \cdots & R_{2n} \\ R_{31} & R_{23} & \cdots & R_{3n} \\ \vdots & \vdots & \vdots & \vdots \\ R_{m1} & R_{m2} & \cdots & R_{mn} \\ \hline R'_{11} & R'_{12} & \cdots & R'_{1n} \\ R'_{21} & R'_{22} & \cdots & R'_{2n} \\ R'_{31} & R'_{23} & \cdots & R'_{3n} \\ \vdots & \vdots & \vdots & \vdots \\ R'_{m1} & R'_{m2} & \cdots & R'_{mn} \end{bmatrix} \quad (4.14)$$

Where, R and R' represents the reflectivity matrix from smooth surface and rough surface respectively, c is the speed of light and f is desired frequency of the constructed individual matrices. Measuring surface roughness is essential in numerous industrial and defense applications. It is used to assess the quality of coatings and paint layers, detect early signs of corrosion, evaluate coating degradation, and characterize aging explosives [10-11]. Terahertz time-domain spectroscopy is based on measurement of the dielectric field in the transmission and reflection modes for transparent and highly absorbing materials. Ilaria Cacciari et al. discussed how THz reflection data can be used to estimate the roughness of archaeological metal surfaces. They explained that the roughness, which causes backscattering from metallic samples, provides valuable tomographic and spectroscopic information [12]. Norikazu Fuses group explained the non-destructive terahertz imaging of alkali products on the coated steel with cathodic disbanding [11,13]. Ortolani et al. groups reported the surface roughness effect on THz reflectance of pure explosive such as RDX & HMX materials. They also discussed the importance of oblique incidence geometry for long-distance object detection [14]. M. Hassan Arbab et al. showcased how surface scattering impacts terahertz time-domain spectroscopy of lactose with varied material grain sizes in both transmission and reflection modes, hindering chemical detection [15]. Y. Dikmelik et al. mentioned that the surface roughness of explosive materials ranges from 50 to 160 μm.

They also addressed how THz reflectance spectra help to reduce the SNR and mitigate the impact of surface roughness on explosive materials [16]. Yang Yu's group show the effect of surface roughness of different grit PTFE samples using THz time-domain transmission spectroscopy and established the analytical model to calibrate the spectra of different types of rough surfaces [17]. J. Kokkoniemi, J. Lehtomaki et al. measured the effect of roughness scattering in the THz band for the shorter usually distance diffuse scattering field theory is used for communication [18]. A. Jaganathan et al. used THz reflection spectroscopy to characterize the roughness of aluminum metallic surface ranging from 5-20 µm. using They explained the periodic behaviour of the cylindrical object [19-20]. R. Piesieicz et al. analyzed the scattering model used for THz communication system [21]. Depew et al. used a spectrophotometer with a tunable wavelength range between 0.2 and 15 µm to determine the surface roughness of aluminum foil, which varied between 0.1 and 0.8 µm [22]. J. Ma et al. described the diffuse scattering effect of THz reflection data from the metallic rough surfaces and influence of wireless channels [23]. Recently, we have reported the 2D THz images of metallic, wood, drugs samples under concealed position and explained the THz based scattering effect from rough surfaces of explosive molecules such as RDX, TNT & NH_4NO_3 mixed in the teflon matrix and nonlinear S doped GaSe crystal [24-26]. In continuation of same study, we have now recorded the 2D THz images of painted and unpainted metallic and explosives targets. The obtained raster scanned data were used for developing a THz surface profilometer system to ascertain the actual strength of reflected signal with respect to surface roughness and incident angle.

4.2 Existing state of art:

One common tool used to obtain topographical data from different sample surfaces is a profilometer. It includes a full three-dimensional scan as well as a single point or line scan. Determining specifics about the surface morphology, step heights, and surface roughness of various materials is the primary goal of profilometry. One way to do this is by using a light source or a physical probe. The two main types of profilometers are (i) optical and (ii) stylus. Stylus profilometers use a probe to physically move along the surface in order to sense the elevation of the surface. This is a mechanical method that uses a feedback mechanism to monitor the force that the sample applies to the probe as it is being scanned. The arm is kept at the so-called "setpoint," or precise torque level, by use of a feedback control system. The surface topography is then recreated by adjusting the arm holder's Z-position. Direct contact with the surface and force feedback are required for stylus profilometry. It is susceptible to

damage on soft surfaces and the probe may become contaminated by the surface material, even with its high sensitivity and good Z resolution. Furthermore, there's a chance that this technique will damage some surfaces. In comparison to non-contact approaches, stylus profilometry is slower because of the motions in the X, Y, and Z axes that occur when the stylus is in touch with the surface. Additionally, the dimensions and shape of the stylus tip can impact the measurements and restrict the lateral resolution.

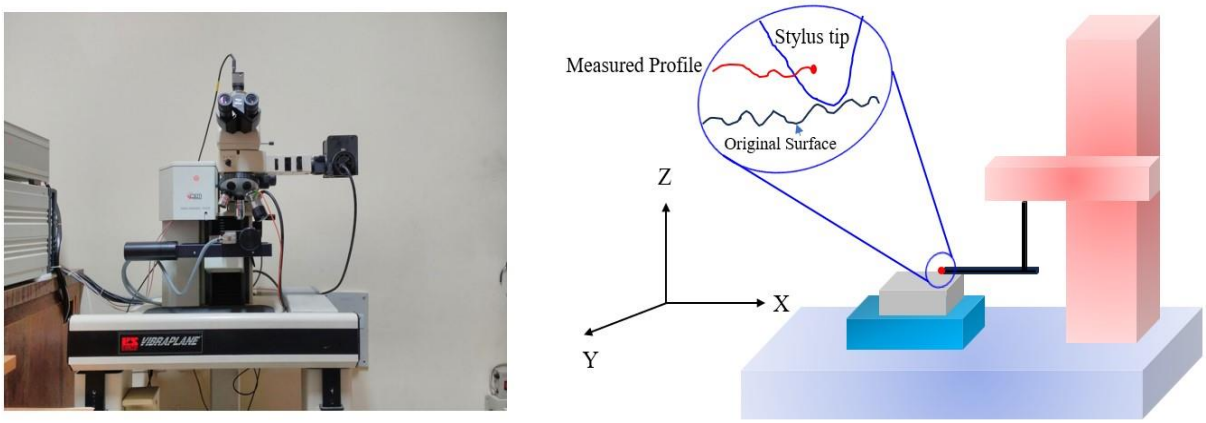

Figure.4.3 Schematic diagram of (a) AFM at HCU & (b) stylus profilometer

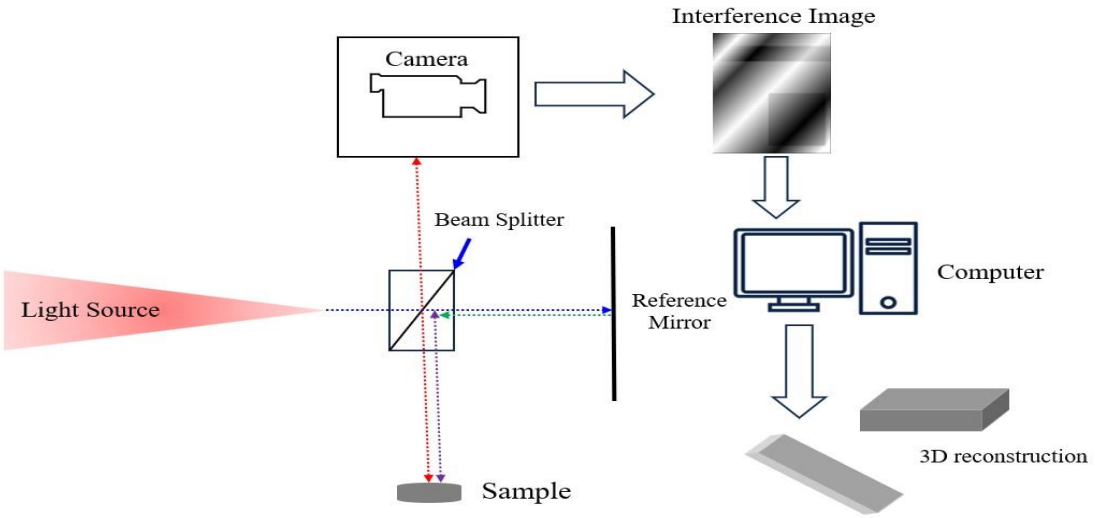

Figure.4.4 Schematic diagram of an Interferometric Profilometer

Optical profilometry uses a variety of techniques to replace a physical probe with light. The main component of this method is using light direction to identify the surface in three dimensions. Optical interference, confocal aperture use, focus and phase detection, and pattern projection onto the optical image are some of the techniques used. Generally speaking, an optical profilometer is made up of two primary parts: a sample stage and a detector. The sample

stage holds the sample in place while the detector locates points on it. The sample stage moves in certain systems while the detector and sample stage move in others. Thus, there exists a need for this type of model which helps us to calculate the THz surface roughness and we can say, why the image resolution of the objects is changing. Some of groups not of reported the surface roughness measurement model for metallic and explosive materials but they are using continuous wave, broadband wave with filters and FTIR data [23-25].

4.2.1 Atomic Force Microscopy:

One of the best methods for examining sample material properties and nanoscale surface metrology is to use an atomic force microscope. On the other hand, the visible light wavelengths of a typical compound light microscope limit the highest sample magnification to approximately 1000x. As such, it provides a ~0.2 μm resolution, which means it cannot distinguish spots that are approximately 200 nm away. In recent decades, the shortcomings of this resolution have grown more evident, particularly with the introduction of cutting-edge technologies such as atomic force microscopy (AFM) and scanning electron microscopy (SEM). It is a scanning probe microscopy, offers the capability to obtain surface information such as surface roughness and profile with a resolution down to the order of nm. Its effectiveness stems from the utilization of piezoelectric elements, enabling extremely small movements with exceptional accuracy & precision. The interaction potential between two particles in close proximity, known as the Lennard-Jones potential, is given by equation (4.15)

$$V = K\{\left(\frac{r_m}{r}\right)^{12} - 2\left(\frac{r_m}{r}\right)^{6}\} \tag{4.15}$$

where K is the constant denoting the depth potential, r_m is the distance corresponding to the minimal potential, and r is the distance between the two particles. This summarizes the interaction potential between the tip and the nearby material surface, which is the basis for the operation of AFM. With this technology, specimen surface properties are evaluated with atomic precision in terms of both vertical and lateral dimensions using a physical probe. It works on the basis of surface detection, using a micromachined silicon probe with an incredibly sharp tip. The probe moves line by line as it methodically scans the specimen's surface in a grid pattern, albeit the precise method can vary greatly depending on the operational mode. Operational modes can be broadly classified into two categories: contact mode and dynamic mode, commonly referred to as tapping mode. A tiny cantilever that doubles as a spring is connected to a nanoscale tip at the heart of the AFM idea. When the tip makes contact with the

surface, the cantilever bends, and this bending is detected. The cantilever bends when the tip makes contact with a surface, and this deformation is recorded by using a split photodetector in conjunction with a laser diode. The amount of interaction between the tip and the specimen is indicated by the degree of bending. When in contact mode, the tip is pressed up against the surface, and the tip-sample interaction force is monitored by an electrical feedback mechanism that keeps the deflection constant as it scans the grid. On the other hand, tapping mode minimizes contact between the specimen's surface and tip in order to prevent damage. In this mode, the tip oscillates in a sinusoidal pattern as a result of the cantilever oscillating at or close to its resonance frequency. This movement is affected by either attractive or repulsive forces as the tip nears the specimen.

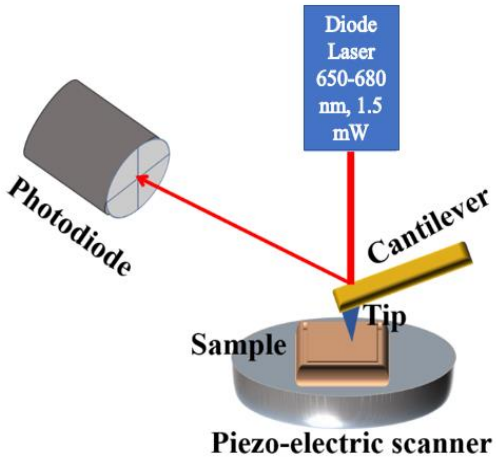

Figure.4.5 Schematic diagram of atomic force microscopy setup

Figure 4.5 depicts the schematic representation of an atomic force microscope (AFM), comprising a cantilever with a tip (having a diameter in the range of 10-20 nm) attached to it. A laser beam is focused onto the cantilever and upon reflection, it is detected by a photodiode. The movement of the cantilever over the material surface in a raster pattern leads to deflection dependent on the surface topography due to piezoelectric motion. This deflection alters the laser beam, which is sensed by arrays of photodiodes. The collected light is subsequently processed and analyzed computationally to generate a three-dimensional image of the material surface. In tapping mode, a feedback mechanism functions akin to contact mode but retains a constant tapping motion amplitude as opposed to quasi-static deflection. This enables the tracing of the topography of the sample in a line-by-line manner. AFM instruments serve as highly adaptable instruments that go beyond topographic assessments and imaging tasks. They are widely employed for the evaluation of mechanical and electrical characteristics of

materials, encompassing properties such as ferroelectric, piezoelectric, magnetic, and thermal properties. These characterizations are typically performed using variations of either contact mode or tapping mode, often requiring specialized probes. For instance, piezo response force microscopy (PFM) employs atomic force microscopes (AFMs) to investigate the electromechanical interactions within a material system by applying electrical stimuli through the probe tip. This method may necessitate the application of high tip-bias voltages to achieve the required sensitivity levels. While dynamic mode is more commonly used than contact mode, the latter is particularly effective for evaluating the electrical properties of samples during imaging, as the tip can function as a nanoscale electrode. AFM instruments have a wide range of applications across various fields, including polymer science, semiconductor technology, thin films, energy storage materials, and the study of biomolecules, cells, and tissues, among other areas. Existing systems cannot measure the surface roughness of metallic objects' painted layers because they are mostly visible-range profilometers, which cannot penetrate the paint layer. If the material's surface roughness is on the order of millimeters, the available technology based on visible light is inadequate. Additionally, the complexity of existing systems, which often involve interferometric arrangements, poses a challenge. Optical profilometers and AFMs may face difficulties in accurately measuring the depth of features, especially in structures with complex geometries. However, our developed system is capable of measuring the penetration depth of samples, with significantly higher resolution compared to existing systems.

4.3 Advantage of 3D Profilometer over 1D Profilometer:

A 3D profilometer offers a more comprehensive, accurate, and versatile approach to surface measurement than a 1D profilometer, making it the preferred choice in many applications. It provides a detailed, three-dimensional view of a surface, capturing the entire topology for a complete analysis of features such as texture, roughness, and form. Unlike a 1D profilometer, which measures along a single line and may miss critical features, a 3D profilometer can measure intricate shapes, including slopes, curves, and undulations, essential for applications like semiconductor wafer inspection, MEMS, and microfluidics. 3D profilometry achieves higher accuracy and resolution, detecting minute variations and providing precise surface representations crucial for quality control and assurance. The comprehensive data allows for advanced analysis techniques, such as statistical surface analysis, wear tracking, and defect identification, enhancing the ability to predict performance and reliability of materials and components. Additionally, 3D profilometers are versatile and can be used in various applications, from industrial manufacturing to scientific research,

offering valuable insights across different fields. Their three-dimensional visualization capabilities make it easier to understand and communicate surface characteristics, aiding in research and development by facilitating the identification of issues and development of solutions.

4.4 Theoretical Consideration:

The Kirchhoff approximation is a mathematical technique used in the field of electromagnetic scattering. It is commonly applied to analyze the scattering of electromagnetic waves, such as radar or radio waves, from rough surfaces. This approximation assumes that the surface being examined is significantly greater than the incident wavelength of radiation and that the surface roughness is considerably smaller than the wavelength. In essence, the Kirchhoff approximation simplifies the calculation of scattered electromagnetic fields by considering the surface as a collection of small scattering elements. Each of these elements' scatters radiation independently, and their contributions are summed to estimate the total scattered field. This approach is particularly useful for modeling the scattering from surfaces with irregularities, such as terrain, buildings, or ocean waves. let's briefly introduce some key parameters associated with the Kirchhoff approximation (i) rho (ρ) is the correlation length of the surface irregularities. It quantifies the spatial variation of the surface features. In the Kirchhoff approximation, the statistical properties of surface irregularities, including their correlation length, play a significant role in determining the scattering behavior (ii) The parameter "g" is often used to describe the surface roughness in terms of statistical properties. It characterizes the height fluctuations of the surface and their distribution. The specific definition of "g" can vary depending on the scattering model being used. The Kirchhoff approximation has found applications in various fields, including radar imaging, remote sensing, and communications, where understanding how electromagnetic waves interact with complex surfaces is essential for system design and analysis. By utilizing modified Fresnel equations, coupled with the corresponding impedance and the modified reflection coefficient, and assuming a surface roughness factor of one, one can ascertain the scattering losses in the specific direction using equation (2.17) & (2.18) respectively in the Chapter 2.

4.5 Results and Discussion:

We deal with optical image, temporal/spectral profile of metallic and explosive targets in reflection mode. In the next part, deals with THz images at f = 0.5,1.0, 1.5 and 2.0THz frequency range, 3D surfaces images, roughness effect, reflection coefficient of both types of objects in TE & TM. Finally, we discuss the dependency of quality factor of the THz signal strength and contrast of THz image.

4.5.1 Terahertz time/frequency domain reflected signal & optical property of old metallic target

The time- domain waveforms of reflection mode from reference and the targets are shown in Figure. 4.6 (a-iii). For all types of measurement, the vertical position of sample surface with respect to the reference surface was adjusted such that the zero crossing points of initial reference cycles coincided both the waveforms and we get the signal when zero delay.

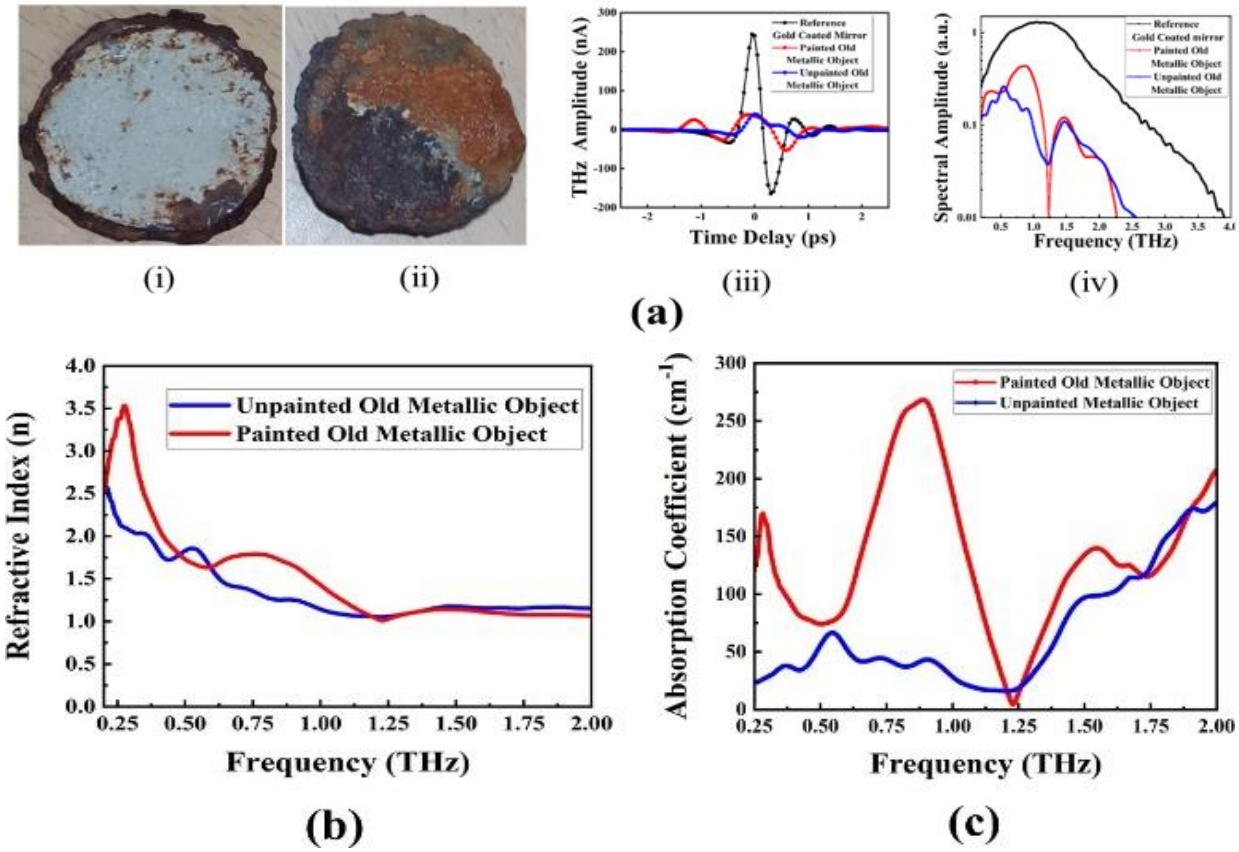

Figure 4.6: (a) Optical images of (i) a painted metallic object and (ii) an unpainted metallic object. (iii) Time-domain waveforms from the reference (gold-coated mirror) and both types of objects. (iv) Frequency-domain waveform of the reference and both test samples. (b) Refractive index and (c) absorption coefficients of the test samples with respect to THz frequency.

The THz waveforms for both painted and rusted/unpainted old metallic objects show broadening effect as compared to reference waveform obtained from gold coated mirror. Discrete fourier transforms waveform of reference and objects are shown in Figure.4.6 (a-iv). We observed that the spectral amplitude of both objects lies up to 2.5 THz frequency range whereas reference gold coated mirror spectrum extended upto 4.0 THz range. We get the signal amplitude of both metallic objects at 2.0 THz. The optical constants such as refractive indices and absorption coefficients are shown in Figure. 4.6 (b & c). Finally, the refractive index of

painted old metallic object varies between 3.5-1.08 and 0.2-2.0 in the given THz frequency range. However, in case of unpainted old metallic object it varies between 2.8-1.9 in the same frequency range. Similarly, the value of absorption coefficients of both types of objects has a significant deep at 1.25 THz range which shows the metallic signature of absorption features for both the objects. It was observed that the strong absorption peaks are located at 0.284, 0.884 and 1.537 THz, respectively for painted old metallic object whereas in case of unpainted object absorption peaks have almost nearby lower values at 0.367, 0.534, 0.721, 0.91 and 1.502 THz, respectively.

4.5.2 2D THz imaging, 3D surfaces profiling, surface roughness effects, and reflection coefficients in TE mode for painted and unpainted/rusted metallic targets

For defense and security point of view the THz radiation from the source is directed to the target for the surface scanning and reflected signal carries the information of the surface roughness in terms of intensity. This can also be visualized in terms of image quality and resolution recorded on a pixel-by-pixel basis. The quality of images depends on three principal parameters such as (i) frequency (ii) angle of Incidence (iii) scattering parameters due surface roughness and also measured in terms of TE mode of reflection coefficients. Four sets of THz based recorded images of painted old metallic object are shown in Figure.4.7(a) whereas their corresponding 3D surface profiles are shown Figure.4.7 (b) respectively.

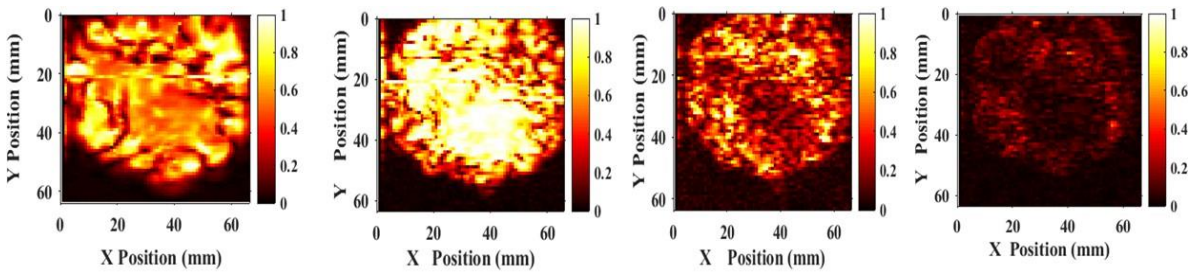

(a)

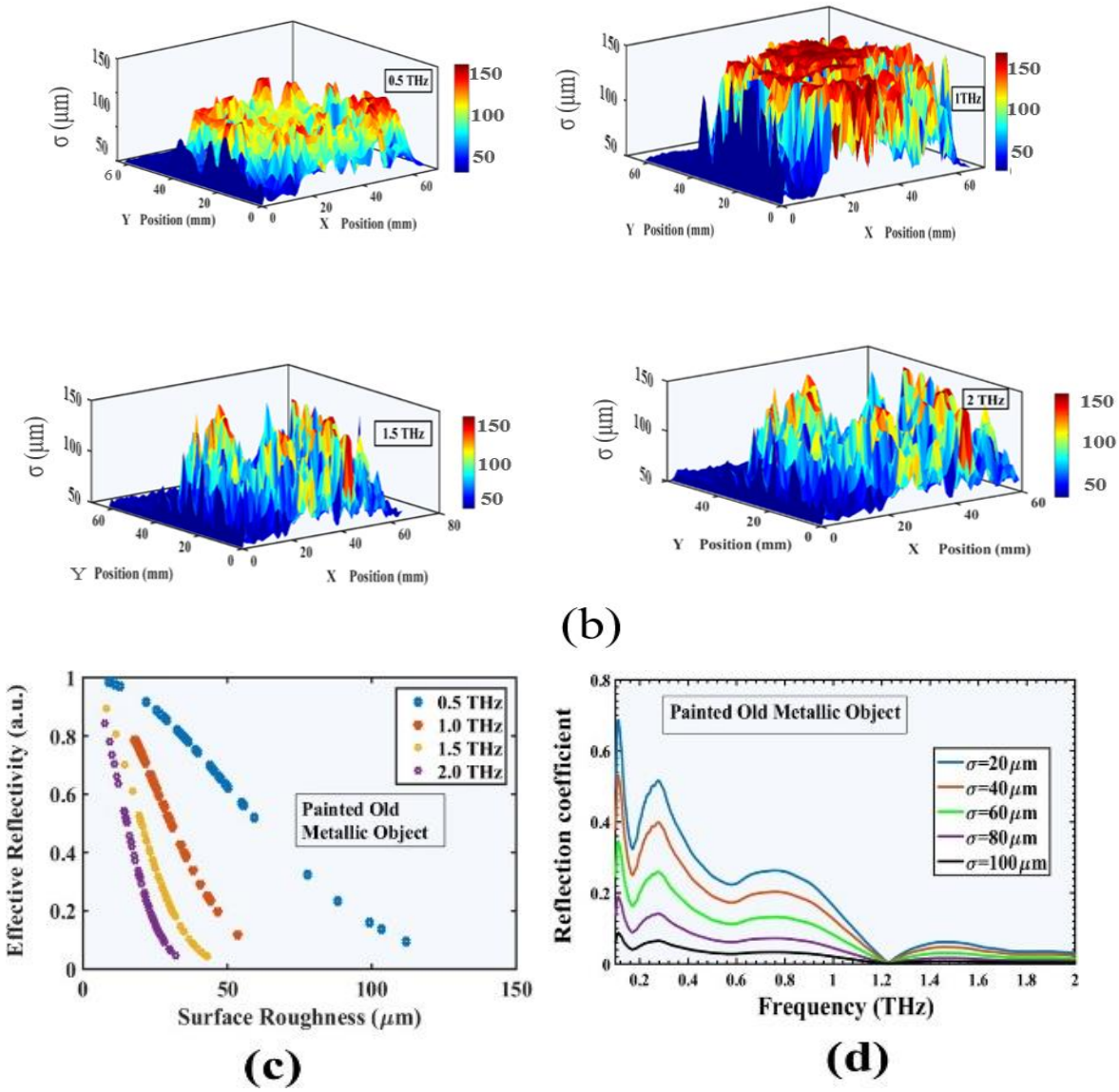

Figure 4.7: (a) 2D-THz images of a painted old metallic object at frequencies of 0.5, 1.0, 1.5, and 2.0 THz, respectively. (b) 3D surface images of the same object at frequencies of 0.5, 1.0, 1.5, and 2.0 THz, respectively. (c) Effect of surface roughness on the effective reflectivity of the painted surface at given THz frequencies. (d) Reflection coefficients versus THz frequency for different levels of roughness in TE mode.

The surface roughness of painted old metallic object varies between 15-120 μm range which is also correlated with respect to incident frequency such as 0.5,1.0,1.5 & 2.0 THz, respectively. The calculated results of the surface roughness for mentioned THz frequencies are shown inthe Figure. 4.7(c). The effective reflectivity representing the deconvolution of the painted old metallic object spectra with respect to the gold coated mirror is shown in Figure.4.7(d). The strength of reflection coefficient in transverse electric (TE) mode is having high values for smooth surfaces whereas it becomes very

low for rough surfaces. The strength of the reflected signal is directly related tothe high-quality images.

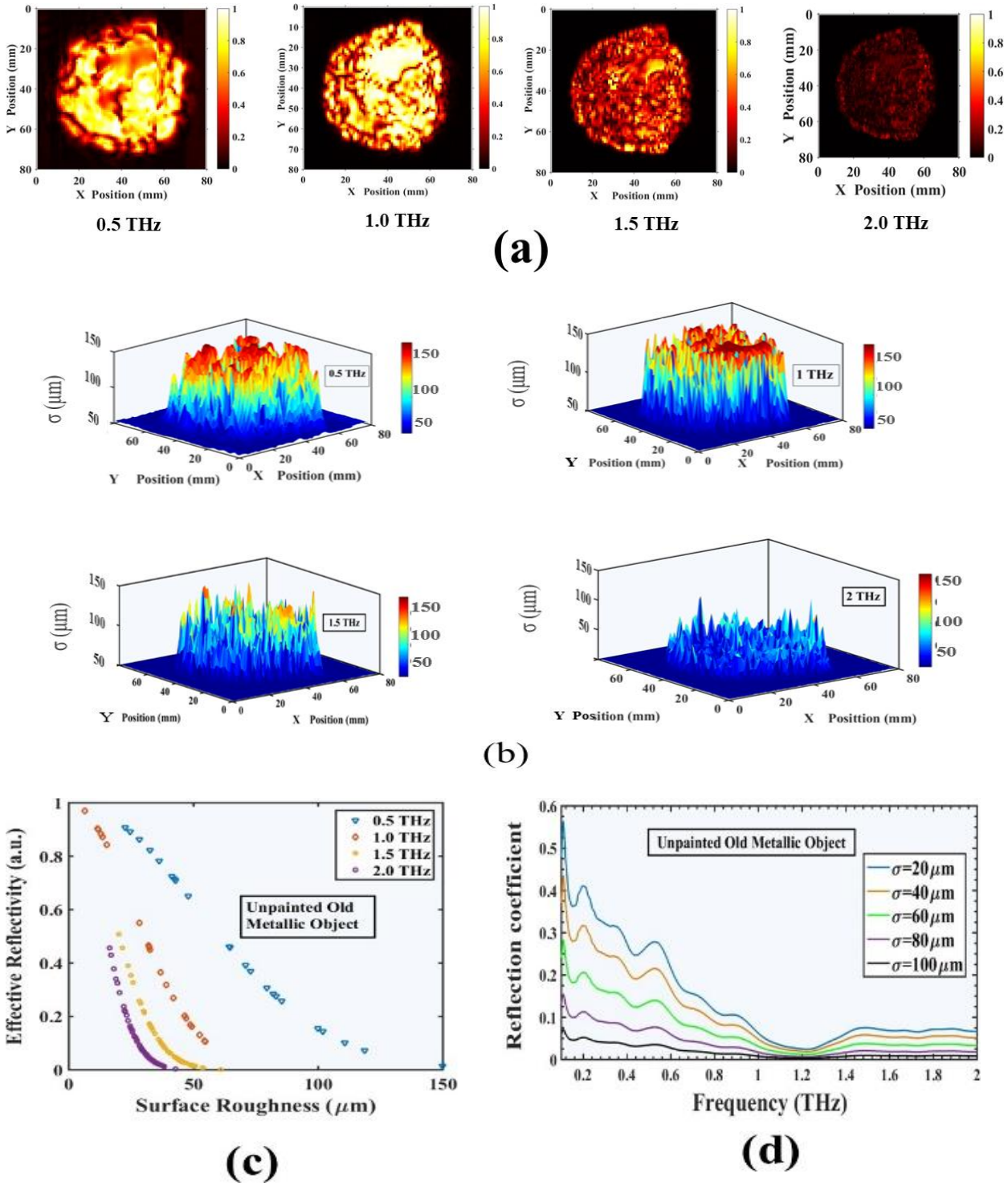

Figure 4.8: (a) 2D-THz images of a unpainted/rusted old metallic object at frequencies of 0.5, 1.0, 1.5, and 2.0 THz, respectively. (b) 3D surface images of the same object at frequencies of 0.5, 1.0, 1.5, and 2.0 THz, respectively. (c) Effect of surface roughness on the effective reflectivity of the rusted surface at given THz frequencies. (d) Reflection coefficients versus THz frequency for different levels of roughness in TE mode.

Figure.4.8 (a) shows the images of unpainted/rusted surface at four different THz frequencies. Surface roughness of unpainted/rusted old metallic object varies between 18-130 μm range. The standard deviation of surface height distribution of unpainted metallic object is shown in Figure.4.8 (b). The effective reflectivity from these surfaces is shown in Figure.4.8(c). We have calculated the reflection coefficients from the painted/rusted old metallic objects using modified Fresnel's equation in terms of scattering [25-27]. Finally, Figure.4.8 (d) shows the variation in the value of reflection coefficient with respect to incident THz frequency and surface roughness σ = 20, 40, 60, 80 and 100 μm, respectively. The quality of reflected signal used in form of pixel to frame a good image can be explained using a cross multiplication of matrix of corresponding wavelength ($\lambda_{v)}$ associated with incident THz frequency and surface roughness ($\sigma_{v)}$ of the surface at given frequency as mentioned in eq. no.4.16.

$$[\lambda_{0.5} \quad \lambda_{1.0} \quad \lambda_{1.5} \quad \lambda_{2.0}] \begin{bmatrix} \sigma_{0.5} \\ \sigma_{1.0} \\ \sigma_{1.5} \\ \sigma_{2.0} \end{bmatrix} = \begin{bmatrix} \lambda_{0.5}\sigma_{0.5} & \lambda_{0.5}\sigma_{1.0} & \lambda_{0.5}\sigma_{1.5} & \lambda_{0.5}\sigma_{2.0} \\ \lambda_{1.0}\sigma_{0.5} & \lambda_{1.0}\sigma_{1.0} & \lambda_{1.0}\sigma_{1.5} & \lambda_{1.0}\sigma_{2.0} \\ \lambda_{1.5}\sigma_{0.5} & \lambda_{1.5}\sigma_{1.0} & \lambda_{1.5}\sigma_{1.5} & \lambda_{1.5}\sigma_{2.0} \\ \lambda_{2.0}\sigma_{0.5} & \lambda_{2.0}\sigma_{1.0} & \lambda_{2.0}\sigma_{1.5} & \lambda_{2.0}\sigma_{2.0} \end{bmatrix} \tag{4.16}$$

4.5.3 Q factor depending the signal strength:

The Q factor for different types of rough surfaces is determined from the graphs shown in Figure 4.9. This quality factor represents the size of the scattering surface in relation to the wavelength of the incident radiation. It helps determine whether the Kirchhoff approximation is valid for a given scattering problem. When Q is much smaller than 1, the approximation is usually accurate. The image quality factor includes five numbers of important parameters such as contrast, blur, noise, artifacts & distortion as shown in our previous figure. The most important image quality factor is sharpness. The sharpness determined the amount of detail an image can carried out. The primary challenges lie in the significantly low signal-to-noise ratios, stemming from the diffused field caused by multiple Mie scattering events, which in turn affect the absorption signature of both painted and unpainted surfaces.

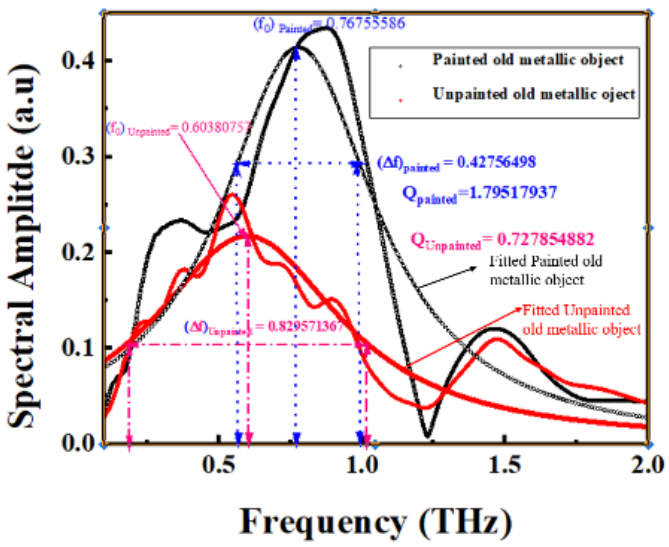

Figure 4.9: Quality factor of coated and uncoated old metallic objects as a function of THz frequency.

The quality factor "Q" helps the define the degree of losses involved in the strength of reflected signal from the rough surfaces and it is directly proportional to the bandwidth of the concerned the central frequency. In the present case, the Q factors of painted & unpainted old metallic objects are 1.79 and 0.73, respectively whereas, the bandwidth of painted and unpainted old metallic objects is 0.43 & 0.82, respectively. 0.73 lowest quality factor represents the highest quality of the image & 1.79 represents the most compressed image. In 2D terahertz imaging for applications like material characterization and security screening, the quality factor of the materials being examined can significantly impact the quality and interpretability of the images. Materials with distinct terahertz absorption features (high Q) are often preferred for applications where precise identification and differentiation of substances are critical. Conversely, low-Q materials may be preferred when minimal absorption and deeper penetration are required. When imaging materials with low-Q values in the terahertz range, the resulting images may exhibit lower contrast. This is because the absorption features are less pronounced, making it challenging to distinguish different components within the material. High-Q materials can produce higher-contrast terahertz images. The sharp absorption peaks in the THz spectrum make it easier to identify and differentiate various components within the material being imaged. Though the low Q factor represents the low spectral amplitude as a result the image is having low shining effect and enhances the visibility of the roughness. TABLE -4.1 comprises the Q factor related data of painted and unpainted surfaces.

Table-4.1 Values of Q-factor and signal to noise ratio of painted and unpainted/rusted objects

Frequency (THz)	Painted old metallic object		Unpainted/Rusted old metallic object	
	Q-factor	SNR	Q-factor	SNR
0.5	1.79	18	0.73	23
1.0		32		35
1.5		58		68
2.0		10		12

4.6 Real time metallic object detection and surface roughness effects:

The motivation for studying the effect of surface roughness on real-time metallic objects stems from its profound influence on electromagnetic interactions, particularly in applications where accurate and timely information about these objects is crucial. Surface roughness significantly affects the scattering, absorption, and reflection of electromagnetic waves, and understanding these effects is vital for various practical scenarios. In real-time applications involving metallic objects, such as security screening, industrial inspections, and quality control, the interaction between electromagnetic waves and surface roughness becomes a critical factor. The modulation of electromagnetic signals by surface roughness can impact the detection and characterization of metallic objects, including their shape, composition, and potential threat level. For instance, in security screening at airports or border checkpoints, where rapid and accurate identification of metallic objects is paramount, understanding how surface roughness influences electromagnetic interactions is essential. The ability to differentiate between harmless objects and potential threats relies on precise information about the metallic surfaces, and surface roughness plays a role in shaping the electromagnetic response. In industrial settings, where the quality and integrity of metallic components are crucial, real-time monitoring and inspection benefit from a comprehensive understanding of surface roughness effects. Surface roughness can impact the performance of metallic objects, such as sensors or structural components, and studying these effects aids in optimizing their design and functionality. Furthermore, in applications like autonomous vehicles and robotics, where real-time sensing is essential for navigation and obstacle avoidance, the influence of surface roughness on electromagnetic interactions with metallic objects becomes a consideration for enhancing the reliability of detection systems.

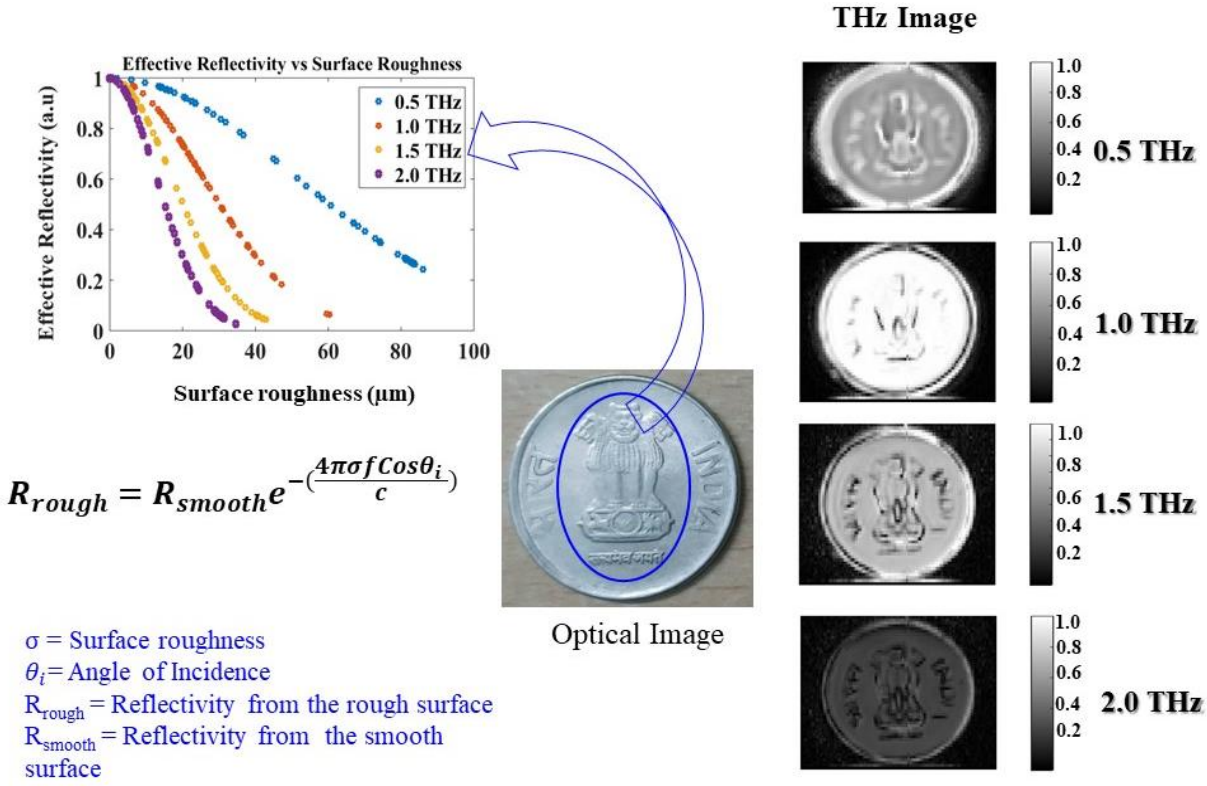

Figure 4.10: Influence of surface roughness on optical and THz imaging of a coin.

Figure.4.10 shows the optical and 2D THz image of real time metallic object. The surface roughness effect of coin. The surface roughness of coin varies from 30 -100 μm in THz domain. We have demonstrated the use of 2D THz imaging system for development of 3D profilometer for recording of surface roughness of old painted/unpainted surfaces. The study was focused on the surface scattering property which directly affects the quality and strength of the reflected THz signal. The signal was recorded in the frequency range f = 0.5,1.0,1.5 and 2.0 THz respectively. The surface roughness profiles of an old painted and unpainted metallic objects lie between 15 μm-130 μm at given range of THz frequency and angle of incident of THz radiation. The contrast of image lies between 0.5-1.5 THz range possesses highest reflection coefficient for surface roughness less than 50 μm. We also explained the role of Q factor on the contrast of images.

4.7 Surface roughness effect on explosive materials:

The modulation of absorption and reflection characteristics by surface roughness significantly impacts the spectroscopic signatures of explosive substances. Within the domain of THz spectroscopy and imaging, particularly for applications in homeland security and defense, a comprehensive understanding of how surface roughness shapes the interaction with THz radiation is imperative. This understanding is critical for augmenting the capabilities of

explosives detection and identification. The distinctive fingerprint absorption spectra exhibited by various explosives, including RDX, TNT, PETN, HMX, NH_4NO_3, within the THz range, play a pivotal role in their unambiguous identification. Surface roughness introduces alterations in the reflective properties of materials, thereby influencing the strength and quality of signals obtained through THz techniques. This knowledge is fundamental for the optimization of detection methodologies, enhancing sensitivity, and minimizing the occurrence of false positives or negatives in security and defense applications

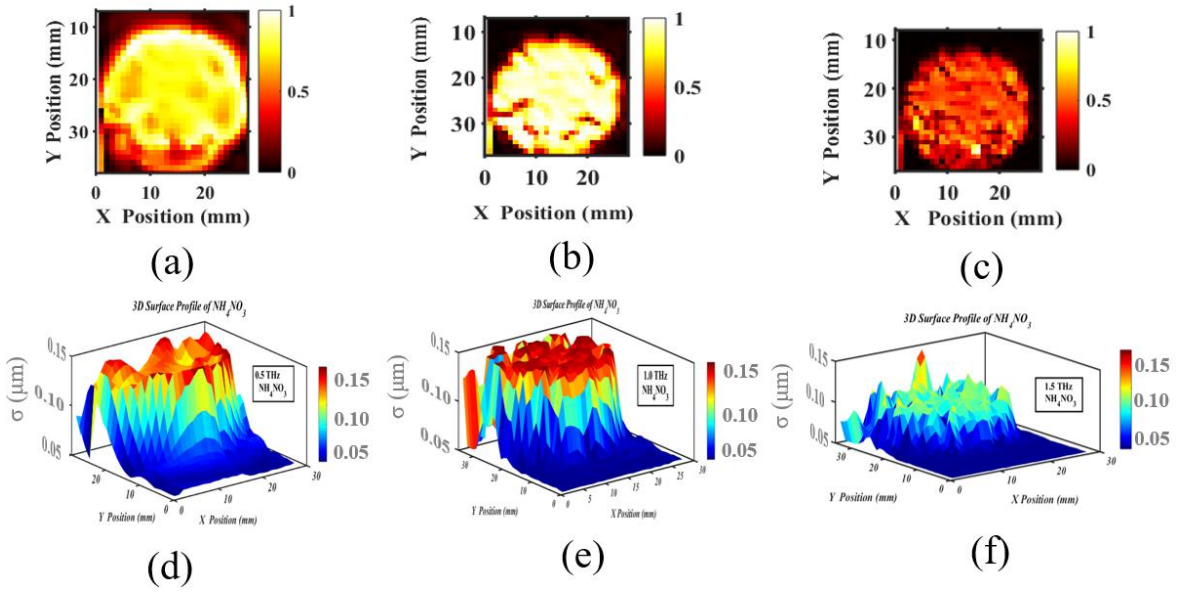

Figure 4.11: THz 2D imaging of NH_4NO_3 at frequencies (a) 0.5 THz, (b) 1.0 THz, and (c) 1.5 THz, with corresponding 3D surface profiles at (d) 0.5 THz, (e) 1.0 THz, and (f) 1.5 THz.

Figure 4.11 shows the 2D THz imaging of NH_4NO_3 at (a) 0.5 THz, (b) 1.0 THz, and (c) 1.5 THz, demonstrating its potential in defense and public security applications. The corresponding 3D surface profiles at these frequencies are shown in Figure 4.11 (d-f). THz imaging, using the peak-to-peak value of THz time-domain signals, is commonly used in non-destructive detection. For the identification of NH_4NO_3, we imaged the frequency domain data using its spectral amplitudes. Surface roughness plays a crucial role in identifying the quality and resolution of the sample. THz radiation offers higher spectral resolution than microwaves due to its shorter wavelength. The surface roughness of ammonium nitrate varies from 0.05 to 0.15 μm and differs at each frequency, such as 0.5, 1.0, and 1.5 THz. The relationship between surface roughness and effective reflectivity at different roughness values is shown in Figure 4.12 (a).

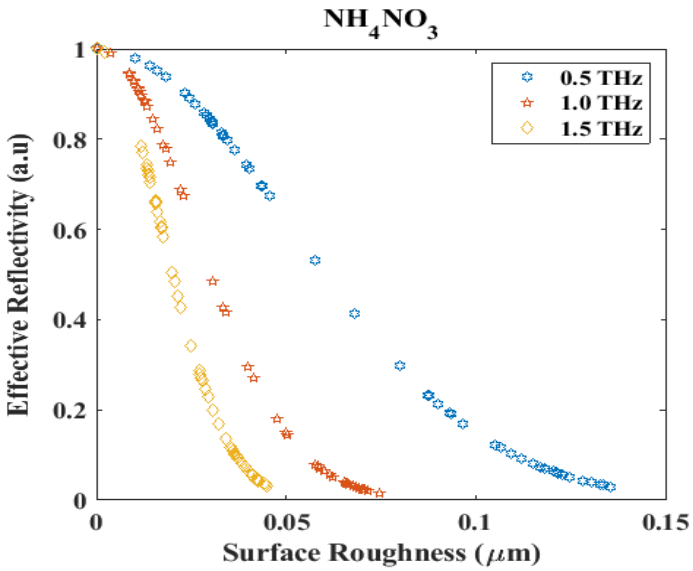

Figure.4.12 Surface roughness effect on NH_4NO_3

Figures 4.12(a) illustrate the surface roughness effects on hazardous materials NH_4NO_3. This graph represents the relationship between surface roughness and effective reflectivity for NH_4NO_3 (ammonium nitrate) at three terahertz frequencies: 0.5 THz, 1.0 THz, and 1.5 THz. The x-axis represents surface roughness in micrometers, while the y-axis shows effective reflectivity in arbitrary units (a.u). These graphs depict how the reflectivity at a fixed angle of incidence depends on frequency for surfaces with different levels of roughness for the high-energy materials. To the best of our knowledge, longer wavelengths are less affected by surface roughness, while shorter wavelengths are more impacted by it. This significantly influences the effective reflectivity of NH_4NO_3. At lower frequencies (0.5 THz), effective reflectivity is higher compared to higher frequencies (1.0 THz and 1.5 THz) for the same surface roughness. As surface roughness increases, effective reflectivity decreases across all three frequencies. The rate of decrease in reflectivity is steepest at 1.5 THz, indicating that reflectivity is more sensitive to surface roughness at higher frequencies. For smooth surfaces (Zero roughness), effective reflectivity is close to 1 for all frequencies. As surface roughness increases to about 0.05 µm, there is a noticeable drop in reflectivity for all frequencies, with the most significant drop observed at 1.5 THz. Beyond 0.05 µm roughness, reflectivity continues to decrease more gradually. NH_4NO_3 shows high reflectivity for smooth surfaces (low roughness) across all measured frequencies. As the surface becomes rougher, the scattering of THz waves increases, leading to a decrease in reflectivity, an effect that is more pronounced at higher frequencies. In this study, we found that surface roughness effects are influenced by the correlation length of the Gaussian surface of hazardous materials. We present a THz surface roughness-based

analytical model, demonstrating that reflection from surfaces with varying degrees of roughness results in a Gaussian frequency roll-off in the THz spectral amplitude, affecting the signal-to-noise ratio of THz TDS. The measurement of terahertz spectral amplitude reflected from the secondary high-energy materials NH_4NO_3 provides experimental evidence for the surface roughness effects. The graph suggests that THz reflectivity measurements can be used to infer the surface roughness of NH_4O_3. The sensitivity of reflectivity to surface roughness varies with frequency, providing a means to select appropriate THz frequencies for specific surface roughness detection needs. In the context of THz spectroscopy, understanding the impact of surface roughness on reflectivity is crucial for accurate material characterization. This is especially important for substances like ammonium nitrate, which are used in various applications, including homeland security for detecting explosives. The graph provides valuable insights into how THz waves interact with ammonium nitrate surfaces, demonstrating the potential of THz spectroscopy for non-destructive testing and material characterization.

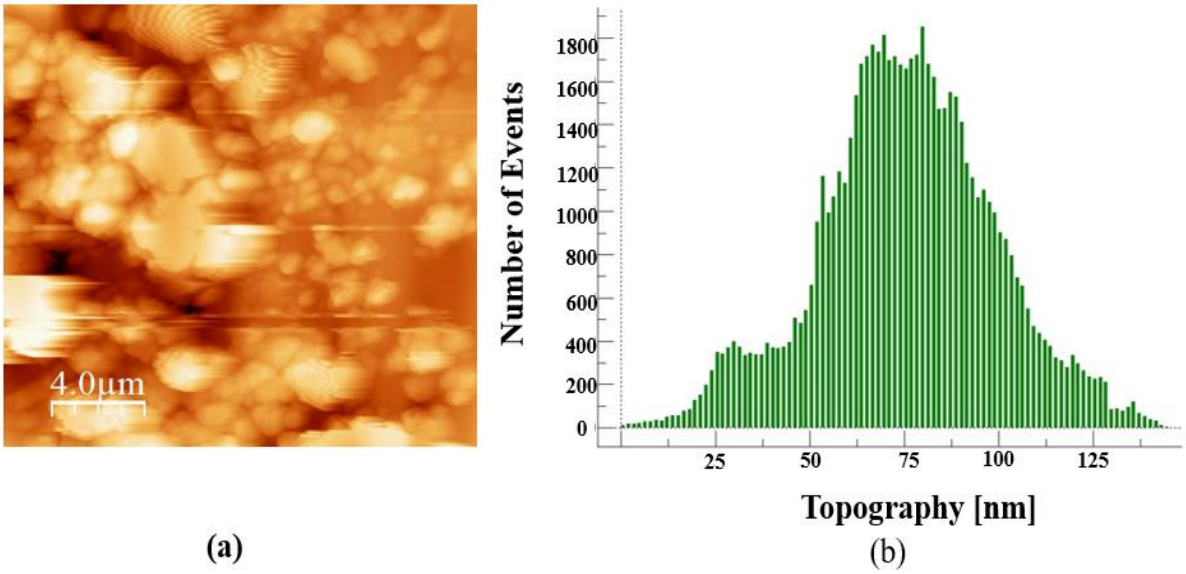

Figure.4.13 (a) AFM image (b) surface analysis of NH_4NO_3

Figure.4.13 (a) & (b) shows confirms that the surface roughness of those materials is equal to the measured THz profilometer values.

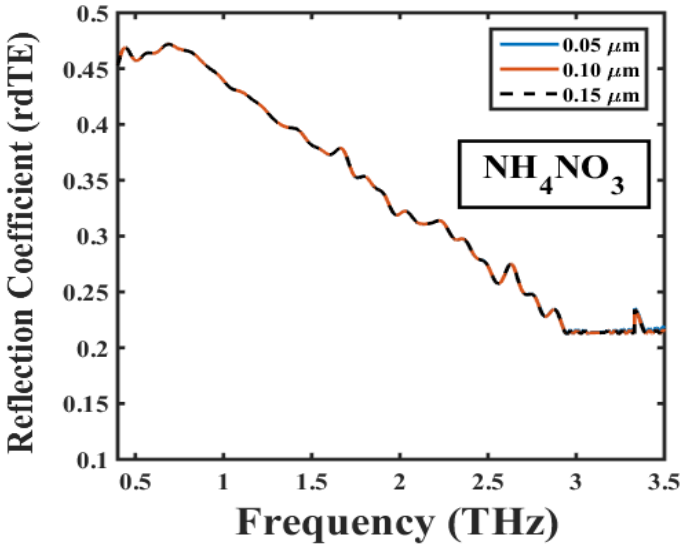

Figure.4.14 Reflection Coefficient of NH_4NO_3

Finally, we discussed the reflection coefficient of rough high-energy materials NH_4NO_3 at 4^0 angles of incidence, which we obtained from the reflectance of the samples and the reflectance of reference. We also verified Fresnel's approximations model. Acquiring data at 4^0 angles of incidence from both NH_4NO_3 increased the sample reflectivity and reduced the smearing of spectral signatures caused by surface roughness. Figures 4.14 display the reflection coefficients of ammonium nitrate in TE mode. The reflection graph of NH_4NO_3 exhibits an exponential delay. These reflection coefficient graphs confirm the deconvolution signal from NH_4NO_3.

4.8 Surface roughness effect on high energy fertilizer materials:

The examination of surface roughness effects on urea is propelled by the imperative to comprehend the influence of physical surface characteristics on the behavior and interactions of urea molecules. Surface roughness assumes a consequential role in shaping the adsorption, desorption, and diffusion processes of urea across diverse materials, a comprehension integral to applications in agriculture, material science, and environmental science. In the realm of agriculture, wherein urea serves as a ubiquitous fertilizer, the interplay between urea and soil surfaces is intricately influenced by surface roughness. A nuanced understanding of how surface roughness modulates the adsorption and release dynamics of urea from soil particles holds the potential to refine fertilizer application methodologies, optimizing nutrient assimilation by plants while mitigating environmental impact. Material science pursuits center on the adhesion of urea to surfaces, a facet pertinent to the development of coatings, membranes, and assorted materials. Surface roughness emerges as a determinant, influencing the binding affinity of urea molecules to diverse substrates and thereby dictating the

performance and durability of materials in manifold applications. In the domain of environmental science, the investigation into urea adsorption on surfaces assumes significance for elucidating nutrient cycling in natural systems. The surface roughness of particles within aqueous bodies or soil matrices can wield influence over the sorption capacity for urea, thereby affecting its bioavailability to microorganisms and plants. Furthermore, in the realm of biomedical research, the consideration of urea's interaction with biomaterial surfaces is paramount, especially in domains such as drug delivery and biomaterial design. Surface roughness exerts a discernible impact on the adsorption and release kinetics of urea in these applications, thereby influencing the overall efficacy and efficiency of the systems. The scientific exploration of surface roughness effects on urea seeks to unravel fundamental mechanisms governing these interactions. This newfound knowledge contributes substantively to the evolution of more efficacious and environmentally sustainable practices in agriculture, the progression of material design technologies, and a heightened comprehension of urea behavior across diverse scientific and industrial domains.

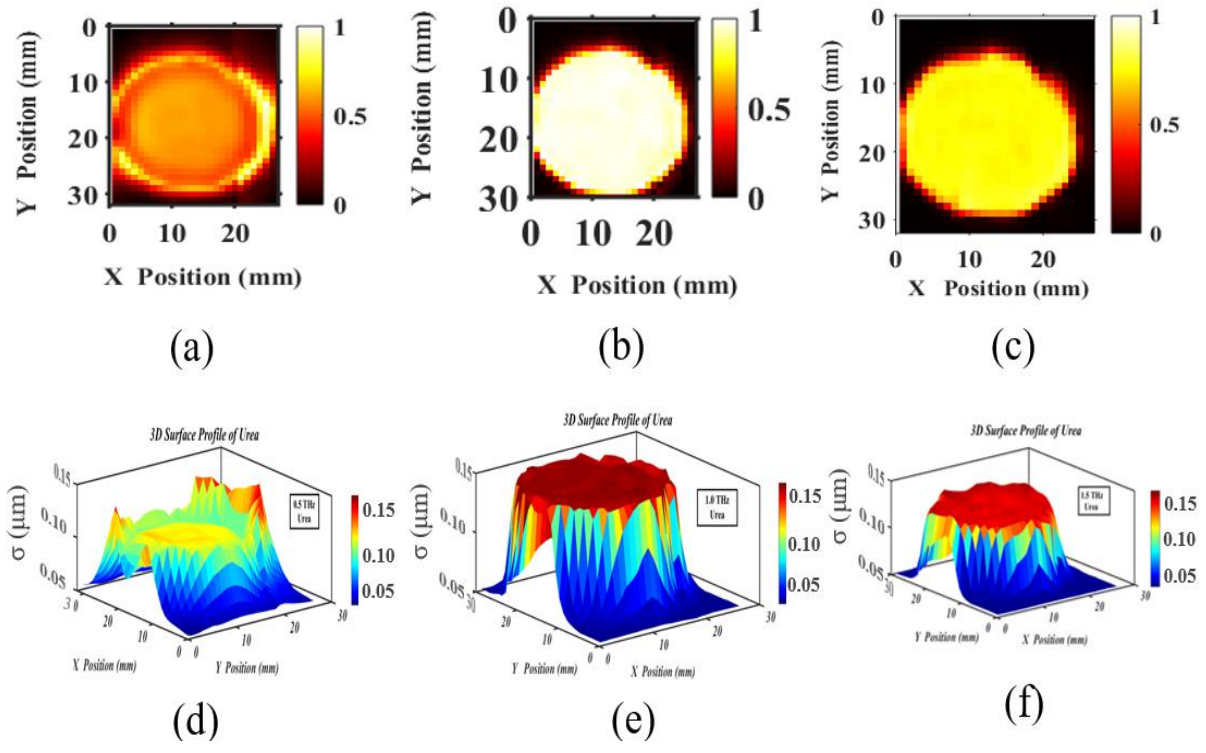

Figure.4.15 THz 2D imagining of Urea at (a) 0.5 THz (b) 1.0 THz (c) 1.5 THz corresponding the 3D Surface Profile at (d) 0.5 THz (e) 1.0 THz & (f) 1.5 THz

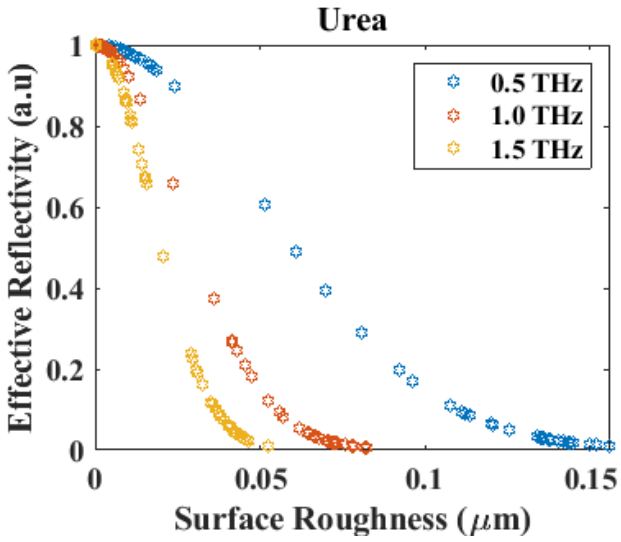

Figure.4.16 Surface roughness effect on Urea

Figure.4.16 illustrate the surface roughness effect on high energy fertiliser urea. The surface roughness of Urea varies between 0.05 µm to 0.15 µm which was match with the existing system AFM (Figure.4.17). The measurement of terahertz spectral amplitude reflected from the secondary high-energy materials Urea provides experimental evidence for the surface roughness effects.

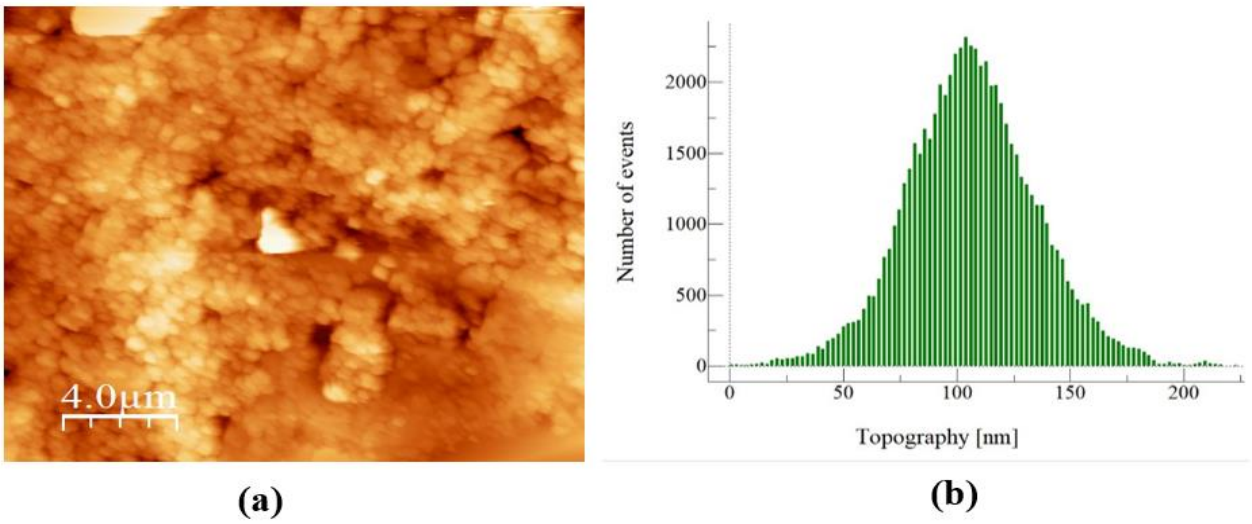

Figure.4.17 (a) AFM image (b) surface analysis of Urea

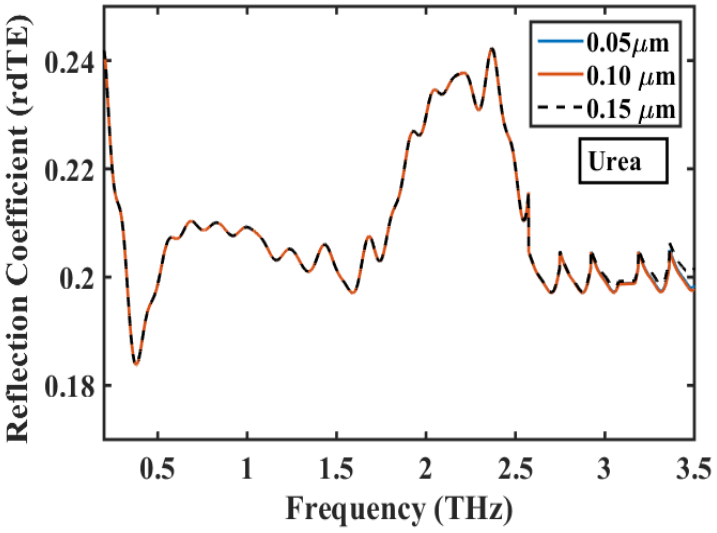

Figure.4.18 Reflection Coefficient of Urea in TE mode.

Finally, we discussed the reflection coefficient of rough high-energy materials urea at 4^0 angles of incidence, which we obtained from the reflectance spectra of the samples and the reflectance spectra of a smooth gold-coated mirror. We also verified Fresnel's approximations model. Acquiring data at 4^0 angles of incidence from urea increased the sample reflectivity and reduced the smearing of spectral signatures caused by surface roughness. Figures 4.18 display the reflection coefficients of urea in TE mode. The reflection graph of urea's graph shows an abrupt change in nature. These reflection coefficient graphs confirm the deconvolution signal from urea. We conducted THz 2D imaging of these high-energy materials, studied their THz-based 3D surface roughness, and examined reflection coefficients in TE mode using modified Fresnel's equations. These investigations reveal unique characteristics of the low THz reflected signal from various rough surfaces, which could have applications in automotive radar systems. Our research on NH_4NO_3 and urea serves as a valuable resource for understanding secondary high-energy materials. We believe that our experimental and theoretical work on these explosives and high-energy materials will pave the way for the development of stable high-energy optical materials with applications in defense (for detection purposes), public safety, homeland security, pyrotechnics, and optoelectronic devices. We have compared two well techniques with our innovation THz profilometer in the TABLE-4.2.

Table 4.2 Comparision of surface roughness of different types of materials using AFM, optical profilometer & THz profilometer

Sample Name	AFM Value	Optical Profilometer Value	THz Profilometer
Painted old metallic Object	-	100 µm	30-130 µm
Unpainted old metallic Object	-	120 µm	30-150 µm
RDX	0.05-0.4 µm	0.27 µm	0.1-0.3 µm
NH_4NO_3	0.025-0.13 µm	0.27 µm	0.05-0.15 µm
Urea	0.018-0.18 µm	0.25 µm	0.05-0.18 µm

Intentional Blank Page

Reference:

[1].Sherrington and E. H. Smith, Precis. Eng. **8**, 4, 79–87, (1986).

[2].Technical forum document, FEINPRUF Corp. West Germany, Beijing, (1988).

[3].WYKO Corp., "Non-contact Micro surface Measurement System", (1988).

[4].G. Makosch and B. Drollinger, ''Surface profile measurement with a scanning differential ac interferometer,'' Appl. Opt. **23**,24, 4544, (1984).

[5]. H. Long, Z. Zhang, and H. Tan, "The Polarization of Light and Its Applications", Mechanical Industrial Press, Beijing, China, (1989).

[6].J. Kokkoniemi, J. Lehtomaki, and M. Juntti, "Measurements on Penetration Loss in Terahertz Band, in 2016 10th European Conference on Antennas and Propagation", (EuCAP) (IEEE), 1–5, (2016).

[7].A. Jagannathan, "Effect of surface roughness on the scattering of terahertz waves from metals and dielectrics", (University of Massachusetts Lowell, 2010).

[8].A. Gerrard and J. M. Burch, "Introduction to Matrix Methods in Optics", Wiley (1975).

[9].M. Ortolani, J.S. Lee, U. Schade, and H.-W. Hübers, "Surface roughness effects on the terahertz reflectance of pure explosive materials", Appl. Phys. Lett. **93**, 81906, 1-3, (2008).

[10]. P. Beckmann and A. Spizz chino, "The scattering of electromagnetic waves from rough surfaces", Norwood (1987).

[11]. M. Naftaly, N. Vieweg, and A. Deninger, "Industrial Applications of Terahertz Sensing: State of Play", Sensors, **19**,4203, 1-35, (2019).

[12]. T. Fukuchi, N. Fuse, M. Mizuno, and K. Fukunaga, "Surface Roughness Measurement Using Terahertz Waves", in Proc. 3rd International Conference on Industrial Application Engineering, 294–299, (2015).

[13]. I. Cacciari and S. Siano, "Use of THz Reflectometry for Roughness Estimations of Archeological Metal Surfaces", Journal of Infrared, Millimeter, and Terahertz Waves, **38**, 503 (2017).

[14]. N. Fuse and K. Sugae, "Non-destructive terahertz imaging of alkali products in coated steels with cathodic disbanding", Progress in Organic Coatings, 137, 105334,1- 7, (2019).

[15]. M. Ortolani, J. Lee, U. Schade, and H.-W. Hu¨bers, "Surface roughness effects on the terahertz reflectance of pure explosive materials", Appl. Phys. Lett, **93**, 081906,1-4, (2008).

[16]. M. H. Arbab, A. Chen, E. I. Thorsos, D. P. Winebrenner, and L. M. Zurk, "Effect on surface scattering on time domain spectroscopy of chemicals, in Terahertz Technology and Applications", SPIE**, 6893**, 92–99, (2008).

[17]. Y. Dikmelik, J. B. Spicer, M. J. Fitch, and R. Osiander, "Effects of surface roughness on reflection spectra obtained by terahertz time-domain spectroscopy", Optics Letters, **31**, 3653-3655, (2006).

[18]. Y. Yu, Z. Zhang, T. Zhang, X. Zhao, Y. Chen, C. Cao, Y. Li, and K. Xu, "Effects of surface roughness on terahertz transmission spectra", Optical and Quantum Electronics, **52**, 1 (2020).

[19]. A. Jagannathan, A. J. Gatesman, and R. H. Giles, "Characterization of roughness parameters of metallic surfaces using terahertz reflection spectra" Optics Letters, **34**, 1927 (2009).

[20]. R. Piesieicz, C. Jansen, D. Mittleman, T. Kleine-Ostmann, M. Koch, and T. Kurner, "Scattering Analysis for the Modeling of THz Communication Systems", IEEE Transactions on Antennas and Propagation, **55**, 3002 (2007).

[21]. C. Depew and R. Weir, "Surface Roughness Determination by the Measurement of Reflectance", Applied Optics, **10**, 969-970, (1971).

[22]. J. Ma, R. Wang, R. Shrestha, W. Zhang, L. Moeller, and D. M. Mittleman, "Effects of surface roughness on terahertz wireless links", in AOPC 2019: Optoelectronic Devices and Inte- gration; and Terahertz Technology and Applications, SPIE, **11334**, 343–349, (2019).

[23]. N.P. Kumar, M. Nagaraju, K.V. Arjun, A.K. Razdan and A.K. Chaudhary, "Comparative study of real time Terahertz imaging of concealed metallic objects, drug, wood and TNT explosive in transmission/reflection modes using uncooled microbolometer and ultrafast pulsed terahertz imaging systems", **108**, IJP, 2023.

[24]. A. V. Kidavu, N. Nagaraju, G. Damarla, and A. K. Chaudhary, "Scattering Analysis of Explosive Materials mixed in Teflon Matrix in THz regime", 2019 Workshop on Recent Advances in Photonics (WRAP) (IEEE),1–3 (2019).

[25]. Chandan Ghorui, Kidavu V Arjun, P Naveen Kumar, Subhasis Das, Anil K Chaudhary, Yuri Andreev, "Comparative studies of terahertz-based optical properties in transmission/reflection modes of GaSe: S and measurement of its scattering losses due to surface roughness for efficient terahertz generation", IOP Phys. Scr. **98** 025508, 1-12, (2023).

[26]. T. Fukuchi, N. Fuse, M. Mizuno, and K. Fukunaga, "Surface roughness measurement using terahertz waves", in Proc. 3rd Int. Conf. Ind. Appl. Eng. pp. 294–299, (2015).

[27]. Y. Dikmelik, J.B. Spicer, M.J. Fitch, and R. Osiander, "Effects of surface roughness on reflection spectra obtained by terahertz time-domain spectroscopy", Opt. Lett. **31**, 3653-3655, (2006).

Intentional Blank Page

Chapter 5

5. Calibration of Silicon Germanium 0.3 THz horizontal radar system for homeland, defense and food processing applications:

Abstract

This chapter describes the calibration of a prototype THz horizontal radar system for several real-world applications such as classification of various metallic, explosive targets and food processing industry. In addition, an artificial intelligence model was developed for the assessment of the freshness of meat. We also explained the working principle of 0.3 THz SiGe bipolar junction-transistor- complementary-metal-oxide-semiconductor radar system. For the first time, we have made an attempt to explain the joule's effect on silicon micro lens which is responsible for excessive heating of the radar system. In additions, we have experimentally and theoretically verified the THz radar cross section (TRCS) of canonical objects. We have also classified the metallic and explosive targets using artificial intelligence-based machine learning tools

A part of the research work presented in this chapter has published in the following scientific peer reviewed journals, international conference proceeding & Indian Patent

a) ***Chandan Ghorui*** *and Anil Kumar Chaudhary, "Detection of real-time hidden metallic object using prototype THz radar system for public security and defense application" SPIE, DOI: 10.1117/12.3025308 (2024).*
b) *A. K. Chaudhary,* ***Chandan Ghorui*** *and Tejas Kannampuzha "Artificial Intelligence coupled Tera Sensor for non-contact Meat Freshness Tester", Indian Patent, Provisional accepted by R & D office, University of Hyderabad.*
c) ***Chandan Ghorui,*** *Anil Kumar Chaudhary, "Study of 300 GHz Silicon Radar based Cross-Sections of Canonical Objects using Integrating Physical Optics and Numerical Simulation Techniques for Security Applications",* ***(Communicated).***
d) ***Chandan Ghorui****, Tejas Kannampuzha, Anil Kumar Chaudhary, "AI based Identification of different types of Explosives and Metals in Concealed and Non-Concealed Conditions Using a 0.3 THz Radar System for Defense Applications,"* ***(Communicated)***

5.1 Introduction:

RADAR stands for “Radio Detection and Ranging”. This technique makes the use of radio waves to find and identify distanced targets. Radar systems are extensively employed in different types of field applications, such as meteorological observation, air traffic management, military operations, maritime navigation, and vehicle safety. It can operate in different frequency bands from very low-frequency radar used for long-range detection to high frequency radar used for short-range precise measurements. In weather monitoring, radar can detect precipitation such as rain, snow and hail and track its movement to provide information about storms and movement of aircraft to ensure safe and efficient air travel [1,2]. THz radar offers unique capabilities (such as high resolution, non-ionising radiation, low atmospheric attenuation, penetration ability, high data rate and high imaging capabilities) that make it promising for various applications, especially in the fields where conventional radar and imaging technologies face limitations. Traditional radar systems operate in the radio frequency (RF) range between a few megahertz (MHz) to several gigahertz (GHz). While THz radar offers these unique capabilities, it also comes with some challenges. Terahertz waves are more easily absorbed by atmosphere and are subjected to scattering, limiting their range and effectiveness for long-range applications compared to RF radar. Efe Öztürk et al., measured the velocity and range of metallic object upto 30 m distance using SiGe based 60 and 122 GHz radar source [3]. Most recently, Steffen Scherr et al. achieved micrometer-level accuracy over varying distances using a 122 GHz frequency-modulated continuous wave (FMCW) radar source with a 1 GHz bandwidth [4]. Akansha Bhutani et al. focused on measuring the distance of both standard and complex targets within a short range of a few meters, emphasizing the role of target choice and the medium for radar signal propagation in determining distance measurement accuracy when using 24, 61, 80 and 122 GHz FMCW radar sensors [5].

To the best our knowledge 0.3 THz silicon radar system is a part of an emerging technology that hold promise for various applications. Silicon based radar systems operating at terahertz frequencies have the potential to offer a cost-effective solution for high frequency radar applications. The use of 0.3 THz radar, has several potential applications in real life. Its high frequency allows for precise spatial resolution, making it suitable for detecting and imaging small objects. Silicon based radar at terahertz frequencies can be employed in advanced driver-assistance system (ADAS) to enhance automotive safety. It could improve collision detection

and avoidance, especially in urban environments where higher spatial resolution is crucial. A millimeter-wave antenna integrated into a wire bond chip assembly package utilizing low-temperature co-fired ceramic (LTCC) technology is one documented approach [6]. LTCC technology boasts numerous advantages, including high integration capability for passive devices and cost-effectiveness, rendering it well-suited for high-volume production. While a sub-THz antenna integrated in LTCC has been reported, ongoing efforts are directed towards developing a low-loss, wideband monolithic microwave integrated circuit (MMIC)-to-antenna interconnection [7]. Consequently, an on-chip antenna solution currently stands out as one of the optimal choices for a THz transceiver, accompanied by a silicon (Si) lens antenna to mitigate surface wave excitation. This approach aims to maximize radiation efficiency, antenna gain, and bandwidth [8]. Furthermore, the removal of connectivity loss, which may be accomplished using techniques like wire connecting the antenna to the transceiver integrated circuits, makes an on-chip antenna with a Silicon lens a feasible choice. This reduces waste and makes the production process easier, which improves module performance in the end. The demonstration of an amplitude shift keying (ASK) receiver MMIC for wireless communications at 300 GHz is one recent development [9].

5.2. FMCW (frequency-modulated continuous wave) radar operating principles

In FMCW radar, a continuous radio frequency (RF) signal is transmitted from the radar antenna. However, this signal is not a constant frequency; instead, it continuously changes its frequency over time. This modulation typically occurs in a linear or ramp-like fashion, where the frequency gradually increases or decreases over a specified period. The modulated RF signal is emitted from the radar antenna and propagates through space. As it travels, it encounters objects in its path. When the RF signal strikes an object, a portion of it is reflected back towards the radar antenna. This reflected signal, or echo, contains valuable information about the distance and relative velocity of the object. The key principle behind FMCW radar is the doppler effect. This phenomenon causes a shift in frequency between the transmitted and received signals when they bounce off a moving object. The amount of frequency shift is directly proportional to the velocity of the object along the radar line of sight. By measuring this frequency shift, FMCW radar can determine the speed of the objects. FMCW radar offers several advantages, including its ability to provide both distance and velocity information simultaneously, its precision in measuring stationary and moving objects, and its resistance to interference from other radar systems. These qualities make it well-suited for various safety and monitoring applications.

5.3 Design and performance of fully integrated 122 and 60 GHz SiGe transceiver for industrial radar applications:

Here we will discuss in detail the design and characteristics of a differentially-coupled receiver and transmitter front end module that is tuned to be used in a 120 GHz phased array transceiver suitable for FMCW radar applications. SiGe bipolar junction-transistor-complementary-metal-oxide-semiconductor (BiCMOS) are advanced version of metal oxide semiconductor field effect transistor (MOSFET). SiGe BiCMOS transmitter, integration with other electronic components (such as baseband processing and power management circuits) is possible due to the inherent advantages of BiCMOS technology, which combines the high-speed performance of bipolar transistors with the low power consumption and integration density of CMOS. The modified device enables us to control the dark current, high change mobility and low threshold voltage. It can be used in fabricating nanoscale electronic which operates beyond the scientist Morris Tanenbaum prediction. This act as a base module for 300 GHz. The modules take advantage of advanced 0.13 μm SiGe bipolar junction-transistor-complementary-metal-oxide-semiconductor (BiCMOS) technology providing considerable frequency performance characteristics having f_T/f_{max}=250/340 GHz. The receiver (R_X) channel, a Gilbert-cell based vector modulator type I/Q phase shifter in combination with low-noise amplifier (LNA) is integrated that provides an outstanding 15 dB peak gain over a wide bandwidth of 14 GHz [3,5 10]. The transmitter (Tx) generates a very high frequency 0.3 THz signal. Since this signal is relatively weak and requires amplification to be effectively transmitted over a distance. SiGe BiCMOS technology allows for efficient amplification at these high frequencies, leveraging the high-speed capabilities of SiGe transistors. Tx modulated the signal with an information, depending on the different types of application. Modulation schemes such as amplitude, frequency, or phase modulation, among others, to encode data onto the 300 GHz carrier wave. The signal generation starts with an external phase-locked loop **(**PLL**)**, which controls a voltage-controlled oscillator (VCO). The VCO generates a signal at 60 GHz, which can be fine-tuned (V_{fine}) and coarsely adjusted (Vcoarse) based on inputs from the PLL. This 60 GHz signal is doubled to produce a 120 GHz signal. The 120 GHz signal is likely fed into a frequency multiplier or is directly doubled to achieve a 240 GHz signal. The 120 GHz signal combined with a secondary signal to achieve the desired transmission frequency. It is amplified using a power amplifier (PA). A power detector is monitoring the output signal power to ensure the correct transmission power level. The amplified 120 GHz signal (or a higher frequency if multiplied) is fed into the transmitting (Tx)

antenna for transmitted the signal. The incoming signal is received by the receiving antenna (Rx). Since, the received signal is very weak, so it first passes through a low-noise amplifier (LNA), which amplifies the signal while adding minimal noise. The amplified signal is down converted to a lower intermediate frequency (IF) using mixers. A 90^0-phase shifter is used in conjunction with the local oscillator to provide the necessary phase shift for accurate demodulation. The down converted signal at IF is processed in the baseband section, where it undergoes further filtering, amplification, and demodulation to extract the original transmitted data. This baseband helps to convert digital signal to the analog signal. In this technology provides constant 360^0 phase shifting ability for fully differential core front-ends and requires the total area no more than 0.4 mm × 0.25 mm which enables their perfect functionality in phased array radars integration process. However, as the demand for phased array transceivers working on frequencies of millimeter-waves have been a growing need in applications that comprise avionics and military, these arrays are used by different sectors like civil application due to their ability at providing high-rate and high-resolution radar data communication. The development of cost-effective, highly integrated, and high-performance designs would provide an accessible route towards meeting the requirements of a changing market. Therefore, for these reasons advancement in silicon technology supplemented with allocation of high bandwidth has developed direction for satisfying market requirements. Although this paper does not directly deal with a design, it aims at formulating an efficient scheme for addressing the considerations related to low-cost SiGe BiCMOS receiver and transmitter modules dedicated for phased array radars where channel integration would be important [10]. A two-stage cascode topology is one of the two unique elements of the LNA design that were selected due to its high gain and low noise figure characteristics. This is because differential architecture has a number of advantageous features, such as wire bond strength, low execution cost, predictive elimination of even order harmonic, and common mode noise rejection. Circuit design and subsystem trade-off decisions, pink-blue separation, system bandwidth options are some of the key aspects that should be considered when designing a phased array system in order to effectively address or mitigate complexities, limitations as well as ensure robust performance under real world applications. As for the related SiGe BiCMOS phased arrays, it deals with transceivers that also demonstrate an extraordinary result in terms of characteristics both in the form of impressive performance metrics like high gain, wide bandwidth, low losses etc and based on their size to be thoughtfully designed as ultra-compact modules. These modules, with their potential for convenient insertion into the so-called phased array radar

systems clear a path towards creating radars of high capability and complex performance usable in various commercial as well as military areas.

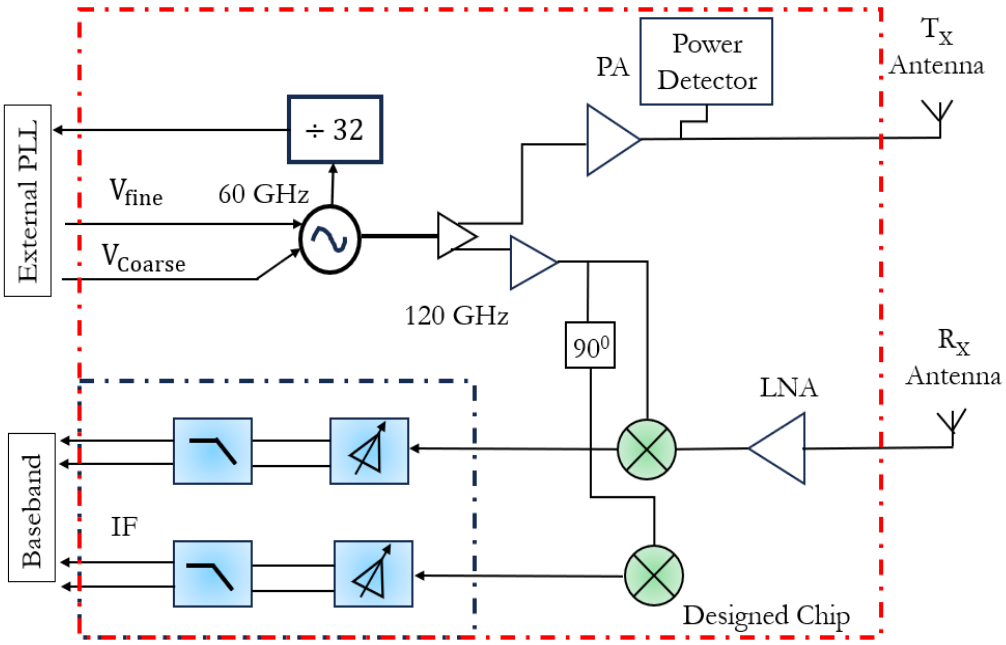

Figure 5.1 Block diagram of a single-channel, bistatic TRx chip for 122-GHz radar operation (PLL-Phase Locked Loop, TRx-Transceiver)

A schematic illustration of a flexible single-channel TRx system is shown in Figure 5.1. The receiver (Rx) is outfitted with a passive power splitter to split the amplified signal into two parts. These signals supply the in-phase and quadrature (I/Q) mixer cores from the transconductance stages. In addition, a low-noise amplifier (LNA) is used to improve the incoming signal with the least amount of noise. Before the I/Q signals are sent to the switching stages, they travel through one more passive structure for additional processing. In addition to removing picture frequencies, this I/Q processing enhances intermediate frequency (IF) gain and makes phase data easier to obtain. Variable-gain amplifiers (VGAs) in succession and filters are used both internally and externally to handle the I/Q differential IF outputs. A voltage-controlled oscillator (VCO) with center frequencies of either 60 or 122 GHz operates within the necessary frequency range in the transmitter (Tx) portion. The desired center frequencies are obtained by internally multiplying the 30 and 61 GHz that the circuit cores supply, respectively. Depending on the chip architecture, a power amplifier (PA) is integrated into the VCO, at least during the driving stage, to guarantee adequate output power. A frequency-tuning mechanism is integrated for external phase-locked-loop (PLL) operation,

offering multi-bit capabilities for fine- and coarse-sweep choices. This is usually achieved using a series of parallel variable capacitors in the VCO core. Furthermore, for the 60 and 122 GHz TRx systems, an integrated frequency divider with a ratio of 32 produces an output of roughly 1-2 GHz [4-5]. The Tx channel is linked to the main PA for additional power amplification, and the VCO output is shared between the Rx and Tx channels. As an integrated self-test function, power detectors can be installed at the PA output as needed to check output power. By combining the Tx and Rx channels for monostatic operation, this bistatic TRx design can be set up for a single antenna output. Alternatively, by modifying the VCO division circuitry, it can be configured for multiple channel outputs for phased-array radar (PAR) or multiple-input/multiple-output (MIMO) applications [5,7]. Every configuration has unique benefits and drawbacks. Bistatic radars operate effectively up to many tens of meters at high frequencies with good precision and resolution, despite these difficulties. One possible solution to lessen the disadvantages of the bistatic setup is to use a monostatic strategy (see Figures 5.2 and 5.3). By sharing an antenna, this arrangement avoids coupling between distinct antenna structures for the Tx and Rx channels. However, this configuration creates a direct link between channels, which could exacerbate leakage if there are manufacturing flaws or undetected effects from inadequate electromagnetic modelling in simulations. The transmitted power through the radiating elements is also decreased by integrating a high-isolation power-combining structure at the front end, which also introduces noise to the Rx channel, reduces conversion gain, and adds additional loss to the Tx channel. The monostatic technique has major benefits despite these drawbacks. Because of its adaptable antenna design, fabrication costs can be minimized by either constructing larger antenna elements for stronger antenna directivity or by using a single antenna to reduce chip size. Additionally, because of its adaptability, the antenna radiation pattern can be optimized for various uses [3].

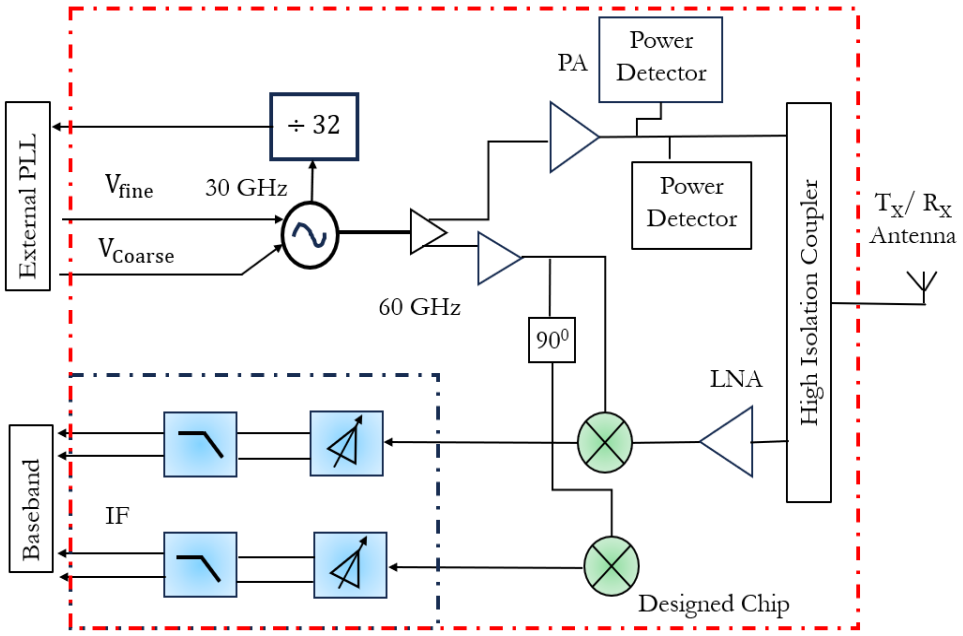

Figure 5.2 Block diagram of a single-channel, monostatic TRx chip, for 60-GHz operation.

The transceiver is package using new eWLBs (embedded Wafer Level Ball Grid Array) technology that enables multiplexed chip components of newer products several wires and package T_X/R_X module direct embedding two dipole antennas into the package. However, after this thorough assessment in an FMCW setup, the transceiver can show satisfactory performance. These comprise a broader range of tuning and high efficiency, exhibiting an output power as much as 3 dBm at a base level consumption of less than 1.0 W. Infineon's low-cost, high-performance silicon germanium Bi micro pdp B7HF200 technology is used in fabrication of the transceiver chip to ensure effective mass production and RF performance capabilities. The team of eWLBs packaging technology is a compact and low-cost solution that it allows integration passive devices as well as antennas straight into the package. The structural diagram of a transceiver consists of fundamental building elements like a colpitts voltage-controlled oscillator (VCO), amplifiers, vector modulation, and an IQ receiver.

Importantly, in respect to the VCO core, it possesses a significant tuning slope and negligible phase noise translating to very precise frequency generation throughputs in the ISM band. Additionally, both the vector modulator and IQ receiver deliver excellent performance data in terms of standard output power and minimum noise figures. Dipole antennas are integrated directly to the package leading to an increase in system efficiency also reduces on costs. In summary, the fully integrated 60 GHz SiGe transceiver within eWLB packaged technology provides an attractive solution for industrial radar systems that run on ISM band at a 60 GHz

which offers exceptional performance in terms of its compactness and cost-effective side [10-11].

5.4 Calibration & performance evaluation of 300 GHz (0.3 THz) FMCW radar source

To attain micrometer resolution accuracy, a frequency-modulated continuous wave (FMCW) radar system that is downsized in the 300 GHz industrial, scientific, and medical (ISM) band is utilized. Liquid crystal polymer (LCP) off-chip antennas and a SiGe single-chip radar sensor make up this radar system. An integrated quad flat no lead (QFN) package is house these antennas. Figure 5.3 displays the schematic block diagram of the single channel, monostatic TRx device for a 300 GHz radar source. An external phase-locked loop (PLL) controls a voltage-controlled oscillator (VCO). The VCO generates a 150 GHz signal, which can be fine-tuned with V_{fine} and coarsely adjusted with V_{coarse}. The generated 150 GHz signal is frequency multiplied by a factor of 2 to produce a 300 GHz signal. This signal is passed through a power amplifier (PA) to boost its strength, making it suitable for transmission.

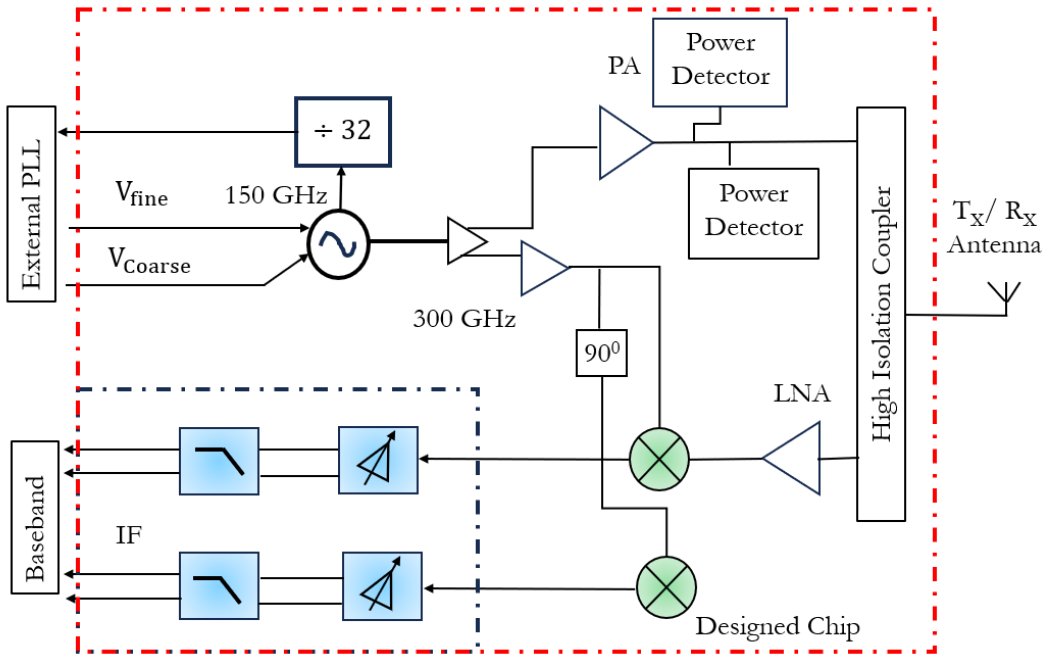

Figure 5.3 Block diagram of a single channel, monostatic TRx chip, for 300 GHz (0.3 THz) operation.

Power detectors are monitoring the output signal to ensure it meets the required power levels before transmission. The amplified 300 GHz signal is fed into a high isolation coupler, which directs the signal to the T_X/R_X Antenna for transmission. This component also helps to isolate the transmitted signal from the received signal, ensuring minimal interference between the two. The incoming 300 GHz signal is received by the T_X/R_X Antenna and directed through the high

isolation coupler to the LNA. The LNA boosts the weak incoming THz signal with minimal added noise. The amplified 0.3 THz signal is then mixed with a local oscillator signal, passed through a 90-degree phase shifter, to down convert the signal to a lower Intermediate Frequency (IF). The down converted IF signal is then processed in the baseband section. Here, the signal undergoes filtering, further amplification, and possibly demodulation to extract the transmitted data. It converts the digital signal to analog signal. To enhance the radar gain, an additional dielectric lens is utilized. The radar sensor, known as the 'Evalkit SiRad Simple Easy 0.3 THz,' is a compact board measuring 40 × 40 mm, The chip itself is visible as a black square, with dimensions of 2 × 2 mm. The T_X/R_X antennas are already integrated into the chip. Each antenna features four patch elements and is manufactured on a separate ceramic substrate, which can be placed directly onto the silicon IC. This integration enables the creation of extremely fine structures down to a few microns in size. These high-performance integrated antenna structures are suitable for frequencies up to the THz range. The antennas are directly connected to the IC structures, ensuring maximum efficiency and making them suitable for designs ranging from 60 GHz to 0.3THz, with high bandwidth capabilities.

5.4.1 Antenna working mechanism and Joule heat effect on silicon microlens antenna:

The system, antenna(s), and packaging must be given top priority by designers because, in addition to the chip itself, all of these components have a substantial impact on the finished product. For example, if high-frequency wire bond connections are undesired, incorporating the antenna on-chip can be advantageous, leading to a wide-band response with good input matching [12, 13]. However, on-chip antennas have limitations, including restricted directivity, negative packaging effects, and increased fabrication costs, especially when more channels or antennas are needed. Although it incurs additional costs, localized backside etching can be utilized to improve directivity. On the other hand, onboard antennas provide more size freedom. They can be made with higher directivity, cheaper production costs, and thinner, sharper beams [14]. Subsequently, the chip can be conveniently packed using the quad flat no-lead (QFN) standard packaging. Nevertheless, this calls for wire bond interfaces to antenna inputs, which adds to the radiation path's losses and calls for compensating networks [15]. This can limit measuring capabilities by reducing transferred power and necessitating precise wire bond lengths. With precise simulation models, both antenna designs may be appropriate for a given system and application. Because molding and shielding materials affect antenna and chip performance, proper packaging is essential. It may occasionally be essential to use technologies

such as embedded wafer level ball grid array (eWLBs) or a modified QFN with open tops above the antennas [12,16,17]. Antenna integration in high-frequency devices (particularly above 60 GHz) might be challenging, despite the cost-effectiveness and dependability of QFN packaging [12, 18–20]. The complexity and cost of producing the PCB rise when an onboard antenna constructed on high-frequency laminates or an in-package antenna wire attached to the chip using high-precision printing is needed. Short wire bond lengths can introduce significant inductance, disrupting antenna performance. Placing the IC in a cavity onboard can reduce wire bond lengths but requires high precision to avoid deteriorating performance. By connecting antennas on high-frequency materials with solder balls instead of wire connections, flip-chip packaging lowers inductance [21–27]. Wire bonding the integrated circuit (IC) within the package or designing the IC with pads for direct ball contact are the two methods available for IC-to-board interconnects. Since the substrate of a flip-chip BGA does not come into contact with the package, heat transfer problems may arise if the IC uses a lot of power. Adding more pads may improve the package's point of contact. With additional connecting layers that enable accurate antenna designs and flexible fan-out, the eWLB packaging technique has advantages. The package is attached onto a PCB, which acts as an antenna reflector, at a height defined by the ball size that can be changed for the best antenna performance [20,28–30].

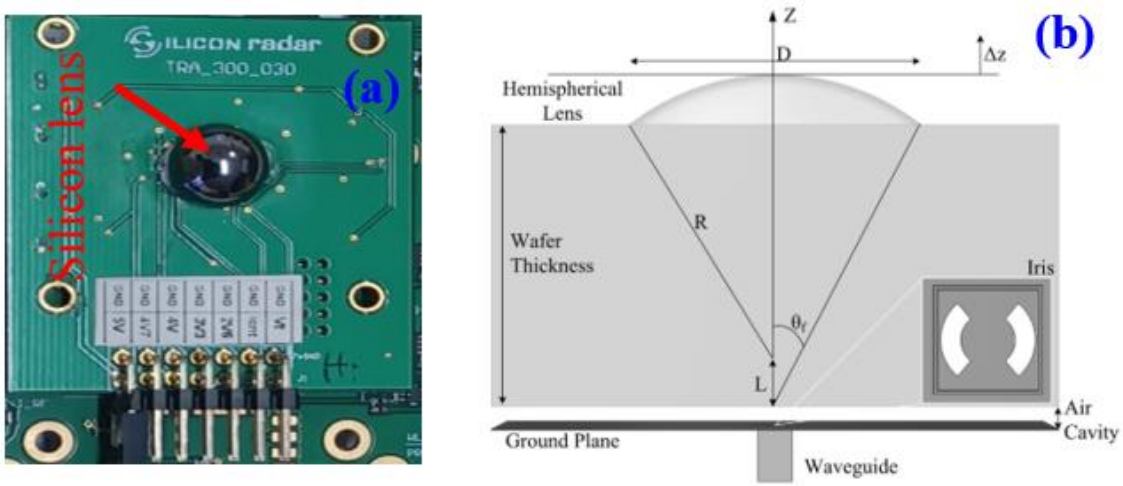

Figure 5.4 (a) Photograph of Silicon microlens antenna (b) Geometry of Silicon microlens antenna copywrite [31]

The working principle of a silicon microlens antenna involves integrating a microlens with an antenna structure to enhance performance at millimeter-wave and terahertz (THz) frequencies. Silicon is chosen for its excellent dielectric properties at high frequencies and compatibility

with standard semiconductor fabrication techniques. The microlens is typically fabricated using lithography and etching methods common in semiconductor manufacturing, while the antenna is either fabricated directly on the same substrate or assembled nearby using precise alignment techniques [31]. The microlens focuses THz waves onto the antenna, improving gain and directivity. It collects and concentrates incoming waves onto the antenna or efficiently radiates waves from the antenna. The antenna, which can be a dipole, patch, or other suitable structure, is integrated near the microlens's focal point for optimal focusing. Incoming THz waves strike the microlens, which focuses them onto the antenna, increasing its effective aperture and ability to receive weak signals from specific directions. When the THz wave is transmitted, the microlens collimates the emitted THz waves, reducing beam divergence, resulting in a more directional beam with higher gain and improved transmission efficiency. This increased gain makes the antenna more sensitive to incoming signals, enhancing the signal-to-noise ratio. The microlens also improves beam directivity, reducing interference from unwanted directions. Integrating the microlens with the antenna results in a compact and efficient design, suitable for miniaturized and integrated circuit applications. Silicon, exhibits thermal expansion ($\alpha = 2.6\times10^{-6}\ K^{-1}$) in response to changes in temperature. This expansion has the potential to impact the dimensions and shape of the lens, thereby potentially modifying its performance. Additionally, the dielectric properties of silicon are subject to temperature dependence, and fluctuations in temperature may consequently influence the refractive index of silicon, thereby affecting the overall performance of the lens antenna. It is imperative for silicon lenses to maintain performance stability under varying temperatures. Exposure to high temperatures can result in material degradation or other alterations that may impact the functionality of the antenna. A comprehensive understanding of how temperature affects the electromagnetic properties of silicon is crucial in the design of antennas to ensure effective operation across different temperature ranges

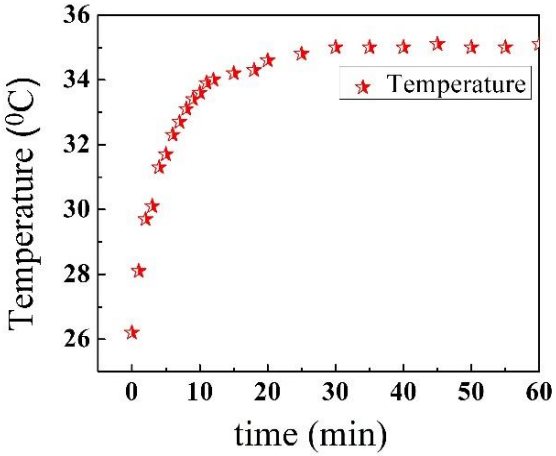

Figure 5.5. Silicon lens affected by varying temperature

Figure 5.5 displays the temperature effect curve for a silicon lens from a silicon radar system over a period of 60 minutes. Initially, the temperature increases rapidly from approximately 26°C at 0 minutes to around 33°C by around 10 minutes. The rapid increase in temperature at the beginning indicates that the silicon lens heats up quickly when the system starts. This could be due to initial power-up or exposure to an external heat source. After the initial rise, the temperature continues to increase but at a slower rate, reaching a plateau around 34°C to 35°C. After reaching around 34°C, the temperature rise slows down and stabilizes, indicating that the lens has reached thermal equilibrium with its surroundings. From approximately 20 minutes onwards, the temperature stabilizes and remains relatively constant between 34°C and 35°C for the rest of the duration up to 60 minutes. The consistent temperature between 34°C and 35°C from 20 minutes onwards suggests that the system maintains a steady operating temperature under continuous operation.

5.5 Physical optical methods for measuring radar cross section (RCS) of two canonical objects

The physical optics (PO) method is widely employed to analyze and predict the scattering behavior of complex canonical objects or targets [32-33]. This approach offers a high level of accuracy and reliability in forecasting the target radar cross section (TRCS) of objects. Unlike simpler approximation methods, the PO method generates more realistic TRCS by simulating the physical mechanisms involved in radar scattering. It accounts for both specular and diffuse reflections, thereby capturing the complex interaction between electromagnetic waves and the target's surface. The PO method is particularly well-suited for analyzing the TRCS of complex objects with large and curved surfaces of aircraft, ships, vehicles, or

structures [34-35]. These objects often exhibit intricate scattering behavior that cannot be accurately modelled using simple geometric shapes. Engineers use the PO method to assess and enhance the radar signatures of objects, improving their detectability or stealthiness. Engineers can use TRCS analysis to pinpoint areas for improvement, reducing a target's radar reflection and enhancing its radar stealth. In essence, PO methods provide a potent and adaptable tool for scrutinizing and comprehending the radar scattering behavior of complex canonical objects. To find the applications in electromagnetic compatibility testing, advanced technology development, and the design, analysis, and optimization of radar systems. The TRCS involves the scale where the polarization, relative direction to the target being measured as well as other major factors come in play various factors include the reflection of heat, incident energy, and target material coating, and these vary depending on the aspect, azimuth, tilt, and elevation angles of incident THz rays. We used 0.3 THz Silicon components in the making of our controller. Silicon Germanium radar (SiGe) at a few different distances in order to confirm experimentally the simulated results. data. Along that, we have created analytical MATLAB based approach for 0.3 THz SiGe source defining the characteristics of various angular objects like circular plates of different kinds. Finite-length cylindrical and elliptical targets of carrying out effective machine learning tasks.

A. circular flat plate:

We have considered a flat circular plate of radius r placed in the x-y plane. Centre of the disc is located at the origin as shown in Figure.5.6. Due to circular symmetry, the backscattered RCS depends on θ, i.e., in the x-y plane, and does not depend on the elevation angle ϕ. The cross section of circular flat plate is given by equation (5.1)

$$\sigma = \frac{2\pi^3 r^4}{\lambda^2} \tag{5.1}$$

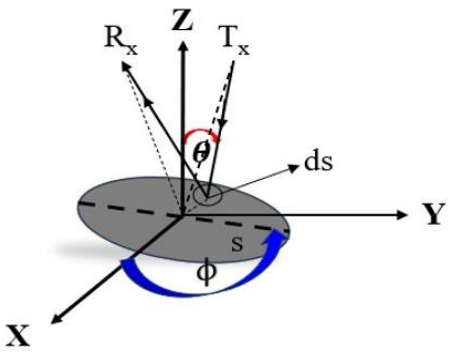

Figure.5.6 Circular flat plate and radar position

For a radius of r = 40 cm, the RCS return of a circular flat plate is displayed in the frequency range of 0.1 to 2.0 THz. The RCS of a flat plate changes with both frequency and radius. Therefore, the extremely variable goal is represented by the circular flat plate. For the physical optics model, the RCS is highest at 1.0 THz with respect to an aspect angle ranging from 0^0 to 180^0.The TRCS is smallest at an aspect angle of 90^0, but for non-normal incidence, equations (5.2) and (5.3) provide two estimates for the circular flat plate backscattered TRCS for any linearly polarized incidence wave.

$$\sigma = \frac{\lambda r}{8\pi \sin\theta tan^2\theta} \tag{5.2}$$

$$\sigma = 4\pi k^2 a^4 \left[\frac{J_1(2rksin\theta)}{2rksin\theta}\right] cos^2\theta \tag{5.3}$$

Here, $k = \frac{2\pi}{\lambda}$ and J_1 is the spherical Bessel function of the first order one. The back scattered terahertz TRCS corresponding to equation (5.2) and equation (5.3) for r = 40 cm and a frequency range between 0.1-0.6 THz.

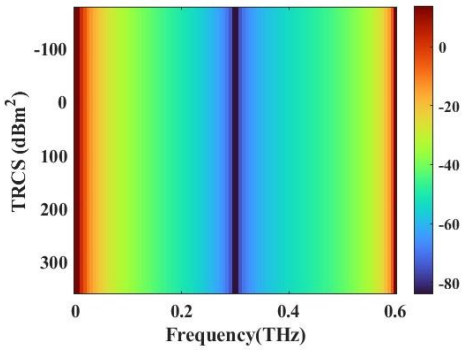

Figure.5.7 Radar cross-section simulation for circular flat plate

Figure.5.7 shows that the RCS simulation for circular flat plate with respect to the THz frequency gives the maximum value at 0.1 THz and 0.6 THz whereas it is minimum at 0.3 THz. The amount of radar energy that a target scatters back toward the radar system is known as the backscattered THz radar cross section, or TRCS. It gauges how well an object reflects radar signals. The size, shape, composition, and incidence angle of the radar signal are some of the variables that affect the TRCS. The capacity of a circular flat plate to reflect radar waves back towards the THz radar system is measured by its TRCS.

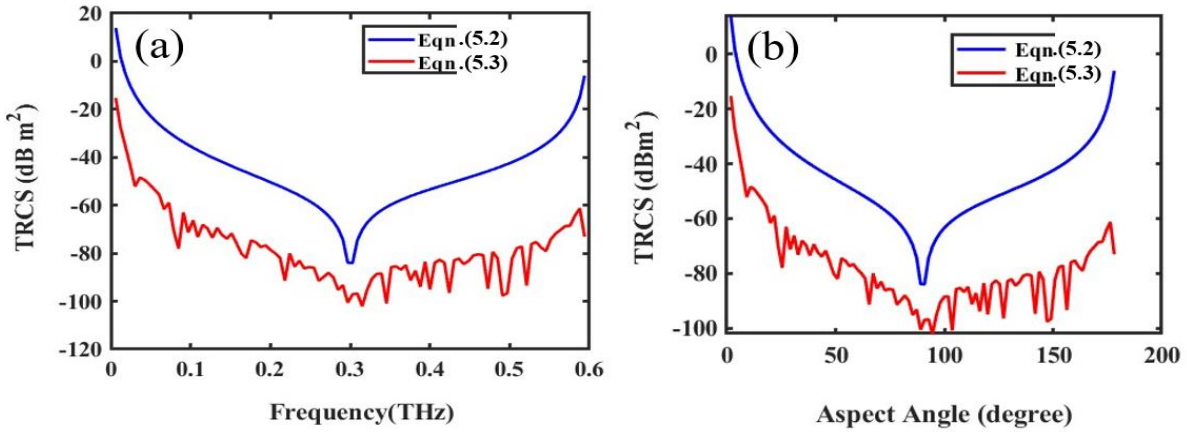

Figure.5.8 Back scattered TRCS for a flat circular plate w.r.t (a) THz frequency (b) aspect angle

The angle formed between the target object's orientation and the radar system's line of sight the direction from which the radar signal is transmitted, is known as the aspect angle. It has an impact on the target's ability to reflect radar radiation and, in turn, the detected TRCS. Figure.5.8 (a) and 5.8 (b) shows the backscattered TRCS circular flat plates with respect to an aspect angle and THz frequencies of a circular flat plate can be influenced by other factors such as THz frequency, and polarization of the incident radar waves, surface roughness, and the presence of any additional structure or features on the plate. That's why we used the advanced numerical computational method to determine the accurate RCS of the circular plate. These physical optics numerical techniques take into account the specific characteristics of the plate, the incident radar waves, and surrounding environment to provide a comprehensive understanding of the plate's radar reflection properties. Generally, RCS decreases as the aspect angle deviates from the maximum scattering direction. The energy reflected back toward the radar system drops when the radar wave strikes the circular flat plate at an increasingly oblique angle. Less energy is scattered back straight into the radar, and more energy is deflected away from the radar, which causes the energy to drop. Typically, the maximum RCS of circular flat plate is observed maximum at aspect angle of 90^0, when the incident 0.3 THz radar wave is aligned with the circular flat plate's broadside or normal to its surface. This is often referred to as the "maximum radar cross section" or "maximum scattering" direction. When the incident THz radar wave is aligned with the circular flat plate's edge or tangent to its surface, the radar energy tends to be directed away from the radar system, resulting in a lower observed RCS at both ends of the circular flat plate.

B. Rigid circular cylinder:

Equations (5.4) and (5.5) approximate the back scatter radar cross section in relation to a linearly polarized incident wave from a circular cylinder of radius r with normal and non-normal incidence, respectively.

$$\sigma_0 = \frac{2\pi H^2}{\lambda^2} \tag{5.4}$$

$$\sigma = \frac{r\lambda sin\theta}{2\pi}\left[\frac{\sin(kHcos\theta)}{cos\theta}\right]^2 \tag{5.5}$$

When the incident power is dispersed even in all directions, the target's imaginary circular flat plate area intercepts it and generates an echo at the radar which is equal to the amount coming from the target. The rigid cylinder's RCS with respect to azimuth angle is shown in Figure 5.9. At an elevation angle of 0^0, we obtain the highest value.

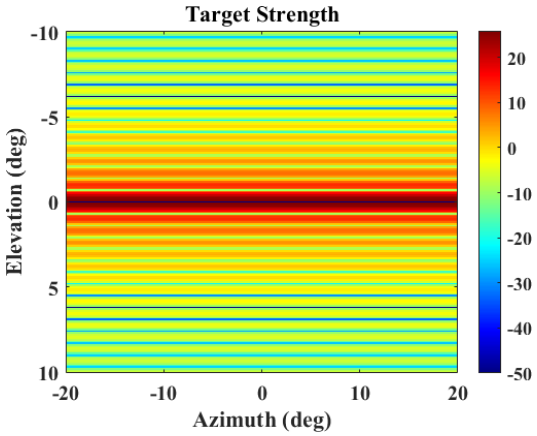

Figure.5.9. Rigid cylinder cross-section simulation

The ability of a rigid cylinder to reflect radar waves in the direction of the radar system is measured using the backscattered terahertz radar cross-section (RCS) of the cylinder. The incident THz radar signal's frequency and aspect angle are two factors that influence the TRCS. The aspect angle plays a crucial role in determining the RCS of a rigid cylinder. The RCS pattern varies significantly with changes in the aspect angle as different parts of the cylinder become more or less exposed to the incident THz radar waves. When the aspect angle is zero degrees or close to it (head on or broadside view), the RCS of a cylinder tends to exhibit a series of peaks and null. The peaks occur when the THz radar waves strike the cylindrical surface perpendicularly, resulting in strong THz radar reflections. The nulls occur when the THz radar waves interact with the cylindrical ends, causing the energy to be directed away from the radar system. As aspect angle deviates from the broadside direction, the TRCS pattern changes. The peaks, null intensity and magnitude of TRCS decreases. A lesser amount of the

energy is reflected back towards the radar system when the THz radar waves hit the cylinder at more oblique angles. A completely conducting cylinder is seen in Figure 5.10 (a) and is often of finite length for practical use.

special case:

A stiff cylinder experiences resonance effect because of creeping waves when the applied electric field is perpendicular to the cylinder's axis. In the case of a parallel incident wave, the influence of creeping waves is negligible. It is discovered that the fluctuation is not influenced by the cylinder's dimensions.

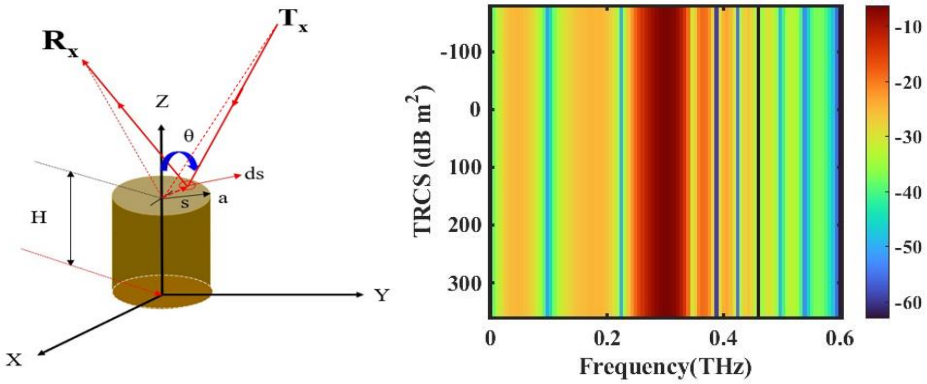

(a) **(b)**

Figure. 5.10 (a) Circular cylindrical configuration and radar position (b) Finite length cylinder cross section with respect to THz frequency

Figure.5.10 (b) shows that THz RCS simulation of finite length cylindrical object, and we get the maximum peak value at 0.3 THz. When the aspect angle is approximately 90 degrees (edge on or tangential view), the TRCS of a finite length cylinder tends to increase significantly.

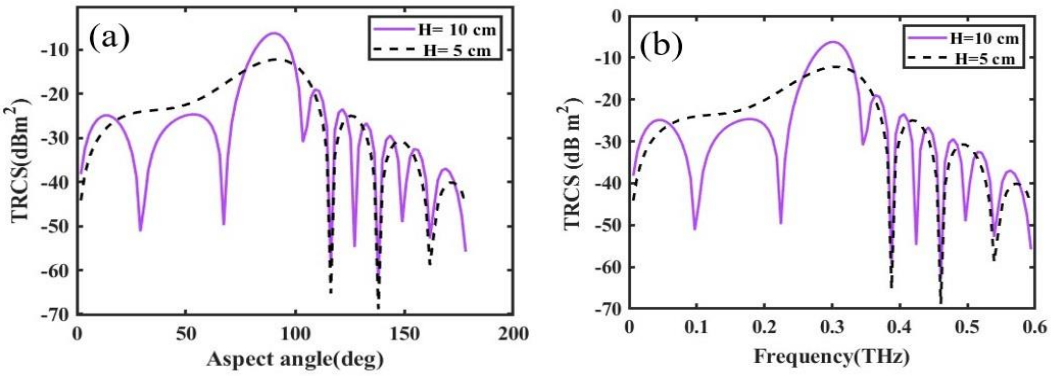

Figure.5.11 Back scattered TRCS for a circular cylindrical target with respect to (a) aspect angle (b) THz frequency.

Figure.5.11 (a) and (b) shows the backscattered TRCS circular cylindrical target with respect to an aspect angle and THz frequency. The variation of TRCS with THz frequency is found to be linear and exhibits higher values for large and rigid cylinders. In the THz domain at normal incidence, we get TRCS for circular cylindrical objects with a peak value at an aspect angle of 90^0. However, for large cylinders, the peak value of TRCS is also large.

5.6 Experimentally verification of modelled TRCS of brass cylindrical object:

Our study presents a physical optics (PO) modeling and experimental investigation of backscattered radar cross section (RCS) for basic canonical objects in the THz domain. These experiments were conducted in standoff mode using a SiRad Easy 0.3 THz frequency-modulated continuous wave (FMCW) radar source.

5.6.1 Data collection of 300 GHz radar source and data processing:

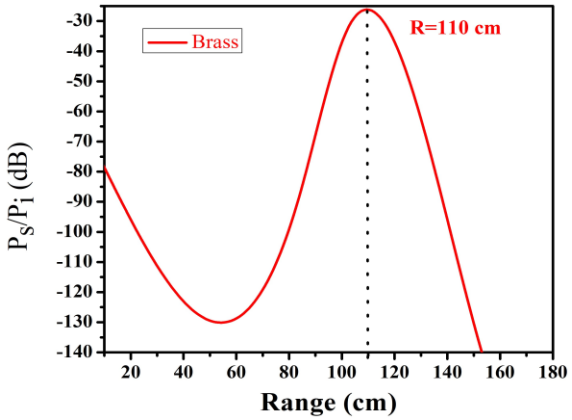

Figure. 5.12 Measurement of range of brass cylindrical object using 0.3 THz SiGe radar source.

Figure 5.12 confirms the maximum distance up to which we can measure a brass cylindrical object. From an experimental perspective, we can measure distance up to 110 cm using a 0.3 THz SiGe FMCW radar source, as determined by equation (5.8). The range of radar measurements for cylindrical objects depends on factors such as the target's size, radar system capabilities, and environmental conditions. It is important to note that different radar systems may have varying specifications and limitations, so the measurement range can differ among them, even for the same cylindrical object. In the equation,

$$2R = ct_o \tag{5.8}$$

Where, R is the distance between radar and target, c is speed of the light and t_0 is the ramping time.

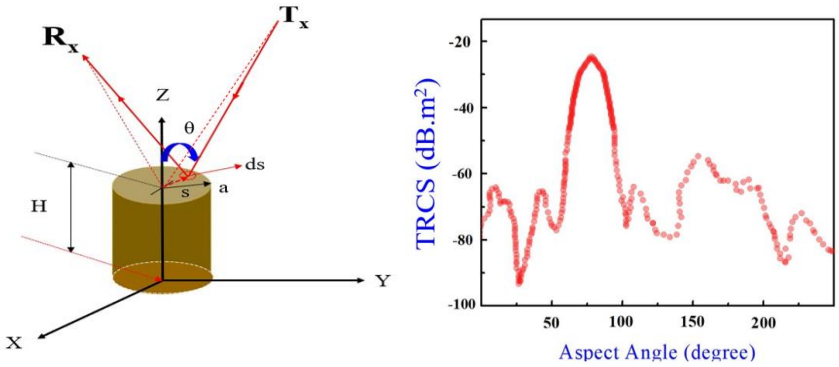

(a) (b)

Figure.5.13 (a) Finite length circular brass cylinder configuration (b) experimentally verifies THz RCS for a circular rigid cylinder.

For experimental validation, we took a perfectly conducting finite-length (10 cm) circular brass cylinder, as depicted in Figure 5.13 (a). Our experimental results confirmed that the simulated predictions (explained in Chapter 2) closely approximate the THz radar cross section (TRCS) of circular brass cylinders with finite lengths, as calculated using equation no 5.9. This comparison is illustrated in Figure 5.13 (b). TRCS, expressed in units of area, quantifies the power of the wave reflected back to the radar. A widely accepted definition of TRCS is provided by [35].

$$\mathrm{TRCS} = \lim_{R\to\infty} 4\pi R^2 \frac{P_s}{P_i} \tag{5.9}$$

where R is the distance between the radar and the target, and Ps and Pi are the incident and scattered electric fields respectively. As required by the optical architecture of the setup, the limiting process is introduced first in this specification to guarantee that the incident wave is a plane wave. The maximum TRCS for a conducting cylinder occurs at the specular reflection angle, which is represented by $2\pi rh^2/\lambda$. A target-detector distance-independent parameter for the target would be TRCS, if possible. This is only accurate at sufficiently great distances. For objects with a smaller radius of curvature, the distance at which RCS achieves its far-distance value is shorter. Furthermore, the distance from the target affects the angular distribution of the scattered electric field. The target's dimensions and form, incident and reflected angles, target-to-wavelength ratio, and polarization of the radiation being detected and emitted all have a major impact on TRCS. We observed that when we rotate the target toward the radar, the TRCS is maximized at an aspect angle of 90^0. Experimentally verify THz RCS for a circular rigid cylinder. For experimental validation, we selected a perfectly conducting finite-length circular brass cylinder.

5.7 Direct and concealed detection of metallic object using prototype THz radar system

THz waves can effectively penetrate various materials, including clothing and packaging, while providing valuable information about the composition of hidden objects. Moreover, terahertz radar can provide valuable insights into the nature of hidden items without the need for physical contact or the use of ionizing radiation. The detection and identification capabilities of terahertz radar make it a powerful tool in the field of security, particularly in scenarios where the concealed objects may pose a threat to public safety.

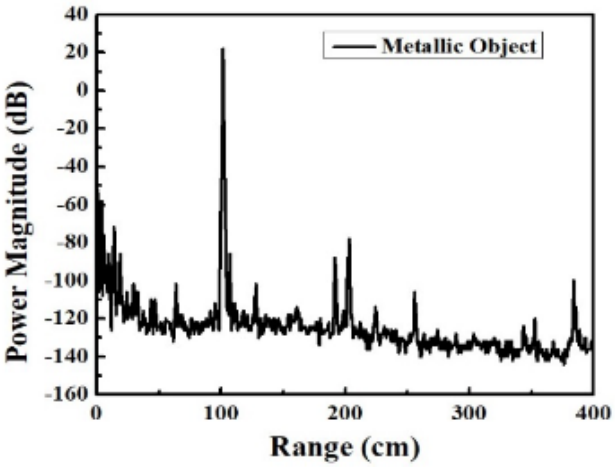

Figure 5.14 Direct detection of metallic target using 0.3 THz radar source

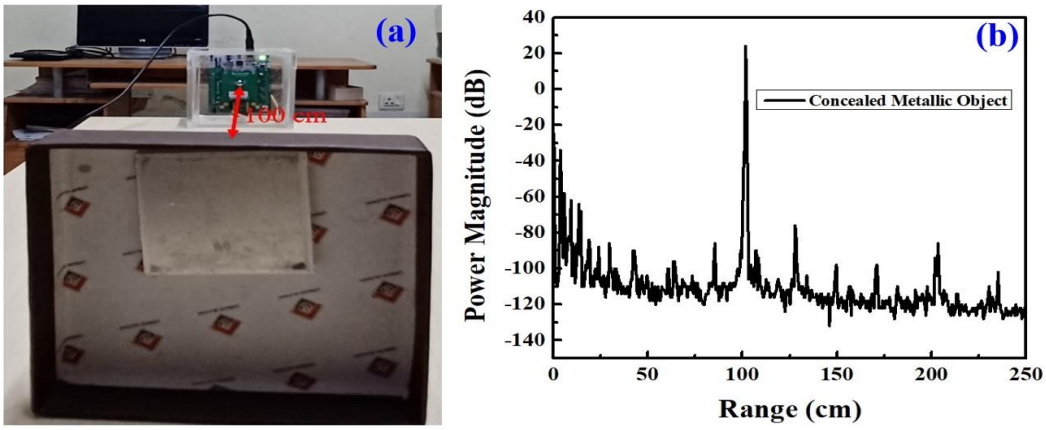

Figure 5.15 (a) Metallic object inside the cardboard (b) Detection response from metallic object at 1.0 m distance using 0.3 THz Silicon radar source.

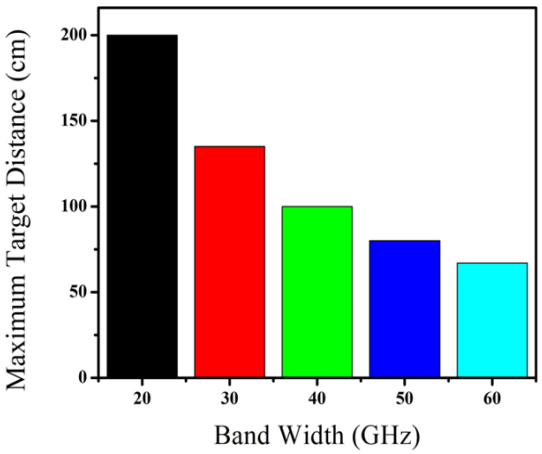

Figure 5.16 Response of bandwidth to achieve maximum target distance using 0.3 THz radar source

Figure 5.16 detailed analysis reveals the system's capabilities, response of bandwidth to achieve maximum target distance using 0.3 THz radar detailed analysis reveals the system's capabilities, with the maximum target distance spanning 2.0 m for a 20 GHz bandwidth, 1.46 m for 30 GHz, 100 cm for 40 GHz, 80 cm for 50 GHz, and 63 cm for 60 GHz. The 300 GHz SiGe radar source outperforms its lower-frequency counterparts, demonstrating unparalleled spatial resolution for radar imaging and sensing applications. The key is the signal pattern reflection used to receive clearly the 6'11" distant target weakly associated with the signal high frequency and the signal bandwidth. The key ratio and the ratio of high and low power lies between 289 GHz and 329. With a spatial resolution of 0.016 arc-sec, 0.029 arc-sec respectively, the noise signal (SNR) is 60 dB at a distance of 2.0 arc-sec m. The 300 GHz SiGe radar source outperforms lower-frequency counterparts, demonstrating higher spatial resolution for radar imaging and sensing applications. The fact that the wavelength of the reflected signal coming from the target is from 63-200 cm is what brings the distinction between 20-60 GHz range. These experiments were conducted in standoff mode using a SiRad Easy 0.3 THz frequency-modulated continuous wave (FMCW) radar source.

5.8 AI based classification of different types of metallic objects using THz radar source

THz frequencies offer a powerful tool for material identification due to their unique interaction with various substances [36]. THz radiation is lies between microwaves and infrared light, is non-ionizing and can penetrate a wide range of non-metallic materials, making it ideal for inspecting and identifying materials without causing damage [37]. Our aim was to employ our 0.3 THz radar in detecting materials. We have collected samples of various materials

relevant to defence with the evaluation kit. We tried to identify metals and explosives using the radar. We have collected different samples of aluminium, copper, stainless steel, brass, titanium, zinc, lead and nickel for the identification of metals. For the identification of explosives, we chose Tetryl (CE), TEX, CL-20 and TNT. We have calculated the density of each sample using the mass and volume of the sample as follows

density = mass of sample /volume of the sample

The metals and explosive samples were then used as a target at a fixed mean distance of 53.2 cm from the radar system and the reflected THz signals was collected (referred to as 'dataset' in later discussions). A cardboard sheet of fixed dimensions (50 × 40 × 2 mm) was used to conceal samples and the same was repeated to get another set of datasets. A total of 482 distinct individual data points of all materials in concealed and non-concealed conditions was obtained using the collected samples, with an average of 20 data points for each material. The data was analysed for a resulting patterns and distinguishable features across the materials. The conclusions drawn were used to construct a machine learning algorithm (k-nearest-neighbours or k-NN) to make a prediction system that can predict the material's identity from its peak reflected signal from the THz radar and the value of density, which can be obtained using the routine formula to find density using mass and volume, or otherwise. A k-nearest neighbour algorithm [38] is a traditional machine learning tool routinely used to classify objects, materials, images, etc. using a formula based on Euclidean (or other) distance. It classifies a data point as belonging to the class of the data points closest to the given data point in question. accuracy of the k-NN algorithm's prediction is defined to be the following:

accuracy = number of samples correctly predicted/ total number of samples predicted

The accuracy of this model was thus used to quantify the efficacy of the above methodology to classify materials.

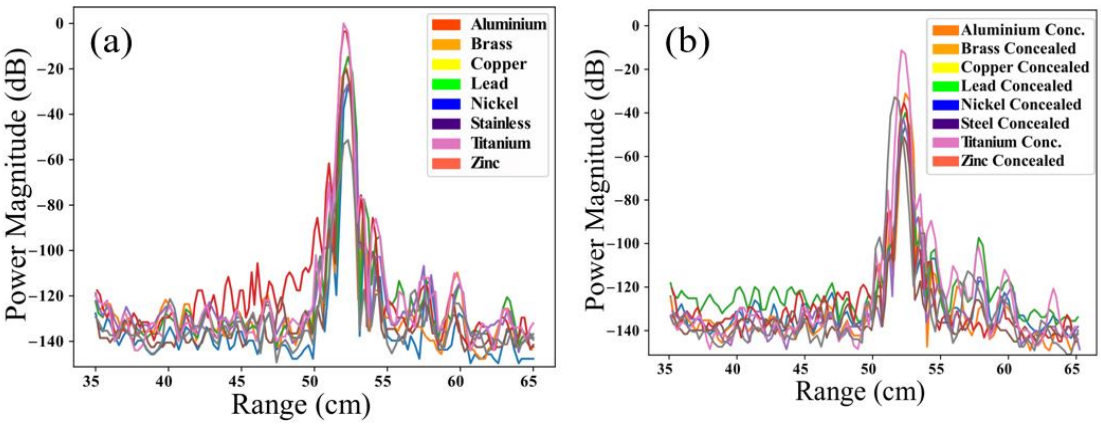

Figure 5.17 Detection of radar signal of different types metallic objects (a) direct and (b) concealed condition

Figure 5.17 (a) and (b) shows that samples, when targeted with the 0.3 THz radar source, produce a peak in the magnitude of reflected signal strength (measured in dB). This peak occurs at the distance (measured in cm) where the sample is kept in both direct and concealed conditions. The system was able to give reflected signals for all materials as discussed with a signature peak. The average of peak values for each sample was calculated and plotted with density of samples to study the relationship between the two, as shown in Figure. 5.18 represents for metals in concealed and non-concealed conditions.

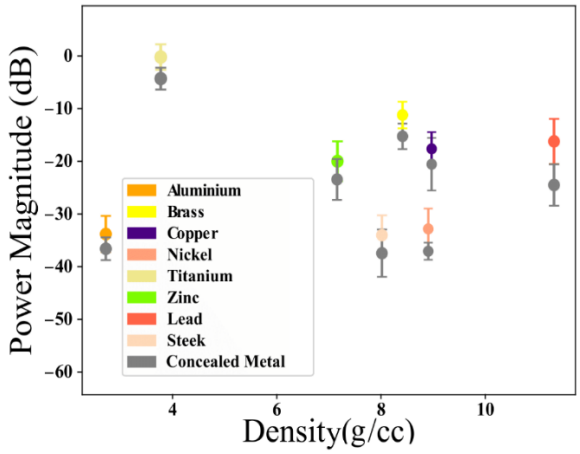

Figure 5.18 Average peak power of different types of metallic targets in concealed and non-concealed conditions.

The mean of all distinct categories was tested for the alterative hypothesis using a one-way ANOVA (p -value= 2.54×10^{-267} for metal and 2.866×10^{-15} for explosives) and found to be distinguishable by their Power value. Figure 5.19 illustrates that the detection of explosives materials in direct and concealed conditions. A pairwise t-test between each possible pair of the metals or explosives was also performed, with no p-value reported to be above the significance threshold of 0.05, rejecting null hypothesis. It can be clearly inferred from Figures 5.18 and 5.20 that each material gives a characteristic peak value for a given density of the sample, provided that other samples are kept at the same distance as the one that needs to be identified. This signature peak suggests that the reflected signals from the THz radar and the density of the material can provide a reasonable prediction about the identity of the material, such as explosives, drugs, metals, or other articles.

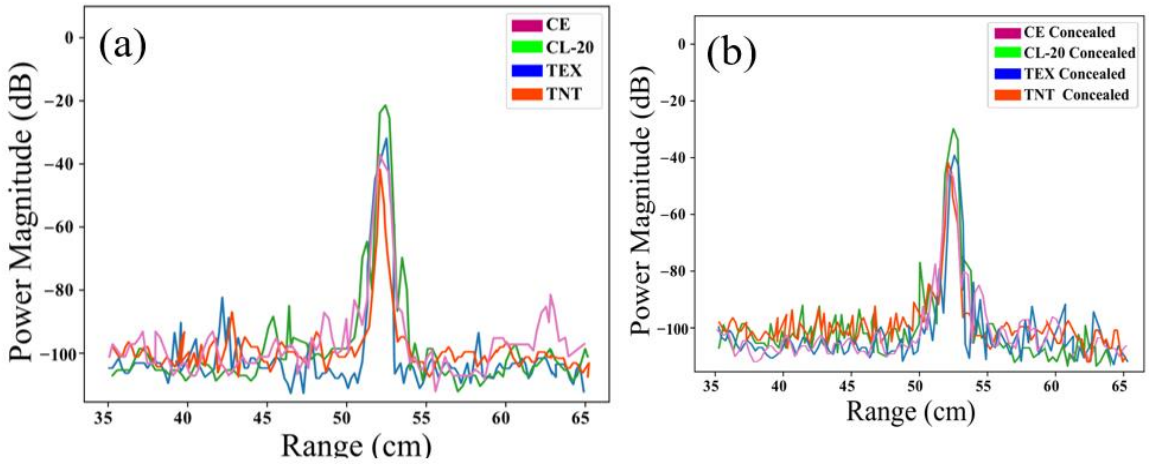

Figure 5.19 Detection of radar signal of different types of explosive materials (a) Direct and (b) concealed condition

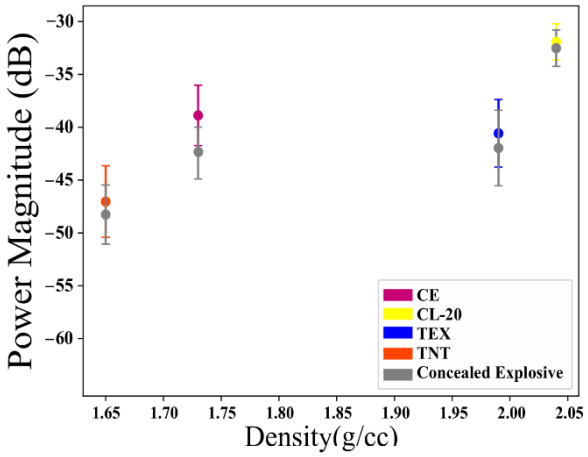

Figure 5.20 Average peak power of different types of explosive targets in concealed and non-concealed conditions.

This aspect of the radar makes it an ideal candidate for real time and quick detection of materials in situations when it is unfeasible to do a chemical analysis. We show proof of concept further by creating a machine learning system using a standard k-nearest neighbour classification algorithm. This system was trained on 453 individual data points and could successfully predict 30 untrained samples from the collected datasets. The accuracy achieved was 87.5% for metals and 92.3% for explosives, regardless of being concealed or non-concealed, using the same model. The model's predictions are shown separately in Figure. 5.21 and 5.22 for detailed view. It must be highlighted that the same model was used for both metals and explosives. The representation is for the purpose of clarity of image since the density of the aforesaid explosives is much lower than that of metallic objects.

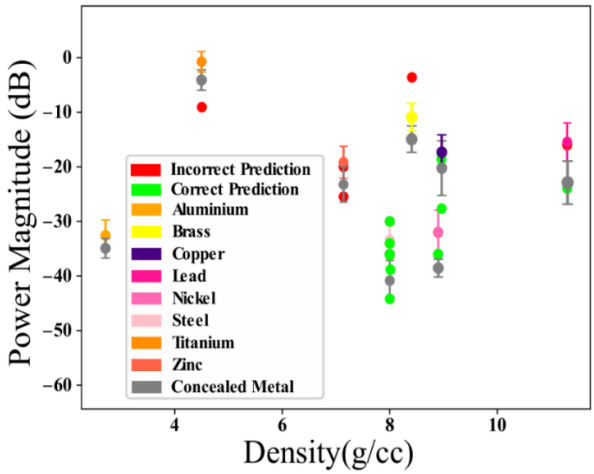

Figure 5.21 k-NN algorithm classification of object samples into various metals, with accuracy of 87.5% in metals.

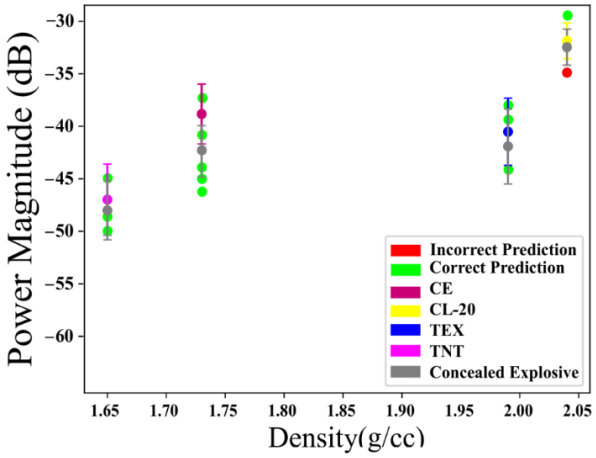

Figure 5.22 k-NN algorithm classification of explosive substances into Tetryl (CE), TEX, TNT and CL-20 with accuracy of 92.3%

5.9 Using the calibrated system for freshness detection in meat – A unique utility:

As previously discussed, many materials often of defence interest, have a unique peak visible with the calibrated system. However, an important question to ask is, 'Does the radar capture changes in a given material?" For example, what happens if a material with high water content is heated to remove some water and then measured with the THz system? Intuition would say that the signal may change, which leads to another question. Put in a different way, one can ask if THz reflected signals distinguish between fresh and stale meat, leading into possible utility in the meat/food processing industry.

Necessity and Utility:

Spoiled meat can be lethal, posing a significant risk to human health. The determination of meat freshness is a challenging task, as visual inspection alone cannot ascertain its condition. The key indicator of freshness lies in the microbial content, notably fecal bacteria such as E.

coli. However, assessing bacterial levels is arduous, typically requiring a process known as culturing, which spans 5-7 days. Subsequent microscopic examination and counting are necessary, presenting logistical challenges in practical application [39].

In market settings, individuals often resort to subjective methods to evaluate the freshness of meat. Companies commonly rely on expiration dates, which denote the time elapsed since the meat was cut, as a standardized approach for assessing freshness [40-41].

Within market environments thus, the assessment of meat freshness often lacks standardized and objective criteria, leading individuals to employ subjective methods. One common approach adopted by companies is the utilization of expiration dates. These dates serve as reference points indicating the duration since the meat was cut or processed. By referencing these dates, consumers and sellers alike aim to gauge the relative freshness of the meat being offered for sale. Despite its widespread usage, this method inherently relies on the assumption that the meat's freshness correlates directly with the time elapsed since its preparation. However, it's essential to acknowledge that factors such as storage conditions, handling practices, and the initial quality of the meat can significantly influence its overall freshness, making the determination of freshness a multifaceted and nuanced endeavour.

The major impediment in current freshness detection systems lies in the paucity of comprehensive data. Freshness dynamics are influenced by a plethora of factors, encompassing microbial activity, oxidative processes, environmental variables like temperature and humidity, species-specific characteristics, regional variations, and handling procedures [42]. These factors contribute to varying rates of freshness degradation across different parts of meat, species, temperature zones, altitudes, and processing methods [42]. However, acquiring verified and comprehensive data, endorsed by food quality assessment authorities, proves to be a time-consuming and expensive undertaking. This limitation hampers the practical implementation of freshness detection systems in market settings, where timely and accurate assessment of freshness is crucial for ensuring food safety and quality. Therefore, the pursuit of a real-time, non-contact freshness detection system capable of swiftly collecting primary data holds significant promise for enhancing the efficacy of freshness assessment. This motivation underscores the exploration of THz technology as an alternative approach to detecting meat freshness. THz technology offers the potential to provide rapid and non-invasive assessment of freshness dynamics, facilitating the acquisition of comprehensive data essential for developing a more effective freshness detection system.

5.10 Existing work – THz for meat freshness

To guarantee a complete awareness of the current research environment and to identify gaps, difficulties, and possibilities in the area, a thorough literature analysis was carried out prior to the experiment. This review encompassed a wide range of scholarly articles, research papers, and relevant literature pertaining to freshness detection methods, including but not limited to THz technology. By synthesizing and critically analyzing prior studies, the researchers aimed to inform the experimental design, methodology, and interpretation of results, thereby laying a solid foundation for advancing knowledge and contributing to the body of research on meat freshness detection. Xiaohong Wu et al. [42] has systematically compiled an extensive list of studies investigating the application of terahertz (THz) technology in meat freshness detection. Additionally, Xing B. Huang et al. [43] conducted a preliminary investigation into the temporal effects on signature peaks in the frequency domain of a terahertz spectrometer, revealing variations in signals over time.

In this study, we delved deeper into the potential of employing our time domain system to directly predict meat freshness. If successful, this system could extend its applicability beyond meat to assess the freshness of various other edible products. The rapid assessment of food deterioration in extreme climatic conditions, such as high altitudes, is currently lacks reliable systems. This research represents a step forward in addressing such challenges and progressing towards the development of effective freshness assessment methods in diverse environmental settings.

5.11 Preliminary data collection – biological correlations:

Preliminary data were gathered over a 12-hour time-frame employing the Terahertz (THz) system on a single 12 × 12 × 2 mm slice of chicken liver. The time varying signal from 300 GHz source is plotted in figure 5.23. The plot illustrates an upward trend in reflectivity signals observed over the duration. These findings support the inference that the Terahertz (THz) signal exhibits temporal variability, as confirmed by previous reports (Xing B. Huang et al. [43] and others) and studies have indicated that the output derived from the reflected signal can serve as a predictor of the k value of meat and demonstrates a correlation with time [45]. It is also recognized that water absorption from the radar system can exert an influence. Variations in the concentrations of Na^+ ions have been established to provoke alterations in the output power of reflected signals [46].

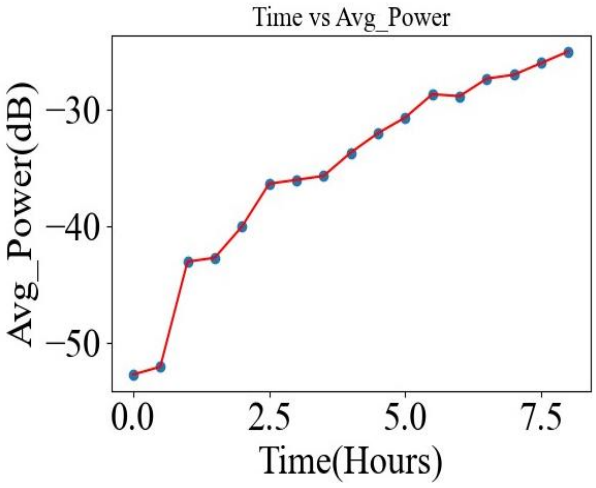

Figure 5.23 Trend in reflectivity signals observed over time duration in a single day for a biological sample.

These findings illustrate the biological correlation between changes in molecule concentration and signal strength. THz spectra have the capability to reflect changes in the content of biological molecules such as amino acids and polypeptides or proteins. Under the influence of various spoilage bacteria, muscle proteins undergo hydrolysis, initially breaking down into polypeptides, then into amino acids, and ultimately decomposing into a myriad of organic substances. This is thus an example of a complex system affected by a variety of parameters, which may not be linear. The nonlinearity is well studied, Shen et. Al [46] found that the relationship between ATP-related content and spectral data in the spectrum is nonlinear, indicating that nonlinear models offer superior fitting performance in comparison to linear models.

5.11.1 Collection of polutry data for training AI model – primary data collection:

Nasir Akbar Mir et al. and others have detailed the factors that affect meat deterioration in a variety of conditions [70]. We identified the following as the most practical and economical way to monitor and record meat freshness in our lab setting: (i) pH of meat sample, (ii) room humidity, (iii) sample temperature, (iv) room temperature, (v) mass of the sample & (vi) sample volume (for density measurement). The reflected power of THz signal was recorded along with these various external and internal parameters that are measurable, as given in the above exhaustive list. We have collected chicken breast samples cut into equal volumes, with one sample every day for a total of 7 days. For homogeneity and to avoid complexity in the data, we recorded the data only for samples of chicken breast. The data for these 7 days was collected at intervals of held an hour for 8 hours each day, from 10 AM to 6 PM evening. It spanned

during the month of June (an average temperature of 27.6 degrees and average humidity levels of 55%). Subsequent data analysis was performed and a prediction model made by consulting relevant literature.

5.11.2 Analysis, interpretation and model making:

We assumed the following two propositions for this system:

- Meat 'freshness' is a combination of various effects, namely the formation of toxins, bacterial growth, continuous water loss changing the texture, changes in pH and breakdown of biological molecules.
- The averaged-out effect of these changes in meat over time will be measurable through changes in the signal intensity of reflected beams from a THz radar. A change in the parameters of freshness thus, will lead to changes in the signal strength.

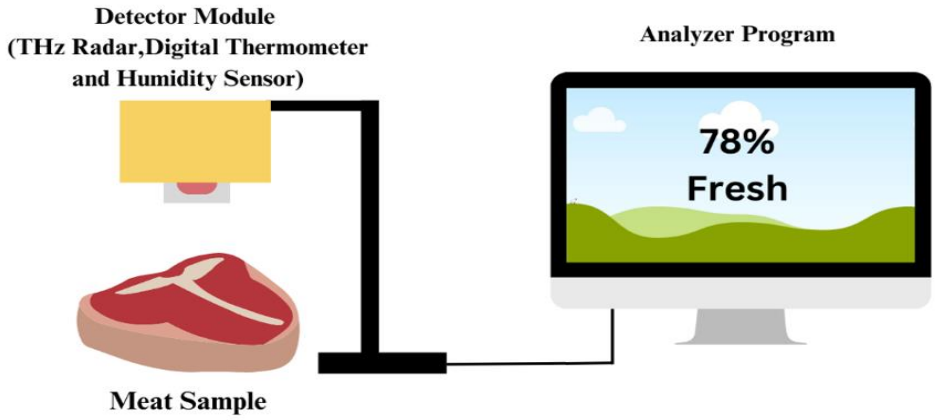

Figure 5.24 Prototype 0.3 THz Radar system with all components

The system consists a specially calibrated 0.3THz monolithic microwave integrated circuit (MMIC) based radar. Alongside the radar module, digital modules to measure humidity and temperature are integrated into the radar system which is connected to a computer analyser (Figure 5.24), together they comprise the 'detector' module of the system, which is portable. First, THz radiation is emitted from the source and hit a target meat sample kept at a fixed distance from the radar, and reflected signals are captured by the radar. Ideally the meat sample for the analysis must be large enough to prevent scattering outside and causing noise due to externally reflected rays, depending on the dimensions of the radar, the distance to sample, and specific calibration parameters of the radar. The obtained reflected signal's intensity is sent to an analyser program that runs on a computer of appropriate capacity, depending on the algorithm. It may perform the analysis and return on screen a 'freshness index', which is the

probability of the meat being fresh in percentage. The input parameters the analysis system receives is the power of reflected signals, temperature and the humidity

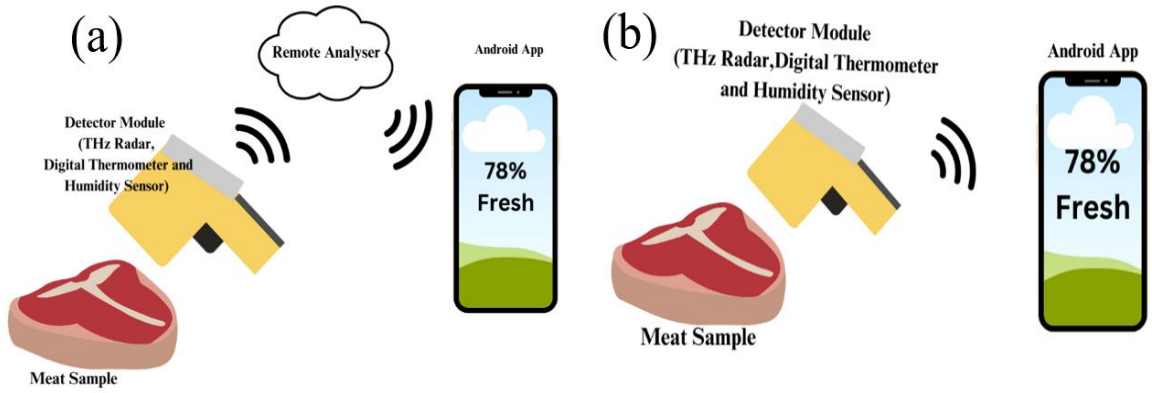

Figure. 5.25: System with analysis system with analysis in smartphone via a remote server. Another embodiment of the same idea is as in same figure no. used

It consists of the same detector module, with a manual hand operated trigger that is connected wirelessly to a server hosted on the internet, and the analysis is done over a remote server. The results are then to be displayed on a smartphone screen. Yet another embodiment of the same idea is Figure 5.25(b) the integration of the analyser program into an android application, and the detector module being connected to the smartphone via a Wi-Fi connection. Many such designs are possible, and are essentially the same in principle, one or more specific such designs may be ideal in different settings.

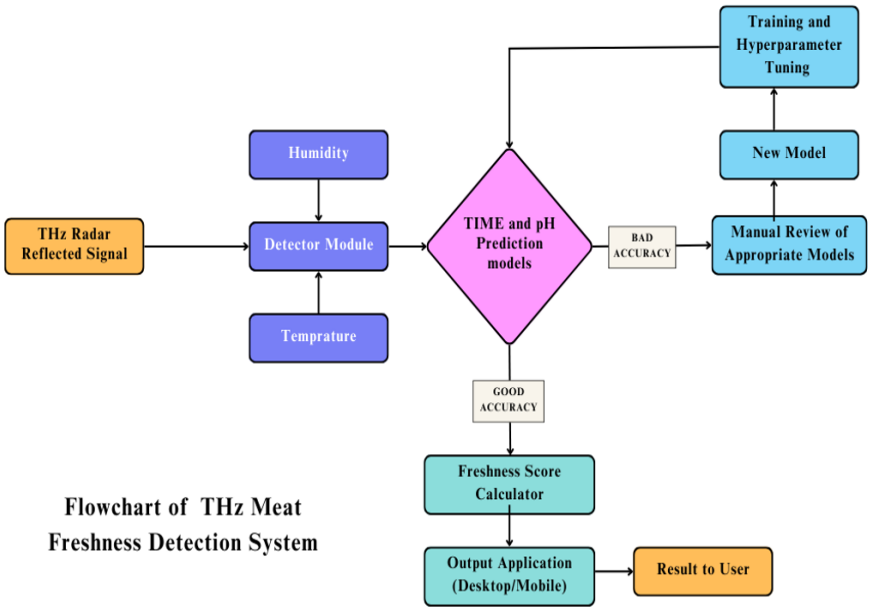

Figure 5.26. Flowchat of THz meat freshness detection system

Working of the meat detection system is as described by the flow diagram in Figure 5.26. The reflected signal can be obtained from different locations within the sample to be analysed to reduce the effect of surface effects, which are noise to the output. Several plots for each variable with respect to each other variable was plotted using matplotlib and Python. The trends observable in three out of all are of relevance and shall be discussed here

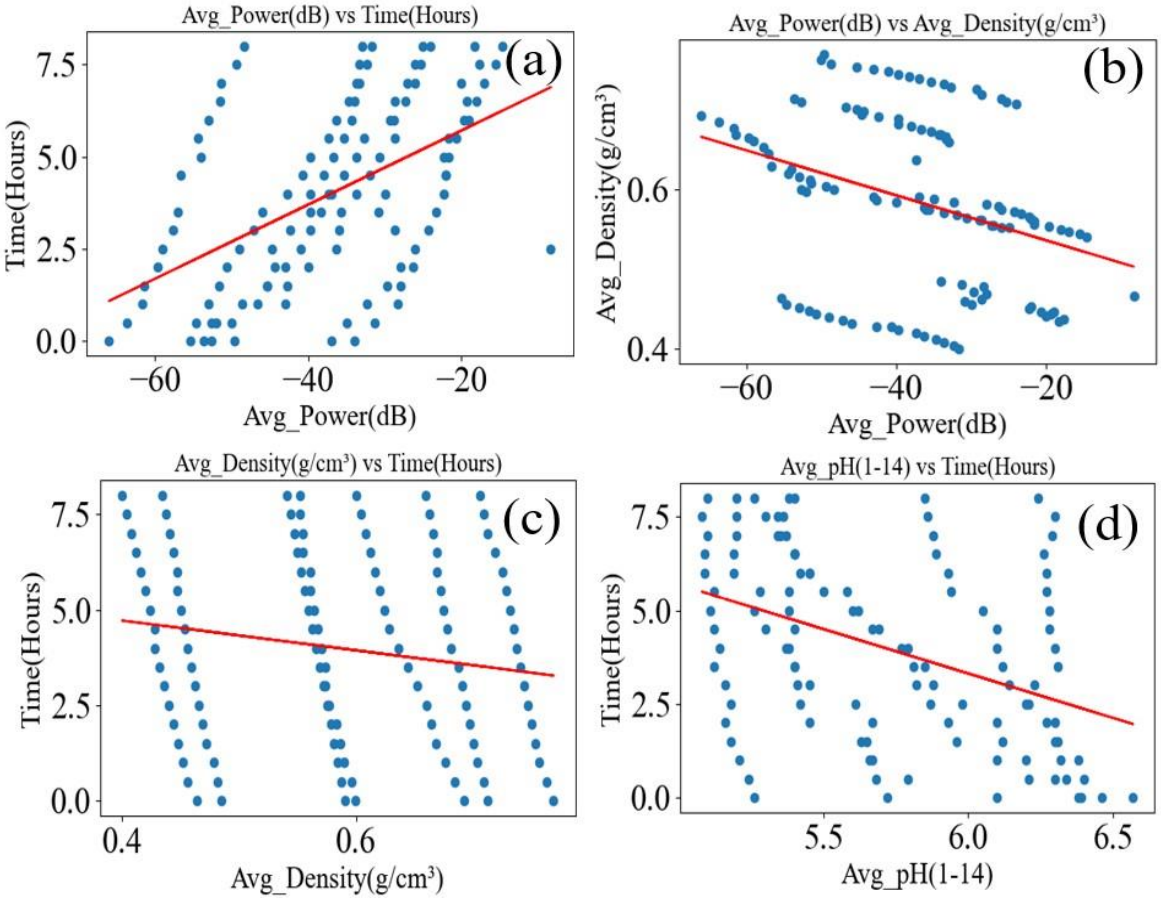

Figure. 5.27 Trending data of the 0.3 THz radar source (a) average reflected power signal with respect to time (b) average reflected power vs average density (c) average time vs average density (d) average pH with average time.

First is the trend of the average signal at a given time from the meat data versus time, as given in the above figure (Figure 5.27). This trend suggests a general trend with almost constant rate of change of power with time. It is similar to Figure 5.27 (c), the plot of avg. density with hours for all days. This may suggest a direct causation between the density and the signal from the THz radar. This however, is refuted from the plot of avg. power vs avg. density. For a given density on two different days, the data suggests that there can be two different possible values

of power. Which clearly shows that there is only a correlation, not a direct causation by the density. Had the signal strength been a function of density alone, the density value corresponding to 0.45 gm/cc would not have possibility had two different signals of power. The only possibilities cause is error due to the system and changes due to external environmental factors. These however, were kept at almost a constat rate and the system has been verified to not have signals varying locally in time for an unchanging target. This suggests clearly that the variation in density with power can be only a correlation and not suggestive of a direct causation. Indeed, the density may contribute to the value of the power output of the signal, however it is not the only cause. It is also clear in Figure. 5.23 that the slope of hours vs power may change abruptly as seen for certain days, which are suggestive of changes in the freshness. One gets more insight about the internal concentrations of various molecules in the meat from Figure 5.27 (d), which plots the average pH vs time. There is a trend which is not as linear as that of power or density vs time, but pH generally is decreasing with time. This is consistent with Nasir Akbar et al. [47], the pH is an important factor in determining freshness of meat. The sudden changes in rate of change are suggestive of internal changes in the meat correlating with freshness. The slopes, however, are not as constant as those in power. It can be noted that the sudden signature changes in power vs Hour's graph correspond to sharp, sudden changes in the pH. This important finding indicates that the signal strength necessarily accounts for important changes in the pH, albeit remaining more or less a constant rate for insignificant changes in the pH. Thus, it can be concluded that the THz signal is a much more robust and useful tool to measure changes in the freshness, as it is less non-linear than pH, yet still accurately describes important changes as required. In other words, trends are smoothed out by the power values, while still accounting for abrupt changes. The added advantage of the method is that it is a non-contact system, which results in zero contamination of the meat as compared to pH meter which needs to be inserted into the meat deep enough to make a measurement. It can also be concluded from these graphs that the correlation between water loss and power value (which is also an important factor determining freshness) is not the only cause for changes in the value of freshness.

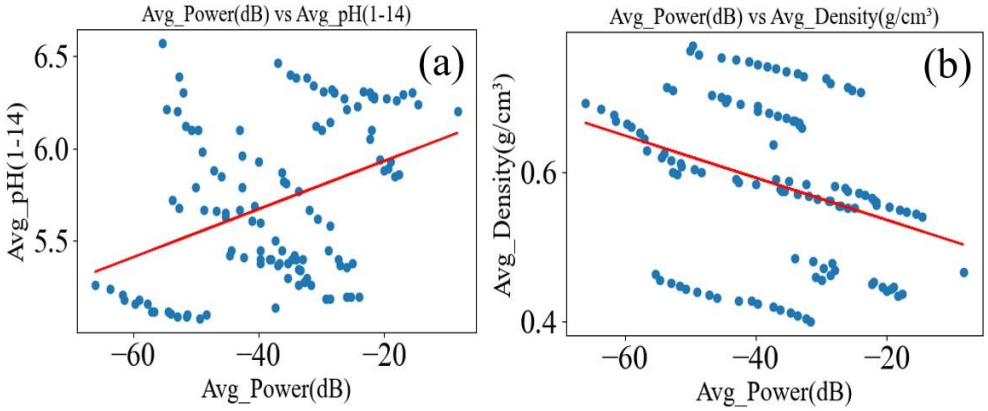

Figure 5.28 (a) Local non-linear corelation with pH (b) Trend of density with power

Figure 5.28 (a) and (b) further elucidate the fact that the power signal accounts for both water loss and changes in pH at the same time. One can observe a range of pH for a given range of power in Figure 5.28 (a). For example, Figure 5.28 (a) illustrates that an average power of -50 to -20 corresponds to a pH in the range 5.4 to 6.0, as shown by the straight red line. However, the power is a function of time as well, so there is a local trend in the pH as the day passes, observable by the avg. power signal. Figure 5.28 (b) shows that a given value of density does not have an exactly corresponding value of average power. In fact, the same density of chicken tissue can have power values at two extremes of the spectrum, depending on the local conditions. Thus, this discussion elucidates the fact that the value of power signal obtained from meat corresponds to a correlation with parameters affecting its freshness, namely, pH and time. The pH accounts for internal changes in the concentrations of nitrogenous toxins, ATP changes and other chemical changes whereas water loss is an indicator of the amount of time that has passed since the meat was cut and exposed to air. The rate of water loss is more or less or a constant. The non-linear trends in the data point towards a model such as an artificial neural network to predict time and pH, but one should first verify if a linear model is able to account for the trends, which is discussed in the next section.

5.11.3 Linear model to predict freshness:

We first employed an ordinary linear regression with input variables as the average power value of a sample, the density, humidity and temperature of the sample to make a linear predictor of time and pH of the meat sample. The results from this are as discussed in figure 5.29.

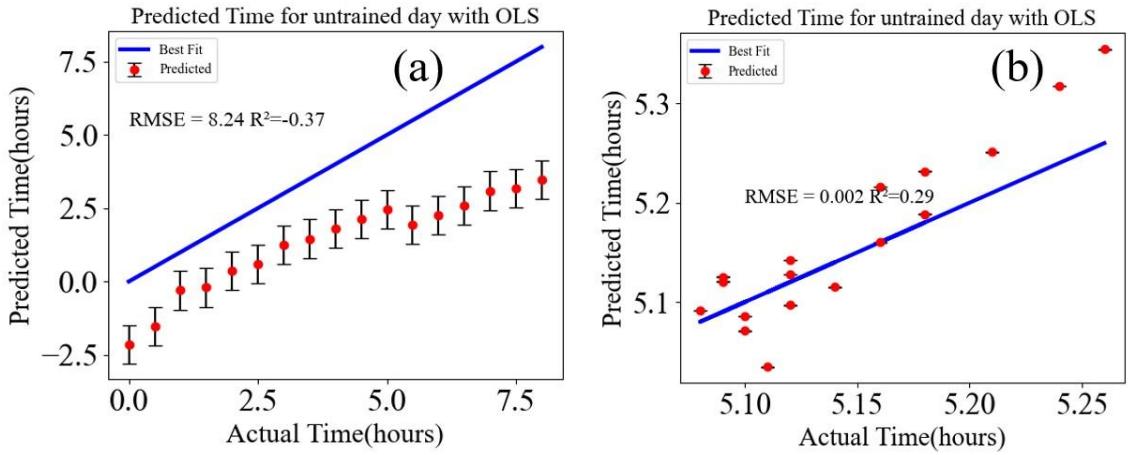

Figure 5.29 (a) Actual vs Predicted values for a typical untrained day (Time and pH)

The root mean square error (RMSE) for the prediction in pH is 0.12 units and for time is 4.86 hours respectively. The units of RMSE and its range is the same as the units in which the predictions are made. The R^2 value is an indicator of the effectiveness of the best fit line, which is -0.37 and 0.29 for the two, both indicating a underfit model. This model is thus unable to account for the changes in pH and time with useful accuracy. It may be noted that the data used for testing was not used to train the model, which is an essential criterion to know the accuracy for 'blind' data. It may also be noted that models were made with and without the use of scaling (min-max scaling, normalization and Python standard scaler) to make the trends more visible. The best result achieved has been reported herein, which was using the min max scaler, which scales each value relative to the minimum and maximum of the respective column. We thus propose a neural network to model the problem and predict time and pH in place of linear models. It has been well discussed that the biological factors affecting freshness are most likely to behave in a non-linear fashion, necessitating the use of modern paradigms such as an Artificial Neural Network to be used for predicting freshness.

5.12 Feed forward artificial neural network-introduction and architecture:

Feed-forward neural networks (FNN) are one important kind of artificial neural network (ANN) utilized for supervised learning tasks like regression and classification. Each neuron in a layer is connected to every other layer's neuron through a network of interconnected layers seen in FNNs. "Feedforward" refers to the direction in which information flows from input via hidden layers to output. An activation function is used to the weighted total of the inputs plus a bias factor to determine the output of a neuron. During training, weights and

biases are modified to reduce the discrepancy between expected outputs and actual objectives. Neuron output in a layer may be described mathematically as follows:

$$z_i^l = \sigma(\sum_{j=1}^{n^{l-1}} w_{ij}^l z_j^{l-1} + b_i^l) \quad (5.3)$$

An essential part of neural networks is the activation function, σ which determines a neuron's output by adding up all of its weighted inputs $w_{ij}^l z_j^{l-1}$. b_i^l is the bias term for neuron i in layer l. - n^{l-1} is the number of neurons in the previous layer. The network's capacity to learn and form predictions is greatly influenced by the weight of the link between a neuron in one layer and another neuron in a later layer. There is more flexibility in modeling complicated datasets because to the bias term for a neuron in a particular layer. The dimensionality and data representation capability of the network are influenced by the quantity of neurons present in the preceding layer. In feedforward neural networks (FNNs), a variety of activation functions are often used, including the sigmoid, hyperbolic tangent (tanh), and rectified linear unit (ReLU) functions. Using techniques such as gradient descent to minimize a loss function that quantifies the difference between expected and realized results. To compute the gradients of the loss function with respect to the neural network parameters and enable iterative weight and bias adjustments, backpropagation is a basic approach. Fundamentally, FNNs are adaptable models that are skilled at identifying complex patterns in data, and they may be used in a variety of industries, including financial prediction, natural language processing, and picture identification.

5.12.1 Backpropagation:

Weights and biases are modified using backpropagation in the order to reduce output variance. The network parameters are updated via loss function gradients. Both forward and backward passes are part of the algorithm. Layer by layer, input data is calculated to produce output during a forward pass. The difference between the actual and expected outputs is measured by the loss function. Gradients adjust parameters in the backward pass in order to reduce loss. Until the convergence or halting requirement is satisfied, the process is iterative. The layer's parameter update rule has a mathematical expression. Size of parameter updates is controlled by learning rate. The gradient and loss function are essential elements. The parameter updating rule for a weight w_{ij}^l in layer l may be represented mathematically as follows:

$$w_{ij}^l = w_{ij}^l - \eta \frac{\partial L}{\partial w_{ij}^l} \quad (5.4)$$

Where, η is the learning rate, which controls the size of the parameter updates, L is the loss function & $\partial L/(\partial w_{ij}^{l})$ is the gradient of the loss function with respect to the weight w_{ij}^{l}.

5.12.2 Cross validation:

Cross-validation assesses predictive model performance by dividing dataset into subsets. Model trained on one subset and evaluated on the rest, repeated multiple times. Commonly used k-fold cross-validation divides dataset into equal-sized folds. Model trained k times using different folds as validation set. Performance averaged across iterations for robust estimate. The average performance metric CV_{avg} across k folds may be calculated mathematically as follows:

$$CV_{avg} = \frac{1}{k}\sum_{i=1}^{k} Metric_i \tag{5.5}$$

Where, on the validation set for the i^{th} fold, $Metric_i$ is the performance measure (accuracy, mean squared error, etc.). When evaluating how effectively a model generalizes to unknown data over numerous dataset divisions, cross-validation offers a more accurate indication of the model's performance than a single train-test split.

5.12.3 Optimizing backpropagation

The Adam optimizer combines AdaGrad and RMSProp for training neural networks effectively. It initializes two parameters (first and second moment) to zero vectors of the same length as gradient parameters. During each iteration, Adam calculates an exponentially decaying average of past gradients to capture gradient direction and smooth fluctuations. Adam adjusts learning rates per parameter using gradient moments for faster convergence. A neural network predicts chicken sample time using power signal, temperatures, and density. pH prediction also utilizes these parameters. Exponential activation function with 'a' determined by cross validation is used. The model is illustrated in a figure 5.30.

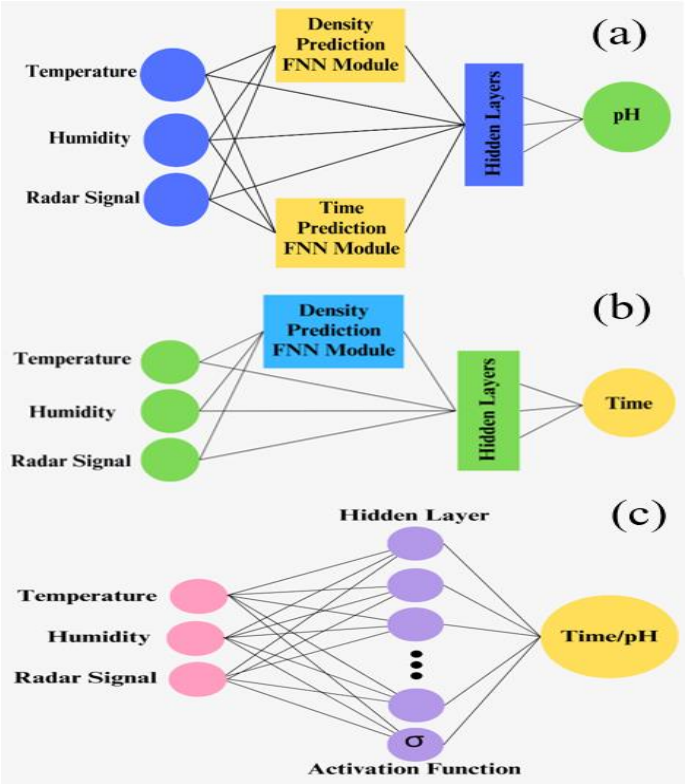

Figure 5.30 (top to bot Feedforward ANN architecture used in our system. Modular ANN for prediction of (a) pH and (b) time respectively. (c) The density module is trained separately using weight and volume as parameters alongside Temperature, humidity and signal.

5.12.4 Prediction and accuracy:

Accuracy is defined in the following results as, accuracy = (number of predictions within the RMSE value / total predictions) × 100, provided where RMSE value is judged to have been satisfactorily useful for predictions, i.e., the predictions within the RMSE values are deemed to be 'correct'. The best models to predict time and pH were obtained using a backpropagation based artificial neural network with an Adam optimizer and an exponential activation function $e^{(ax)}$ with a = 0.056. This was obtained by cross-validation process as described in the previous section.

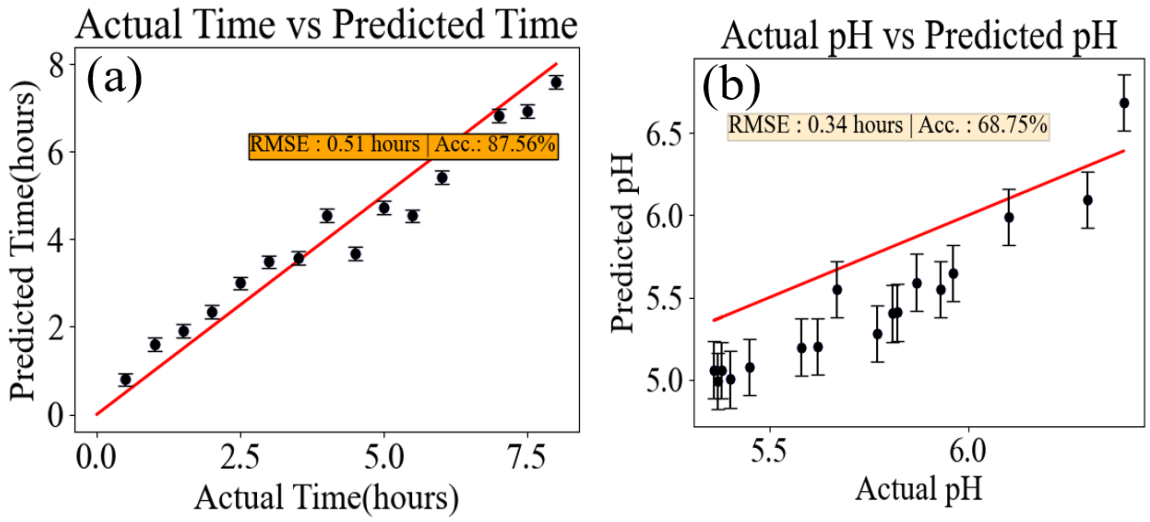

Figure.5.31 Feed forward ANN based model for prediction of (a) time & (b) pH

Figure 5.31 shows the feed forward ANN mode for prediction of time and pH of the meat sample. The feed-forward ANN reports a best RMSE of 1.53 hours, which translates to an accuracy of about 87.56% in time domain. The model could predict pH of the same untrained blind data with a satisfactory RMSE of 0.34 and an accuracy of about 68.75 %. Ordinary least square (OLS) has a better RMSE value than the neural network, but the trend is much well captured and understood by the feed forward ANN as compared to the OLS, which is clear from the slope value of the two (1.315 is the slope of the ANN's prediction curve, which is much closer to 1 than 0.332, slope of the OLS predictor) thus indicating performance being far superior when compared to the ordinary regression model. It has been thus demonstrated that an artificial neural network performs reasonably well in predicting time and pH, which can be used to compute a 'freshness index' that can be used in the commercial setting. However, it remains a fact that the amount of data trained to this model is insufficient to make a robust model that can be used in an actual commercial setting. It remains a matter of data collection to devise the same methodology as described herein to develop a real system that can accurately detect fresh and stale meat. A useful freshness score can be derived only after such data is collected and subsequently analysed for patterns. Arbitrarily making a freshness score without the right kind of data will not be useful, hence this work has not focused on the creation of such a freshness score. What has been thus demonstrated is the feasibility of using the THz system to predict freshness in meat using relevant parameters and the required amount of data/processing tools. The code for the above research was done in Python 3.8.

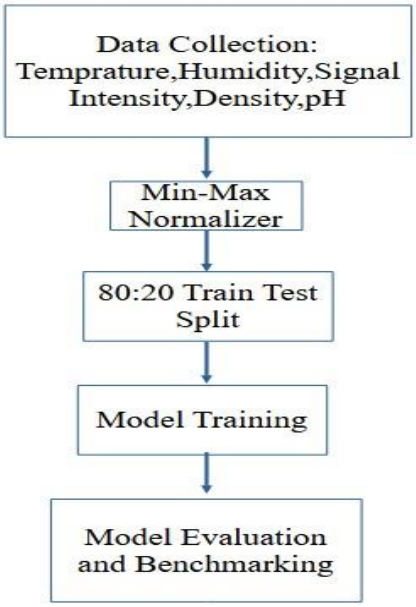

Figure.5.32 A flowchart summarising the model creation process is as attached adjacent.

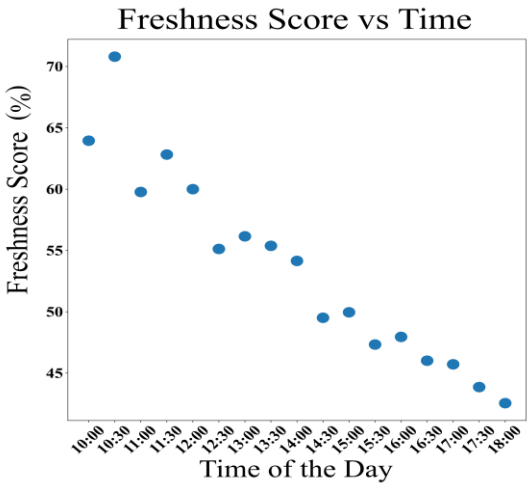

Figure.5.33 Freshness score with respect to the time of the day

The Feedforward ANN without scaling applied on input parameters had the best accuracy of 88.24 % for time, and the modular ANN without scaling achieved a 94.12 % accuracy on the pH data. A combination of these methods may yield better accuracies. Moreover, the predictions can be dynamically improved by training under user specific circumstances, to account for seasonal patterns, regional differences and topographical changes, such as change in humidity. Input parameters for all models were the signal strength of reflected rays, temperature and humidity of the surroundings. Since no other internal parameters need to be measured, our system is a non-contact method to determine freshness which shows in figure

5.32.

Table 5.1: Results from analysis methods used for determining Time and pH

Model	Input Parameter	Predictor	Min-Max Scaling	6-fold Cross Validated RMSE value	RMSE value for untrained day	Accuracy for Novel Data
Ordinary Linear Regression	Power	Time	Yes	1.771 hours	2.459 hours	17.65%
	Temprature		Yes	2.359 hours	1.621 hours	29.41%
	Humidity		No	1.712 hours	2.633 hours	17.65%
	Humidity, Temperature		No	1.587 hours	2.271 hours	0.58%
	Power, Temperature		Yes	1.380 hours	2.682 hours	17.65%
	Power, Humidity		Yes	0.676 hours	1.732 hours	41.18%
	Power, Humidity, Temprature		No	0.385 hours	0.655 hours	58.88%
	Power	pH	No	0.456	0.45	26.47%
	Temprature		No	0.333	0.976	23.53%
	Humidity		No	0.237	0.275	61.76%
	Humidity, Temperature		Yes	0.277	0.261	76.47%
	Power, Temperature		Yes	0.366	0.803	36.47%
	Power, Humidity		No	0.288	0.237	76.47%
	Power, Humidity, Temprature		No	0.12	0.179	88.24%
Random Forest	Power	Time	Yes	2.045 hours	1.856 hours	11.76%
	Temprature		No	2.379 hours	3.264 hours	5.88%
	Humidity		No	3.43 hours	2.941 hours	8.82%
	Humidity, Temperature		Yes	2.376 hours	1.706 hours	2.94%
	Power, Temperature		No	1.728 hours	5.574 hours	5.88%
	Power, Humidity		No	1.661 hours	1.435 hours	20.59%
	Power, Humidity, Temprature		No	0.578 hours	1.499 hours	17.65%
	Power	pH	No	0.478	0.541	32.35%
	Temprature		No	0.896	0.385	20.59%
	Humidity		No	0.345	0.387	61.76%
	Humidity, Temperature		No	0.286	0.604	35.29%
	Power, Temperature		No	0.337	0.795	23.53%
	Power, Humidity		Yes	0.288	0.237	88.24%
	Power, Humidity, Temprature		Yes	0.0631	0.225	82.35%
	Power	N.A*				
	Temprature	N. A				

Feedforward Neural Network	Humidity	N.A				
	Humidity, Temperature	Time	Yes	0.347 hours	2.047 hours	5.88%
	Power, Temperature		Yes	0.447 hours	1.839 hours	5.88%
	Power, Humidity		Yes	0.729 hours	1.399	76.47%
	Power, Humidity, Temprature		No	0.142 hours	0.5 hours	88.24%
	Modular Network		No	0.497 hours	2.034 hours	25%
	Power	N. A				
	Temprature	N. A				
	Humidity	N. A				
	Humidity, Temperature	pH	Yes	0.391	0.766	61.76%
	Power, Temperature		Yes	0.326	1.338	23.53%
	Power, Humidity		No	0.848	0.325	41.18%
	Power, Humidity, Temprature		No	0.083	0.34	70.59%
	Modular Network		Yes	0.142	0.179	94.12%

* Not Applicable since single input in FNN is equivalent to a linear regression with minimization of the chosen loss function (Mean Square Error).

5.13 Conclusion:

We have successfully demonstrated the system's operational capacity, achieving remarkable precision up to a distance of 3.0 meters. This was realized using a miniaturized 0.3 THz industrial, scientific, and medical (ISM) band frequency-modulated continuous wave (FMCW) radar system. The reflected signal strength exhibits a second-order polynomial nature intricately correlated with the signal bandwidth and the target's distance. The system's showing of maximum and minimum peak power at 289 and 329 GHz, respectively. The signal-to-noise ratio (SNR) of the order of 60 dB at a detection distance of 3.0 m. A detailed analysis underscores the system's capabilities, revealing a maximum target distance spanning 2.0 m for a 20 GHz bandwidth, 1.46 m for 30 GHz, 100 cm for 40 GHz, 80 cm for 50 GHz, and 63 cm for 60 GHz. This comprehensive investigation contributes valuable insights into the potential applications and performance like exciting parameters of TRCS measurements in the THz frequency range. Materials such as explosives, metals, wood, and acrylic have distinct peaks in THz signals. The K-nearest neighbours algorithm can identify materials quickly by measured the reflected signals and density of the materials. This system is useful in situations like bomb diffusion where material identification is not possible. It can be used in various settings like malls, metros, and airports for real-time testing. An innovative system is proposed to detect meat freshness efficiently in contemporary markets. The system promises swift and convenient

freshness assessment in meat. The challenge lies in the vast amount of data needed for meaningful results. Access to diverse raw data is crucial for a reliable model for commercial use. Artificial intelligence models are essential for interpreting trends effectively. The system can revolutionize meat quality assurance across industries. It uses silicon radar-like technology to create miniaturized THz sensor guns for non-contact meat inspection. This system's key feature is its non-contact nature, eliminating direct contact with meat.

Intentional Blank Page

References:

[1]. Angulo, D. de la Vega, I. Cascón, J. Cañizo, Y. Wu, D. Guerra, P. Angueira, "Impact analysis of wind farms on telecommunication services", Renewable and Sustainable Energy Reviews, **32**,84-89, (2014).

[2]. Philippe Lacomme, Jean Philippe Hardange, Jean Claud Marchais, Eric Normant, "Radar Applications and Roles", William Andrew Publishing, 347-369 (2001).

[3]. Efe Öztürk, Dieter Genschow, Uroschanit Yodprasit, Berk Yilmaz, Dietmar Kissinger, Wojciech Debski, and Wolfgang Winkler, "Measuring Target Range and Velocity, IEEE Microwave Magazine", **17**,1527-3342, (2017).

[4]. S. Scherr et al., "Miniaturized 122 GHz ISM band FMCW radar with micrometer accuracy," 2015 European Radar Conference (EuRAD), Paris, France, 277-280, (2015).

[5]. Bhutani, Akanksha, Marahrens, Sören, Kretschmann, Marius, Ayhan, Serdal, Scherr, Steffen, Göttel, Benjamin, Pauli, Mario and Zwick, Thomas, "Applications of radar measurement technology using 24 GHz, 61 GHz, 80 GHz and 122 GHz FMCW radar sensors" tm- TechnischesMessen, **89**, 2, 107-121(2022).

[6]. H.J. Song and T. Nagatsuma, "Present and future of terahertz communications," IEEE Trans. THz Sci. Technol., 1, 1, 256–263, (2011).

[7]. Y. P. Zhang, M. Sun, K. M. Chua, L. L. Wai, and L. Duixian, "Antenna in package design for wire bond interconnection to highly integrated 60-GHz radios," IEEE Trans. Antennas Propag., **57,** 10, 2842–2852, (2009).

[8]. T. Tajima, H.J. Song, K. Ajito, M. Yaita, and N. Kukutsu, "300-GHz step-profiled corrugated horn antennas integrated in LTCC," IEEE Trans.Antennas Propag., **62**, 11, 5437–5444, (2014).

[9]. S. E. Gunnarsson, N. Wadefalk, J. Svedin, S. Cherednichenko, I. Angelov, H. Zirath, I. Kallfass, and P. Leuther, "A 220 GHz single-chip receiver MMIC with integrated antenna," IEEE Microw. Wireless Compon. Lett., **18**, 4, 284–286, (2008).

[10]. Zhou Peigen, Chen Jixin, Tang Siyuan, Yu Jiayang, Wang Chen, Li Huanbo, Lu Haiyan, Yan Pinpin, Hou Debin, Chen Zhe, and Hong Wei "Research on Silicon-Based Terahertz Communication Integrated Circuits," Chinese Journal of Electronics, **31,** 3, (2022).

[11]. I. Sarkas, J. Kasch, A. Balteanu, and S. P. Voinigescu, "A fundamental frequency 120-GHz SiGe BiCMOS distance sensor with integrated antenna," IEEE Trans. Microwave Theory Tech., **60**, 3,795–812, (2012).

[12]. T. Jaeschke, C. Bredendiek, and N. Pohl, "A 240 GHz ultra-wideband FMCW radar system with on-chip antennas for high resolution radar imaging," in Proc. IEEE MTT-S Int. Microwave Symp. Dig. Tech. Papers, 1–4, (2013).

[13]. J. Lee, Y. A. Li, M. H. Hung, and S. J. Huang, "A fully-integrated 77-GHz FMCW radar transceiver in 65-nm CMOS technology," IEEE J. Solid-State Circuits, **45**, 12, 2746–2756, (2010).

[14]. S. Beer, C. Rusch, H. Gulan, B. Gottel, M. G. Girma, J. Hasch, W. Winkler, W. Debski, and T. Zwick, "An integrated 122-GHz antenna array with wire bond compensation for SMT radar sensors," IEEE Trans. Microwave Theory Tech., **61**, 12, 5976–5983, (2013).

[15]. M. Furqan, F. Ahmed, R. Feger, K. Aufinger, and A. Stelzer, "A 120-GHz wideband FMCW radar demonstrator based on a fully-integrated SiGe transceiver with antenna-in-package," in Proc. IEEE Int. Conf. Microwaves Intelligent Mobility, 1–4 (2016).

[16]. Y. Sun, M. Marinkovic, G. Fischer, W. Winkler, W. Debski, S. Beer, T. Zwick, M. G. Girma, J. Hasch, and J. C. Scheytt, "A low-cost miniature 120 GHz SiP FMCW/CW radar sensor with software linearization," in Proc. IEEE Int. Solid-State Circuits Conf. Dig. Tech. Papers,148–150, (2013).

[17]. A. Bhutani, B. Goettel, T. Streitz, S. Scherr, W. Winkler, and T. Zwick, "Low-cost antenna-in-package solution for 122 GHz radar module," in Proc. IEEE 46th European Microwave Conf., 1469–1472, (2016).

[18]. M. G. Girma, S. Beer, J. Hasch, M. Gonser, W. Debski, W. Winkler, Y. Sun, and T. Zwick, "Miniaturized 122 GHz system-in-package (SiP) short range radar sensor," in Proc. IEEE 10th European Radar Conf., 49–52, (2013).

[19]. S. Beer, C. Rusch, H. Gulan, B. Gottel, M. G. Girma, J. Hasch, W. Winkler, W. Debski, and T. Zwick, "An integrated 122-GHz antenna array with wire bond compensation for SMT radar sensors," IEEE Trans. Microwave Theory Tech., **61**, 12, 5976–5983, (2013).

[20]. G. Mangraviti, K. Khalaf, Q. Shi, K. Vaesen, D. Guermandi, V. Giannini, S. Brebels, F. Frazzica, A. Bourdoux, C. Soens, W. V. Thillo, and P. Wambacq, "A antenna-path beamforming transceiver for 60 GHz multi-Gb/s communication in 28 nm CMOS," in Proc. IEEE Int. Solid-State Circuits Conf. Dig. Tech. Papers, 246–247, (2016).

[21]. A. Tomkins, A. Poon, E. Juntunen, A. E. Gabaly, G. Temkine, Y. L. To, C. Farnsworth, A. Tabibiazar, M. Fakharzadeh, S. Jafarlou, A. Abdellatif, H. Tawfik, B. Lynch, M. Tazlauanu, and R. Glibbery, "A 60 GHz, 802.11ad/WiGig-compliant transceiver for

infrastructure and mobile applications in 130 nm SiGe BiCMOS," IEEE J. Solid State Circuits, **50**, 10, 2239–2255, (2015).

[22]. E. Cohen, M. Ruberto, M. Cohen, O. Degani, S. Ravid, and D. Ritter, "A CMOS bidirectional 32-element phased-array transceiver at 60 GHz with LTCC antenna," IEEE Trans. Microwave Theory Tech., **61,** 3, 1359–1375, (2013).

[23]. A. Townley, P. Swirhun, D. Titz, A. Bisogni, F. Gianesello, R. Pilard, C. Luxey, and A. Niknejad, "A 94 GHz 4 Tx-4 Rx phased-array for FMCW radar with integrated LO and flip-chip antenna package," in Proc. IEEE Radio Frequency Integrated Circuits Symp., 294–297, (2016).

[24]. B. H. Ku, O. Inac, M. Chang, H. H. Yang, and G. Rebeiz, "A highlinearity 76–85-GHz 16-element 8-transmit/8-receive phased-array chip with high isolation and flip-chip packaging," IEEE Trans. Microwave Theory Tech., **62,** 10, 2337–2356, (2014).

[25]. M. S. Dadash, J. Hasch, and S. P. Voinigescu, "A 77-GHz active millimeter-wave reflector for FMCW radar," in Proc. IEEE Radio Frequency Integrated Circuits Symp., 312–315, (2017).

[26]. T. Fujibayashi, Y. Takeda, W. Wang, Y. S. Yeh, W. Stapelbroek, S. Takeuchi, and B. Floyd, "A 76- to 81-GHz packaged single-chip transceiver for automotive radar," in Proc. IEEE Bipolar/BiCMOS Circuits Technology Meeting, 166–169, (2016).

[27]. D. G. Kam, D. Liu, A. Natarajan, S. Reynolds, and B. A. Floyd, "Low-cost antenna-in-package solutions for 60-GHz phased-array-systems," in Proc. IEEE 19th Electrical Performance and Electronics Packaging Systems, 93–96, (2010).

[28]. M. Furqan, F. Ahmed, R. Feger, K. Aufinger, and A. Stelzer, "A 120-GHz wideband FMCW radar demonstrator based on a fully-integrated SiGe transceiver with antenna-in-package," in Proc. IEEE Int. Conf. Microwaves Intelligent Mobility,1–4, (2016).

[29]. M. Pour Mousavi, M. Wojnowski, R. Agethen, R. Weigel, and A. Hagel Auer, "Antenna array in eWLB for 61 GHz FMCW radar," in Proc. Asia-Pacific Microwave Conf., 310–312, (2016).

[30]. I. Nasr, R. Jungmaier, A. Baheti, D. Noppeney, J. S. Bal, M. Wojnowski, E. Karagozler, H. Raja, J. Lien, I. Poupyrev, and S. Trotta, "A highly integrated 60 GHz 6-channel transceiver with antenna in package for smart sensing and short-range communications," IEEE J. Solid State Circuits, **51,** 9, 2066–2076, (2016).

[31]. M. Alonso-DelPino *et al.,* "Design Guidelines for a Terahertz Silicon Micro-Lens Antenna," in IEEE Antennas and Wireless Propagation Letters*,* 12, 84-8, (2013

[32]. M. Vogel, The Physical Optics Approximation in the Near-Field. Region, TNO Physics and Electronics Laboratory, Rep. no. FEL 1989- 100n, Mar. (1989).

[33]. K. Iwaszczuk, H. Heiselberg and P.U. Jepsen, Terahertz radar cross section measurements, Optics Express, **18**, 26399-26408, (2010).

[34]. Punam Pande, Sreemathy R and Mousami Turuk, "Radar Cross Section Modelling and Analysis of Static and Dynamic Targets using MATLAB", Journal of Aircraft and Spacecraft Technology, **6**,1-20, (2022).

[35]. Park, H.; Son, J.H. Machine Learning Techniques for THz Imaging and Time-Domain Spectroscopy, Sensors, 1186, **21**,1-25, (2021).

[36]. V.A. Trofimov, S.A. Varentsova, I.G. Zakharova, D.Y. Zagursky, "New Possibilities of Substance Identification Based on THz Time Domain Spectroscopy Using a Cascade Mechanism of High Energy Level Excitation," Sensors 2728, **17** (12), 1-24, (2017).

[37]. Guo, Gongde & Wang, Hui & Bell, David & Bi, Yaxin. KNN Model-Based Approach in Classification, Lecture Notes in Computer Science, **2888**, 986-996 (2004).

[38]. Ma L, Yi J, Wisuthiphaet N, Earles M, Nitin N, "Accelerating the Detection of Bacteria in Food Using Artificial Intelligence and Optical Imaging," Appl Environ Microbiol 89: e01828-22 (2023).

[39]. Chen, Jun et al. "Freshness Evaluation of Three Kinds of Meats Based on the Electronic Nose," Sensors, **19**,3 605. 31 (2019).

[40]. Yuandong Lin, Ji Ma, Da Wen Sun, Jun-Hu Cheng, Chenyue Zhou, "Fast real-time monitoring of meat freshness based on fluorescent sensing array and deep learning: From development to deployment," Food Chemistry Volume **448,**139078, (2024).

[41]. Felicia WXL, Rovina K, 'Aqilah NMN, Vonnie JM, Yin KW, Huda N. Assessing Meat Freshness via Nanotechnology Biosensors: Is the World Prepared for Lightning-Fast Pace Methods? Biosensors (Basel), **13(**2), 217, (2023).

[42]. Xiaohong Wu, Xinyue Liang, Yixuan Wang,Bin Wu, and Jun Sun, "Non-Destructive Techniques for the Analysis and Evaluation of Meat Quality and Safety: A Review, Foods. **11**, 22, (2022).

[43]. Xin B. Huang, Di B. Hou, Ping J. Huang, Ye H. Ma, Xian Li, Guang X. Zhang, "The meat freshness detection based on terahertz wave," Proc. SPIE 9795 in Photoelectronic Technology Committee Conferences, 97953D (2015). https://doi.org/10.1117/12.2211973.

[44]. Q. Liang, Z. Maocheng, Z. Jie, & T. Yuweiyi, “Preliminary investigation of Terahertz spectroscopy to predict pork freshness non-destructively.” Food Science and Technology, **39,**563–570 (2019).

[45]. T. Suzuki, K. Takayama, S. Yamauchi, Y. Imai and M. Tonouchi, "Measurement of water absorption coefficient using terahertz time-domain spectroscopy," 34th International Conference on Infrared, Millimeter, and Terahertz Waves, Busan, Korea (South), 1-2, (2009).

[46]. Y. Shen, P. Upadhya, E. Linfield, & A.G. Davies, “Temperature-dependent low-frequency vibrational spectra of purine and adenine,” Applied Physics Letters, **82** (14), 2350-2352 (2003).

[47]. Mir, Nasir Akbar et al. “Determinants of broiler chicken meat quality and factors affecting them: a review,” Journal of food science and technology, **54**,10, 2997-3009 (2017).

Intentional Blank Page

Chapter 6

6. Study of ultra-thin & free-standing α-MoO_3/β-PVDF composites for radar shielding applications

Abstract

In this chapter, we have demonstrated the multiple strategic applications of α-MoO_3/β-polyvinylidene fluoride (PVDF) composites in the THz domain. The free-standing thin sheets (~100 µm thick) of α-MoO_3/β-polyvinylidene fluoride (PVDF) composites were prepared using a simple solution casting-coagulation method. These composites are chosen for their scientifically rational constituents that exhibit electromagnetic shielding (SE) by means of absorption band between 0.2-1.6 THz range. The shielding effect in terms of absorption of these composites lie between 30.10 to 42.38 dB range. The SE by means of absorption is well-correlated to their dielectric behaviour. The rapid advancement of terahertz (THz) technology has heightened the demand for innovative shielding materials with high shielding effectiveness (SE) in the THz band spectrum. These materials show great potential by reducing the detectability of aircraft, ships, and vehicles through minimized radar cross-section (RCS). Also, these materials are used in aerospace and maritime industries to enhance stealth, in automotive vehicles to protect critical infrastructure from hostile radar targeting. Additionally, they find civilian uses in telecommunications, meteorology, and environmental monitoring by minimizing radar interference and improving signal quality. Overall, α-MoO_3/β-PVDF composites are essential for applications requiring reduced radar signature for improved operational effectiveness, safety, security, and stealth. This material is perfect THz absorbing materials duo to its outstanding (99.99% absorbing) EMI (THz signal) absorbing properties.

A part of the research work presented in this chapter has communicated in the following scientific peer reviewed journal

a) *Chandan Ghorui, Venkata Sreenivasulu Kummari, Anil Kumar Chaudhary and Venkata Satya Siva Srikanth Vadali, Ultra-thin Sheets of α-MoO_3/β-PVDF Composites for THz Shielding by Transmission and Reflection* ***(Communicated)***

6.1 Introduction:

Terahertz (THz) radiation is widely used in various applications such as wireless communication, imaging, radar systems, and sensing due to its accessibility and safety compared to X-rays [1-6]. The rapid development of THz technology has increased the demand for novel shielding materials with high shielding effectiveness (SE) in the THz band spectrum. In daily life, electronic devices for military, commercial, and aerospace purposes employ electromagnetic interference (EMI) shielding materials that function at high temperatures. For example, efficient EMI shielding materials are needed for battery management systems, which frequently operate at temperatures above 50°C. Consequently, there is a growing demand for a variety of THz shielding materials, including metallic [7], ceramic [8], semiconducting [9], magnetic [10], MXenes-based [11-13], meta [14], carbon-based [15-17], and novel composite materials [18-22] with high SE. However, developing lightweight, easily processable, flexible, and efficient THz shielding materials are highly desirable to protect specific components and their surroundings. Recently, nanomaterial/polymer composites have gained prominence in this context (Table 6.1) [23-28]. These composites exhibit excellent THz shielding ability, mainly through absorption. When nanocarbons are used as fillers, the Maxwell–Garnett model predicts strong absorption of high-GHz to several THz electromagnetic (EM) waves, depending on the fillers' aspect ratio and electrical conductivity [29]. In dilute nanomaterial/polymer composites, such as graphene/epoxy composites [25], the strong absorption of THz radiation is also attributed to the interaction between the active atomic vibrations in epoxy and the π-band to polaron band transitions in graphene, which are in resonance with THz radiation [23,31-33].In materials with excellent percolation networks, primarily metals [30], graphene [34], and composites [35-37], the incident electromagnetic wave interacts with the free carriers in the material, resulting in shielding through reflection. Multiple internal reflections may also contribute to the shielding if the filler flake size is comparable to the wavelength of the incident wave [30].

Table 6.1. THz electromagnetic shielding of nanomaterial/polymer composites with optimal characteristics.

Composite	Thickness (mm)	Frequency (THz)	SE (dB)	Ref.
10 wt % graphene/polydimethylsiloxane (PDMS)	0.6	0.6	34	[23]
14.44 vol % carbon black (CB)/ethylene co-butyl acrylate (EBA)	1	0.9	80	[24]

1.2 wt % graphene/epoxy	1	1.6	70	[25]
12.5 wt % carbon nanofiber (CNF)/poly (methyl methacrylate) (PMMA)	0.9	0.6	56.8	[26]
40 wt % Fe_3O_4/CNF/PMMA/Polyvinylidene fluoride or polyvinylidene difluoride (PVDF)	0.054	1.2	60	[27]
0.33 vol % CVD graphene/PMMA	0.0033	2	60	[28]

Even though excellent nanomaterial/polymer composites are prepared for THz shielding by absorption and reflection, there is still room to develop practically viable ones for THz shielding by transmission. In this regard, selecting the constituents (i.e., the polymer matrix) based on scientific rationale may help develop suitable composites. In this work, β-PVDF and α-MoO_3 are selected as the polymer matrix and the filler, respectively, to prepare α-MoO_3/β-PVDF composites based on specific scientific rationale. β-PVDF is an excellent matrix material because it can be easily processed, is lightweight and flexible, is bio-compatible and sustainable, and, more importantly, its excellent dielectric and piezoelectric characteristics (due to its polar chains) [38] aid in its significant shielding of 8-26.5 GHz frequency range [39]. It can effectively host highly conductive fillers and metal oxides for EM wave shielding applications [22,40]. PDVF also allows blending with other suitable polymers for EM wave shielding applications [40]. α-MoO_3 is a van der Waals semiconductor and a hyperbolic metamaterial that can facilitate strong EM wave-matter interactions with negative refraction [41]. High dielectric loss and suitable impedance of α-MoO_3 may help in enhancing the shielding when used as a filler in test composites [42]. MoO_3 has been incorporated in polyethylene matrix for neutron shielding,[43]. The poly (vinyl alcohol) and PVDF matrices are being employed for flexible electronics, and for other applications, respectively [44-46]. N-doped MoO_3 has been used in GHz absorption, [47] and when defective MoO_3 was heterogeneously interfaced with other metal oxides, it was helpful in microwave absorption [48]. In this work, the advantages of β-PVDF and α-MoO_3 are tapped by preparing free-standing thin sheets of α-MoO_3/β-PVDF composites with varied amounts of α-MoO_3 for extraordinary THz shielding by transmission and reflection.

α -molybdenum trioxide (α -MoO_3) materials used as a radar shielding material, particularly in the form of diverse morphology at micro & nanoscale. α-MoO_3 exhibits fascinated electrical and optical properties which were make it suitable for radar shielding applications [49-51]. In radar shielding, α-MoO_3 can be applied as a coating on surfaces to attenuate or reflect radar waves. Its ability to absorb and reflect electromagnetic radiation, particularly in the microwave

and terahertz frequency ranges, makes it useful for reducing radar cross-section (RCS) and improving stealth characteristics of objects or structures. In our experiment, α-MoO_3 materials blocked the THz signal and reduces the radar cross section (RCS) and improve the stealth characteristics of metallic targets. α-Molybdenum trioxide (α-MoO_3) is considered a promising radar shielding material compared to other metal oxide materials for several reasons, (i) α-MoO_3 has a relatively wide bandgap, which allows it to interact with electromagnetic radiation in a broad range of frequencies, including microwave and terahertz frequencies typically used in radar systems. (ii) The electrical and optical properties of α-MoO_3 can be tailored by adjusting its composition, structure, and processing conditions. This tunability allows for optimization to match specific radar frequency bands, enhancing its effectiveness as a radar shielding material. (iii) α- MoO_3 exhibits a relatively high dielectric constant, which influences its ability to interact with electromagnetic waves. This property can be advantageous for absorbing and attenuating radar waves, thereby reducing radar cross-section. (iv) Molybdenum is relatively abundant in the Earth's crust, making α-MoO_3 potentially more cost-effective compared to other radar shielding materials. Additionally, the manufacturing processes for α-MoO_3 thin films or coatings can be relatively simple and scalable. (v) α-MoO_3 is chemically stable under various environmental conditions, which is crucial for long-term performance and durability in practical radar shielding applications. (vi) α-MoO_3 can be deposited as thin films on various substrates, including flexible and rigid surfaces, allowing for versatility in design and application.

6.2 Experimental methods and sample preparation:

6.2.1 Starting materials & preparation of the thin sheets of β-PVDF and α-MoO_3/β-PVDF composites:

Polyvinylidene fluoride (α-PVDF) with a molecular weight of 180000 g/mol, molybdenum (VI) oxide (α-MoO_3), and N, N-Dimethylformamide (DMF) were procured from Alfa Aesar (India), Sigma Aldrich (India) and SRL Private Ltd (India).

A simple solvent casting method followed by a water coagulation process was used to prepare the thin sheets of β-PVDF and α-MoO_3/β-PVDF composites. 1 g of α-PVDF was mixed in 10 mL of DMF in a 50 mL glass beaker. This solution was stirred at a temperature of 65 °C until it turned into a transparent viscous solution, which was cast in a typical Petri dish. Finally, water coagulation released the 100 µm thick free-standing sheet of β-PVDF (named PVDF-F) from the Petri dish. In the case of the thin sheets of α-MoO_3/β-PVDF composites, appropriate amounts of α-MoO_3 and α-PVDF (such that the total amount was always 1 g) are mixed

simultaneously in 10 mL of DMF in the first step while the rest of the steps remain the same. For example, M1 is prepared by taking 0.01 g of α-MoO_3 and 0.99 g of α-PVDF. Figure.6.1 (a) represents the synthesis process of ultrathin sheets of α-MoO_3/β-PVDF composites.

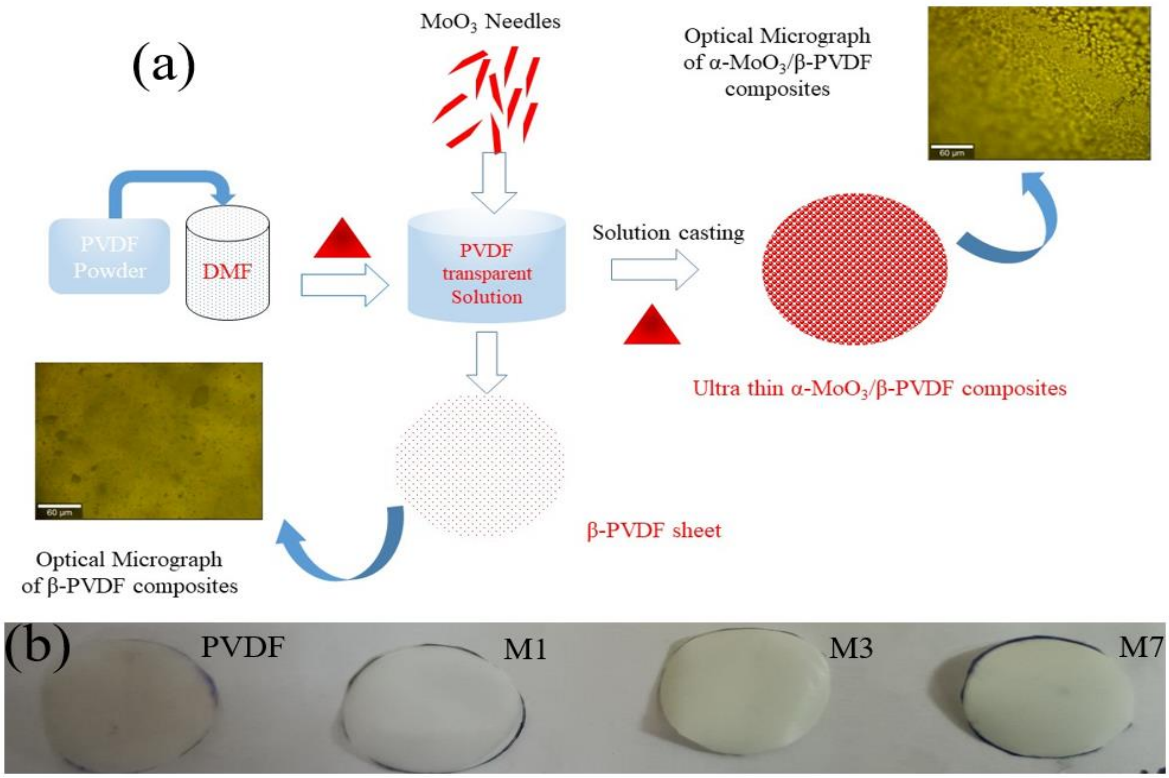

Figure 6.1 (a) Sample preparation process of ultra-thin α-MoO_3/β-PVDF composites (b) optical image of PVDF-F, M1, M2, M3, M5, and M7 samples by prepared 1 wt%, 3 wt%, 5 wt% & 7 wt% of α-MoO_3 respectively.

6.2.2 Experimental techniques of measurement of THz electromagnetic shielding values of α-PVDF composites:

The terahertz electromagnetic shielding performance and reflection behaviors were measured using terahertz time-domain spectroscopy (THz-TDS-TOPTICA FemtoFErb THz FD 6.5) in both transmission and reflection modes. The test room's humidity was kept below 5 % for the measurements, which were carried out at room temperature (300 K). An Erbium-based femtosecond laser was used to excite an InGaAs photoconductive antenna, producing the terahertz pulse. Detection of the terahertz signal was performed by an InAlAs photoconductive antenna. For each measurement, the sample was affixed to a hollow aluminum plate, and a 2.5 mm THz beam was focused on the sample from a distance of 3 mm. The EMI SE values were calculated using the following equation

$$\text{EMI SE} = -20\log\left(E_{sample}/E_{air}\right) \quad (6.1)$$

where the terms "E_{sample}" and "E_{air}" stand for the transmission terahertz pulse amplitudes for the samples and the air, respectively. With ESample representing the measured amplitude of the electric field reflected via the sample and EReference representing the measured amplitude of the electric field reflected from the reference, the sample's reflectivity (R) was determined using the formula $R=E_{Sample}/E_{Reference}$. A gold-coated mirror was used as a reference. Care was taken to arrange the distances among the sample, antenna, and THz source to avoid phase errors in reflection geometry [52]. The THz beam was directed onto the sample surface at an angle of incidence of 8° to minimize the paraxial error significantly. Then, the shielding effectiveness (SE) by absorption, reflection, and transmission and total SE (SE_{Total}) were calculated using the standard relations in the frequency 0.2-1.6 THz [53,54]. The specific shielding effectiveness (SSE) of the samples was calculated by using the relation SSE (dB cm^3 g^{-1}) = SE_{Total}/Density of the sample. The densities of the samples PVDF-F, M1, M2, M3, M5, and M7 are taken as 1.78, 4.67, 4.61, 4.55, and 4.50 g/cm^3, respectively, in calculating SSE in respective cases. The samples' absolute shielding effectiveness (SSE_t) was calculated using the relation, SSE_t (dB cm^2 g^{-1}) = SSE/Thickness of the sample. The thickness of the sample in each case was taken as 100 µm.

6.3 Measurement of concealed metallic target using 300 GHz radar source

To attain micrometer accuracy, a frequency-modulated continuous wave (FMCW) radar system that is downsized in the 0.3 THz industrial, scientific, and medical (ISM) band is utilized. This radar system is made up of liquid crystal polymer (LCP) off-chip antennas and a silicon single-chip radar sensor that are combined into a quad flat no-lead (QFN) device. Another important component in producing THz frequencies is the microcontroller, which usually generates the high-frequency THz signal via direct digital synthesis (DDS) or phase-locked loops (PLLs). Terahertz waves can effectively penetrate various materials, including clothing and packaging, while providing valuable information about the composition of hidden objects. The beauty of the terahertz techniques is it can detect the hidden objects. Moreover, terahertz radar can provide valuable insights into the nature of hidden items without the need for physical contact or the use of ionizing radiation. The detection and identification capabilities of terahertz radar make it a powerful tool in the realm of security, particularly in scenarios where the concealed objects may pose a threat to public safety. In our experiment, firstly, we have recorded the direct metallic target signal using 0.3 THz FMCW radar source and after that we have recorded the metallic signal with the wrap of α-MoO_3/β-PVDF composites.

6.4 Results and Discussion:

6.4.1 Crystallographic information & Raman spectroscopy:

The X-ray diffractograms of as-procured PVDF (PVDF-O) and α-MoO_3 (MP), as-prepared PVDF film (PVDF-F), and different free-standing films of α-MoO_3/PVDF composites (named M7, M5, M3, and M1) are shown in Figure 6.2. M1, M3, M5, and M7 are prepared using 0.01, 0.03, 0.05, and 0.07 g of α-MoO_3 in 0.99, 0.97, 0.95, and 0.93 g of PVDF, respectively. In the case of PVDF-O, the diffraction peaks at 2θ = 18.4°, 19.8° and 26.4° are indexed to (020), (110), and (021) planes, respectively, in α-PVDF. In the case of PVDF-F, the diffraction peak in the 2θ range of 20.2°-20.6° confirms the formation of the required β-PVDF [38,52-54]. This diffraction peak is also observed in the case of M1, M3, M5, and M7, indicating that β-PVDF matrices constitute the composite sheets. In the case of MP, M1, M3, M5, and M7, the other diffraction peaks are indexed to orthorhombic α-MoO_3 in agreement with the card number JCPDS-05-0508 [55-57]. To clarify the formation of β-PVDF in the presence of α-MoO_3, the indexed x-ray diffractograms of the samples in the 2θ range of 16°-29° are shown in Figure 6.3.

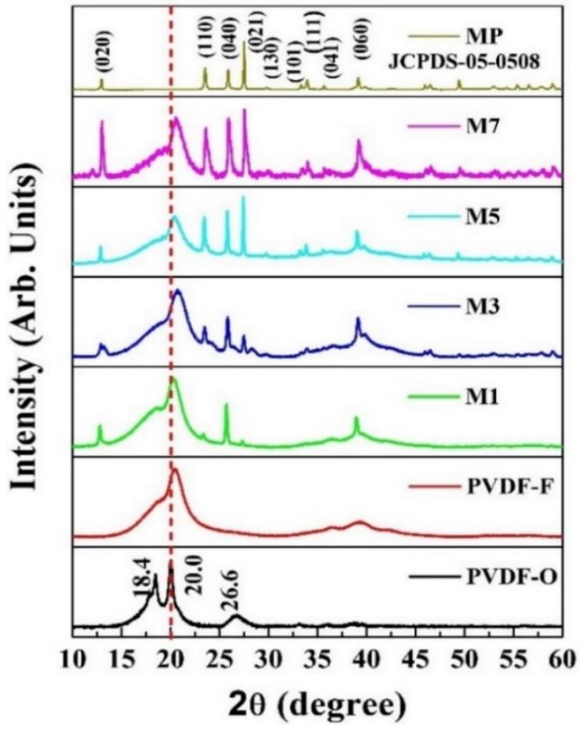

Figure 6.2. X-ray diffractograms of PVDF-O, MP, PVDF-F, and different free-standing α-MoO_3/PVDF composite films (M1, M3, M5, and M7). The X-ray diffractograms are recorded using Copper Kα radiation.

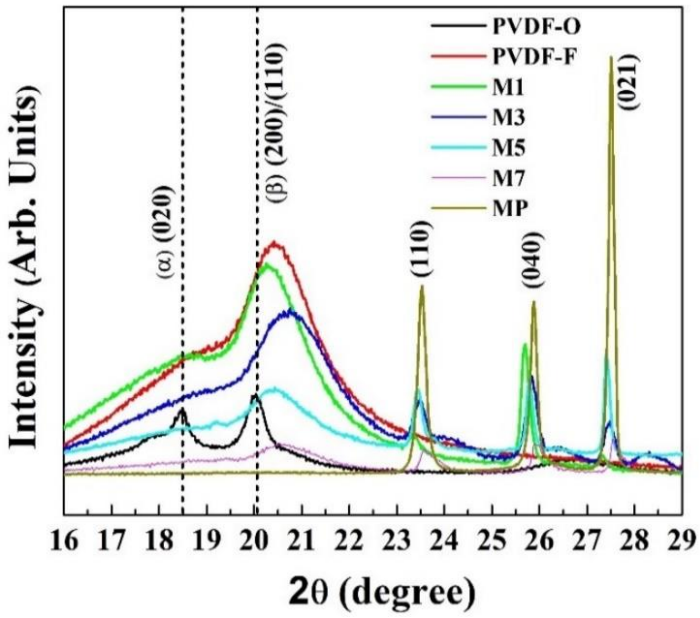

Figure 6.3. X-ray diffractograms of PVDF-O, MP, PVDF-F, and different free-standing α-MoO_3/β-PVDF composite films (M1, M3, M5, and M7) in the 2θ range of 16°-29°. The crystallographic planes in α and β phases of PVDF are indicated.

In addition to confirming the formation of α-MoO_3/β-PVDF composites using the x-ray diffraction analysis, Raman scattering was used to complement. Raman spectra of all the samples are shown in Figure 6.4. Raman bands at 813 cm^{-1}, 841 cm^{-1}, and 882 cm^{-1} concomitants with the rocking vibrations of CH_2 (ω), CH2 (Γ), and CC (ν_s), respectively, in γ-, β-, and α+β- PVDF are observed [58,59]. Raman scattering results show that α-PVDF is not wholly transformed into β-PVDF in the case of PVDF-F, M1, M3, M5, and M7 samples, implying that the presence of minute amounts of other polymorphs of PVDF that x-rays could not pick. In other words, β-PVDF is the dominant polymorph in these samples. Also, it was observed that the β-PVDF was even more dominant with higher α-MoO_3 content in the composites. The Raman band at 661 cm^{-1} in PVDF-F is attributed to the defective linkages in the skeletal chains of PVDF [55]. This Raman band overlapped with the 666 cm^{-1} (B_{2g}, B_{3g}) Raman band of α-MoO_3 in MP, M1, M3, M5, and M7 samples [60]. The prominent Raman bands at 819 cm^{-1} (A_g, B_{1g}) and 995 cm^{-1} (A_g, B_{1g}), as indicated in Fig. 6.3, further confirm the presence of α-MoO_3 in MP, M1, M3, M5, and M7 samples [60-65].

Table 6.2: Vibrational mode wavenumbers (cm^{-1}) of undoped PVDF

Band	Phase	Group, Vibrational Mode
485	γ	
513	β	CF_2 δ
610	α	CF_2 δ
795	α	CH_2 r
812	γ	CH_2 ω
840	β	CH_2 r
881	α, β	CC ν_s
		CC ν_s
1076		CC ν_a
1171		CH_2 ω
1265		CC ν_s CCC δ
1430		CH_2 δ; CH_2 ω
2440		CH_2 deform.
2980		CH_2 ν_s

ν_s Symmetric Stretching**; ν_a** asymmetric stretching**; δ** scissoring**; ω** wagging**; r** rocking

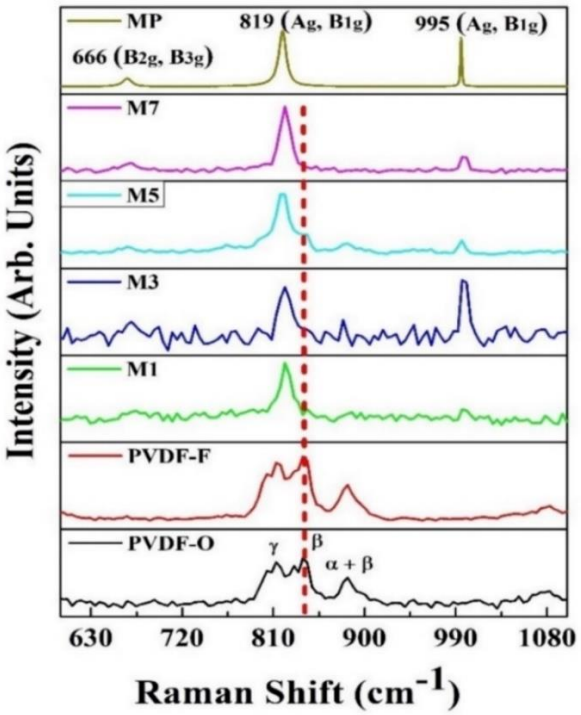

Figure 6.4. Raman spectra of PVDF-O, MP, PVDF-F, and different free-standing α-MoO_3/β-PVDF composite films (M1, M3, M5, and M7). 532 nm LASER was used to record these spectra.

For, α-MoO_3, the Raman vibrational modes are written as follows the equation (6.2)

$$\Gamma = 8A_g + 8B_{1g} + 4B_{2g} + 4B_{3g} + 4A_u + 3B_{1u} + 7B_{2u} + 7B_{3u} \quad (6.2)$$

Herein the Raman active modes are A_g, B_{1g}, B_{2g} and B_{3g}. whereas A_u is an inactive and all others are infrared active modes.

Optical micrographs have been captured during the Raman spectroscopy measurements using 532 nm green laser at 25 mW power. In the observed micrographs, M0 indicates Pure PVDF and M1, M5 and M7 are 1 wt%, 5 wt% and 7 wt% of molybdenum oxide reinforced with PVDF samples. Molybdenum oxide isolated nano particles are distributed homogeneously throughout the PVDF free standing micro sheets as well as cluster formation were observed in case of M1, M5 and M7. It is clearly observed from the micro graphs that increased weight percentage of molybdenum oxide nano particles increasing the cluster formation, which is shown in Figure 6.5.

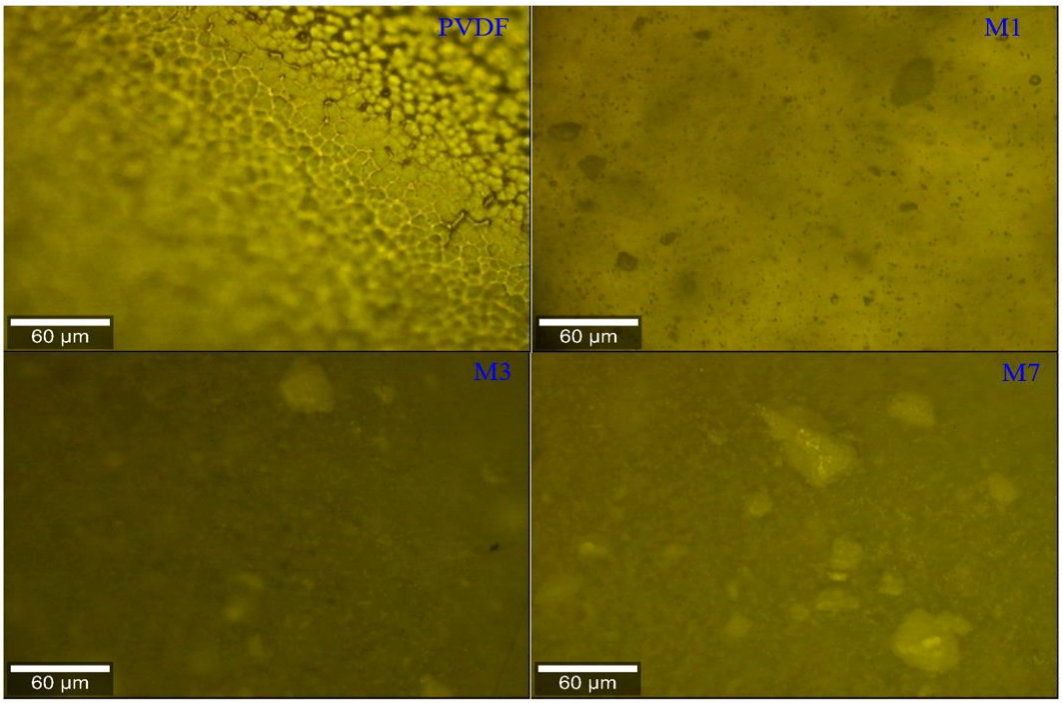

Figure 6.5: Raman optical Micrographs of PVDF (M0) and its α-MoO_3 composites at 1 wt% (M1), 3 wt % (M3) and 7 wt % (M7).

In comparison to the optical micrographs, we have also performed Scanning Electron Microscopy (SEM) experiments to observe the size shape and morphology of the PVDF and its molybdenum oxide composites M0, M1, M3 and M7. SEM micro graphs are in good agreement with the optical micrographs. During the synthesis process an agglomeration of molybdenum oxide nano needles lead to formation of clusters, which is increasing with increased weight percentages of molybdenum oxide in PVDF/MoO_3 composites, which is clearly observed in the Figure 6.6 shown below.

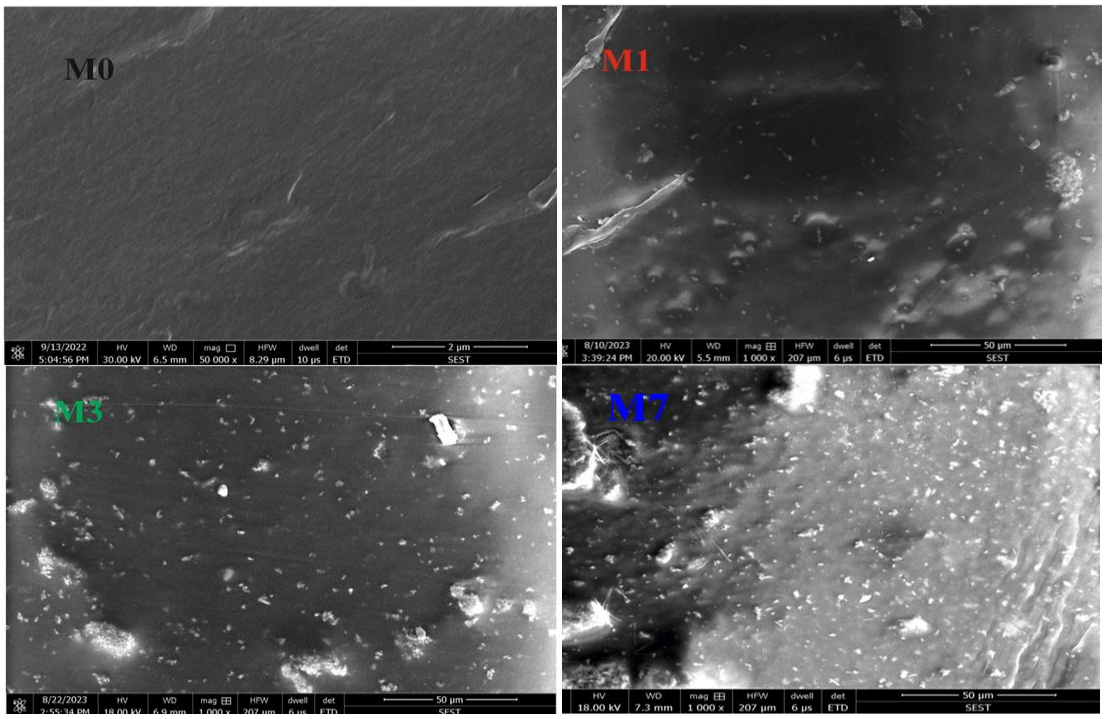

Figure 6.6: Scanning Electron Micrographs of PVDF (M0) and its α-MoO_3 composites at 1wt% (M1), 3 Wt % (M3) and 7 wt % (M7)

Table 6.3: Energy dispersive x-ray spectrum (EDX) analysis of PVDF and its α-MoO_3 composites

Elemental Analysis of PVDF and Its α-MoO_3 composites

Elemental Analysis of PVDF and Its α-MoO_3 composites								
Elements	Weight percentage (%)				Atomic percentage (%)			
	M0	M1	M3	M7	M0	M1	M3	M7
C	56.8	52.2	54.5	53.5	67.5	63.7	66.2	65.2
F	43.2	46.9	43.7	43.1	32.5	36.1	33.6	34.1
Mo	-	0.9	1.8	3.4	-	0.1	0.3	0.7
Total	100	100	100	100	100	100	100	100

Elemental analysis was done by using energy dispersive X-ray spectroscopy (EDXS). Weight and atomic percentages of presence of elements in PVDF alone and α-MoO_3/β-PVDF composites have been shown in Table 6.3. It is clearly observed from the elemental analysis that Presence of PVDF alone and its Molybdenum oxide composites were confirmed with respect to the presence of elements in atomic and weight percentages. weight and atomic percentages of Mo is increased with increasing Molybdenum oxide weight percentage, which is confirmed and occurred with respect to the weight and atomic percentages of elements shown in Table 6.3.

6.4.2 Electromagnetic shielding interface of α-MoO_3/β-PVDF composites in THz range:

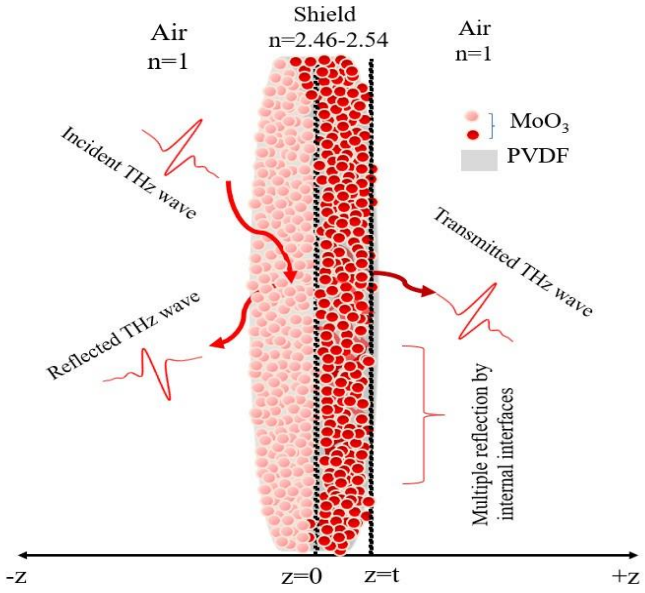

Figure 6.7. Graphical representation of THz EMI shielding for α-MoO_3/β-PVDF composites

Figure 6.7 presents the graphical representation of THz electromagnetic shielding for α-MoO_3/β-PVDF composites. The quasi-optic free-space method was used to determine scattering parameters of composites. THz spectroscopy at 0.2-1.6 THz frequency range in transmission and reflection modes was employed. Measurements were conducted at room temperature with humidity below 5% using a reference and sample. A femtosecond laser excited an InGaAs antenna to generate terahertz pulse, detected by an InAlAs antenna. The sample, placed on an aluminum plate, was exposed to a 2.5 mm THz beam from 3 mm distance. The obtained scattering characteristics were then converted to analyze. The reflection R & transmission T was measured by equations (6.3) & (6.4) respectively,

$$R = \frac{E_{Sample}}{E_{Reference(Gold\ Coated\ Mirror)}} \tag{6.3}$$

$$T = \frac{T_{Sample}}{T_{Reference(Air)}} \tag{6.4}$$

Equation (6.5) & (6.6) provides the absorption coefficient, A, and the effective absorption coefficient, Aeff, which were computed using the acquired R and T.

$$A=1-T-R \tag{6.5}$$

$$A_{eff} = \frac{A}{(1-R)} \tag{6.6}$$

The shielding due to transmission, reflection & absorption are calculated by the equations (6.7), (6.8) & (6.9) respectively

$$SE_T = -20\log(1 - T) \tag{6.7}$$

$$SE_R = -20\log(1 - R) \tag{6.8}$$

$$SE_A = -20\log(1 - A_{eff}) \tag{6.9}$$

Total shielding of the material is calculated by equation (6.10)

$$SE_{Total} = SE_T + SE_R + SE_A \tag{6.10}$$

Since some of the EM energy is reflected off the material's surface, one must take into account that Aeff represents the material's true absorption properties. The transmission (T) and reflection (R) for α-MoO_3/β-PVDF composites with α-Molybdenum trioxide content ranging from 1.0 to 7.0 wt% are shown in Figures 6.8 (a), (b). Figure 6.8 (a) highlights the bottom limit of the transmission coefficient (T<3.5%), which allows for a distinct distinction of transmission for the pure PVDF-F materials. It is evident that a small addition of α-Molybdenum trioxide (1.0−7.0 wt%) significantly reduces the transmission but does not significantly change the specimens' electromagnetic wave reflection.

The shielding α-MoO_3/β-PVDF composite material's electromagnetic interface absorption properties are defined by both parameters. The top limit of the effective absorption coefficient (Aeff > 96%) is shown in Figure 6.8d, which clearly allows the Aeff values for the composites with α-MoO_3/β-PVDF content greater than 1 wt % to be distinguished from one another. The data shown in Figure 6.7 clarifies that absorption is the main EM wave shielding mechanism in composites with a low graphene content (1−7 wt%). When just 93–97 wt% α-MoO_3/β-PVDF composite fillers are present in the M1-based composite, the absorption, A, increases from 7% for M7 to more than 1% (see Figure 6.8c). For the composites having an α-MoO_3/β-PVDF content of 1 wt% or more in this frequency range, the absorption continuously increases with frequency (see Figure 6.8c, d).

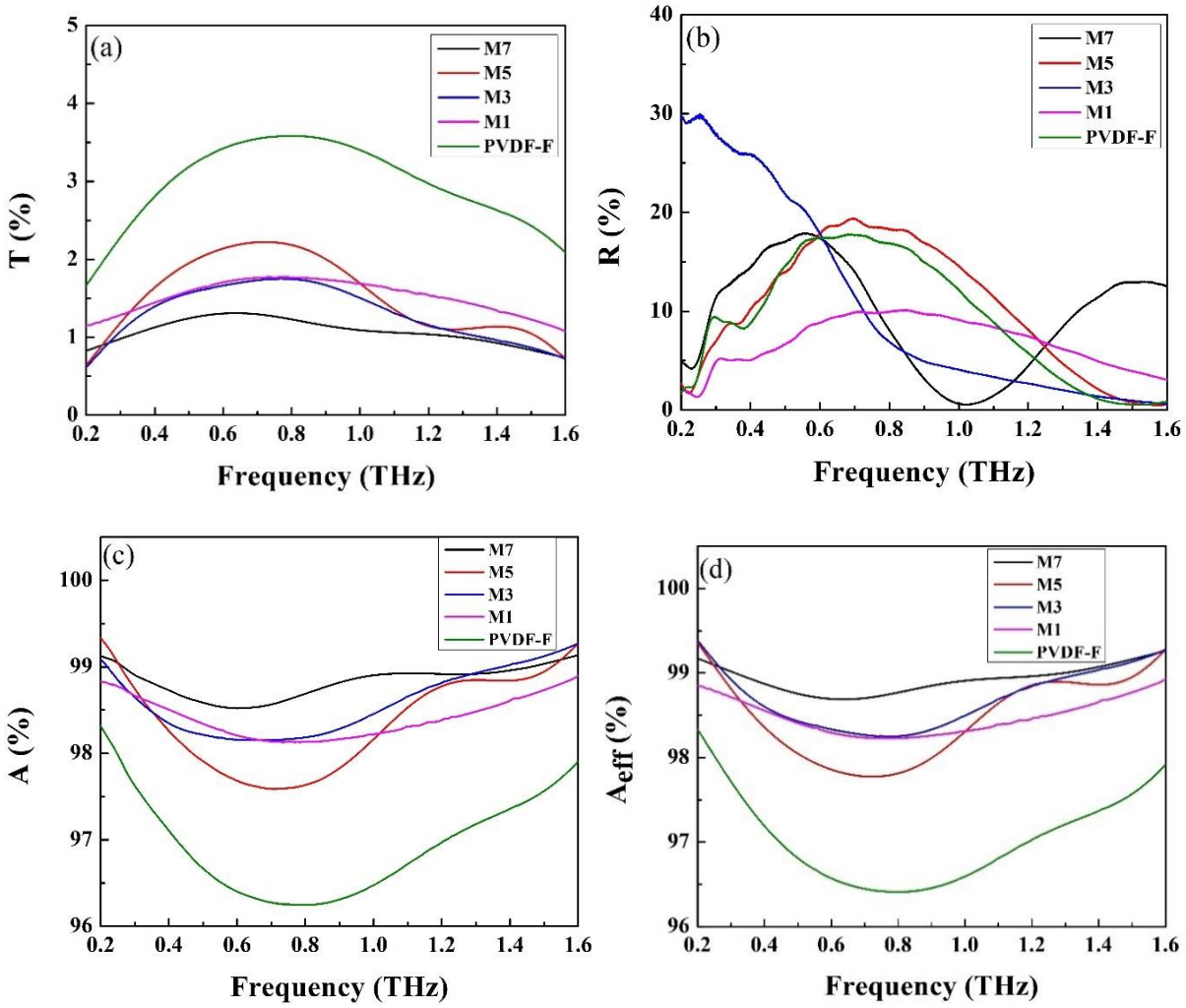

Figure 6.8. (a) transmission (b) reflection (c) absorption and (b) effective absorption for α-MoO_3 in the composites with different weight percentage of MoO_3 sample.

SE values as a function of THz frequencies (0.2-1.6 THz) of PVDF-F, M1, M3, M5, and M7 are shown in Figure 6.9. The SE values due to transmission (SE_T) (Fig. 6.9(a)) and reflection (SE_R) (Fig. 6.9(b) are either negligible or very low (in the range ~0.2 and 1.6 dB) for all the samples. On the contrary, high SE due to absorption (SE_A) and total SE (SE_{Total}) values (in the range ~41.44 and 42.73 dB) (Figures. 6.9(c) and (d)) due to absorption are recorded for all the samples in the considered THz frequencies range. The average SE_{Total} values (Fig. 6.9(d)) of PVDF-F, M1, M3, M5, and M7 are ~36.44, 39.41, ~38.05, 38.04, and 38.94 dB, respectively, at 0.2-1.6 THz region. PVDF-F, M1, M3, M5, and M7 also showed excellent shielding through absorption between 0.2-1.6 THz (Figure 6.9 (d). Figure 6.10 shows the absolute shielding effectiveness (SSE_t) values for all the samples in the range ~840 dB cm^2 g^{-1} - 884 dB cm^2 g^{-1}, respectively, in the considered THz frequencies range. The absolute shielding effectiveness value of pure PVDF-F is 205 dB cm^2 g^{-1}.

The different EMI SE values shown in Figure 6.8 indicate that the shielding by absorption can be tailored at different THz frequencies by incorporating different amounts of α-MoO_3 in the composites.

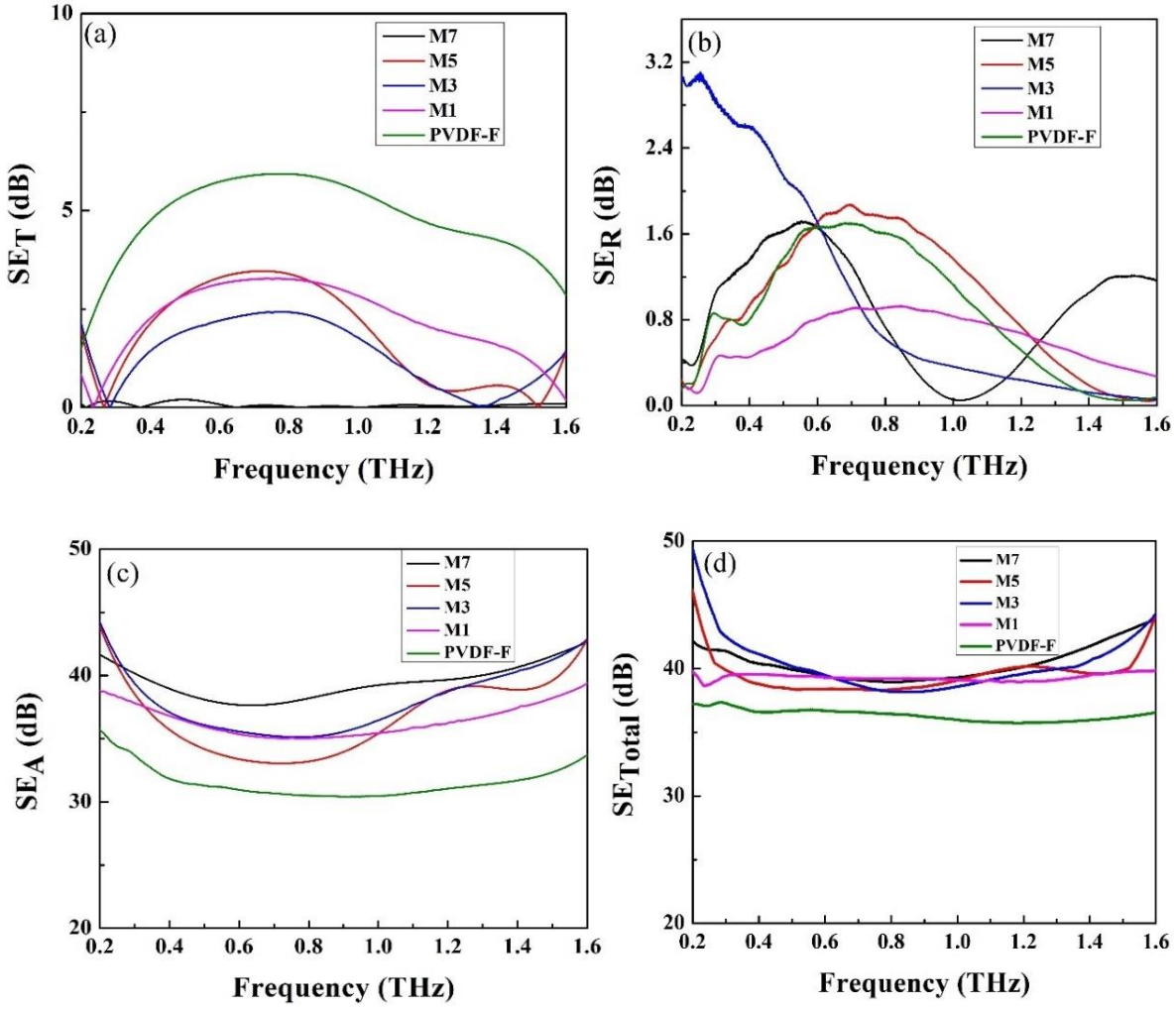

Figure 6.9. (a) EMI shielding by transmission, (b) EMI shielding by reflection, (c) EMI shielding by absorption, and (d) total shielding of PVDF-F and α-MoO_3/β-PVDF composite films (M1, M3, M5, and M7) as a function of THz frequencies.

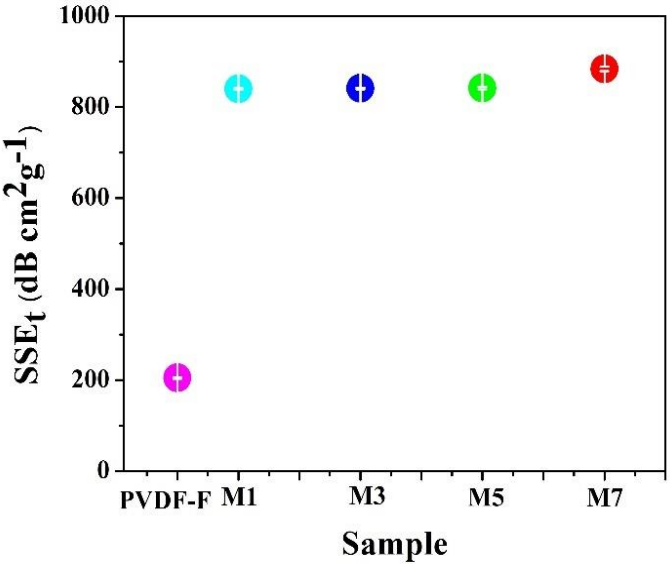

Figure 6.10 Absolute Shielding values of 100 µm thick PVDF-F, M1, M3, M5, and M7 at 205, 840, 841, 842 and 888 dBcm^{2}g^{-1}, respectively. The calculations are done by considering twenty measurements for each sample.

The real and imaginary parts of the dielectric constants (Figure 6.11) for the 100 µm thick free-standing M7, M5, M3, M1, and PVDF-F samples were calculated as a function of the considered THz frequencies using standard procedures and Maxwell's relations. It is well known that higher values of the real part of the dielectric constant generally correspond to better THz shielding through transmission, while higher values of the imaginary part of the dielectric constant generally correspond to better THz shielding through absorption [66]. Figure 6.11 (a) shows that the M7, M5, M3, M1, and PVDF-F samples exhibited appreciable dielectric permittivity values. The M1, M3, M5, and M7 samples, in particular, demonstrated similar behavior, with permittivity values ranging from 1 to 6 across the 0.2-1.6 THz frequency range. These samples also exhibited the highest values of the imaginary part of the dielectric constants at the THz frequencies where peak SE_{Total} values (Figure 6.9(d)) were measured for samples of the same thickness. These samples showed significant shielding through absorption in the 0.2-1.6 THz range (Figure 6.9 (d)), and shows strongly correlation with the required peak permittivity values (Figure 6.11 (a)) and the highest values of the imaginary part of the dielectric constants at corresponding frequencies (Figure 6.11 (b)). These observations are consistent with the highest SE_A values recorded for these samples at the same THz frequencies, as discussed (Figure 6.9(c)).

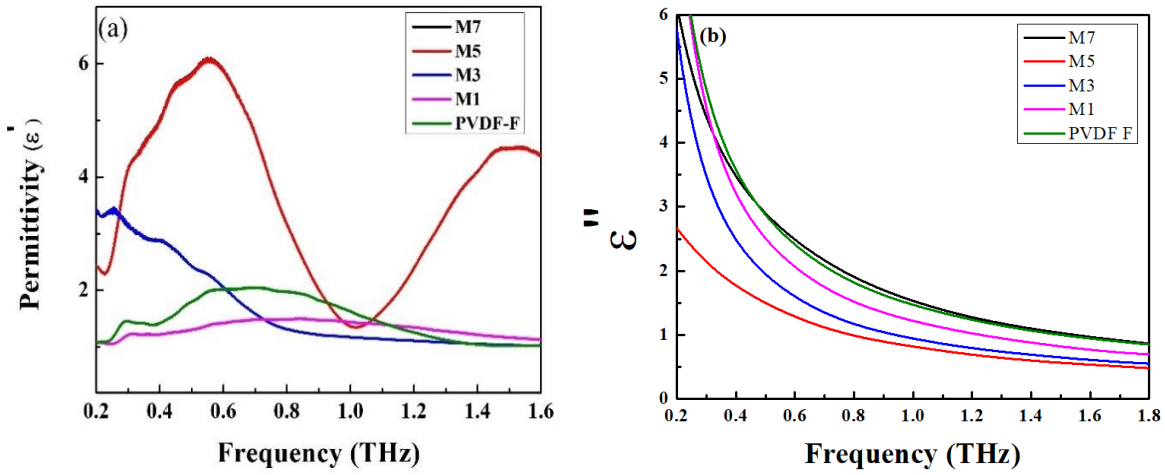

Figure 6.11. (a) The real part (i.e., permittivity) and (b) imaginary part of the dielectric constants (ε'') of the 100 µm ultra-thin free-standing M7, M5, M3, M1 and PVDF-F samples as a function of the considered THz frequencies.

6.4.3 Radar shielding application:

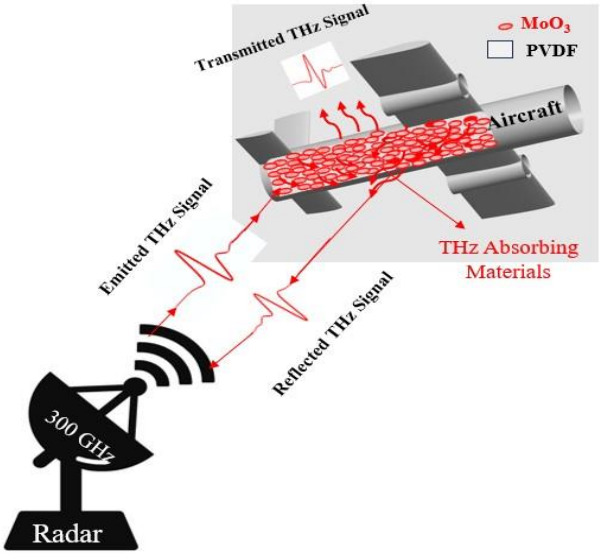

Figure 6.12. EMI Shielding by reflection of α-MoO_3/β-PVDF composite films for radar applications.

Figure 6.13 (a) represents the radar signal from direct and concealed metallic targets wrapped with α-MoO_3/β-PVDF composites.

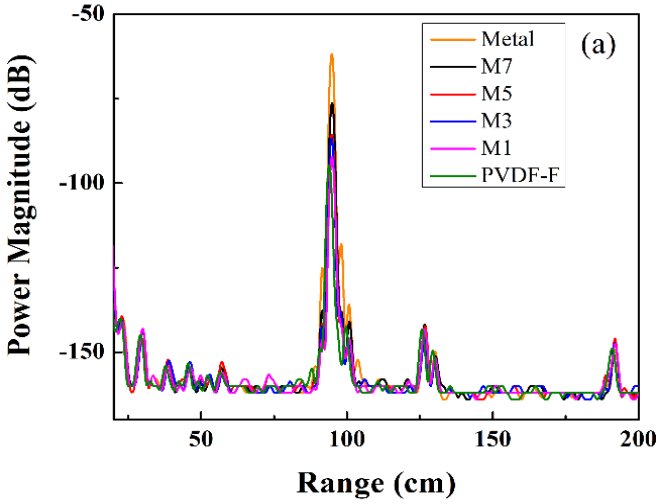

Figure 6.13. (a) Radar signal of direct metal & concealed metal with wrap of α-MoO_3/β-PVDF composites

M7, M5, M3, and M1 samples block almost 99.99% of radar signals, indicating that they effectively attenuate nearly all of the incoming radar waves. This level of blocking suggests a relatively different concentration of α-MoO_3 in the samples, resulting in significant radar signal absorption or reflection. This percentage indicates that α-MoO_3 in the samples is the perfect THz absorbing materials in nature due to Mo materials completely block the EMI THz signal. Overall, the varying concentrations or weight percentage of α- MoO_3 in the samples on PVDF matrix demonstrate how the radar shielding capabilities can be tailored by adjusting the composition of the material. Higher concentrations of MoO_3 generally lead to more effective radar signal blocking, while lower concentrations offer reduced shielding capabilities. The choice of concentration depends on factors such as the desired level of radar stealth, material cost, and application requirements. The choice of concentration depends on factors such as the desired level of radar stealth, material cost, and application requirements shown in Figure.6.12.

In summary, 100 µm ultrathin free-standing films of α-MoO_3/β-PVDF composites have been prepared to address the challenge of achieving excellent THz shielding through transmission, reflection, and absorption. It has been demonstrated that the shielding through absorption can be controlled by varying the α-MoO_3 content in the composites. Different shielding values through transmission at various THz frequencies have been achieved. A 100 µm sheet of β-PVDF exhibited an average shielding value of 42.38 dB at 0.2-1.8 THz. The shielding through transmission has been well-correlated with the dielectric behavior of the thin sheets of β-PVDF and α-MoO_3/β-PVDF composites. This work paves the way for developing polymer composites for THz shielding via reflection for THz radar shielding applications.

Intentional Blank Page

Reference:

[1]. Y.M Bahk, K. H. Kim, K. J. Ahn, H.R. Park, "Recent Developments in Terahertz Nano sensors", Adv. Photonics Res. **5**, 2300211, (2024).

[2]. M. S. Nikoo, E. Matioli, "Electronic meta devices for terahertz applications", Nature, **614**, 451, (2023).

[3]. H. Tian, G. Huang, F. Xie, W. Fu, X. Yang, "THz biosensing applications for clinical laboratories: Bottlenecks and strategies", Trends Anal. Chem, **163**, 117057 (2023).

[4]. A.G. Markelz, D.M. Mittleman, "Perspective on Terahertz Applications in Bioscience and Biotechnology, ACS Photonics, **9**, 1117, (2022).

[5]. X. Fu, Y. Liu, Q. Chen, Y. Fu, T.J. Cui, "Applications of Terahertz Spectroscopy in the Detection and Recognition of Substances", Front. Phys.,**10**,869537, (2022).

[6]. V. K Khanna, "Practical Terahertz Electronics: Devices and Applications", Institute of Physics Publishing, Bristol, United Kingdom, (2021).

[7]. P. Yang, M. Dai, H. Xiong, S. Hao, W. Zhang, B. Zhang, C. Ouyang, Q. Li, F. He, J. Miao, X. Wu, "3D Nickel Skeletons as Ultrabroadband Terahertz Absorbers", Adv. Electron. Mater., **7,** 2100626, (2021).

[8]. J. Huang, H. Wan, M. Li, Y. Zhang, J. Zhu, X. Li, W. Shui, Y. Li, X. Fan, Q. Wen, X. Xiao, Huang, Q., "In-situ growth of MAX phase coatings on carbonised wood and their terahertz shielding properties", J. Adv. Ceram., **10**, 1291, (2021).

[9]. T. Braniste, S.Zhukov, M. Dragoman, L.Alyabyeva, V.Ciobanu, M. Aldrigo, D. Dragoman, S. Iordanescu, S.Shree, S. Raevschi, R.Adelung , B. Gorshunov, I. Tiginyanu, "Terahertz shielding properties of aero-GaN", Semicond. Sci. Technol.,**34**,12LT02, (2019).

[10]. G. Li, S. Ma, Z.Li, Y. Zhang, Y. Cao, Y. Huang, "Temperature-Induced Self-Decomposition Doping of Fe_3GeTe_2 to Achieve Ultra-High Tc of 496 K for Multispectral Compatible Strong Electromagnetic Wave Absorption", Adv. Funct. Mater, **33**,2210578, (2023).

[11]. M. Luo, J. Guo, W. Shui, Y. Tan, H. Huang, Q. Yang, H. Zhang, X. Deng, Q.Y. Wen, "$Ti_3C_2T_x$ MXene-Based Superhydrophobic Broadband Terahertz Absorber with Large Pore-Size Foam Architecture", Adv. Mater. Interfaces, **10,** 2201767, (2023).

[12]. J. Liu, V. Nicolosi, "When MXenes meet terahertz radiation"**,** Nat. Photonics, **17**, 556, (2023).

[13]. A. Satapathy, K.K. Sawant, S. Mondal, A.A.B Raj, K. Mahimkar, B. Kanda Subramanian, "Recent Progress on MXenes as an Attenuator of Terahertz Radiation", J. Electron. Mater. **52**, 1749, (2023).

[14]. C. Chen, M. Chai, M. Jin, T. He, "Terahertz Metamaterial Absorbers", Adv. Mater. Technol., **7**, 2101171, (2022).

[15]. L. Sun, M. Zhu, C. Zhao, P. Song, Y. Wang, D. Xiao, H. Liu, S.H. Tsang, E. H. T. Teo, F. Hu, L. Tu, "Wafer-scale vertically aligned carbon nanotubes for broadband terahertz wave absorption", Carbon, **154**, 503, (2019).

[16]. Z. Huang, H. Chen, Y. Huang, Z. Ge, Y. Zhou, Y. Yang, P. Xiao, J. Liang, T. Zhang, Q. Shi, G. Li, Y. Chen, "Ultra-Broadband Wide-Angle Terahertz Absorption Properties of 3D Graphene Foam", Adv. Funct. Mater., **28**, 1704363, (2018).

[17]. S. Venkatachalam, K. Zeranska-Chudek, M. Zdrojek, D. Hourlier, "Carbon-based terahertz absorbers: Materials, applications, and perspectives", Nano Select, 1,471, (2020).

[18]. Z. Huang , H. Chen , S. Xu , L.Y. Chen, Y. Huang , Z. Ge , W. Ma, J. Liang , F. Fan , S. Chang , Y. Chen, "Graphene-Based Composites Combining Both Excellent Terahertz Shielding and Stealth Performance", Adv. Opt. Mater., **6,** 1801165, (2018).

[19]. H. Chen ,Z. Huang ,Y. Huang , Y. Zhang ,Z. Ge , W. Ma, T. Zhang , M. Wu , S. Xu, F. Fan, S.Chang , Y. Chen , "Consecutively Strong Absorption from Gigahertz to Terahertz Bands of a Monolithic Three-Dimensional Fe_3O_4/Graphene Material", ACS Appl. Mater. Interfaces ,**11,** 1274, (2019).

[20]. W. Ma, H. Chen, S. Hou, Z. Huang, Y. Huang, S. Xu, F. Fan, Y. Chen, "Compressible Highly Stable 3D Porous MXene/GO Foam with a Tunable High-Performance Stealth Property in the Terahertz Band", ACS Appl. Mater. Interfaces, **11**, 25369, (2019).

[21]. Z. Barani, F. Kargar, Y. Ghafouri, S. Ghosh, K. Godziszewski, S. Baraghani, Y. Yashchyshyn, G. Cywinski, S. Rumyantsev, T. Salguero, A.A Balandin, "Electrically Insulating Flexible Films with Quasi-1D van der Waals Fillers as Efficient Electromagnetic Shields in the GHz and Sub-THz Frequency Bands", Adv. Mater. **33**, e2007286, (2021).

[22]. S. Lee, M. Kim, V.A. Cao, J.Park, I.J. Yoon, P.Park, J. Nah, "High performance flexible electromagnetic interference shielding material realized using ZnO nanorod decorated polyvinylidene fluoride (PVDF)-MXene composite nanofibers", J. Mater. Chem. C, **11**, 1522,(2023).

[23]. M.Zdrojek,J.Bomba,A.Lapinska,A.Duzynska,K.Zeranska-Chudek,J.Suszek, L.Stobinski, A.Taube, M.Sypek, J.Judek, "Graphene-based plastic absorber for total sub-terahertz radiation shielding", Nanoscale,**10,**13426, (2018).

[24]. K. Zeranska-Chudek, A.Siemion, N. Palka, A.Mdarhri, I. Elaboudi, C. Brosseau, M. Zdrojek,"Terahertz Shielding Properties of Carbon Black-Based Polymer Nanocomposites", Materials,**14**, 835, (2021).

[25]. Z. Barani, K.Stelmaszczyk, F. Kargar, Y. Yashchyshyn, Cywiński , S. Rumyantsev, A.A. Balandin, "Efficient terahertz radiation absorption by dilute graphene composites", Appl. Phys. Lett., **120,** 063104, (2022).

[26]. N. Rubab, M. Mumtaz, M.Zakria, I. Ahmad, S.D. Khan, S. Shahzada, M. Raffi, "Studies on electromagnetic wave absorption characteristics of PMMA-CNF nanocomposite films in terahertz frequency range", Appl. Phys. A, **127**, 961, (2021).

[27]. N. Arooj, T.M. Khan, M. Mumtaz, A. Rehman, I. Ahmad, A. Shah, M. ul Hassan, M. Raffi, "Polymeric Fe_3O_4 Nanoparticle/Carbon Nanofiber Hybrid Nanocomposite Coatings for Improved Terahertz Shielding," ACS Appl. Nano Mater., **6**, 5264, (2023).

[28]. C. Pavlou, M.G. Pastore Carbone , A.C.Manikas ,G.Trakakis, C. Koral Papari, G.A. Andreone, C.Galiotis, "Effective EMI shielding behaviour of thin graphene/PMMA nanolaminates in the THz range", Nat. Commun., **12**, 4655, (2021).

[29]. D.Bychanok, P.Angelova,A.Paddubskaya, D. Meisak, L.M. Shashkova, A. Demidenko Plyushch , E.Ivanov, R. Kraste, R. Kotsilkova, F.Y. Ogrin, P.Kuzhir, "Terahertz absorption in graphite nanoplatelets/polylactic acid composites", J. Phys. D: Appl. Phys., **51**, 145307, (2018).

[30]. Lloyd-Hughes, J. and Jeon , T.I., "A Review of the Terahertz Conductivity of Bulk and Nano-Materials", J. Infrared Millim. Terahertz Waves , **33**, 871, (2012).

[31]. S.N. Taraskin , S.I. Simdyankin , S.R. Elliott, J.R Neilson, T. Lo, "Universal Features of Terahertz Absorption in Disordered Materials", Phys. Rev. Lett, **97**, 55504, (2006).

[32]. T.Unuma, K.Fujii ,H.Kishida, A.Nakamura, "Terahertz complex conductivities of carriers with partial localization in doped polythiophenes, " Appl. Phys. Lett, **97**, 033308, (2010).

[33]. P. Chamorro-Posada, J.Vázquez-Cabo, Ó Rubiños-López, S.J. Martín-Gil, Hernández-Navarro, P.Martín-Ramos, F.M.Sánchez-Arévalo, A.V.Tamashausky, C. Merino-Sánchez , R.C. Dante, "THz TDS study of several sp^2 carbon materials: Graphite, needle coke and graphene oxides", Carbon, **98**, 484,(2016).

[34]. B. Sensale-Rodriguez , R.Yan, M.M. Kelly, T. Fang, K.Tahy, W.S. Hwang, D. Jena, L.Liu,H.G.Xing, "Broadband graphene terahertz modulators enabled by intraband transitions", Nat. Commun , **3**,780, (2012).

[35]. M.A. Seo, J.H. Yim, Y.H. Ahn , F.Rotermund, D.S. Kim, S. Lee, and H. Lim, "Terahertz electromagnetic interference shielding using single-walled carbon nanotube flexible films"**,** Appl. Phys. Lett., **93,** 231905, (2008).

[36]. L. Ren, C. L. Pint , L.G. Booshehri , W.D. Rice , X. Wang , D.J. Hilton, K. Takeya, I. Kawayama, M. Tonouchi, R.H. Hauge, J.Kono, "Carbon Nanotube Terahertz Polarizer", Nano Lett., **9**, 2610, (2009).

[37]. L. Liu, A. Das, C.M. Megaridis, "Terahertz shielding of carbon nanomaterials and their composites -A review and applications", Carbon ,**69**, 1, (2014).

[38]. L. Ruan, X.Yao, Y.Chang, L. Zhou, G. Qin Zhang , "Properties and Applications of the β Phase Poly(vinylidene fluoride) ", Polymers ,**10**, 228, (2018).

[39]. D. M. Nivedhitha, S. Jeyanthi, "Polyvinylidene fluoride-An advanced smart polymer for electromagnetic interference shielding applications-A novel review", Polym. Adv. Technol., **34,** 1781, (2023).

[40]. A. Naseer, M. Mumtaz, M. Raffi, I. Ahmad, S.D. Khan , R.I. Shakoor, S. Shahzada, "Reinforcement of Electromagnetic Wave Absorption Characteristics in PVDF-PMMA Nanocomposite by Intercalation of Carbon Nanofibers", Electron. Mater. Lett., **15**, 201, (2018).

[41]. M. Ye, B.Qiang, S. Zhu ,M. Dai, F.Wang, Y. Luo, Q.Wang ,Q.J Wang, "Nano-Optical Engineering of Anisotropic Phonon Resonances in a Hyperbolic α-MoO_3 Metamaterial", Adv. Opt. Mater.,**10**, 2102096, (2022).

[42]. L. Lyu, F. Wang, J.Qiao, X.Ding, X.Zhang, D. Xu, W. Liu, J.Liu, "Novel synthesis of MoO_3/Mo_4O_{11}/MoO_2 heterogeneous nanobelts for wideband electromagnetic wave absorption", J. Alloys Compd., **817**,153309, (2020).

[43]. M.I. Sayyed, A.H. Abdalsalam, M.M. Taki, M.H.A. Mhareb, B. Alim, A.Baltakesmez, E.Şakar, "MoO_3 reinforced Ultra high molecular weight PE for neutrons shielding applications", Radiat. Phys. Chem., **172**, 108852, (2020).

[44]. K. Parangusan, V. Subramaniam , A.B. Ganesan, P.S.Venkatesh, D.Ponnamma, "Molybdenum oxide reinforced polyvinyl alcohol composite as high-performance dielectric material for flexible", J. Mater. Sci. Mater. Electron., **34,** 1110, (2023).

[45]. C.Q Li, X.Shen, R.C.Ding, G.S.Wang, "Controllable Synthesis of One-Dimensional MoO_3/MoS_2 Hybrid Composites with their Enhanced Efficient Electromagnetic Wave Absorption Properties", ChemPlusChem, **84,** 226, (2019).

[46]. W. Peng , W.Zhou, T. Li, J. Zhou, T.Yao, H.Wu, X. Zhao, J. Luo, J. Liu, D. Zhang, "Towards inhibiting conductivity of Mo/PVDF composites through building MoO_3 shell as an interlayer for enhanced dielectric properties", J. Mater. Sci. Mater. Electron., **33,** 14735, (2022).

[47]. S. Cheng, F.Qiao, X. Wang, A.Xie, X.Pan, C.Zhang, Z.Chen, W.Dong, B.Ouyang, E. Kan, "N-plasma modulation for boosting electromagnetic wave absorption behavior of MoO_3 ceramic based on non-metallic doping", Materialia, **28,** 101727, (2023).

[48]. F. Hu, F. Zhang , X.Wang , Y. Li, H.Wang, R. Zhang, H.Li, B.Fan, "Ultrabroad band microwave absorption from hierarchical $MoO_3/TiO_2/Mo_2TiC_2T_x$ hybrids via annealing treatment", J. Adv. Ceram.,**11**,1466, (2022).

[49]. J. Zhu., Cheng, Le., Liang.J., Zhao.Y., Gong.Y., Zhang.Y. Ping Wang. W., "Ultra-broadband mid-infrared absorber based on hyperbolic α-MoO_3", Results in Physics, **54,**107093, (2023).

[50]. Seong-Hwang Kim., Lee. S. Y, Zhang. Y., Soo-Jin Park, and Junwei Gu, "Carbon-Based Radar Absorbing Materials toward Stealth Technologies", Adv. Sci.,**10,** 2303104, (2023).

[51]. S. Priyambada, S. Lokesh, A. Dixit, Microwave-absorbing materials for stealth application: a holistic overview, Oxford Open Materials Science, **3**, 1, (2023).

[52]. R. Koalla, N. Periketi, C. Ghorui, S. Mangali, A. K. Chaudhary, "Terahertz time-domain spectroscopy, imaging and density functional theory based studies of 3, 4, 5 Trinitro 1 H Pyrazole", J. Mol. Struct., **1265,** 133449, (2022).

[53]. S. K. Marka, V. V. S. S. Srikanth, B. Sindam, B. K. Hazra, K. C. James Raju, S. Srinath, "Graphene-Wrapped MgO/Poly(vinyl alcohol) Composite Sheets: Dielectric and Electromagnetic Interference Shielding Properties at Elevated Temperatures", ACS Appl. Mater. Interfaces,**11**,23714, (2019).

[54]. V. V. S. S. Srikanth, K. C. James Raju, "Graphene/Polymer Nanocomposites as Microwave Absorbers in Graphene-Based Polymer Nanocomposites in Electronics" (Eds. K. K. Sadasivuni, D. Ponnamma, J. Kim and S. Thomas), Springer, 307–343, (2015).

[55]. H. Negishi, S.Negishi, Y.Kuroiwa, N.Sato, S.Aoyagi, "Anisotropic thermal expansion of layered MoO_3 crystals", Phys. Rev. B, **69**, 064111, (2024).

[56]. T. Leisegang, A. A. Levin, J.Walter, D.C. Meyer,"In situ X-ray analysis of MoO_3 reduction", Cryst. Res. Technol., **40**, 95, (2005).

[57]. A.Chithambararaj, N. Rajeswari Yogamalar, A.C Bose, "Hydrothermally Synthesized h-MoO_3 and α-MoO_3 Nanocrystals: New Findings on Crystal-Structure-Dependent Charge Transport", Cryst. Growth Des.,16, 1984, (2016).

[58]. K. Tashiro, "Crystal structure and phase transition of PVDF and related copolymers", in: H. S. Nalwa (Ed.), Ferroelectric Polymers, CRC Press, **74**, (1995).

[59]. T.Boccaccio, A.Bottino, G.Capannelli, P.Piaggi, "Characterization of PVDF membranes by vibrational spectroscopy", J. Membr. Sci., **210**, 315, (2002).

[60]. O, Lupan, V. Trofim,V. Cretu, I. Stamov, N. N. Syrbu, Y.K. I. Tiginyanu, R. Adelung Mishra, "Investigation of optical properties and electronic transitions in bulk and nano-microribbons of molybdenum trioxide", J. Phys. D:Appl.Phys.,**47**,085302, (2014).

[61]. N. Syrbu, I.Stamov, "The superposition of the lattice radiation and reflectivity spectra of MoO_3 and $PbMoO_4$ crystals", Cryst. Res. Technol., **29**, 133,(1994).

[62]. G.Mestl, P.Ruiz , B. Delmon, H.Knozinger, "Oxygen-Exchange Properties of MoO_3: An in Situ Raman Spectroscopy Study", J. Phys. Chem., **98**,11269,(1994).

[63]. L. Seguin , Figlarz Cavagnat, M. R; Lassegues, J. C, "Infrared and Raman spectra of MoO_3 molybdenum trioxides and $MoO_3 \cdot xH_2O$ molybdenum trioxide hydrates", Spectrochim. Acta A, **51**, 1323,(1995).

[64]. S. Phadungdhitidhada, P.Mangkorntong ,S.Choopun Mangkorntong,"Raman scattering and electrical conductivity of nitrogen implanted MoO_3 whiskers", Ceram. Int, **34**, 1121, (2008).

[65]. B. C Windom, W. Sawyer, D.W Hahn, "A Raman Spectroscopic Study of MoS_2 and MoO_3: Applications to Tribological Systems",Tribol. Lett, **42**, 301, (2011).

Chapter 7

7. Conclusion and future scope:

7.1 Conclusion:

This chapter provides a summary of all previous chapters, along with potential future directions for this work. The thesis covers three important aspects i.e. (i) Efficient THz generation and detection from three different types of Inorganics, semiconductor and semimetals nonlinear crystals such as BIBO, S-doped GaSe, and α-TeO_2. We have extracted optoelectronic properties such as refractive index, absorption coefficient, dielectric constant, and scattering constant of different inorganic, semimetal and semiconductor crystals. (ii) The transmission and reflection spectroscopic studies enable us to investigate the shielding effectiveness of emerging materials such as α-MoO_3, hBN, graphene used for radar shielding applications. A significant challenge in THz technology is overcome the atmospheric water absorption, which limits the use of THz spectroscopy and imaging over varying distances. (iii) Finally, we have calibrated a SiGe BiCMOS 0.3 THz radar source for homeland security, defense, and food processing applications.

We have used lab built versatile experimental setup for THz generation and detection, allowing us for various experiments such as optical pump-terahertz probe, and generation and detection of THz radiation using different materials. The setup permits interchangeability between generator and detector components, enabling combinations such as PCA antenna-PCA antenna, PCA antenna-nonlinear (NLO) crystals, NLO crystals-PCA antenna, and NLO crystals-NLO crystal as source and detector. This setup operates in both THz transmission and reflection modes.

Consequently, we have evaluated different indigenously grown semiconductor, semimetal, and inorganic crystals, including BIBO, S-doped GaSe, and α-TeO_2. These crystals were characterized in terms of optical transmission range, refractive index, absorption coefficients, dielectric constant, and scattering coefficient in both transverse electric and transverse magnetic modes. Due to their excellent linear and nonlinear optical properties, such as transmission from the visible to far-infrared range, high anisotropy, second-order nonlinearity, and high damage threshold, these crystals demonstrate potential as efficient THz sources. The impact of sulfur doping on the THz generation ability of GaSe crystals has also been discussed. These crystals also have potential applications in laser technology,

telecommunications, quantum optics, sensing and imaging, medical applications, and material science research. BIBO, S-doped GaSe, and α-TeO_2 crystals have excellent nonlinear optical properties making it suitable for applications in frequency conversion processes such as second harmonic generation (SHG), and optical parametric oscillation (OPO).

We have developed a modality to convert a 2D imaging system into a 3D THz profilometer. This device enables accurate measurement of the surface roughness of various surfaces, including metallic, painted, and rusted naval vessels, and explosive warhead targets. The nonlinear optics-based THz system is pumped by femtosecond laser pulses, and its detection systems can be both coherent and incoherent. This makes the system suitable for short-distance measurements in transmission and reflection modes. THz profilometry can be used to detect and identify explosives and other hazardous materials through non-invasive inspection, enhancing security measures.

To demonstrate the long-range applications, we selected a single-frequency 0.3 THz electronic source combined with a facility for aligning the source and detector at very short or acute angles (2°). We calibrated the prototype SiGe BiCMOS 0.3 THz silicon radar system for detection up to 3 meters, testing it on various target materials such as explosives, metals, and dairy products. Our research has advanced in miniaturizing THz sources and exploring their potential for detecting food freshness, particularly in meat. These technologies have broad applications in different sectors, including residential utilities. Integration of AI with THz systems play very crucial role for testing the freshness of the dairy and agro products. AI enables the process of analysis by combining inputs received from different sensors for predicting important variables related to the freshness factor of diary and agro product. The newly designed THz systems is a handy tool for commercial and research purposes.

Additionally, we evaluated the same system for assessing the shielding effect of α-MoO_3 materials in EMI radar applications. α-MoO_3 is being researched for use in lithium-ion and sodium-ion batteries due to its high capacity and excellent cycling stability. It can be used as a catalyst or catalyst support in fuel cells, enhancing their efficiency and stability.

7.2 Future Scope:

The research work carried out in this thesis can be extended for following future applications such as

a) The modified THz time domain experimental setup can be used to study the charge carrier dynamics and decay life time of different types of semiconductors, organic and inorganic and bio materials.
b) THz profilometry can be used to measure the surface roughness of missile warheads and detect explosives and other hazardous materials in the form of non-invasive inspection.
c) Our developed THz profilometer can used in the examination and preservation of cultural heritage artifacts, multi-layer structures in coatings which enabled detailed profiling of historical objects and paintings without causing damage.
d) The THz TDS can be used to measure the EMI shielding for 2D and carbon-based emerging materials.
e) The 0.3 THz radar system set-up can be used for 2D /3D THz imaging of metallic, explosive and powder samples for long distance detection.
f) The radar system can be used for development of ultra-high-speed wireless communication networks, enabling faster data transfer rates with minimal latency for 6G and beyond.
g) This radar system can used for non-invasive biomedical imaging and diagnostics, particularly in detecting skin and breast cancers, and other tissue abnormalities.

Appendix A- Radar Code Flowchat

The flowchart describes the process of configuring and reading data from a sensor, likely part of a radar system, and plotting the data on a graph. Here is a detailed explanation of each step in the flowchart:

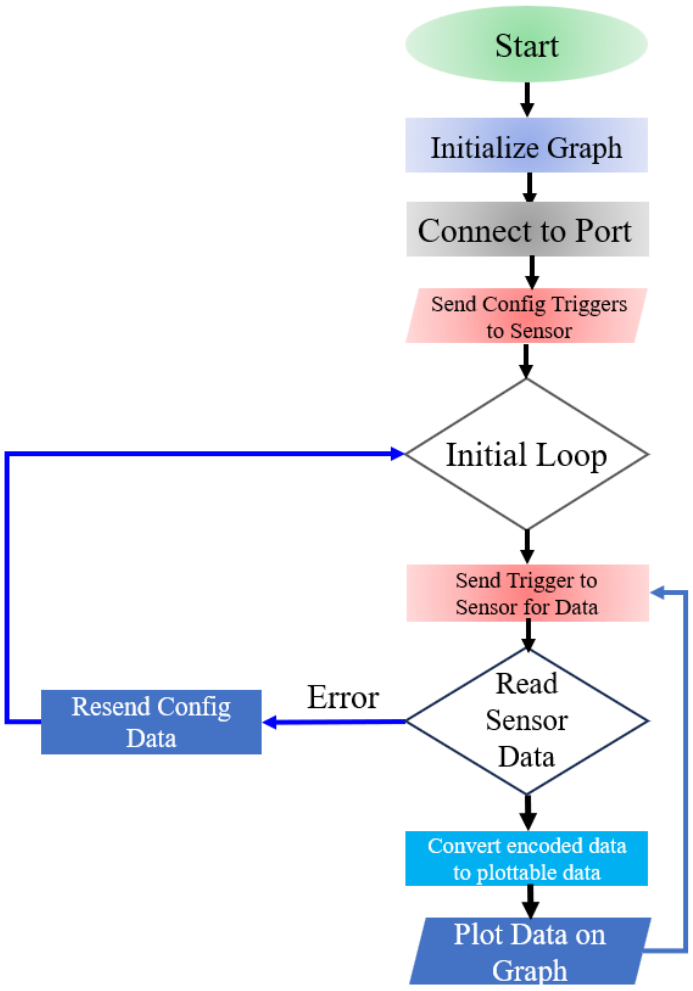

Start:

The process begins here.

Initialize Graph:

The system initializes the graph that will be used to plot the sensor data.

Connect to Port:

The system establishes a connection to the sensor through a specific port.

Send Config Triggers to Sensor:

Configuration triggers are sent to the sensor to set it up for data collection.

Initial Loop:

The system enters an initial loop to start the data collection process.

Send Trigger to Sensor for Data:

A trigger is sent to the sensor to prompt it to start sending data.

Read Sensor Data:

The system reads the data sent by the sensor.

Error Check:

The system checks if there was an error in reading the sensor data. If an error is detected, the process goes to the "Resend Config Data" step. If no error is detected, the process moves to the next step.

Convert Encoded Data to Plottable Data:

The encoded data received from the sensor is converted into a format that can be plotted on the graph.

Plot Data on Graph:

The converted data is plotted on the graph.

Loop Back:

After plotting the data, the process loops back to the "Send Trigger to Sensor for Data" step to continuously collect and plot new data.

Resend Config Data:

If an error occurs, the configuration data is resent to the sensor, and the process loops back to the "Initial Loop" step to reinitialize and restart the data collection.

This flowchart effectively outlines the steps involved in initializing a graph, setting up a sensor, continuously collecting and plotting data, and handling errors by reconfiguring the sensor.

Appendix B- THz Radar Cross Section Simulation using MATLAB Software

THz Radar Cross Section (TRCS) is defined as the ratio of the power reflected back to the radar to the power density of the incident wave from the target. TRCS is primarily defined in the far-field region. Essentially, TRCS is a function of the target's size, shape, and dielectric characteristics. Locating the exact position of large objects, such as full-size ships, submarines, vessels, and aircraft, poses significant challenges. It is a complex, time-consuming, and cost-ineffective task. Iterative design and experimental testing applications are impractical due to the sheer size of these platforms. Therefore, modern software tools like MATLAB, CST, FDTD, and Ansys are commonly used for calculating the TRCS values, albeit with some limitations [1-6]. Simulating the THz Radar Cross Section (TRCS) using MATLAB involves several steps, including defining the geometry of the target, setting up the incident wave, and calculating the scattered fields.

1. Define the Target Geometry

First, we need to define the shape and size of the object whose TRCS we want to calculate.

```
% Define parameters
radius = R ;                                  % radius of the object
[x, y, z] = Object ( ) ;                      % create the object with mesh grid
% Scale the object to the desired radius
X = radius*x;
Y= radius*y;
Z= radius*z;
% Plot the objects geometry
figure;
surf (x, y, z);
xlabel('X');
ylabel ('Y');
zlabel ('Z');
title ('Target/Object Geometry');
```

2. Set Up the Incident Wave

Next, we define the incident electromagnetic wave parameters such as frequency, wavelength, and direction of incidence.

```
% Define wave parameters
frequency = 10e12 ;                                  % frequency in THz
c = 3e8;                                             % speed of light in m/s
wavelength = c./frequency ;                          % wavelength in meters
k = 2 *pi /wavelength;                               % wavenumber
% Incident wave direction (unit vector)
Incident Direction = [0, 0, -1] ;                    % along the negative z-axis
% Define the incident electric field (assuming a plane wave)
E0 = [1, 0, 0] ;                                     % THz Electric field vector
```

3. Calculate the Scattered Fields

The method to calculate the scattered fields depends on the shape of the object. Here, we'll use a simplified physical optics method with Mie theory for a sphere.

```
% Define a function for TRCS calculation using Mie theory
function TRCS = calculate TRCS (frequency, radius, E0, incident direction)
 % Constants
  c = 3e8;                                           % speed of light in m/s
  wavelength = c / frequency;
  k = 2 * pi / wavelength;
 % Mie scattering coefficients (simplified)
  ka = k * radius;
 TRCS = Equation of different types of canonical objects;
 end
 % Calculate TRCS
   TRCS = calculate TRCS (frequency, radius, E0, incident direction);
   disp (['TRCS: ', num2str (TRCS), ' m^2']);
```

4. Visualize the Results:

We can visualize the TRCS as a function of the incident angle or frequency.

```
% Define a range of incident angles
theta = linspace (0, pi, 180);
```

```
% Calculate TRCS for each angle
TRCS values = zeros(size(theta));
for i = 1: length(theta)
incident direction = [sin(theta(i)), 0, cos(theta(i))];
TRCS values(i) = calculate TRCS (frequency, radius, E0, incident direction);
end
% Plot the TRCS as a function of incident angle
figure;
plot(rad2deg(theta), TRCS values);
xlabel ('Incident Angle (degrees)');
ylabel ('TRCS (m^2)');
title ('TRCS vs Incident Angle');
grid on;
```

%% Calculation of TRCS of Finite length Cylinder

```
L = 10;
H=5;
a = 0.125;
c = 3e10;
el =linspace (0,180,181);
freq =linspace (0,0.6,181) *1e12;
lambda=c./freq;
% lamda=3.5e9;
k = 2*pi. /lambda;
beta =L.*k.*cosd(el);
A =H.*k.*cosd(el);
gamma = cosd(el);
RCS =(a.*sind(el). /k). *(((sind(beta). *(sind(beta)). /(gamma). ^2)));
rcs=(a.*sind(el). /k). *(((sind(A). *(sind(A)). /(gamma). ^2)));
tsdb =10*log10(RCS);
tsdb1 =10*log10(rcs);
TRCS=tsdb';
```

```
angle=el';
hold on
plot (freq/1e12, tsdb);
plot (freq/1e12, tsdb1)
hold off
xlabel ('Frequency (THz)')
ylabel ('TRCS (dB m^2)')
% title ('Elevation Profile of Target Strength')
hold on
plot (el, tsdb)
plot (el, tsdb1)
hold off
xlabel ('Aspect angle(deg)')
ylabel ('TRCS (dBm^2)')
% imagesc (freq/1e12, el, tsdb)
xlabel ('Frequency (THz)')
ylabel ('TRCS (dB m^2)')
imagesc (freq/1e12, el, tsdb1)
%% Calculation of TRCS of circular flat plate
a = 0.40;
c = 3e8;
el =linspace (0,180);
freq =linspace (0,0.6) *1e12;
lambda=c./freq;
%lambda=10e9;
k=2*pi. /lambda;
A=4*pi*a.^4. *cosd(el);
B=2*a.*k.*sind(el);
P =a.*lambda;
```

```
Q= ((8*pi*sind(el). *sind(el). *sind(el)). /(cosd(el). *cosd(el)));

RCS =P./Q;

tsdb =10*log10(RCS);

D=(sin(B). /(B.^2))-(cos(B). /B);

rcs1=A.*(D./B);

tsdb1 =10*log10(rcs1);

hold on

plot (freq/1e12, tsdb);

plot (freq/1e12, (tsdb1));

hold off

xlabel ('Frequency (THz)')

ylabel ('TRCS (dB m^2)')

title ('Elevation Profile of Target Strength')

hold on

plot (el, tsdb)

plot (el, tsdb1)

hold off

xlabel ('Aspect Angle (degree)')

ylabel ('TRCS (dBm^2)')

imagesc (freq/1e12, el, tsdb)

xlabel ('Frequency (THz)')

ylabel ('TRCS (dBm^2)')
```

Reference:

[27]. M. I. Skolnik, Radar handbook (McGraw-Hill Education, 2008).

[28]. A. Divyalakshmi, A. Bhuvana and G. V. Babu, Analysis of radar cross section and detection, International Journal of Pure and Applied Mathematics 119, 469 (2018).

[29]. T.I.O Ahmed and M. Mirghani, Estimation of Radar Cross Sectional Area of Target using Simulation Algorithm., International Journal of Research Studies in Electrical and Electronics Engineering, 4 (2018).

[30]. Y-L. Xu, T. Kennedy and E. Stansbery, Radar Cross Section of orbital debris objects, in International Orbital Debris Conference (IOC), IOC 6164 (2019).

[31]. I. Chibuisi, Modeling of high voltage distribution system using Simulink, International Journal of Trend in Research and Development 2, 6 (2015).

[32]. B.R. Mahafza, Radar systems analysis and design using MATLAB (Chapman and Hall/CRC, 2005).

Research Article Vol. 60, No. 19 / 1 July 2021 / Applied Optics 5643

applied optics

Efficient second-harmonic and terahertz generation from single BiB_3O_6 crystal using nanosecond and femtosecond lasers

Chandan Ghorui,[1] A. M. Rudra,[2] Udit Chatterjee,[3] A. K. Chaudhary,[1,4,*] and D. Ganesh[1]

[1]Advanced Centre for Research in High Energy Materials (ACRHEM), University of Hyderabad, Telangana 500046, India
[2]Physics Department, Raj College, Burdwan, West Bengal 713104, India
[3]Laser Laboratory, Department of Physics, Burdwan University, Burdwan, West Bengal 713104, India
[4]e-mail: akcphys@gmail.com
*Corresponding author: akcsp@uohyd.ernet.in

Received 11 March 2021; revised 19 May 2021; accepted 30 May 2021; posted 2 June 2021 (Doc. ID 424241); published 25 June 2021

The paper reports the efficient UV and terahertz generation from a 1.29 mm thick and Type I, $\theta = 28.9°$ cut BiB_3O_6 (bismuth triborate, BIBO) crystal using femtosecond and nanoseconds laser pulses. We have employed 800 nm wavelength pulses of 50 and 140 fs obtained from a Ti:sapphire laser amplifier and oscillators at 1 kHz and 80 MHz repetition rates, respectively. The conversion efficiency of second-harmonic generation (SHG) was ∼ 50% while that obtained for terahertz (THz) generations was of the order of 1.85×10^{-5}%. In addition, LDS-698 dye laser radiation tunable between 650–700 nm was also used as a source for SHG between the 325–350 nm range. The dye laser was pumped by SHG (532 nm) radiation from an electro-optically *Q*-switched Nd:YAG laser having a pulse repetition rate of 10 Hz and a pulse width of 10 ns. A conversion efficiency of 4.01% was obtained for generation of UV at 343.5 nm. Finally, we have measured the transmission, refractive index, absorbance, and conductivity properties of BIBO crystal in the THz domain. We also ascertained the coherence length, relative permittivity and reflectivity of the crystal. © 2021 Optical Society of America

https://doi.org/10.1364/AO.424241

1. INTRODUCTION

There is a continuous need for growing new nonlinear optical materials with improvised linear and nonlinear optical properties which can cover a wide range of transmission between the deep-UV to far-infrared range. It is possible to generate efficient deep-UV to mid-IR radiation by employing different types of nonlinear frequency conversion processes such as second-harmonic generation (SHG), sum-frequency mixing and difference-frequency mixing (DFM), etc. Some of the well-known nonlinear crystals such as KH_2PO_4 (KDP), KD * P, β-BaB_2O_4 (β-BBO), LiB_3O_5 (LBO), LAP, $KTiOPO_4$(KTP), BNA, DAST, etc., are widely used for making efficient nonlinear devices. In addition, some of the selected inorganic and organic crystals such as BBO, KTP, DAST, BNA, etc., can also be used for the generation of powerful terahertz (THz) radiation using DFM, plasma generated from filamentation of femtosecond laser, and optical rectification techniques [1–6]. Among all the BBOs is the first very promising borate group crystal which has found potential applications in the generation of deep-UV to terahertz radiation due to its excellent optical and nonlinear properties. Bhar *et al*. have reported the best use of the phase-matching condition for efficient deep-UV–vis radiation using frequency mixing techniques. They have used *Q*-switched nanosecond pulse in their study and employed sum frequency generaton (SFG) and SHG techniques [7–9]. There are many more groups who have used femtosecond pulse for powerful UV generation from BBO crystal using the 800 nm wavelength [10,11]. The same femtosecond laser is also used for THz generation and measurement of refractive indices in the THz domain [12,13].

The BiB_3O_6 (bismuth triborate, BIBO) crystal was introduced by Hellwig *et al.* in 1998 [14–17]. It is a highly promising negative biaxial nonlinear optical crystal that belongs to monoclinic group C_2 and apart from having a large nonlinear optical coefficient and laser high damage threshold, it is nonhygroscopic as well. It offers an optical transparency between the 160 nm to 2.7 μm region. The UV transmission cutoff of BIBO is at much deeper wavelength than BBO and it offers large effective nonlinearity ($d_{\text{eff}} = 3.2$ pm/V). Its nonlinear coefficient is 3.5–4 times higher than that of LBO and 1.5–2 times higher than that of BBO. These attractive properties have recently been explored to demonstrate the potential of BIBO for efficient SHG using continuous wave [18,19], long pulse, nanosecond, picosecond [20,21], and femtosecond pulsed lasers [22–26]. For example, conversion efficiencies of SHG at 532 nm in the

pulsed regime ranged from 11% with nanosecond pulses [27] to 67.7% with picosecond pulses. However, Ebrahim-Zadeh *et al.* have generated the tunable SHG between 375–435 nm using a tunable femtosecond oscillator and achieved conversion efficiency of the order of 50% [28].

In this paper, we report the systematic studies on generation of SHG and THz radiation from single thin BIBO crystal using the 800 nm wavelength of 50 fs and 140 fs pulse duration that was obtained from a Ti:sapphire laser amplifier and oscillator at 1.0 kHz and 80 MHz repetition rates, respectively. The same crystal was subjected to a 532 nm pumped LDS-698 dye laser for generation of UV radiation between the 300–340 nm wavelength range. It confirms that the conversion efficiency of the SHG process depends on the pulse duration of the laser. The conversion efficiency of SHG using nanosecond pulses is almost 25 times less than those using femtosecond pulses.

Since SFG and optical rectification are second-order nonlinear processes, it is possible to generate SHG and THz radiation simultaneously using the same 800 nm femtosecond laser pulses. Our group has already demonstrated such dual generation in a single DAST crystal using a femtosecond pulsed amplifier [4]. The efficiency of SHG depends on the thickness, d_{eff} value, surface quality, and damage threshold of the crystal, whereas generation of THz further depends on the coherence length. The R.I. of the crystal in the optical domain can easily be calculated using available Sellmeier equations but such equations do not exist in the THz domain. We have carried out an additional exercise to measure the transmission, R.I., and absorption coefficients to ascertain the utility of BIBO crystal as a THz generator.

2. THEORETICAL CONSIDERATION FOR THz-BASED OPTICAL PROPERTIES

The following equations are used for measurements of transmission and other parameters in the THz domain.

The transmitted field T is given by Eq. 1:

$$T = \frac{E_{\text{Sample}}}{E_{\text{Reference}}}, \tag{1}$$

where E_{Sample} and $E_{\text{Reference}}$ are the amplitudes of THz radiation after passing through the BIBO crystal and air, and

$$\text{Absorption coefficient} = -\frac{1}{d}\ln\frac{T_m}{T_s}, \tag{2}$$

where T_m and T_s are the transmitted intensity from material sample and reference, respectively. The refractive index of the sample can be calculated by using Eq. (3):

$$n = 1 + \frac{\Delta\varphi \times c}{2\pi\nu \times d}, \tag{3}$$

where $\Delta\varphi$ is the phase difference between the reference and sample, ν is the frequency, d is the thickness of the sample, and c is the velocity of light.

Equation (4) can be used to determine the imaginary refractive index (k):

$$k = \frac{c}{2\pi\nu \times d} ln\left(\frac{4n}{\rho(n+1)^2}\right), \tag{4}$$

where d is the thickness of the crystal and ρ is the THz field amplitude.

The dielectric and reflectivity of the BIBO crystal are measured using Eqs. (5) and (6) as

$$|\varepsilon_r| = n^2 + k^2, \tag{5}$$

$$R = \frac{(n-1)^2}{(n+1)^2}. \tag{6}$$

The coherent length is given by

$$L_c = \frac{\lambda_{\text{THz}}}{2\left(n_{\text{gr}} - n_{\text{THz}}\right)}, \tag{7}$$

where λ_{THz} is the terahertz wavelength (300 μm), and n_{gr} and n_{THz} are the refractive indices of the optical and THz regions.

The terahertz transmittance of the BIBO crystal was calculated from Eq. (8):

$$T = e^{-\alpha d}(1-R)^2. \tag{8}$$

Here, α is the absorption coefficient, d the thickness, and R is the reflectivity of this BIBO crystal.

The conductivity of the BIBO crystal can be measured by using Eq. (9):

$$\sigma = \frac{n+1}{Z \times d}\left(\frac{1}{T} - 1\right), \tag{9}$$

where $Z = 377\ \Omega$ is the free-space wave impedance and T is the transmittance of the crystal.

3. EXPERIMENTAL DETAILS

This section is divided into four parts. In the first part, we have measured the transmission/absorption in the THz domain using the indigenously designed THz spectrophotometer. In the second part the crystal was used as a THz generator in the time-domain setup. In the third part, SHG was generated in the crystal using a femtosecond amplifier. In the last part, the crystal was used to generate SHG from a nanosecond pulsed DCM dye laser pumped by 532 nm wavelength obtained from a nanosecond Q-switched Nd:YAG laser. Figure 1 shows the schematic experimental setup for THz generation and transmission/absorption measurements.

For transmission measurement, 800 nm wavelength of 140 fs pulse duration obtained from the Ti:sapphire laser (coherent chameleon ultra-II) at 80 MHz repetition rate was used to generate the tunable THz radiation between the 0.1 and 3.5 THz range. The laser pulse was split into two parts using a beam splitter (90/10 beam splitter). The reflected part was directed to LT GaAs based PC antenna for THz generation. The generated THz radiation was focused on the BIBO crystal for transmission measurement using an off-axis parabolic mirror (OPM) set. The transmitted radiation was further collimated and focused on the ZnTe crystal using another pair of OPM set. The generated THz signal was measured using the electro-optic sampling technique made of ZnTe crystal, λ/4 wave plates, a Wollaston prism, and a pair of PIN photodiodes. In the second part, we have replaced the PC antenna by the BIBO crystal for the generation of THz signal, as shown in Fig. 1. The unconverted part of 800 nm

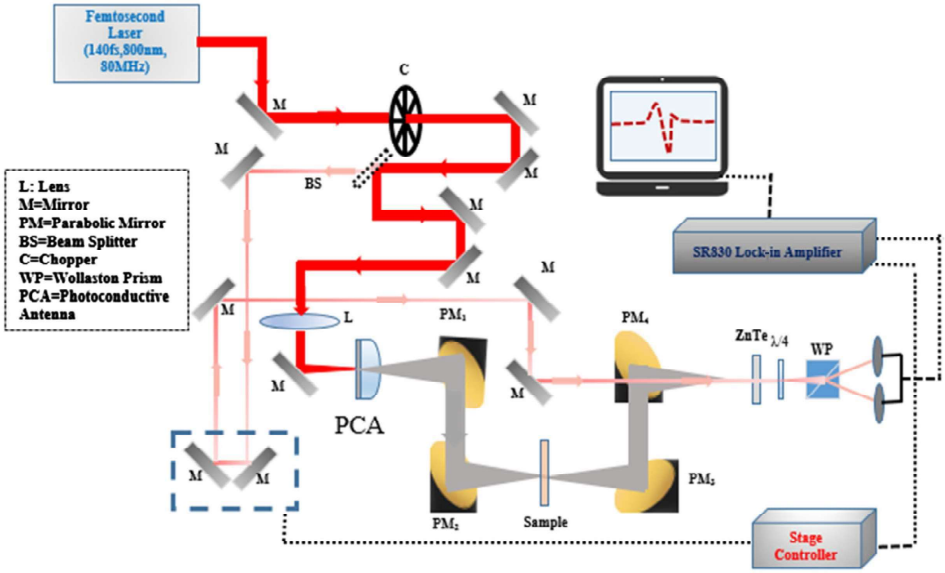

Fig. 1. Schematic of experimental setup for terahertz time-domain transmission spectroscopy (TDS).

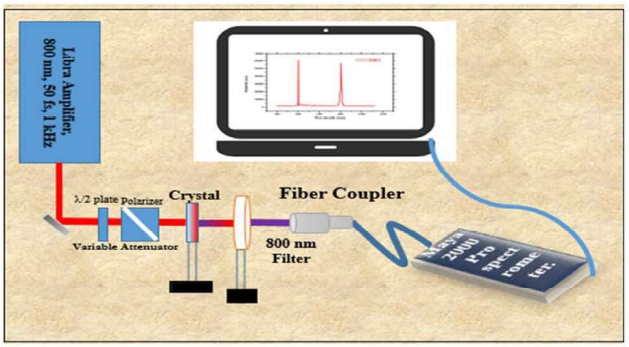

Fig. 2. Experimental setup for the second-harmonic generation of 800 nm wavelength from femtosecond laser amplifier.

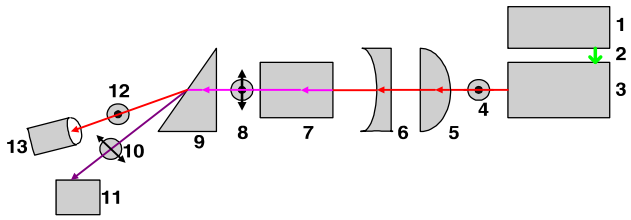

Fig. 3. Experimental setup for second-harmonic generation tunable between 325–340 nm range using nanoseconds laser. Here 1, Nd:YAG laser; 2, 532 nm pump beam for dye laser; 3, dye laser; 4, vertically polarized fundamental dye radiation; 5, plano–convex lens with $f = 50$ cm; 6, plano–concave lens with $f = -25$ cm; 7, BIBO crystal; 8, fundamental and its SHG radiations; 9, CaF_2 prism; 10, horizontally polarized generated UV radiation (SHG); 11, power/energy meter; 12, unconverted vertically polarized fundamental radiation; and 13, beam dumper.

of femtosecond laser was filtered out using a silicon plate. In the third part, the BIBO crystal was used for efficient second-harmonic generation of 800 nm wavelength obtained from same Ti:sapphire laser amplifier. The schematic experimental layout is shown in Fig. 2.

The incident laser power of 800 nm was controlled using a $\lambda/4$ wave plate and polarizer-based attenuator and unconverted part of 800 nm was filtered out using a dichroic mirror. The generated SH, i.e., 400 nm and unconverted part of 800 nm, was detected using a fiber-coupled spectrometer (Maya2000 pro Ocean Optics, USA). In the same experiment the dichroic mirror and fiber detector were replaced by a silicon filter and pyrometer to measure the efficiency of the generated THz power from the crystal. Finally, the crystal was evaluated to generate the tunable UV radiation between the 325–340 nm range using a LDS-698 dye laser. Figure 3 shows the schematic of the experimental setup.

The dye laser (DCR-11, Spectra Physics) was pumped by 532 nm obtained from SHG of 1064 nm wavelength of 10 ns pulse duration obtained from a Q-switched Nd:YAG laser (LAB-170, Spectra Physics) at 10 Hz repetition rate. The vertically polarized 532 nm beam was used to pump the LDS-698 dye laser. The dye laser beam was vertically polarized and

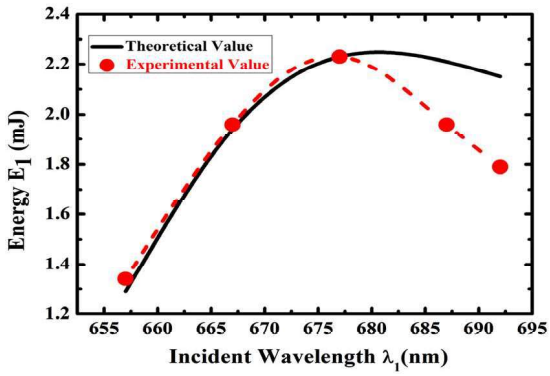

Fig. 4. Variation of the dye laser energy (E_1) with respect to tunable wavelengths (λ_1). The red dots represent the measured experimental values.

tunable between the 650–700 nm range. Figure 4 shows the obtained tuning curve for the dye laser.

The dye beam diameter was about 2.3 mm. It was allowed to pass through a telescopic arrangement made of a

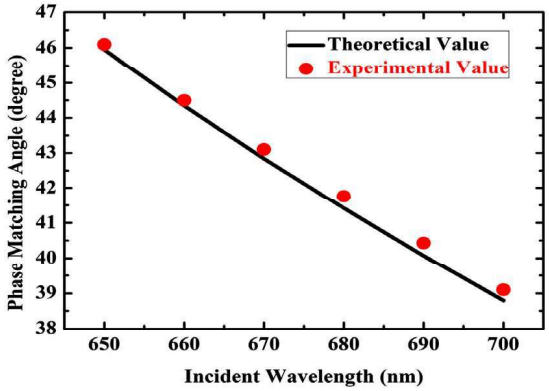

Fig. 5. Phase-matching angle curve for SHG in BIBO. The black line and red dots represent the theoretical and experimental points, respectively.

Table 1. Sellmeier Coefficient of BIBO Crystal: $n_i^2 = A + B/(\lambda^2 - C) - D\lambda^2$ [11] Valid between 0.32–3.09 μm

n_i	A	B	C	D
n_x	3.074	0.0323	0.0316	0.01337
n_y	3.1685	0.0373	0.0346	0.0175
n_z	3.6545	0.05116	0.0371	0.0226

plano–convex–concave lens combination (Fig. 3). It provides the collimated beam of 1.0 mm diameter with long coherence length. The Type I (o e e), $\theta = 28.9°$ cut, 1.29 mm thick crystal was mounted on a spectrometer table having least count of the order of 20″. The X-Z plane of the biaxial crystal was allowed to rotate in the horizontal plane. The generated horizontally polarized second-harmonic radiation was separated out from the fundamental beam using a CaF_2 prism. The energies of the fundamental and its SHG were measured by a power energy meter (Gentec, EG-100 A). Figure 5 shows the phase-matching angle tuning curve for SHG. The black curve is the theoretical one predicted using the reported [19]. The values of Sellmeier coefficients are shown in Table 1, while the red dots are the experimental points. Our experimentally measured values show good agreement with the theoretical prediction.

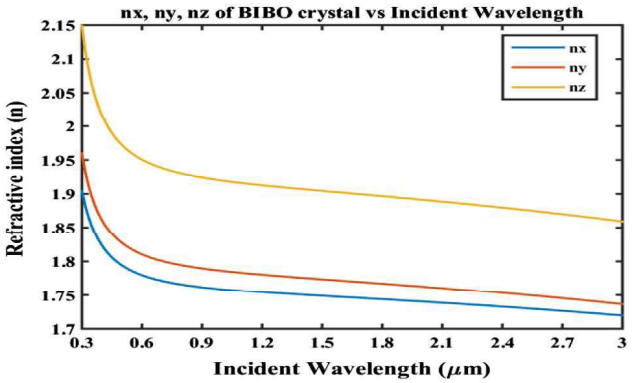

Fig. 6. Refractive index versus wavelength of BIBO crystal.

One of the interesting features of the study is the possible use of the dispersion properties in the UV–visible range. Figure 6 shows the dispersion properties of BIBO in the UV–visible range.

The same Sellmeier equations were used for all other phase-matching calculations. Figure 7(a) shows the measured value of angular acceptance of the crystal. The measured value of $\Delta\theta$ (at full width half-maxima) was 3.84 mrad, which is very close to the theoretical value of 4.01 mrad. The measured value of the spectral acceptance bandwidth, i.e., $\Delta\lambda$ (at full width half-maxima) is 0.90 nm, which is also very close to the theoretical value of 0.913 nm, as shown in Fig. 7(b). In addition, the conversion efficiency for the SHG was measured using Eq. (10). Figure 8 shows the variation of energy for the generated tunable SHG wavelengths. Here the smooth curve represents the theoretical prediction for the conversion efficiency while the dots show the measured values. The crystal is very thin and has very good transmission in the UV–vis region. Therefore, we have neglected the crystal absorption and considered that there is no change in beam diameter, i.e., (1.0 mm). Figure 9 shows the variation in the nonlinear coefficients with respect to the incident wavelength and phase matching angle.

$$E_2 = 8\pi d_{\text{eff}^2} L^2 E_{1^2} / \left[\lambda_{1^2} (n_{1^o})^3 c_{\varepsilon o \tau} r^2\right] \tag{10}$$

and

$$d_{\text{eff}} = d_{12}\cos^2\theta + d_{13}\sin^2\theta + d_{14}\sin(2\theta)\,, \tag{11}$$

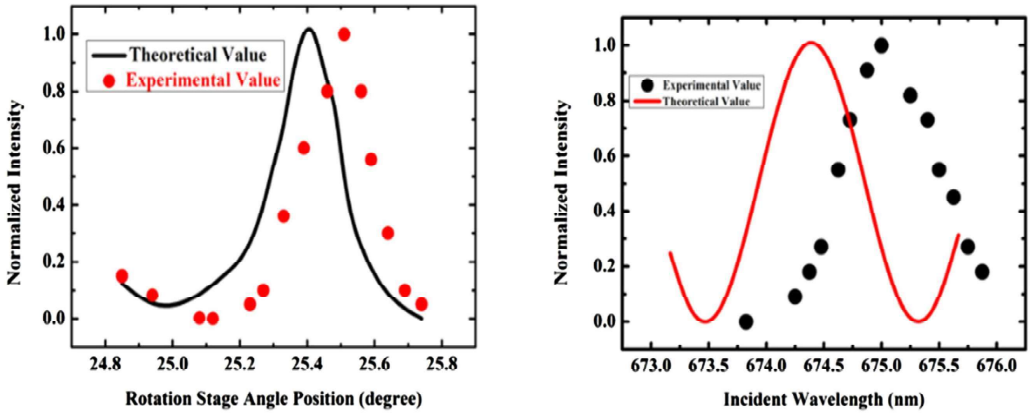

Fig. 7. (a) Angular acceptance bandwidth of SHG at 677 nm. (b) Spectral acceptance bandwidth of SHG in BIBO crystal. The smooth curve shows theoretical values while the dot represents the experimental point.

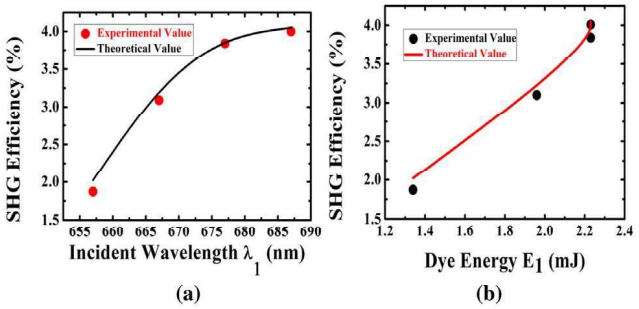

Fig. 8. (a) Incident wavelength versus dye SHG conversion efficiency. The black smooth curve shows the theoretical values whereas the red dots are experimental points. (b) Variation of energy E_1 of dye versus SHG. The black dots are experimental points whereas the red smooth curve shows the theoretical values.

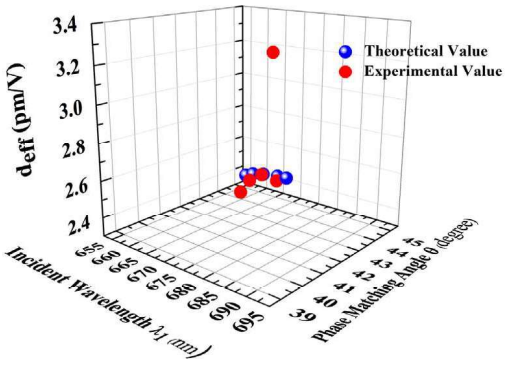

Fig. 9. Nonlinear coefficient (d_{eff}) with incident wavelength (λ_1) and phase-matching angle (θ).

where E_1 and E_2 represent the energies (millijoules) of the fundamental dye beam (λ_1) and its SHG (λ_2); d_{eff} is the effective nonlinear coefficient in pm/V; L is the thickness of the crystal in millimeters; n_1° is the ordinary (o) refractive index of the SHG crystal, which is 1.77668; c is the velocity of light and is 2.98×10^8 m/s; and ε_o is the permittivity of the vacuum 8.854×10^{-12} F/m. Wavelengths are selected in micrometers. τ is the laser pulse duration, which is 10×10^{-9} s for all the interacting beams, and r is the radius of the fundamental beam, which is of the order of 0.50×10^{-3} m.

For an input energy (E_1) of ~ 2.23 mJ, a typical energy conversion efficiency E_2/E_1 of 4.01% was obtained at the peak dye fluorescent region (687 nm).

Our experimentally measured values show good agreement with the theoretical prediction. The efficiency parameter depends on many factors such as crystal cut, incident laser energy, effective nonlinear coefficient, and beam radius. The highest measured conversion efficiency at 687 nm was 4.01% while the theoretical value is 4.09%.

4. RESULTS AND DISCUSSION

This part is divided into two subsections. Subsections (4.A–4.D and 4.F and 4.G) deal with THz evaluation of BIBO crystal while subsection 4.E deals with nanosecond-laser-based characterization.

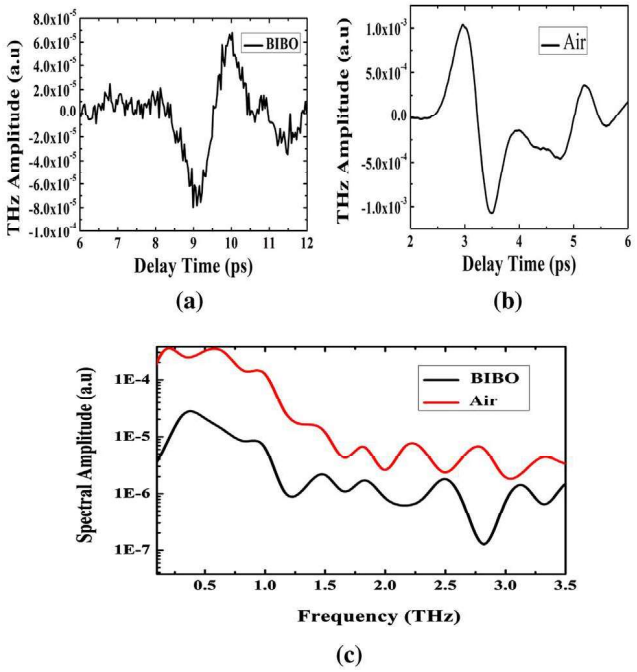

Fig. 10. (a) Time-domain spectra of BIBO crystal, (b) time-domain spectra of air, (c) frequency-domain spectra of BIBO crystal.

A. Terahertz Generation From BIBO

Figures 10(a)–10(c) show the time- and frequency-domain spectra of BIBO with respect to air. The time-domain THz signal received after passing through the BIBO was converted into frequency-domain spectra using FFT. It is very much clear from the dynamic range that the crystal that it can generate efficient radiation up to 2.5 THz range. However, the highest THz generation can be realized at the 1.2 THz range.

B. Transmittance and Absorption Coefficient Measurements

The transmission/absorption data was analyzed to find the absorption coefficients and refractive index of the crystal in the THz domain using Eqs. (1) and (2). The values of the absorption coefficient were calculated from the FFT spectrum.

Figure 11(a) shows that the transmittance of the BIBO crystal between the 0.1–3.5 THz range. There is a drop in transmittance at the 1 THz region and finally reaches to 75%. But it gradually increases up to 90% between the 1.75–3.5 THz range and confirms that BIBO possesses very good transmittance between deep 160 nm to higher THz range and can play a very important role to develop a multipurpose frequency device. Figure 11(b) shows the absorption coefficient of the BIBO crystal in the THz region. It is very interesting to note that BIBO crystal possesses the highest values of absorption coefficient in the THz region. We have identified 1.93, 2.1, 2.3, 2.6, and 2.75 THz absorbance bands, which also matches with the literature.

Figures 12(a) and 12(b) show the real and imaginary refractive indices with respect to THz frequencies between the 0.1–3.5 THz range. The value of the refractive index varies between 1.9 to 2.2 at the 1 THz range. It shows a drop between 1 to 1.5 THz and becomes constant between the 2 and 3.5 THz

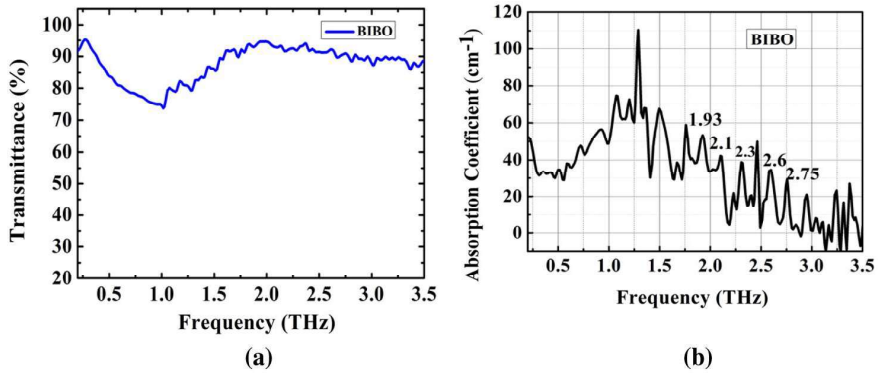

Fig. 11. (a) Transmittance, (b) absorption coefficients of BIBO crystal in the THz domain.

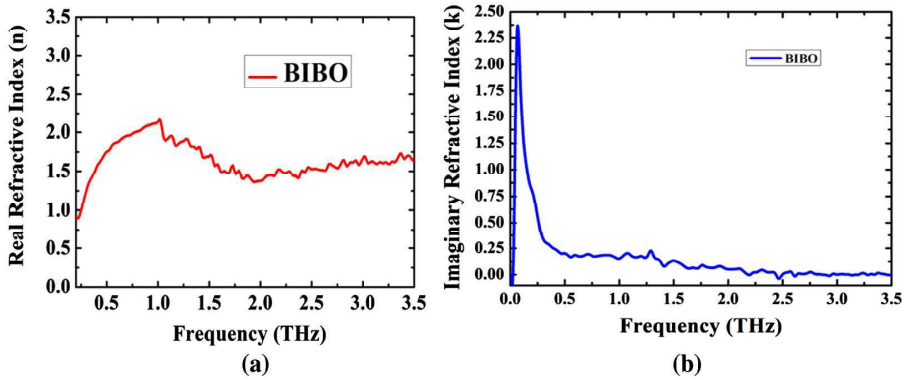

Fig. 12. (a),(b) Real and imaginary refractive indices of BIBO crystal in the THz domain.

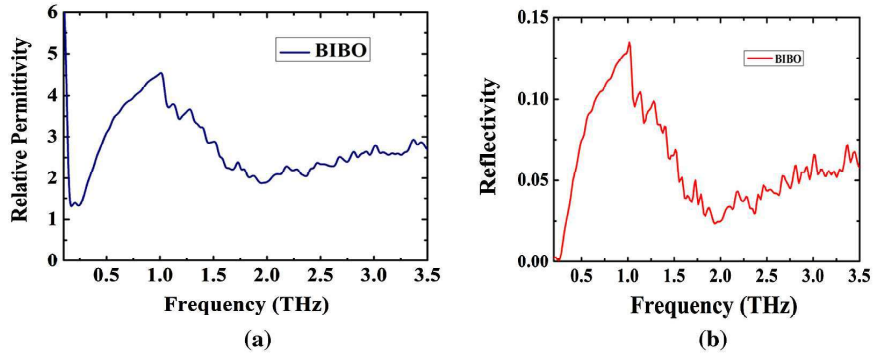

Fig. 13. (a) Relative permittivity, (b) reflectivity of BIBO crystal in the THz domain.

range. However, an average value of refractive index is approximately 1.75, which matches with the extraordinary refractive index in the optical domain derived from the Sellmeier equation [11]. The imaginary value of refractive index exponentially decreases and becomes constant between the 2.25–3.5 THz range.

C. Relative Permittivity and Reflectivity

Figures 13(a) and 13(b) show the relative permittivity and reflectivity of BIBO crystal in the THz domain. The relative permittivity is calculated using Eq. (5); the highest value of the relative permittivity is measured at the 1 THz range, which gradually decreases up to the 2 THz range. The value of elative permittivity remains constant between the 2.5 to 3.25 THz range. The reflectivity curve as shown in Fig. 13(b) has the highest value at the 1.0 THz range and then shows gradual decay up to the 2.0 THz range and becomes constant at a higher THz range.

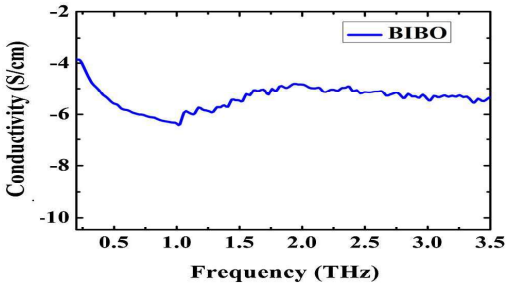

Fig. 14. Conductivity versus THz frequency of BIBO crystal.

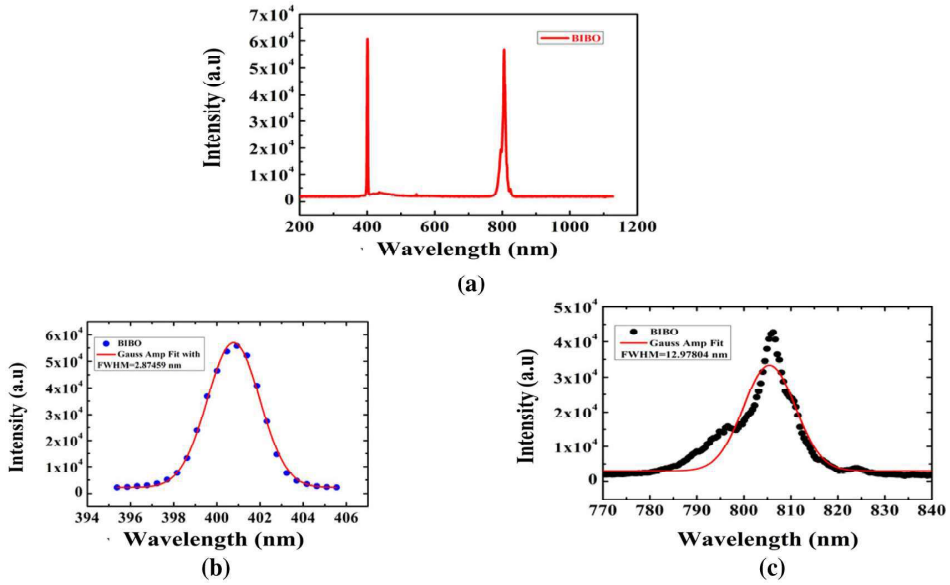

Fig. 15. (a) Spectral distributions of fundamental (1ω) and SH (2ω) pulses. (b) and (c) show the peak profiles of 400 and 800 nm wavelengths. The fitting is done after collecting the data points from the spectrometer and confirms the Gaussian nature of incident and generated radiation.

D. Calculation Conductivity of BIBO Crystal

Figure 14 shows the conductivity measurement of BIBO crystal in the THz domain.

E. Second-Harmonic Generation

Figure 15(a) shows the simultaneous measurement of SHG and THz using a femtosecond amplifier. The broadening effect is observed in the case of the SHG signal with respect to the fundamental signal, which is attributed to the conversion process and rise time of the fiber detector.

F. THz Generation Efficiency

It is very much clear that more that 50% part of 800 nm wavelength photons are converted into 400 nm UV radiation, which is similar to the previous report [14,24]. Figure 16 shows the THz conversion efficiency with respect to incident laser power. However, the conversion efficiency of THz is of the order of 1.85×10^{-5}%, which is recorded highest at 100 mW. The drop in conversion efficiency at higher power is attributed to many factors such as change in coherence length due to variation in R.I. with respect to temperature and transmission/absorption

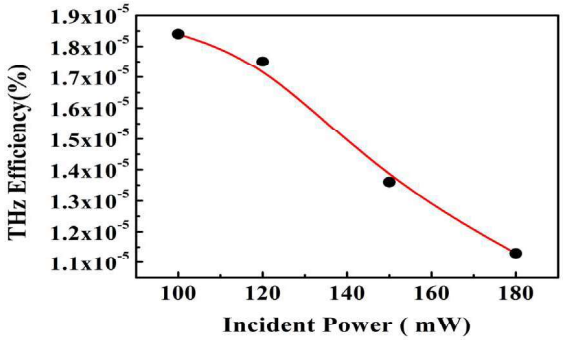

Fig. 16. THz conversion efficiency versus incident laser power.

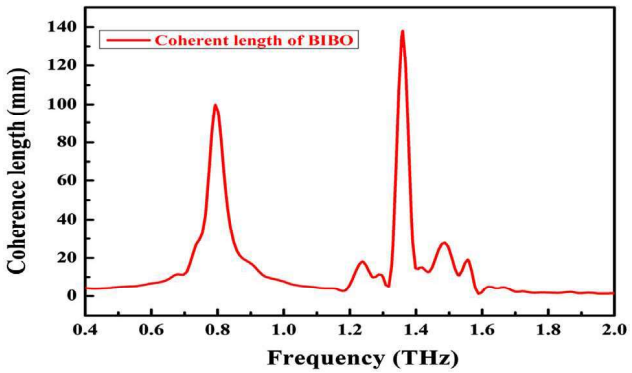

Fig. 17. Coherence length versus THz frequency.

losses. In addition, the conversion efficiency of optical rectification or difference frequency generation used for the THz generation is always much lower than the conversion efficiency of SHG or other parametric generation processes. It is attributed to many factors such as mismatch between group-velocity-based refractive index (ng) of optical pulses and THz refractive index (n_{THz}), which are also responsible for the change in the coherence length and limit the conservation of energy and moment between two interacting wavelengths, i.e., optical and THz. The difference of the refractive index is of the order of 0.102, which is quite high and responsible for the low conversion efficiency in the THz domain. Second, the variation in the transmittance of the crystal in the THz domain. For example, BIBO possesses very high transmission (90%) and low absorption in the UV–vis region while in the THz domain it has very strong absorption due to the presence of optical phonon modes, which is directly linked to the low conversion efficiency in the THz range.

To the best of our knowledge, it is the first report on the conversion efficiency of THz generation in BIBO crystal. However, conversion efficiency in DAST crystal is of the order of 1.61×10^{-2}%, which is almost 1000 times higher than the BIBO crystal.

G. THz Coherent Length

Figure 17 shows the coherence length of BIBO crystal at two different frequencies. It is of the order of 100 mm and 140 mm for 0.8 and 1.4 THz, respectively, which is directly related to the refractive index (R.I.) values in the optical and THz domains.

5. CONCLUSIONS

We have successfully demonstrated the use of Type I, $\theta = 28.9°$ cut BIBO crystal for the generation of UV to 0.1–3.5 THz radiation using nanosecond and femtosecond laser pulses. We have employed 800 nm wavelength pulses of 50 and 140 fs obtained from the Ti:sapphire laser amplifier and oscillator at 1.0 kHz and 80 MHz repetition rates, respectively. The conversion efficiency of SHG of fundamental wavelength 800 nm wavelength obtained from the femtosecond laser was $\sim 50\%$ while the conversion efficiency for the THz generation was of the order of $1.85 \times 10^{-5}\%$. We have also generated tunable UV radiation, which is a SH of a nanosecond dye laser and measured the efficiency $\sim 4.01\%$. In addition, we have also measured the phase-matching angle in the Y-Z plane for the Type I condition and ascertained the angular and spectral bandwidths of the generated signal. Finally, the coherence length, R.I., real and imaginary, absorption coefficients, and conductivity properties of BIBO crystal are ascertained in the THz domain for the first time.

Funding. University Grants Commission (F.530/20/CAS-II/2018 (SAP-I)); Department of Science and Technology, Ministry of Science and Technology, India (SR/FST/PS-II/2018/52(c)); Defence Research and Development Organisation (DRDO/18/1801/2016/01038: ACRHEM-Phase-III).

Acknowledgment. The authors would like to express their thanks to the Defense Research and Development Organization (DRDO), Ministry of Defence Govt. of India for financial support. ACRHEM-Phase-III and the director of ACRHEM for support. U. C. acknowledged ongoing CAS-II programme of UGC, Govt. of India and FIST Programme of DST, Govt. of India for partial financial support for the work.

Disclosures. The authors declare that there are no conflicts of interest.

Data Availability. Data underlying the results presented in this paper are not publicly available at this time but may be obtained from the authors upon reasonable request.

REFERENCES

1. D. M. Lubenko, G. V. Lansky, N. A. Nikolaev, E. A. Sandabkin, V. F. Losev, and Y. M. Andreev, "Generation of THz emission in nonlinear BBO crystal at room temperature," Proc. SPIE **11322**, 113222C (2019).
2. T. Notake, M. Takeda, S. Okada, T. Hosobata, Y. Yamagata, and H. Minamide, "Characterization of all second-order nonlinear-optical coefficients of organic N-benzyl-2-methyl-4-nitroaniline crystal," Sci. Rep. **9**, 14853 (2019).
3. C.-R. Wang, Q.-K. Pan, F. Chen, G. Lanskii, N. Nikolaev, A. Mamrashev, Y. Andreev, and A. Meshalkin, "Phase-matching in KTP crystal for THz wave generation at room temperature and 81 K," Infrared Phys. Technol. **97**, 1–5 (2019).
4. K. S. Rao, A. K. Chaudhary, M. Venkatesh, K. Thirupugalmani, and S. Brahadeeswaran, "DAST crystal based terahertz generation and recording of time resolved photoacoustic spectra of N_2 O gas at 0.5 and 1.5 THz bands," Curr. Appl. Phys. **16**, 777–783 (2016).
5. U. Venkataramudu, C. Sahoo, S. Leelashree, N. S. R. Gopal, D. Ganesh, A. K. Chaudhary, S. Srinath, and R. Chandrasekar, "THz generation, frequency doubling and above room-temperature ferroelectricity in a single-component polar organic crystal," J. Mater. Chem. C **6**, 9330–9335 (2018).
6. G. C. Bhar and U. Chatterjee, "Nonlinear phase matched second harmonic generation in beta barium borate," Appl. Phys. Lett. **54**, 1383–1384 (1989).
7. G. C. Bhar, S. Das, and U. Chatterjee, "Second harmonic generation from non-collinear orthogonally polarised Nd: YAG radiation in β-BaB_2 O_4," J. Phys. D **22**, 562–563 (1989).
8. G. C. Bhar, P. Kumbhakar, U. Chatterjee, A. M. Rudra, Y. Kuwano, and H. Kouta, "Efficient generation of 200-230 nm radiation in beta barium borate by non collinear sum frequency mixing," Appl. Opt. **37**, 7827–7831 (1998).
9. G. C. Bhar, U. Chatterjee, and P. Datta, "Enhancement of second harmonic generation by double-pass configuration in barium borate," Appl. Phys. **51**, 317–319 (1990).
10. T. Wilhelm, J. Piel, and E. Riedle, "Sub-20-fs pulses tunable across the visible from a blue-pumped single-pass non collinear parametric converter," Opt. Lett. **22**, 1494–1496 (1997).
11. A. Shirakawa, I. Sakane, M. Takasaka, and T. Kobayashi, "Sub-5-fs visible pulse generation by pulse-front-matched non collinear optical parametric amplification," Appl. Phys. Lett. **74**, 2268 (1999).
12. J. Liu, X. Guo, J. Dai, and X. C. Zhang, "Optical properties of beta barium borate in terahertz region," Appl. Phys. Lett. **93**, 1171102 (2008).
13. J. Huang, Z. Huang, Y. M. Andreev, G. V. Lanski, A. A. Lisenko, V. F. Losev, D. M. Lubenko, and N. A. Nikolaev, "THz wave generation in nonlinear crystal," in *The International Conference on Infrared, Millimeter, and Terahertz Waves*(IEEE, 2019).
14. H. Hellwig, J. Liebertz, and L. Bohaty, "Exceptional large nonlinear optical coefficients in the monoclinic Bismuth borate BiB_3O_6 (BIBO)," Solid State Commun. **109**, 249–251 (1999).
15. H. Hellwig, J. Liebertz, and L. Bohaty, "Linear optical properties of the monoclinic bismuth borate BiB_3O_6," J. Appl. Phys. **88**, 240–244 (2000).
16. Y. Li, J. Huang, Z. Huang, N. Nikolaev, G. Lanskii, A. Mamrashev, and Y. Andreev, "Optical properties of BiB_3O_6 in the terahertz range," Results Phys. **16**, 1–3 (2020).
17. S. C. Luciano and F. C. Cruz, "External power-enhancement cavity versus intra cavity frequency doubling of Ti:sapphire lasers using BIBO," Opt. Express **15**, 11913–11921 (2007).
18. V. Mottamchetty, T. Karunanithi, S. Brahadeeswaran, and A. K. Chaudhary, "Generation of efficient THz radiation by optical rectification in DAST crystal using tunable femtosecond laser pulses," Indian J. Phys. **91**, 319–326 (2016).
19. Y. Takida, T. Ohira, S. Maeda, and H. Kumagai, "High-efficiency second harmonic generation of mode-locked picosecond Ti: sapphire laser using BiB_3O_6 crystal with external enhancement cavity," J. Laser Micro/Nanoeng. **6**, 231–234 (2011).
20. Z. Wang, B. Teng, K. Fu, X. Xu, R. Song, C. Du, H. Jiang, J. Wang, Y. Liu, and Z. Shao, "Efficient second harmonic generation of pulsed laser radiation in BiB_3O_6 (BIBO) crystal with different phase matching directions," Opt. Commun. **202**, 217–220 (2002).
21. M. Ghotbi and M. Ebrahim-Zadeh, "Optical second harmonic generation properties of BiB_3O_6," Opt. Express **12**, 6002–6019 (2004).
22. A. J. Antonczak, J. Z. Sotor, M. Matysiak, and K. M. Abramski, "Blue 473-nm solid state diode pumped Nd: YAG/BiBO microchip laser," Opto-Electron. Rev. **18**, 71–74 (2010).
23. V. Petrov, M. Ghotbi, O. Kokabee, A. Esteban-Martin, F. Noack, A. Gaydardzhiev, I. Nikolov, P. Tzankov, I. Buchvarov, K. Iyata, A. Majchrowski, I. V. Kityk, F. Rotermund, E. Michalski, and M. Brahim-Zadeh, "Femtosecond nonlinear frequency conversion based on BiB_3O_6," Laser Photonics Rev. **4**, 53–98 (2010).
24. M. Thorhauge, J. L. Mortensen, P. Tidemand-Lichtenberg, and P. Buchhave, "Tunable intra-cavity SHG of CW Ti:Sapphire lasers around 785 nm and 810 nm in BIBO-crystals," Opt. Express **14**, 2283–2288 (2006).
25. Z. Hong, S. A. Rezvani, Q. Zhang, and P. Lu, "Ultrafast mid-IR laser pulses generation via chirp manipulated optical parametric amplification," Appl. Sci. **8**, 744 (2018).

26. M. Baudisch, M. Hemmer, H. Pires, and J. Biegert, "Performance of MgO: PPLN, KTA, and $KNbO_3$ for mid-wave infrared broadband parametric amplification at high average power," Opt. Lett. **39**, 5802–5805 (2014).
27. Y. Yin, J. Li, X. Ren, K. Zhao, Y. Wu, E. Cunningham, and Z. Chang, "High-efficiency optical parametric chirped-pulse amplifier in BiB_3O_6 for generation of 3 mJ, two-cycle, carrier-envelope-phase-stable pulses at 1.7 μm," Opt. Lett. **41**, 1142–1145 (2016).
28. M. E. Zadeh, "Efficient ultrafast frequency conversion sources for the visible and ultraviolet based on BiB_3O_6," IEEE J. Sel. Top. Quantum Electron. **13**, 679–691 (2007).

Physica Scripta

PAPER

Comparative studies of terahertz-based optical properties in transmission/reflection modes of GaSe: S and measurement of its scattering losses due to surface roughness for efficient terahertz generation

RECEIVED
23 May 2022

REVISED
24 November 2022

ACCEPTED FOR PUBLICATION
29 November 2022

PUBLISHED
16 January 2023

Chandan Ghorui[1], **Arjun V Kidavu**[1], **P Naveen Kumar**[1], **S Das**[2], **A K Chaudhary**[1,*] **and Yu M Andreev**[3]

[1] Advanced centre of Research in High Energy Materials (ACRHEM), University of Hyderabad, Telangana, 500046, India
[2] Laser Laboratory, Physics Department, Burdwan University, Burdwan, 713104, India
[3] Serbian Physical-Technical Institute of Tomsk State University, I Novosobornaya Sq, Tomsk 634050, Russia
[*] Author to whom any correspondence should be addressed.

E-mail: akcphys@gmail.com, akcsp@uohyd.ac.in **and** anilphys@yahoo.com

Keywords: THz, GaSe: S wafer, optical rectification, scattering

Abstract

The paper reports the efficient terahertz generation using nonlinear optical rectification process and comparative studies of optical, dielectric, and surface scattering properties of 1.0 mm thin GaSe: S crystal in transmission/reflection modes. We employed 800 nm wavelength of 140 fs and 50 fs pulse durations obtained from Ti: Sapphire oscillator and amplifier systems at 80 MHz and 1 kHz repetition rates, respectively, and evaluated the THz generation potential and optical properties such as refractive index, absorption coefficients, relative permittivity in transmission mode. In the next step, the crystal was subjected to a commercial THz system of 0.3 picosecond pulses at 100 MHz repetition rate in reflection geometry and once again recorded the similar parameters and compared with the transmission mode data. In addition, these data were used to measure the scattering losses from the surface of the crystal in terms of surface roughness, optical impedance, and Fresnel's reflection coefficients. The maximum generated THz power was of the order of 4.5 μW with conversion efficiency (η) $\sim 2.2 \times 10^{-3}$%. The measured THz efficiency was found equivalent to 20 mm thick GaSe crystal used in the difference frequency mixing technique. Finally, we have measured the Rayleigh roughness factor (g) of the crystal surface at different THz frequencies. When $g < 1$ (for small roughness) the Fresnel reflection loss factor becomes 0.75 at 1.4 THz frequency range which helps to enhance the generated signal.

1. Introduction

Generation of efficient terahertz radiation from nonlinear crystals is one of the emerging field of modern technology and having prime attention of researchers belonging to crystal growth as well as looking its applications in different fields such as spectroscopy, biomedical, defense, and homeland security [1–3]. The efficient terahertz (THz) generation is still a challenging task due to poor conversion efficiency of existing nonlinear crystals. It is also attributed to many factors such as crystal length, incident laser energy, low damage threshold, and nonlinear coefficients etc. In addition, the presence of water molecules in the atmosphere contributes to strong absorption in certain bands of generated frequency [4–6]. A large number of semiconductors, organic and inorganic nonlinear crystals are evaluated for the THz generation using different types of optical techniques such as ultrafast switching in Photoconductive antennas, Difference Frequency Mixing (DFM) and Optical Rectification (OR) in ZnTe, GaAs, $ZnGeP_2$, DAST, BNA, OH1 ,CdTe crystals and thin films [6-14].6–14. Vicario, C *et al* groups investigated the high-field THz generation in organic crystals DSTMS, DAST, and OH1 by optical rectification process using femtosecond Cr: fosterite laser pulse at 10 Hz repetition and they have achieved maximum conversion efficiency as high as 3% which corresponds to

energy per pulse up to 270 μJ [15]. Whereas, Zhang B *et al* reported highest energy of the order of 1.4 mJ terahertz radiation from a Lithium Niobates crystal [16]. In addition, GaSe which is one of the oldest nonlinear single crystal and attracted researchers for improvising its optical and surface hardness properties using different types of dopants. S. Das and Vodopyanov *et al* have reported efficient Mid IR generation from the same crystal using difference frequency mixing of CO_2 wavelengths [17]. Finally, AC Das *et al* have reported the comparative study of pure and doped GaSe crystal in terms of hardness, generated frequency range and identified different phonon frequencies in form of absorption peaks [18]. However, very few reports are available related to thin crystal appearing as wafer and showing higher generation efficiency than thick crystal. GaSe is a chalcogenides group III–VI semiconductor, non-isotropic, negative uni-axial crystal which is also available in wafer form and belongs to the point group of $\overline{6}2$ m [19]. It possesses second highest optical damage threshold of the order of 30 MW cm^{-2} at 1.064 μm with 10 ns pulse width. The potential of the crystal in the IR and THz spectral region has already been reported by different groups. The addition of dopant in GaSe crystals not only enhances its surface hardness but also increases the range of generated THz radiation and conversion efficiency [20–23].

Similarly, Wei Shi *et al* reported the generation between 0.57–3.57 THz frequency using DFM (Difference Frequency Mixing) from mixed GaSe crystal with 9.75 nJ energy [24]. Huang *et al* reported the emission between 0.57–3.57 THz frequency using collinear difference frequency generation from $GaSe_{0.91}S_{0.09}$. The THz power conversion efficiency is of 45% higher than that of undoped GaSe with generated power of the order of 21.8 W [25]. Wei Chen Chu *et al* reported the wideband THz generation from GaSe: Te crystal using femtoseconds pulses. The highest power was limited upto 1.3 μW [26]. Jialin Mei *et al* reported the KTP crystal based OPO tunable between 0.41–3.71 from GaSe with conversion efficiency of 7.8×10^{-7} [27]. J. Guo *et al* reported the doping of Al in GaAs which shows 2 to 3 times lower absorption as well as significantly strengthen the structural and optical properties of the crystal. Also, they have reported the effect of doing S in GaSe which enhances the damage threshold by 5 times and generated signal lies between Mid IR to millimetre range [28].

Generally, optical spectroscopy provides significant information about transmission/absorption and Raman scattering etc. of the materials with respect to the intensity of selected wavelength of light in continuous or pulsed modes. But THz time-domain spectroscopy (TDS) directly measures the temporal profile of associated electric field. The Fast Fourier Transform (FFT) of time domain signal provides the significant information about the phase and amplitude of the pulse. Therefore, the real and imaginary fractions of dielectric constants of a crystalline material without using on Kramers-Kronig relation can be obtained. Also, precise measurement of index of refraction and absorption coefficients of the material of interest provides significant information about the different types of phonon modes of the wafer in THz domain [18, 19, 24]. Further, rough surface correction is one of the important aspect of the present study which revealed the Mie scattering losses and corresponding drop in the power of the generated signal. Mittleman *et al* have reported the non-contact measurement of surface roughness scattering properties and optical impedance of building materials, textiles, thin films etc. using THz radiation [29, 30]. In addition, dielectric property of GaSe: S was measured using time-domain THz spectroscopy [18, 19]. The GaSe:S can be treated as one of the suitable alternatives of $LiNbO_3$ and ZnTe crystals for the generation of THz radiation in the laboratory [16, 31]. The first one is used for strong THz generation but possesses big difference between their optical and THz refractive indices which drastically reduces the coherence length of the $LiNbO_3$ and not preferred for the detection purpose. Whereas ZnTe has very small difference between optical and THz refractive indices and shows the long coherence length and most preferred material for generation as well as detection of THz radiation. Now a day, there are methods that make it possible to obtain a large coherence length in a Lithium Niobate crystal and a high conversion efficiency [16].

In the first part, we studied the optical transmission, generation, measurement of refractive index, absorption coefficients and conversion efficiency of the wafer. In second part, we have recorded the reflection mode data from a commercial THz system. Finally, we have measured the surface roughness properties which has utilized to ascertain the corresponding reflection, optical impedance of GaSe: S. The data were used to ascertain the scattering and reflection losses from the crystal surface. These loss is ultimately influences the efficiency of the generated signal. In the present study, GaSe: S crystal shows very small difference in refractive indices in optical & THz spectral range and satisfy the conditions for reasonably high conversion efficiency in THz domain using optical rectification technique. The novelty is attributed to the improvisation of optical properties such as refractive index (n) due modification of structure for efficient THz conversion efficiency of the order of (η) $\sim 2.2 \times 10^{-3\%}$ which was found equivalent to 20 mm thick GaSe crystal used in difference frequency mixing technique [32–34].

2. Experimental details

The experimental details are divided into three parts. In the first part, we measured the transmission/absorption data of 1.0 mm thick GaSe: S crystal ⟨001⟩ cut using time domain THz system. The crystal was grown using a

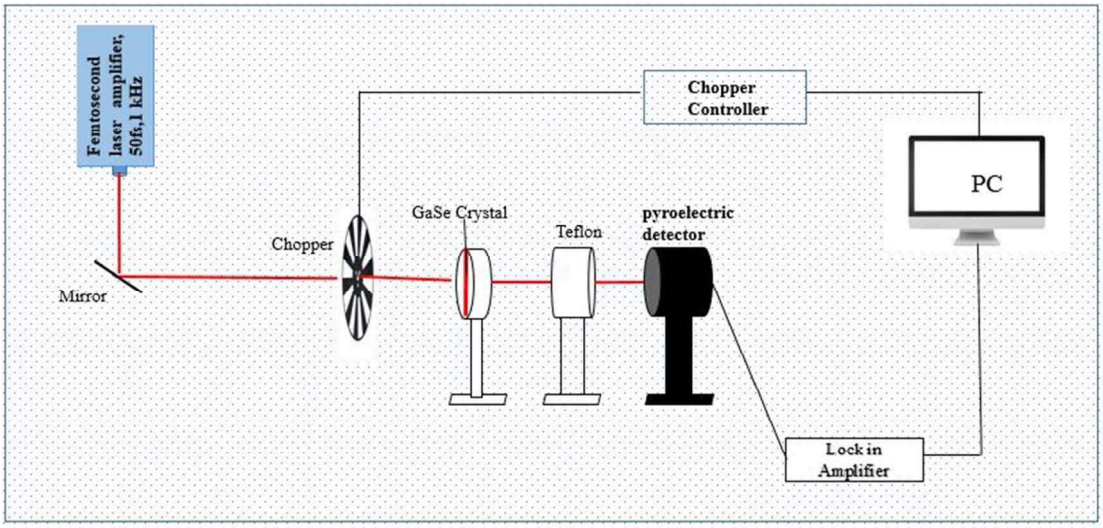

Figure 1. Schematic of experimental setup for measurement of power of terahertz generation of GaSe: S using pyro-electric detector.

vertical Bridgman method at Tomsk State University, Russia by Prof. Andreev [20, 21]. These data were utilised for ascertaining the refractive index and absorption coefficients in THz domain. In step two, the crystal was subjected to femtoseconds' amplifier for measuring the efficiency of the generated THz signal using the pyrometer detector. In third part, the crystal was subjected to a profilometer for surface roughness measurements using modified Fresnel equations. Finally, the data from first parts are used to measure the effect of surface scattering along with optical impedance, dielectric properties. The experimental setup for both transmission and reflection geometry and theoretical consideration are explained in the paper [35–37].

The transmission/absorption data were analysed to find the coefficient of absorption and index of refraction of the test sample in THz range.

In the second part, we employed 800 nm wavelength of 50 fs pulses produced by Ti: Sapphire amplifier at 1 kHz repetition rate for evaluating the conversion efficiency of GaSe: S under optical rectification arrangement. Figure 1 depicts the experimental layout for the pulsed THz generation. The emitted THz was detected radiation using a pyro electric detector (Gentec-EO, Canada made). The unconverted 800 nm pump beam was filtered using a Teflon sheet.

The same setup was utilized for the measurement of maximum power from the crystal. The power of the pump laser was controlled using polarizer and half wave's plate as a coupled beam modulator.

The transmission/absorption data was analysed to find coefficient of absorption and index of refraction of the test sample in THz range using equations nos. (2) and (3). The value of coefficient of absorption (α (ω)) was ascertained from Fast Fourier Transform (FFT) spectrum. Whereas the strength of transmitted THz field T is given by equation (1)

$$T = \frac{E_{Sample}}{E_{Referance}} \tag{1}$$

Here, E_{Sample} represents the strength of THz radiation after transmitted through the GaSe: S crystal, and $E_{Referance}$ stand for the transmission from air and treated as a reference.

$$\text{Absorption Coefficient } (\alpha) = -\frac{1}{d} ln \frac{T_m}{T_s} \tag{2}$$

Where, d is the thickness of GaSe: S and T_m and T_s are the transmittance from the crystal sample and reference, respectively. The real (n) and imaginary part (k) refractive indices of the GaSe: S sample can be ascertained from FFT transmission data by using equations no. (3) & (4), respectively.

$$n = 1 + \frac{\Delta\phi \times c}{2\pi\nu \times d} \tag{3}$$

$$k = ln\left(\frac{4n}{\rho_0(n+1)^2}\right)\frac{c}{2\pi\nu \times d} \tag{4}$$

Where, $\Delta\phi$ represents the phase difference between reference medium (air) and GaSe:S, ν is the THz frequency, d is the thickness of the sample, ρ_0 is the THz field amplitude for GaSe:S in frequency domain and c represents the velocity of light in vacuum.

The magnitude of relative permittivity can be calculated using equation (5):

$$|\varepsilon_r| = n^2 + k^2 \tag{5}$$

The value of Reflectivity (R) of GaSe: S sample can be measured using equation (6):

$$R = \left(\frac{n-1}{n+1}\right)^2 \tag{6}$$

The transmittance (T) of GaSe: S is given by,

$$T = e^{-\alpha d}(1-R)^2 \tag{7}$$

Where, 'α' = Coefficient of absorption, and 'R' = Reflectivity of GaSe: S at normal incidence.

The coherent length can be measured using equation No. (8):

$$L_c = \frac{\lambda_{THz}}{2(n_{gr} - n_{THz})} \tag{8}$$

Where, λ_{THz} is the terahertz wavelength, n_{gr} is the group velocity refractive index and n_{THz} are the refractive indices of THz region.

$$n_{gr} = n_{opt} - \frac{\partial n_{opt}}{\partial \lambda_{opt}}\lambda_{opt} \tag{9}$$

n_{opt} is the index of refraction at near infrared wavelength λ_{opt}.

3. Results and discussion

This part is divided in 6 sub-sections. The first part, deals with time domain spectra of GaSe: S crystal in transmission mode, in second part discusses the measurement of absorption coefficients and index of refraction (R.I.) of the crystal while section 3.3, deals with time domain and frequency domain spectra in reflection mode. The next section 3.4, comprises the absorption coefficients and refractive index data in reflection mode. Section 3.5, covers the coherence length calculation and THz generation efficiency aspects while section 3.6, comprises the surface roughness and reflection coefficients measurements along with the effect of surface losses on the efficiency of the generated signal.

3.1. Time domain THz spectra in transmission mode

Figures 2(a) and (b) shows the THz spectra of GaSe: S in time and frequency domain with respect to air. The frequency domain spectra of crystal were obtained from FFT of time domain terahertz signal passed through the sample. It is very much clear from the dynamic range that the crystal can generate efficient radiation upto 2.5 THz range.

3.2 Measurements of refractive index, absorption coefficients in transmission mode

Figures 3(a) and (b) shows the refractive index and absorption coefficients of GaSe: S between 0.1–2.5 THz range. The absorption coefficient curve shows rapid variation in the fringe pattern for small range which could be attributed to the surface roughness of the crystal [29, 30]. We have identified the effect of optical phonon modes in absorption curves of GaSe: S. Some of the absorption peaks are centred at 0.84, 1.28, 1.58, 1.78 & 2.28 THz, respectively [18].

The crystal shows slightly high refractive index (R I) between 0.1 and 0.2 THz range which decreases gradually upto 2.4 THz range. The average value of real refractive index is approximately 2.0 which matches with the value of extraordinary refractive index in optical domain measured by J F Molloy *et al* [38, 39]. However, imaginary part shows the exponential drop with respect to increasing in frequency. Further, it confirms that major part of incident and generated radiation are being utilized to compensate the different types of inherent absorption losses.

4. Measurement of time domain and frequency domain spectra of GaSe :S in reflection mode

The same GaSe: S was subjected to commercially available optical fiber coupled THz system (Toptica Model No. Tera flash Pro), Germany. The system generates THz pulses of 0.3 ps at 100 MHz repetition rate and recording of

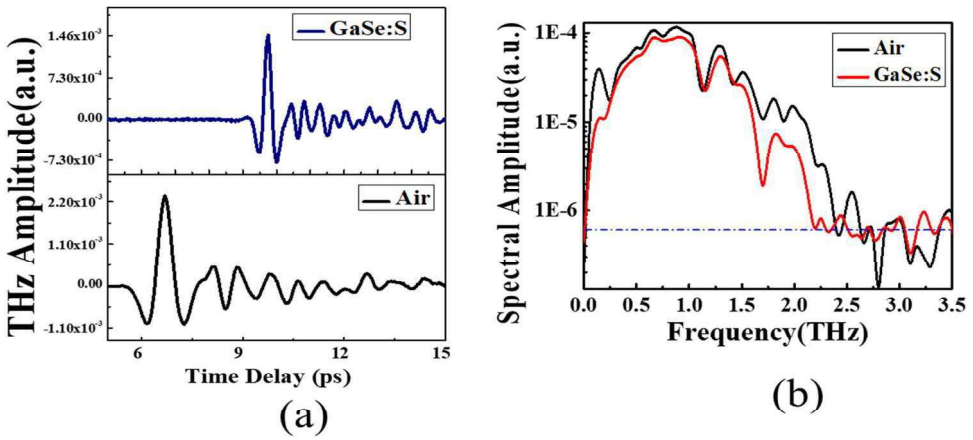

Figure 2. (a) Time domain spectra and (b) Generated THz frequency range of GaSe: S in transmission mode.

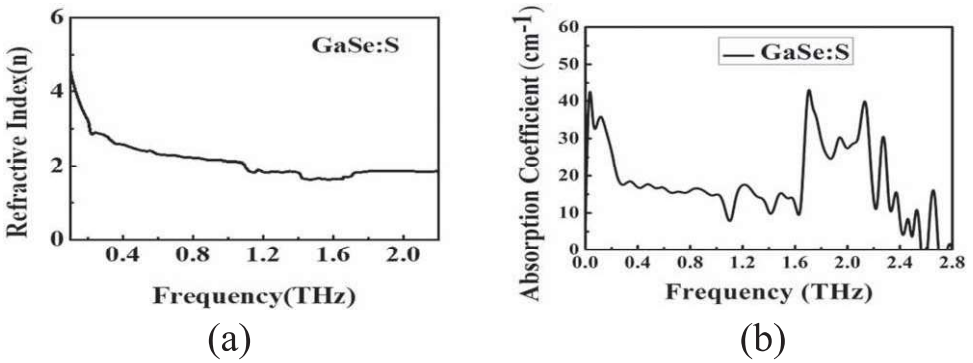

Figure 3. (a) Refractive Index (b) Absorption coefficient GaSe: S sample in THz domain.

data were carried out in reflection mode. The time and frequency domain THz spectra are shown in figures 4(a) and (b) respectively. Since measurements were carried out in reflection mode under dry air purge atmosphere. Therefore, reference time and frequency domain signal were recorded with respect to the gold coated mirror.

It is very much clear from the time domain spectra that the spectra are extended between 0.1 and 4.5 THz range.

4.1. Measurements of refractive index and absorption coefficients in reflection mode

Figures 5(a) and (b) show the refractive index and absorption coefficients of the GaSe: S. The values of R I. in reflection mode are slightly high between 0.3–0.7 THz range whereas the spectra are well resolved and values of absorption coefficients are also slightly high between 0.3–0.6 THz range. But highest recorded value of absorption coefficient is at 1.7 THz range in reflection mode. However, remaining other values of transmission and reflection modes are comparable with each other. The Molloy *et al* have clearly stated the chances of more numbers of phonon absorption peaks are centred at 0.59, 1.0, 2.5 THz range, respectively due to higher percentage of S (11% mass) [38]. The peak appears at 1.8 THz range shows shifting towards higher frequency range is attributed to higher sulfur percentage. The presence of small peaks is attributed to multiple reflection from the different layers of the crystal. But average values of absorption coefficients lie between the range of 20–50 cm^{-1} which is quite similar to the transmission mode data.

4.2. Measurement of coherence length and THz generation efficiency

Figure 6 shows the curve of coherence length of GaSe: S which was measured using equation (8). The value of coherence length is of the order of 1.37 mm at 0.33 THz which is sufficient enough to generate powerful THz radiation from the sample.

Figure 7 shows the measurement of generated THz power versus pump laser power. The trend of the graph clearly indicates the further growth of generated signal. The maximum generated power was of the order

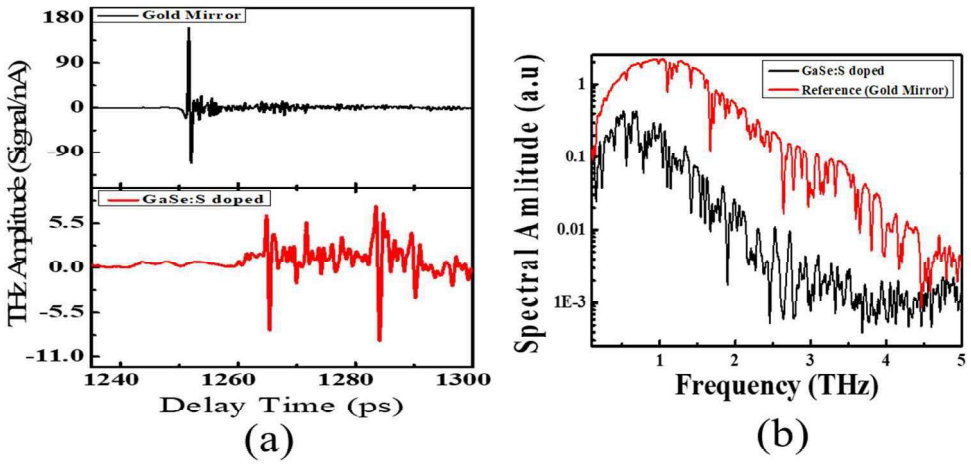

Figure 4. (a) Time domain (b) Frequency domain signal from GaSe: S with gold coated mirror surface as a reference.

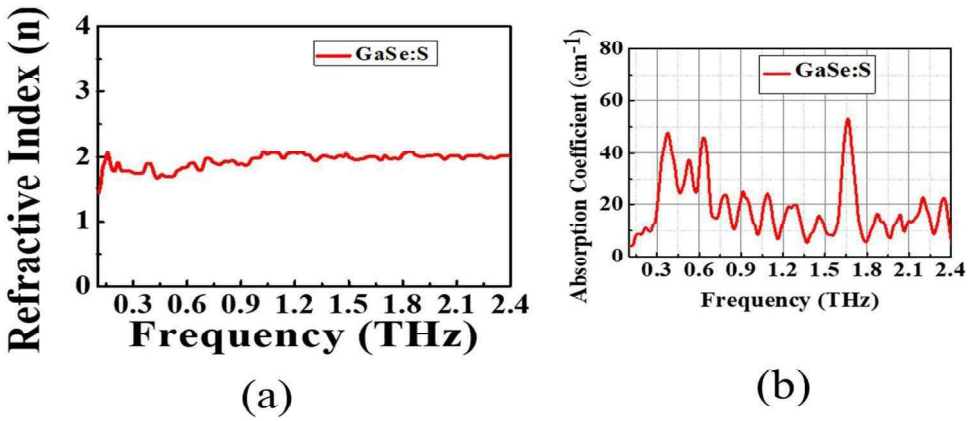

Figure 5. (a) Refractive index (b) Absorption coefficient of GaSe: S.

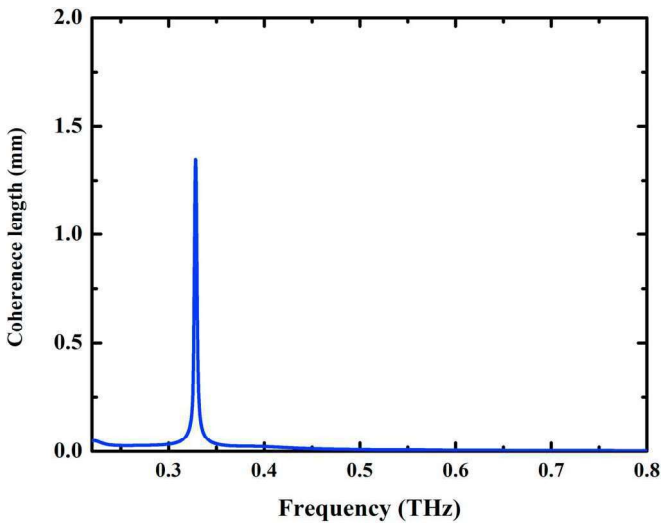

Figure 6. Coherence length versus frequency.

of 4.5 μW which was very significant to carry out all types of spectroscopic studies. We have used the same experimental set-up as shown in figure 1. The maximum output terahertz power was recorded at 200 mW incident power which was much higher than the previously reported work from other nonlinear crystals [10].

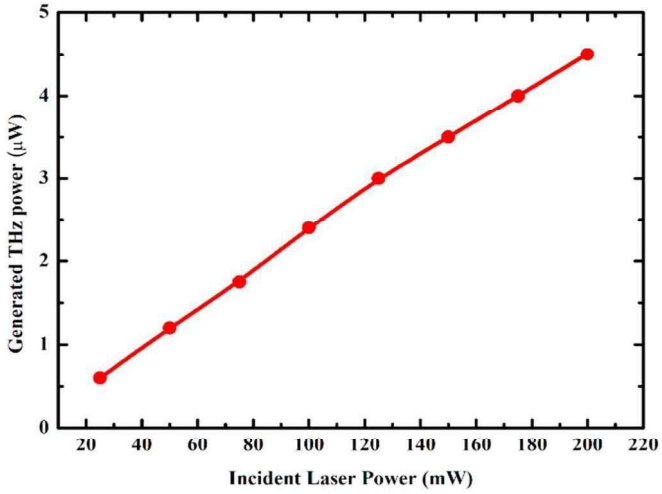

Figure 7. THz generated power Vs incident pump power.

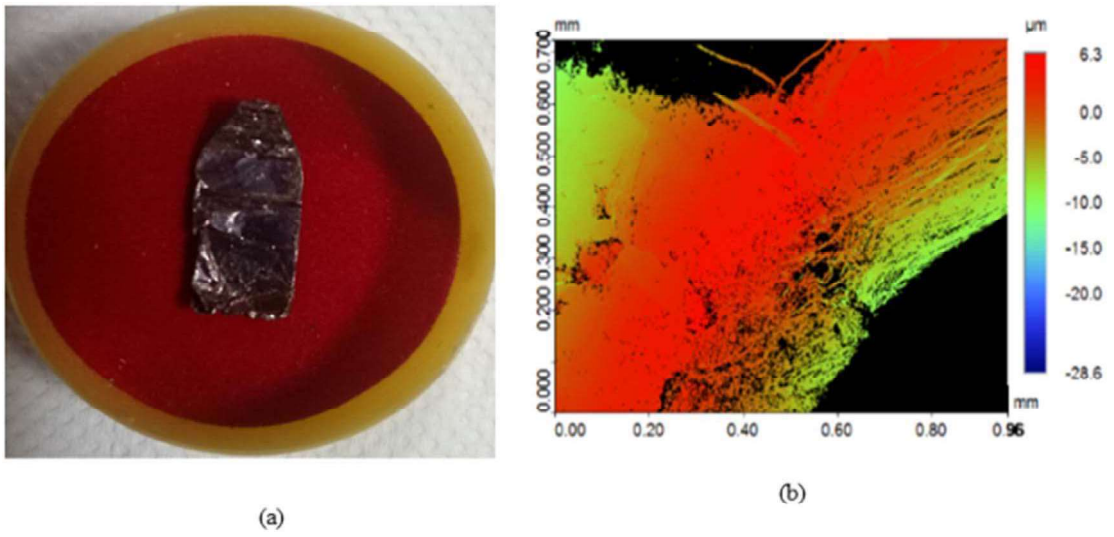

Figure 8. (a) GaSe: S crystal and (b) 2D Surface image.

The corresponding conversion efficiency (η) of GaSe:S was calculated as $2.2 \times 10^{-3\%}$ that is quite high and equal to 20 mm thick GaSe crystal used by Yujie J Ding [40, 41].

4.3. Measurement of surface roughness (g) and reflection coefficients

Figure 8(a) shows that the picture of GaSe: S and (b) shows that 2D surface image of same crystal using profilometer. Figure 9(a) shows that the g value of GaSe: S sample which shows rapid increase in g value upto 2.4 THz and measured using equation no (11) (Raleigh roughness factor of the crystal which is gradually decreases up to 2.4 THz. By solving the underlying Maxwell boundary value problems and adding the experimental values of surface roughness [29, 30, 42]. It helps us to ascertain the surface scattering effect and optical impedance of the GaSe: S. The problem can either be solved by numerical simulation approach which is based on differential equation and complex in nature. Therefore, we have used analytical approximations approach due to availability of refractive index (R.I), absorption coefficients (α) and surface roughness data of the crystal. The present work follows the Kirchhoff scattering theory from rough surfaces.

The Kirchhoff theory of scattering consider that in general smooth surface is free from multiple scattering and shadowing problems i.e. the surface should not possess sharp edges or corners. Moreover, it provides best results, when the surface height distribution profile should be Gaussian in nature. Therefore, calculation of Rayleigh factor would help to determine the surface roughness. In addition, the modified reflection coefficients measured in terms of Rayleigh factor is strongly influenced by an exponent factor σ which represents the

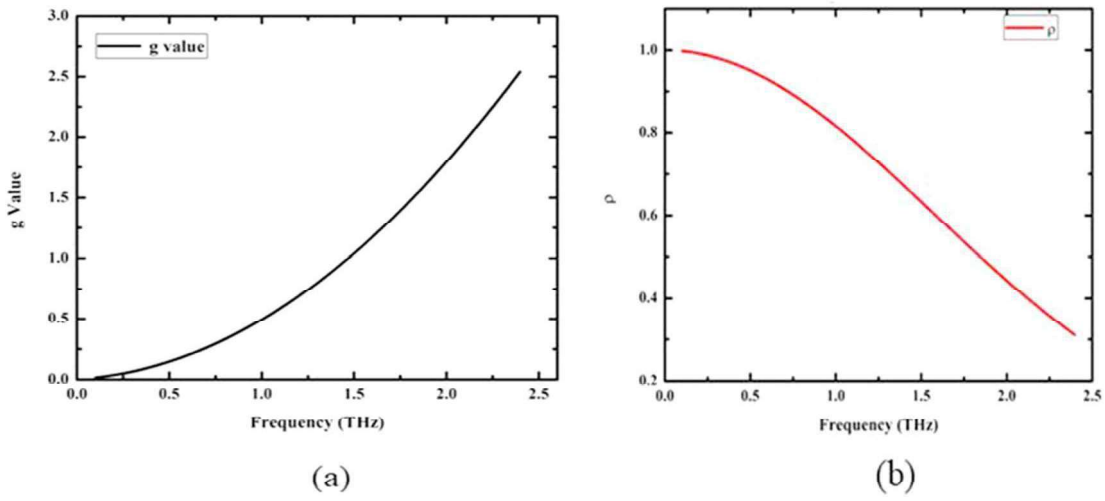

Figure 9. (a) Surface roughness (g) Vs THz Frequency (b) Roughness factor (ρ) Vs THz Frequency of GaSe: S at 25-degree angle of incidence:.

measured value of standard deviation of the surface height of the GaSe wafer. From this we are able to find out the roughness factor. Here the value of g is less than 1.0 at 1.4 THz which defines the surface roughness [29, 30, 42]. Using modified Fresnel equations along with corresponding impedance and modified reflection coefficient and value of surface roughness factor $\rho = 0.606$, the actual loss due to scattering in the particular direction can be ascertained using equations no. (11):

$$\rho = e^{-g/2} \tag{10}$$

$$g = \left(\frac{4\pi.\sigma.cos\theta_i}{\lambda}\right)^2 \tag{11}$$

Where, $\boldsymbol{\theta_i}$ and λ represent the angle of incidence and reflection and incident wavelength of THz radiation. σ represent the standard deviation of the surface roughness. Z is the impedance the reflecting material, which can be ascertained using equation No. (12):

$$Z = \sqrt{\frac{\mu_0}{\epsilon_0\left(n^2 - \left(\frac{\alpha c}{4\pi f}\right)^{\frac{1}{2}}\right)}} \tag{12}$$

Where, μ_0 is the free space permeability and ϵ_0 is the permittivity, n is refractive index of materials, α is the absorption coefficient of the materials and f represents the frequency of the incident THz wave. The surface roughness based modified reflection coefficients that indicates the reduction of the signal power in the specular direction are then.

$$r'_{TE} = \rho.r_{TE} \tag{13}$$

$$r'_{TM} = \rho.r_{TM} \tag{14}$$

where Fresnel reflection coefficients $\boldsymbol{r_{TE}}$ and $\boldsymbol{r_{TM}}$ correspond to TE or TM polarized waves from the smooth surface. We have calculated the reflection coefficient of the GaSe: S in TE and TM mode by using modified Fresnel equation (14 and 15). Usually reflection from the surface is calculated by using Fresnel equation (15 & 16)

$$r_{TE} = \frac{Zcos\theta_i - Z_0 cos\theta_t}{Zcos\theta_i + Z_0 cos\theta_t} \tag{15}$$

and

$$r_{TM} = \frac{Zcos\theta_t - Z_0 cos\theta_i}{Zcos\theta_t + Z_0 cos\theta_i} \tag{16}$$

Where, $\boldsymbol{\theta_t} = \arcsin\left(\sin\boldsymbol{\theta_i} \times \frac{Z}{Z_0}\right)$ represents the angle of refraction and $\boldsymbol{Z_0} = 377\Omega$ the free space wave impedance.

Figure 10 shows the reflection coefficients of TM and TE modes which also confirms the Brewster's angle and intensity of TM mode shows drastic increase in the reflectivity after 60 degrees. Similarly, Fig. 11 shows the

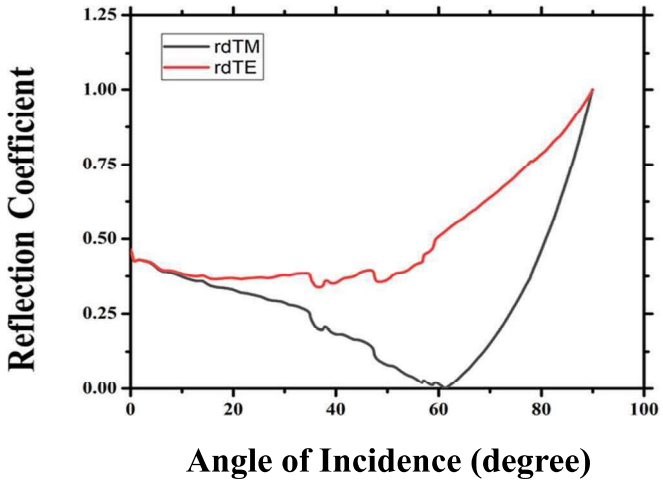

Figure 10. Reflection Coefficients Vs refraction to Angle of Incidence (degree).

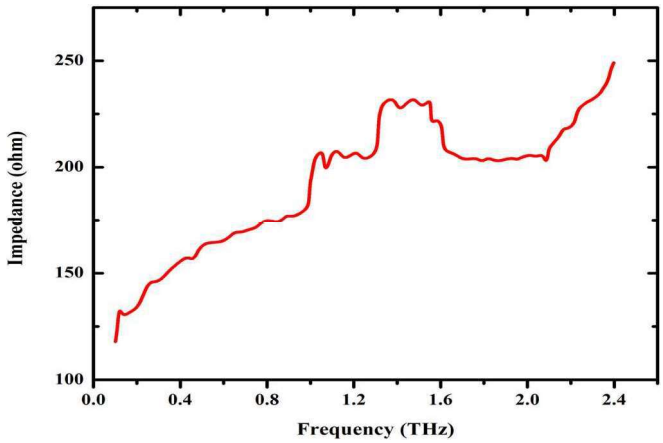

Figure 11. Optical impedance of GaSe: S upto 2.4 THz.

optical impedance curve and its exponential growth behaviour between 0.1 to 2.4 THz ranges. The average value of optical impedance is of the order of 200 Ohms which is lesser than the impedance of air. The value of g also important to predict the strength of generated THz frequency range. For example, if value of g is much smaller than 1 indicates that surface tends to be smooth and generated power in the speculation direction is inappreciably reduced but if its value is near to 1 then the surface is treated as moderately rough and reflection in non-speculation direction will be very high. Finally, when it is greater than 1 less than surface is treated as very rough and diffuse scattering losses dominate the reflection losses. The value of g is upto for 1.4 THz is less than 1, but for 2.4 THz it is 2.5 which clearly indicate that the higher losses and corresponding strength and range of generated signal.

5. Conclusions

We have successfully evaluated the GaSe: S, 1.0 mm thin crystal for generating the efficient THz radiation and measured the real and imaginary refractive index, absorption coefficients in transmission/reflection modes. We recorded the strength of generated power of THz radiation was of the order of 4.5 μW using Optical rectification process. The THz conversion efficiency was of the order of $(\eta) \sim 2.2 \times 10^{-3\%}$. It was found equivalent to 20 mm thick GaSe crystal used in difference frequency mixing technique. The refractive index and absorption coefficients measurements in reflection mode carried out using a commercially available fast THz system of 0.3 ps pulses at 100 MHz repetition rate which find good agreement in wide band of THz frequency. In addition, we also ascertained the surface roughness properties in terms of reflection loss. The surface roughness factor was

used to measure the optical impedance, conductivity, permeability of the crystal for the first time. Finally, transmission/absorption and surface loss data obtained from Fresnel reflection and surface roughness were correlated to understand the efficiency limitations of S doped GaSe crystal. It was also verified that if value of surface roughness (g) is lower than 1, the efficiency of the generated radiation at 0.7 THz has highest value whereas at 1 THz the value of g becomes 2.5 and strength of the signal also becomes minimum.

Acknowledgments

The authors would like to express their sincere thanks to the funding agency Defense Research and Development Organization (DRDO), Ministry of Defence, Govt. of India for financial support under the grant No. DRDO/18/1801/2016/01038: ACRHEM-Phase-III and the Director, ACRHEM for their support. One of author Chandan Ghorui expresses his gratitude to PMRF Fellowship, Govt. of India.

Data availability statement

All data that support the findings of this study are included within the article (and any supplementary files).

Conflict of interest

There is no conflict of interest among the authors.

ORCID iDs

Chandan Ghorui https://orcid.org/0000-0002-9423-5761
A K Chaudhary https://orcid.org/0000-0003-1793-9930

References

[1] Wei L, Yu L, Jiaoqi H, Guorong H, Yang Z and Weiling F 2018 *Front. Lab. Med.* **2** 127–33
[2] Federici J F, Schulkin B, Huang F, Gary D, Barat R, Oliveira F and Zimdars D 2005 *Semicond.Sci. Technol.* **20** S266
[3] Lee Y-S 2009 *Principles of Terahertz Science and Technology* (Boston, MA: Springer)
[4] Globus T, Bykhovski A, Khromova T, Gelmont B, Tamm L K and Salay L C 2007 *Proc. SPIE* **6772** 67720S
[5] Chen C-W, Hsu Y-K, Huang J Y, Chang C-S, Zhang J-Y and Pan C-L 2006 *Opt. Express* **14** 10636–44
[6] Venkatesh M, Rao K S, Abhilash T S, Tewari S P and Chaudhary A K 2014 *Opt. Mater.* **36** 596–601
[7] Karthick S, Santha A, Ganesh D, Thirupugalmani K, Ganesamoorthy S, Chaudhary A K and Brahadeeswaran S 2021 *Growth, J. Mol. Struct.* **1224** 129065 1–9
[8] Liu Y, Zhong K, Wang A, Zhou M, Li S, Gao L and Zhang Z 2022 *Crystals* **12** 1–14
[9] Esaulkov M N, Fokina M I, Zulina N A, Timofeev T V, Shkurinov A P and Denisyuk I Y 2018 *Opt. Laser Techno.* **108** 450–5
[10] Venkatesh M, Thirupugalmani K, Rao K S, Brahadeeswaran S and Chaudhary A K 2017 *Indian J. Phys.* **91** 319–26
[11] Xie X, Xu J and Zhang X-C 2006 *Opt. Lett.* **31** 978–80
[12] Karthick S, Ganesh D, Thirupugalmani K, Chaudhary A K and Brahadeeswaran S 2019 *Mater. Lett.* **246** 95–8
[13] Shi W and Ding Y J 2002 *Opt. Photonics News* **13** 57
[14] Kumbhakar P, Kobayashi T and Bhar G C 2004 *Appl. Opt.* **43** 3324–8
[15] Vicario C, Jazbinsek M, Ovchinnikov A V, Chefonov O V, Ashitkov S I, Agranat M B and Hauri C P 2015 *Opt.Express* **23** 4573–80
[16] Zhang B *et al Laser Photonics Rev.* **15** 1–112021
[17] Das S, Ghosh C, Gangopadhyay S, Chatterjee U, Bhar G C, Voevodin V G and Voevodina O G 2006 *JOSA B* **23** 282–8
[18] Das A C, Bhattacharya S, Jewariya M, Prabhu S S, Mandal K C, Ozaki T and Datta P K 2017 *IEEE J. Sel. Top. Quantum Electron.* **23** 1–7
[19] Mandal K C, Kang S H, Choi M, Chen J, Zhang X-C, Schleicher J M, Schmuttenmaer C A and Fernelius N C 2008 *IEEE J. Sel. Top. Quantum Electron.* **14** 284–8
[20] Guo J, Xie J-J, Li D-J, Yang G-L, Chen F, Wang C-R, Zhang L-M, Andreev Y M, Kokh K A, Lanskii G V and others 2015 *Light: Sci. Appl.* **4** 1–12
[21] Ku S A, Chu W-C, Luo C W, Andreev Y M, Lanskii G, Shaidukoi A, Izaak T, Svetlichnyi V, Wu K H and Kobayashi T 2012 *Opt. Express* **20** 5029–38
[22] Atuchin V V, Andreev Y M, Kokh K A, Lanskii G V, Shaiduko A V, Izaak T I and Svetlichnyi V A 2013 *Nonlinear Opt. Appl.* **VII** 87721Q1–9Q1
[23] Chen C-W, Hsu Y-K, Huang J Y and Chang C-S 2006 *Opt. Exp.* **14** 10636–44
[24] Shi W, Ding Y J, Fernelius N and Ken Hopkins F 2006 *Appl. Phys. Lett.* **88** 101101–3
[25] Huang J, Huang Z, Tong J, Ouyang C, Chu J, Andreev Y, Kokh K, Lanskii G and Shaiduko A 2013 *Appl. Phys. Lett.* **103** 081104-1-081104-4
[26] Chu W-C, Ku S A, Wang H J, Luo C W, Andreev Y M, Lanskii G and Kobayashi T 2012 *Opt. Lett.* **37** 945–7
[27] Mei J, Zhong K, Wang M, Liu Y, Xu D, Shi W, Wang Y, Yao J, Norwood R A and Peyghambarian N 2016 *Opt. Express* **24** 23368–75
[28] Guo J, Xie J-J, Zhang L-M, Kokh K, Andreev Y, Izaak T, Lanskii G, Shaiduko A and Svetlichnyi V 2014 *J. Mater. Sci., Mater. Electron.* **25** 1757–60

[29] Piesiewicz R, Kleine-Ostmann T, Krumbholz N, Mittleman D, Koch M and Kürner T 2005 Terahertz characterisation of bulding materials *Electron. Lett.* **41** 1002–4
[30] Piesiewicz R, Jansen C, Mittleman D, Kleine-Ostmann T, Koch M and Kurner T 2007 *IEEE Trans. Antennas Propag.* **55** 3002–9
[31] Vidal S, Degert J, Tondusson M, Freysz E and Oberlé J 2014 *J. Opt. Soc. Am. B* **31** 149–52
[32] Yu B L, Zeng F, Kartazayev V, Alfano R R and Mandal K C 2005 *Appl. Phys. Lett.* **87** 1–4
[33] Zhang D, Lv Z, Sun L and Yuan J 2007 *Joint 32nd Int. Conf. on Infrared and Millimetre Waves and the IEEE Xplore Int. Conf. on Terahertz Electronics* pp 239–240
[34] Fernelius Nils C 1994 *Progress in Crystal Growth and characterization of materials* **28** 275–353
[35] Ghorui C, Rudra A M, Chatterjee U, Chaudhary A K and Ganesh D 2021 *Appl. Opt.* **60** 5643–51
[36] Arjun A, Ganesh D, Karthick S, Santha A, Venkatesh M, Ganeshamoorthy S, Brahadeeswaran S and Chaudhary A K 2021 *Crystal Growth* **575** 1–5
[37] Koalla R, Periketi N, Ghorui C, Mangali S and Chaudhary A K 2022 *J. Mol. Struct.* **133449** 1–10
[38] Molloy J F, Naftaly M, Andreev Y M, Kokh K, Lanskii G V and Svetlichnyi V A *2015 40th Int. Conf. Infrared, Millimeter, Terahertz Waves* pp 1–2 *(2015)*
[39] Chen C-W, Tang T S-T, Lin S-H, Huang J Y, Chang C-S, Chung P-K, Yen S-T and Pan C-L 2009 *J. Opt. Soc. Am. B* **26** 58–65
[40] Ding Y J 2007 *IEEE J. Sel. Top. Quantum Electron.* **13** 705–20
[41] Shi W and Ding Y J 2004 *Appl. Phys. Lett.* **84** 1635–7
[42] Bänninger D and Flühler H 2004 *IEEE Trans. Geosci. Remote Sens.* **42** 1462–71

Research Article Vol. 62, No. 18 / 20 June 2023 / Applied Optics 4831

applied optics

Linear and nonlinear optical characterization of tellurium dioxide (α-TeO_2) for generation of terahertz radiation using time-domain spectroscopy

CHANDAN GHORUI AND A. K. CHAUDHARY*

Advanced Centre of Research in High Energy Materials (ACRHEM), University of Hyderabad, Telangana, 500046, India
**akcsp@uohyd.ac.in, anilphys@yahoo.com, akcphys@gmail.com*

Received 27 March 2023; revised 18 May 2023; accepted 22 May 2023; posted 22 May 2023; published 12 June 2023

This paper reports the linear and nonlinear optical characterization of $\alpha-TeO_2$ crystal in the optical and terahertz domains for efficient terahertz (THz) generation using a difference frequency mixing technique. We have ascertained the optical properties such as refractive index, absorption coefficients, real and imaginary dielectric constants, and coherence length $l_c = 280$ mm at 1.77 THz range using an indigenously developed THz spectrometer. The value of refractive index was ascertained from temporal and spectral THz profiles of the crystal and employed for calculating the Type I phase-matching angle, i.e., $\theta = 21.15°$ for the generation of tunable radiation between the 0.1 and 1.9 THz range. The figure of merits in the optical and THz domains lie between the 0.02–0.015 range. The effective bandwidth of the crystal lies between the 0.1 and 3.0 THz range. © 2023 Optica Publishing Group

https://doi.org/10.1364/AO.491556

1. INTRODUCTION

Tellurium oxide is one of the most attractive semiconductors which is also treated as a semimetal. It is available in both crystalline and amorphous phase. Tellurium dioxide (TeO_2) in crystalline phase form exists in two phases: paratellurite with tetragonal phases with orthorhombic symmetry [1].

In the paratellurite form, it belongs to point group D4 (422) and exhibits a very high degree of symmetry and possesses useful elastic and piezoelectric properties [2,3]. Several groups have reported the applications of TeO_2 single crystal as an acousto-optic device in the visible region [3–5]. The figure of merit (FOM) of acousto-optic of a single-crystal paratellurite (1.2 X s3 g" for transverse acoustic waves) is the highest among the existing optically transparent materials. Due to high acoustic-optic figure of merit, it shows chemical stability, mechanical durability, wide bandgap, and high dielectric constant. As a result, it is widely used for making active optical devices such as deflectors, modulators, tunable filters, and as a dielectric medium in capacitors. Generally, broadband terahertz (THz) radiation is generated using an ultrashort laser-pumped photoconductive switch, by means of optical rectification in nonlinear crystals (OR), difference frequency mixing (DFM), etc. There has been considerable progress made toward the development of new THz sources such as quantum cascade lasers, Gunn diode lasers, IMPATT diode, semiconductors, and semimetal films, etc. [6–9]. The generated broadband THz pulses on a picosecond time scale offer additional benefits using a phase-coherent detection technique that provides the inherent advantage of a time resolution which may be as short as a few tens of femtoseconds. Many other electronic sources cover only a limited THz range or can emit a particular THz frequency. Whereas nonlinear optics-based sources are of particular interest due to covering of the complete THz frequency band (frequencies from 0.1 THz to beyond 10 THz). In continuation of the search of new materials, $\alpha-TeO_2$ is an ideal colorless compound to scrutinize the role of THz radiation. In contrast to pure Te and InSb, which are optically opaque, broadband semiconductors and behave like an insulator and possess transparency between 0.33 and 6.5 μm range. As a result, no photocharge carriers can be generated by the irradiation of femtosecond laser pulses of 800 nm wavelength. $\alpha-TeO_2$ is a colorless tetragonal with a point group D4 (422). However, at room temperature, $\alpha-TeO_2$ lacks the space inversion symmetry, resulting in piezoelectricity. Due to the large acoustic optic effect, it is widely used as an optical modulation and in making deflection devices in the visible range. Moreover, its application in the THz frequency range at the 300 K temperature range is limited due to high absorption of generated radiation. Furthermore, it was reported that the second-order nonlinear optical coefficient of $\alpha-TeO_2$ has a moderate second-order nonlinearity value of the order of 0.69 ± 0.08 pm/V at 1.064 μm. In addition, $\alpha-TeO_2$ also shows the optical activity for changing the orientation of light. Some of the well-known nonlinear crystals widely used for making efficient nonlinear devices are KH_2PO_4

(KDP), KD*P, $\beta-BaB_2O_4$ ($\beta-$BBO), LiB_3O_5 (LBO), LAP, $KTiOPO_4$ (KTP), BNA, DAST, S-doped GaSe, etc. [10–17]. In addition, we have successfully demonstrated the use of the same OR technique in some selected inorganic and organic crystals such as $ZnGeP_2$, BNA, OH1 GaSe :S, BiBO3, LAP, P-BI, etc., for efficient THz generation. Many of these crystals can also be employed for the generation of THz radiation using DFM, plasma generated from filamentation of femtosecond laser and optical rectification [14,15,18,19]. Sotome *et al.* reported the terahertz radiation in a noncentrosymmetric insulating oxide, paratellurite ($\alpha-TeO_2$), induced by coherent phonon generation via impulsive stimulated Raman scattering in paratellurite using a femtosecond laser pulse at room temperature [20]. Uchida has thoroughly investigated the optical properties of single-crystal paratellurite ($\alpha-TeO_2$), including absorption coefficients at the fundamental band edge, the dispersion characteristics of the refractive indices, and the optical rotatory power [21]. Li *et al.* theoretically performed the first-principles-based structural, electronic, and optical properties of TeO_2 polymorphs using the density functional theory plane-wave pseudopotential method [22]. In 2016, Unferdorben *et al.* reported the polarization and optical properties of single paratellurite crystal using the Lorentz oscillator model in the terahertz domain [23]. Recently, Komandin demonstrated the use of paratellurite as an acousto-optical deflector using terahertz time-domain spectroscopy (TDS) [24]. In continuation of same, we have also reported the efficient THz generation from the annealed TeO_2 thin films using ultrashort laser pulses [25].

In the present work, we have evaluated the role of a positive uniaxial single $\alpha-TeO_2$ crystal as a THz generator using the optical rectification and DFM techniques. Due to the moderate second-order nonlinear susceptibilities and high transmission in the Vis–NIR and THz range indicating the role of the single crystal as a potential candidate for the generating THz radiation. The optical properties, including dielectric constants, refractive index, and absorption coefficients can be ascertained by means of transmission/absorption data of the $\alpha-TeO_2$.

The crystal was purchased from Biotain Crystal Co., LTD., China. The crystal thickness is 0.5 mm with a 110 orientation. We have recorded the time-domain THz spectra using an indigenously designed THz spectrophotometer. The obtained transmission data was used for determining the real and imaginary parts of the dielectric constants, coherence length (l_c) in the case of optical rectification, Type I, DFM phase-matching angle for tunable THz generation and FOM in the optical and THz domains. In addition, response in the broadband infrared region also enabled single crystal suitable for an electro-optic sampling of high-speed digital and microwave circuits. Based on our aforesaid measurement, we found that $\gamma-TeO_2$ crystal may be a good THz material for generation. We have compared the efficiency of the generated THz signal of some prominent crystals such as BNA, DAST, BIBO, GaSe:S, CdTe, TeO_2, etc. Their THz conversion efficiency lies between $10^{-3}-10^{-5}$% and is arranged like BNA > GaSe : S > DAST > TeO_2 > BIBO > LAP.

2. EXPERIMENTAL DETAILS

In this section, we have measured the transmission/absorption data of the $\alpha-TeO_2$ using a terahertz time-domain spectroscopy. These data were utilized for ascertaining the refractive index and absorption coefficients in the THz domain.

The transmission/absorption data were further used to ascertain the coefficient of absorption and index of refraction of the $\alpha-TeO_2$ crystal in the THz range.

For the generation of the THz pulses, we have used a low-temperature (LT) GaAs-based photoconductive (PC) antenna. The required tunability of the pump wavelength was obtained by ultrashort pulses of a Ti:sapphire laser. The central wavelength of 800 nm, pulse duration of 140 fs, and a repetition rate of 80 MHz was used to generate the tunable THz radiation between 0.1 and 3.5 THz. The laser pulse was split into two parts using a 90:10 beam splitter. The reflected signal was directed to the LT GaAs-based PC antenna for low photon energy THz generation. The generated THz beam was focused on the $\alpha-TeO_2$ crystal of 0.5 mm thickness for transmission measurement using an off-axis parabolic mirror (OAPM) set. The transmitted radiation was further collimated and focused on the ZnTe crystal using another pair of OAPM set. The generated THz signal was measured using the electro-optic sampling technique made of ZnTe crystal, $\lambda/4$ wave plates, a Wollaston prism, and pair of PIN photodiodes. The experimental setup for the measurement of optical property using THz TDS and theoretical considerations is in [6].

3. RESULTS AND DISCUSSION

This section is divided into six subsections. The first subsection deals with time/frequency-domain THz spectra of $\alpha-TeO_2$ crystal in the transmission mode while the second part covers measurements of refractive index (RI) and absorption coefficients in the THz domain. The third part deals with the measurements of real and imaginary parts of the dielectric constants. The fourth part discusses the group velocity and coherence length while the fifth subsection is dedicated to Type I DFM and second-harmonic generation (SHG) phase-matching angles. The final subsection deals with the determination of the FOM in the optical and THz domains to ascertain the utility of crystal for device applications.

A. THz Time-Domain Spectroscopy

We have used indigenously designed time-domain THz spectrometer for the recording of temporal and spectral profiles of $\alpha-TeO_2$ in the transmission mode with respect to air. Figures 1(a) and 1(b) show the time-domain and frequency-domain spectra of $\alpha-TeO_2$ with respect to air. Figure 1(b) confirms the dynamical cutoff range of crystal at 2.5 THz.

The intensity fringe pattern in the power spectrum along with peak structure at ~1.6 and 2.0 THz, respectively, which is extended up to ~3.0 THz, is shown in Fig. 1(b).

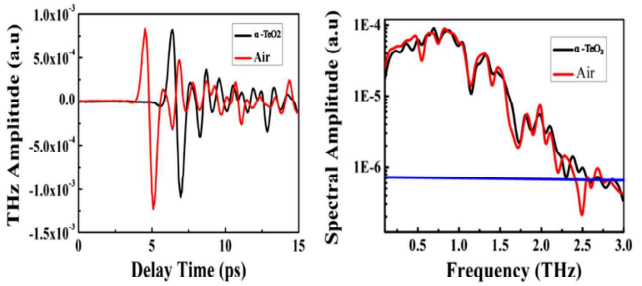

Fig. 1. (a) Time-domain, (b) frequency-domain profile of $\alpha-TeO_2$.

B. Refractive Index and Absorption Coefficient of $\alpha-TeO_2$

The frequency-domain data obtained from Subsection 3.A are used for the measurements of RI and absorption coefficients in the THz domain.

Figure 2(a) shows the value of real refractive indices with respect to THz frequencies between 0.1 and 3.0 THz. It shows exponential drop between 0.1 and 0.5 THz and becomes constant up to 3.0 THz. However, the average value of refractive index is around 2.25 in the entire THz domain which matches with the ordinary refractive index in the optical domain, which is derived from Sellmeier equation using two oscillating model [21].

The high variation in the RI below 0.5 THz is attributed to many reasons. The fast Fourier transform-based data were used in the Kramers–Kroning relationship for calculating the RI in the THz domain, which is not straightforward. The high brightness of ultrashort pulses as compared to CW sources forced recording the transmission at high intensity bright signal, which also increases the high absorption coefficients. Consequently, phase information was lost. It is attributed to the time-domain THz-based coherent measurement technique where the TDS has high signal-to-noise ratio $>10^6$ of power. The refractive index is ascertained using Eq. (1):

$$n = 1 + \frac{\Delta\phi \times c}{2\pi\nu \times d}. \tag{1}$$

Figure 2(b) shows the absorption coefficient of $\alpha-TeO_2$ crystal and it is very interesting to note that $\alpha-TeO_2$ single crystal has the lowest value of absorption coefficient in the THz domain. We found the absorption band of $\alpha-TeO_2$ at 0.55, 1.6, 1.85, 2.3, 2.5, 2.6, and 2.8 THz, respectively, which matches with the literature survey [20–24].

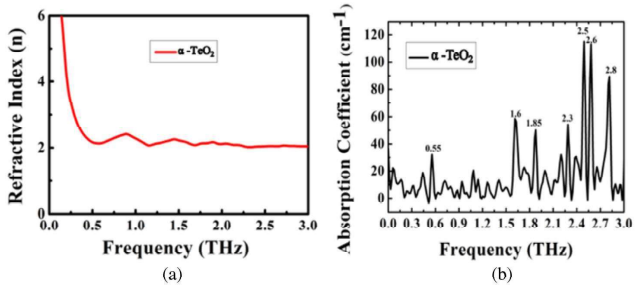

Fig. 2. (a) Refractive index, (b) absorption coefficient of $\alpha-TeO_2$.

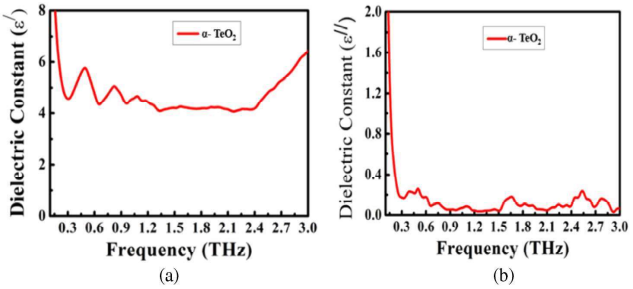

Fig. 3. Complex dielectric constant of $\tilde{\varepsilon} = \varepsilon' + \varepsilon''$ of $\alpha-TeO_2$ [(a) real part of (b) imaginary part of dielectric] shown as a function of frequency at room temperature.

C. Dielectric Property of $\alpha-TeO_2$

Figures 3(a) and 3(b) show the dielectric behavior of $\alpha-TeO_2$ crystal in the THz domain. It confirms that the dielectric constant describes the $\alpha-TeO_2$ crystal ability to interact with a THz electric field without absorbing energy, while the imaginary part of the dielectric constant describes the ability to permanently absorb energy from a time-varying THz electric field. The real value of the dielectric constant decreases with increasing frequency up to 1.3 THz and remains constant up to 2.5 THz and again it is increased up to 3.0 THz. The imaginary part of the dielectric constant exponentially decays up to 3.0 THz. The values of the real and imaginary dielectric constants are calculated by using Eqs. (2) and (3), respectively:

$$\varepsilon' = n^2 - k^2, \tag{2}$$

$$\varepsilon'' = 2nk. \tag{3}$$

Figure 4 shows the birefringence effect of $\alpha-TeO_2$ single crystal and the refractive index of ordinary and extraordinary rays [21].

D. Group Velocity and Coherent Length for Type I (o e e) $\alpha-TeO_2$ Crystal

For generation of efficient THz radiation using optical rectification or the DFM process using ultrashort pulses, the prior knowledge of group velocity dispersion and coherence length is very essential. This also guides us to understand the role of given material as an efficient emitter of a particular frequency. Figures 5(a) and 5(b) show the group velocity and coherent length of $\alpha-TeO_2$ crystal in THz domain. The value of group velocity (v_g) and coherence length (l_c) for terahertz radiation l_c are calculated using Eqs. (4) and (5), respectively:

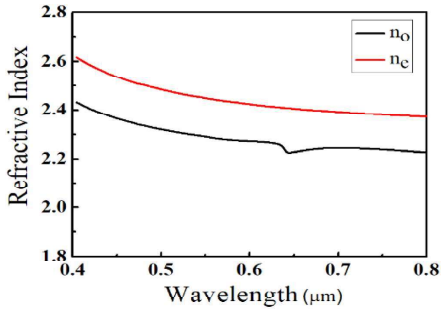

Fig. 4. Ordinary and extraordinary refractive index $\alpha-TeO_2$.

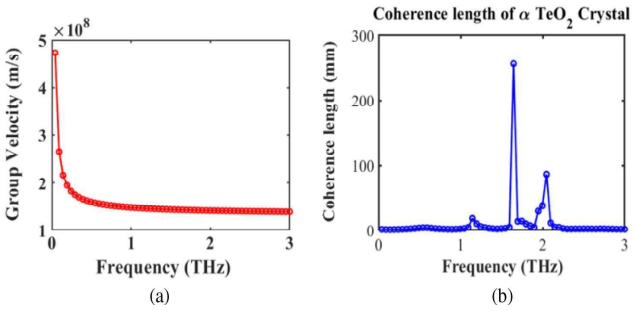

Fig. 5. (a) Group velocity, (b) coherence length of $\alpha-TeO_2$ crystal in the THz domain.

$$v_g = \frac{c}{n_g}, \tag{4}$$

$$l_c = \frac{\lambda_{\mathrm{THz}}}{2(n_g - n_{\mathrm{THz}})}, \tag{5}$$

where λ_{THz} is the terahertz wavelength. In this calculation of l_c we used the value of n_0, which is equal to terahertz refractive index n_{THz} in the terahertz region. Since the electric field of the detected terahertz wave is parallel to the ordinary ray direction.

E. Determination of the Type I DFM Phase-Matching Angle

We propose a Type I DFM scheme for THz generation using tunable 0.7990–0.7960 μm as pump and 800 nm as a signal for generation of tunable THz radiation between 0.1 and 1.9 THz. The calculated phase-matching angle is $\theta \sim 21.15°$ whereas the phase-matching angle for second-harmonic generation (SHG) for the 800 nm wavelength is $\theta \sim 35.5°$.

Figures 6(a) and 6(b) show the theoretical calculation for the Type I phase-matching angle with respect to incident and generated wavelength for second-harmonic generation. The nature of phase-matching angles is showing an exponential trend. The phase-matching condition is given by Eq. (6):

$$\omega^o_{\mathrm{Pump}}(0.796\ \mu\mathrm{m}) - \omega^e_{\mathrm{Signal}}(0.799\ \mu\mathrm{m}) = \omega^e_{\mathrm{THz}}(212\ \mu\mathrm{m} = 1.4\ \mathrm{THz}). \tag{6}$$

Figure 7 shows that the at signal wavelength 800 nm and constant phase-matching angle 20.15° how the pump wavelength changes with respect to the generated wavelength.

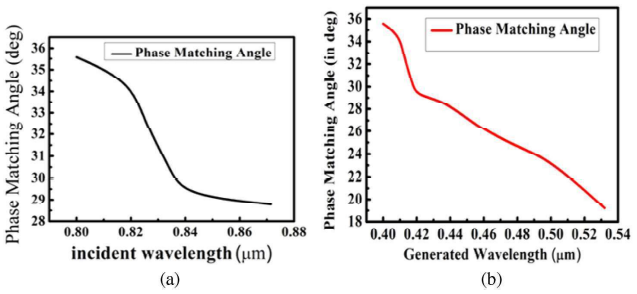

Fig. 6. Type I phase-matching angle with respect to (a) incident wavelength, (b) generated second-harmonic wavelength from $\alpha-TeO_2$ crystal.

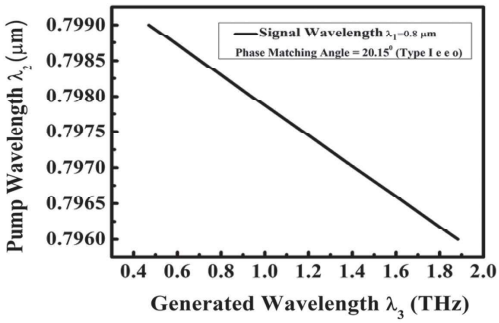

Fig. 7. Pump wavelength versus generated wavelength $\alpha-TeO_2$ crystal in the THz domain.

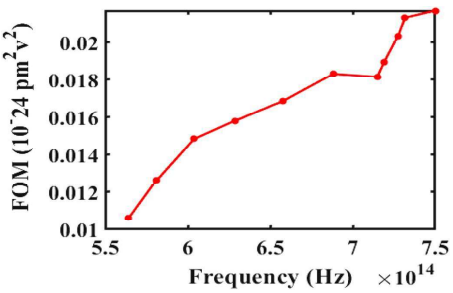

Fig. 8. Figure of merit optical domain in terms of frequency.

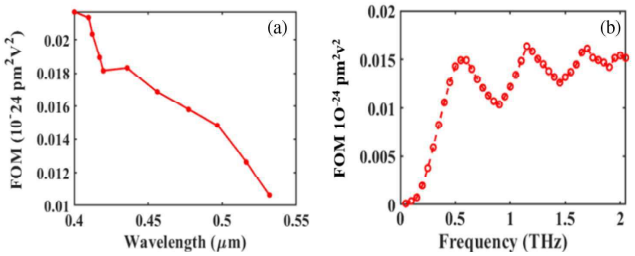

Fig. 9. Figure of merit (a) optical domain, (b) THz domain.

F. Comparative Study of Figure of Merits in the Optical and THz Domains

The optical and commercial values of crystal for making optical devices are evaluated on the basis of its FOM, since TeO_2 is not very popular for SHG and THz applications. Moreover, phase matching and other important parameters are also not available in the THz domain. Therefore, we have made an attempt to compare its FOM in the optical and THz domains. Figure 8 shows the FOM in the optical pump range, which is more than 0.02×10^{-24} $(\mathrm{pm/V})^2$. Whereas in the case of THz, it is oscillating between the 0.015 to 0.01×10^{-24} $(\mathrm{pm/V})^2$ range. Figures 9(a) and 9(b) show the FOM in the optical and THz domains. The value of figure of merit of $\alpha-TeO_2$ single crystal is calculated by using Eq. (7):

$$\mathrm{FOM} = d^2_{\mathrm{eff}}\,\mathrm{Sin}^2\,\theta/n^3_o. \tag{7}$$

Figure 8 shows the figure of merit of this crystal in the optical domain with respect to frequency. The nature of both optical and terahertz follows the same. The figure of merit is more in the optical domain compared to the terahertz domain. But $\gamma-TeO_2$ crystal is more suitable for THz generation since the

effective value of the nonlinear coefficient is 10 times more than $\alpha-TeO_2$.

We have successfully calculated the FOM of $\alpha-TeO_2$ using experimentally generated RI and Type I phase-matching angle both in the optical and THz domains, as shown in Figs. 9(a) and 9(b), respectively.

4. CONCLUSION

Finally, we have evaluated the potential role of $\alpha-TeO_2$ single crystals for generation of THz radiation using two prominent optical techniques—optical rectification and DFM—based on experimental and theoretical generated data from optical and THz spectroscopy for the first time. The phase-matching angle under the Type I DFM condition for generation of tunable radiation generation between 0.1 and 1.9 THz range is $\theta = 21.15°$. The FOMs in the optical and THz domains lie in the 0.02 to 0.015 range. The generated spectral range lies between 0.1 and 3.0 THz.

Funding. Recruitment and Assesment Centre (DRDO/18/1801/2016/01038]ACRHEM Phase-III).

Acknowledgment. The authors would like to express their sincere thanks to the funding agency Defense Research and Development Organization (DRDO), Ministry of Defence, and Govt. of India for financial support ACRHEM-Phase-III, and the first author Chandan Ghorui expresses his thanks to PMRF Fellowship, Govt. of India.

Disclosures. The authors declare that there is no conflict of interest.

Data availability. Data underlying the results presented in this paper are not publicly available at this time but may be obtained from the authors upon reasonable request.

REFERENCES

1. T. Siciliano, M. Di Giulio, M. Tepore, E. Filippo, G. Micocci, and A. Tepore, "Effect of thermal annealing time on optical and structural properties of TeO_2 thin films," Vacuum **84**, 935–939 (2010).
2. M. F. Al-Kuhaili, S. M. A. Durrani, E. E. Khawaja, and J. Shirokoff, "Effects of preparation conditions on the optical properties of thin films of tellurium oxide," J. Appl. Phys. **35**, 910–915 (2002).
3. S. Kumar and A. Mansingh, "Annealing-induced structural changes in tellurium dioxide thin films," J. Appl. Phys. **23**, 1252–1255 (1990).
4. N. Dewan, K. Sreenivas, and V. Gupta, "Properties of crystalline γ-TeO_2 thin film," J. Cryst. Growth **305**, 237–241 (2007).
5. R. Nayak, V. Gupta, A. L. Dawar, and K. Sreemivas, "Optical waveguiding in amorphous tellurium oxide thin films," Thin Solid Films **445**, 118–126 (2003).
6. M. Venkatesh, K. S. Rao, T. S. Abhilash, S. P. Tewari, and A. K. Chaudhary, "Optical characterization of GaAs photoconductive antennas for efficient generation and detection of terahertz radiation," Opt. Mater. **36**, 596–601 (2014).
7. M. Venkatesh and A. K. Chaudhary, "Generation of THz radiation from low temperature gallium arsenide (LT-GaAs) photoconductive (PC) antennas using tunable femtosecond oscillator," in *12th International Conference on Fiber Optics and Photonics*, OSA Technical Digest (online) (Optical Society of America, 2014), paper S5 A. 33.
8. M. Venkatesh and A. K. Chaudhary, "Study of terahertz intensity dependence on time resolved dynamic fringes in the interferometric autocorrelation setup," AIP Conf. Proc. **1620**, 616–621 (2014).
9. D. M. Lubenko, G. V. Lansky, N. A. Nikolaev, E. A. Sandabkin, V. F. Losev, and Y. M. Andreev, "Generation of THz emission in nonlinear BBO crystal at room temperature," Proc. SPIE **11322**, 113222C (2019).
10. T. Notake, M. Takeda, S. Okada, T. Hosobata, Y. Yamagata, and H. Minamide, "Characterization of all second-order nonlinear-optical coefficients of organic N-benzyl-2-methyl-4-nitroaniline crystal," Sci. Rep. **9**, 14853 (2019).
11. C.-R. Wang, Q.-K. Pan, F. Chen, G. Lanskii, N. Nikolaev, A. Mamrashev, Y. Andreev, and A. Meshalkin, "Phase-matching in KTP crystal for THz wave generation at room temperature and 81 K," Infrared Phys. Technol. **97**, 1–5 (2019).
12. M. Venkatesh, K. Trirupugalmani, K. S. Rao, S. Brahadeeswaran, and A. K. Chaudhary, "Generation of efficient THz radiation by optical rectification in DAST crystal using tunable femtosecond laser pulses," Indian J. Phys. **91**, 319–326 (2017).
13. U. Venkataramudu, C. Sahoo, S. Leelashree, N. S. R. Gopal, D. Ganesh, A. K. Chaudhary, S. Srinath, and R. Chandrasekar, "Terahertz radiation and second-harmonic generation from a single-component polar organic ferroelectric crystal," J. Mater. Chem. C **6**, 9330–9335 (2018).
14. G. C. Bhar and U. Chatterjee, "Noncollinear phase-matched second-harmonic generation in beta barium borate," Appl. Phys. Lett. **54**, 1383–1384 (1989).
15. J. Liu, X. Guo, J. Dai, and X. C. Zhang, "Optical properties of beta barium borate in terahertz region," Appl. Phys. Lett. **93**, 171102 (2008).
16. C. Ghorui, A. M. Rudra, U. Chatterjee, A. K. Chaudhary, and D. Ganesh, "Efficient second-harmonic and terahertz generation from single BiB_3O_6 crystal using nanosecond and femtosecond lasers," Appl. Opt. **60**, 5643–5651 (2021).
17. C. Ghorui, A. V. Kidavu, P. N. Kumar, S. Das, A. K. Chaudhary, and Y. M. Andreev, "Comparative studies of terahertz-based optical properties in transmission/reflection modes of GaSe:S and measurement of its scattering losses due to surface roughness for efficient terahertz generation," Phys. Scr. **98**, 025508 (2023).
18. E. Palaniyasan, K. S. Jeyaperumal, P. N. Kumar, A. Radhakrishnan, A. L. Muppudathi, and A. K. Chaudhary, "Optical and terahertz characterization of efficient NLO single crystal: (E)-2-(4-(dimethyl amine) styryl)-1,1,3-trimethyl-1H-benzo[e] indol-3-ium iodide (P-BI)," Pramana J. Phys. **97**, 21 (2023).
19. K. Arjun, D. Ganesh, S. Karthick, A. Santha, M. Venkatesh, S. Ganesamoorthy, S. Brahadeeswaran, and A. K. Chaudhary, "Investigations on aqueous solution grown L- Arginine Phosphate monohydrate (LAP) single crystals for efficient THz generation," J. Cryst. Growth **575**, 126337 (2021).
20. M. Sotome, N. Kida, R. Takeda, and H. Okamoto, "Terahertz radiation induced by coherent phonon generation via impulsive stimulated Raman scattering in paratellurite," Phys. Rev. A **90**, 033842 (2014).
21. N. Uchida, "Optical properties of single-crystal paratellurite (TeO_2)," Phys. Rev. B **4**, 3736–3745 (1971).
22. Y. Li, W. Fan, H. Sun, X. Cheng, P. Li, and X. Zhao, "Structural, electronic, and optical properties of α, B, and γ-TeO_2," J. Appl. Phys. **107**, 093506 (2010).
23. M. Unferdorben, A. Buzády, J. Hebling, K. Kiss, I. Hajdara, L. Kovács, Á. Péter, and L. Pálfalv, "Index of refraction and absorption coefficient spectra of paratellurite in the terahertz region," J. Infrared Millimeter, Terahertz Waves **37**, 703–709 (2016).
24. G. Komandin, V. Nozdrin, S. Chuchupal, V. Lomonov, Y. Pisarevskii, O. Provodnikov, and I. Spektor, "Dielectric permittivity of organ silicate glass thin films on a sapphire substrate determined using time-domain THz and Fourier IR spectroscopy," J. Phys. D **53**, 495102 (2020).
25. M. Mahendar, R. N. V. Krishna, and A. K. Chaudhary, "Effect of the annealing temperature on structural, morphological, and nonlinear optical properties of TeO_2 thin films used for efficient THz generation," Appl. Opt. **62**, 2394–2402 (2023).

Welcome Srinivas Maddipati Sign out

Controller General of Patents, Designs & Trade Marks

सत्यमेव जयते

G.A.R.6
[See Rule 22(1)]
RECEIPT

Docket No 72402

Date/Time 2024/05/24 18:48:09

To
Srinivas Maddipati

UserId: EEVA

Eeva IP & IT Services Pvt Ltd HIG 139,
Bharath Nagar, Moosapet

CBR Detail:

Sr. No.	App. Number	Ref. No./Application No.	Amount Paid	C.B.R. No.	Form Name	Remarks
1	R20244028775	202441040603	4000	34680	FORM 18	
2	202441040603	TEMP/E-1/46761/2024-CHE	1600	34680	FORM 1	A TUNABLE INCIDENT ANGLE AND FREQUENCY BASED 3D TERAHERTZ PROFILOMETER SYSTEM
3	E-106/6099/2024/CHE	202441040603	0	-----	FORM28	----

TransactionID	Payment Mode	Challan Identification Number	Amount Paid	Head of A/C No
N-0001424515	Online Bank Transfer	2405240047735	5600.00	1475001020000001

Total Amount : ₹ 5600.00

Amount in Words: Rupees Five Thousand Six Hundred Only

Received from Srinivas Maddipati the sum of ₹ 5600.00 on account of Payment of fee for above mentioned Application/Forms.

* This is a computer generated receipt, hence no signature required.

Print

Home About Us Contact Us

Detection of real-time hidden metallic object using prototype THz radar system for public security and defense application

Chandan Ghorui and Anil Kumar Chaudhary

Advanced Centre of Research in High Energy Materials (ACRHEM DIA-CoE), School of Physics, University of Hyderabad, Hyderabad 500046, Telangana, India,
[#]Corresponding author e-mail: 19acpp05@uohyd.ac.in ***akcsp@uohyd.ac.in***

ABSTRACT

1. **The present study introduces an innovative approach for a real-time detection of concealed metallic objects using a SiGe 300 GHz radar source. It has achieved remarkable precision distances up to 2.0 m. The system employs a miniaturized 300 GHz Industrial, Scientific, and Medical (ISM) band frequency-modulated continuous wave (FMCW) radar system. This setup includes a SiGe single-chip radar sensor and Liquid Crystal Polymer (LCP) off-chip antennas integrated into a Quad Flat No-Lead (QFN) package, breaking a new ground with millimeter-level accuracy. The system is linked to a user-friendly graphical interface (WebGUI) software, which help the users for fine-tuning the baseboard parameters to visualize radar data, and make real-time adjustments. The strength of reflected signal exhibits a nuanced second-order polynomial nature intricately correlated with signal bandwidth and the target's distance. Notably, the system provides maximum and minimum peak power at 289 and 329 GHz, respectively and helping us to achieve a Signal-to-Noise Ratio (SNR) of the order of 3.78 at a detection distance of 2.0 m. A detailed frequency bandwidth-based analysis reveals the system's detection range. The maximum target distance was obtained 2.0 m at 20 GHz bandwidth range. Similarly, bandwidth of 30, 40 50 and 60 GHz were able to achieve the target range of 146, 100, 80 and 63 cm range, respectively. The 300 GHz SiGe radar source outperforms the lower-frequency (in microwave range) in terms of excellent spatial resolution and minimum interference from microwave devices which are some essentially requirements for radar based imaging and sensing applications. This adaptive radar system act as a powerful tool for enhancing the homeland security and defense system where concealed objects pose threats to public safety.**

Keywords: THz, Radar, QFN, WebGUI, FMCW

1. INTRODUCTION

Terahertz (THz) technology is positioned as a frontier between the well-explored millimeter-wave (mmWave) and optical domains in the electromagnetic radiation spectrum. Often referred to as the THz gap, challenges in this frequency range stem from the scarcity of ultra-compact THz signal sources and detectors that offer both high power and sensitivity. This discussion chapter outlines recent advancements aimed at overcoming these obstacles, focusing on developments at both the device and system levels. The Radar an acronym for **"Radio Detection and Ranging,"** employs radio waves to detect and locate objects in the surrounding environment. Radar systems emit radio waves that bounce off objects and return to the radar antenna. By analyzing the properties of the returned signals, such as their time of arrival and frequency shift, radar can determine the distance, speed, and direction of detected objects. Radar finds extensive use across various applications, including weather monitoring, air traffic control, military operations, navigation at sea, and automotive safety. Weather monitoring radar detects precipitation such as rain, snow, and hail, tracking their movement to provide vital information about storms and ensuring safe air travel. Military radar systems serve multiple purposes, including surveillance, target detection, missile guidance, and battlefield awareness. Radar systems can operate across different frequency bands, from very low-frequency radar for long-range detection to high-frequency radar for short-range precision measurements. In recent years, radar technology has become integral to automotive systems, enhancing safety features

Terahertz Photonics III, edited by Mona Jarrahi, Sascha Preu, Dmitry Turchinovich,
Proc. of SPIE Vol. 12994, 129940I · © 2024 SPIE ·
0277-786X · doi: 10.1117/12.3025308

like collision avoidance and adaptive cruise control. Automotive radar, part of advanced driver-assistance systems (ADAS) and autonomous vehicles, detects nearby objects, pedestrians, and vehicles, enabling various functionalities. Terahertz radar, also known as THz or T-ray radar, is an emerging technology that uses terahertz electromagnetic waves for sensing and imaging. It offers unique capabilities, especially were conventional radar and imaging technologies face limitations. The primary difference between radar and THz radar lies in the frequency range used for detection. Traditional radar operates in the radio frequency (RF) range, while THz radar operates in the terahertz frequency range, offering higher spatial resolution and material identification capabilities. Although THz radar provides unique advantages, it faces challenges such as atmospheric absorption and scattering, limiting its effectiveness for long-range applications compared to RF radar. Terahertz (THz) radar, operating at 300 GHz with silicon technology, holds promise for various real-life applications. Its high frequency enables precise spatial resolution, making it ideal for short-range sensing and imaging of small objects, such as in advanced driver-assistance systems (ADAS) for enhanced collision detection in urban environments. Additionally, 300 GHz silicon radar shows potential for gesture recognition systems, offering finer gesture detection suitable for touchless interfaces and human-machine interactions. It could also be utilized for indoor positioning and tracking, providing accurate location information where traditional GPS systems are less effective. Moreover, silicon-based radar in the terahertz range offers non-destructive testing capabilities for industrial use, enabling material inspection, defect detection, and structural integrity assessment. Although still in early stages, ongoing research aims to address technical challenges and optimize performance for practical applications. Furthermore, THz communications show promise for high-speed data transfer, particularly in short-range applications like near field communication (NFC) and wireless personal area networks (WPANs) [1-2]. The expansive bandwidth of the THz band enables high data rates, even with simple modulation schemes like amplitude shift keying (ASK) and quadrature phase shift keying (QPSK) modulation, as demonstrated in successful transmissions at 300 GHz. To fully utilize this bandwidth, transceiver components, antennas, and their interconnections must exhibit wideband characteristics. For practical mobile applications, there's a demand for compact and cost-effective THz transceiver modules. Current direct bandgap semiconductor technologies, such as Silicon-Germanium (SiGe) and Gallium Arsenide (GaAs), are effective in the millimeter-wave (mm-wave) spectrum. These technologies allow complete integration of a sophisticated RF system, including amplifiers, mixers, oscillators, and couplers, onto a single chip with dimensions as small as several hundred microns [1-5]. An innovative solution has been developed for short-range communication systems operating at 300 GHz, combining compactness and cost-effectiveness. Leveraging low-temperature cofired ceramic (LTCC) technology, this advancement integrates an on-chip antenna with a reflector, along with high-data-rate signal interconnections featuring flip-chip and via transition, all within a carefully designed package. Within this compact package, a small silicon lens antenna coexists with a flip-chip bonded receiver IC, featuring an on-chip antenna. The overall dimensions of the front-end receiver are just $10 \times 10 \times 4$ mm^3, including the 6 mm diameter silicon lens. When integrated onto an evaluation board, this compact terahertz receiver demonstrated wireless links with impressive data rates of up to 27 Gb/s. The advancement in BiCMOS and CMOS silicon technologies has made millimeter-wave applications (30 GHz -300 GHz) achievable and affordable for mass production, leading to higher market penetration in consumer electronics. Compact, low-power, and low-cost sensors are becoming increasingly important, with promising applications in both industrial and consumer sectors. Signal frequencies in the D-band are particularly attractive due to their high spatial resolution, resulting in compact chip sizes and small antenna dimensions. The growing demand for extensive data transfers through handheld devices like mobile phones and tablet PCs is driving wireless data rates to unprecedented levels. A solution involving a millimeter-wave antenna in a package for wire bond chip assembly, based on LTCC technology, has been reported to address this demand effectively. LTCC technology offers numerous advantages, such as high integration capability for passive devices and cost-effectiveness, making it ideal for mass production. Although a sub-THz antenna integrated in LTCC has been reported, current efforts focus on developing a low-loss, wideband monolithic microwave integrated circuit (MMIC)-to-antenna interconnection [6]. As a result, an on-chip antenna solution emerges as one of the top choices for a THz transceiver, complemented by a silicon (Si) lens antenna to reduce surface wave excitation. This strategy aims to optimize radiation efficiency, antenna gain, and bandwidth [7]. Additionally, eliminating interconnection loss, achieved through methods like wire bonding the antenna to the transceiver ICs, positions an on-chip antenna with a Si lens as a feasible option. This not only reduces loss but also streamlines the manufacturing

process, ultimately improving module performance. Recent progress includes the demonstration of an ASK receiver MMIC for wireless communications at 300 GHz [3]. Utilizing InP-based HBTs with a 250 nm emitter and base junction width, the integration of a non-chip dipole antenna, RF amplifier, envelope detector, and output amplifier into a single chip has been achieved. However, the practical application of the metal package, in which the MMIC is die-bonded on the Si lens and wire-bonded to the DC supply and signal lines, faces challenges due to its bulkiness [8]. For imaging applications, a compact package solution has been proposed, utilizing a reduced-sized Si lens and low-cost FR-4 substrate to house a 288 GHz oscillator chip in 65 nm CMOS technology. In this paper we discuss a 300 GHz front-end ASK receiver based on LTCC technology, compact enough for practical use in THz short-range wireless communications. An LTCC package with a reduced-size lens antenna was designed, fabricated, and assembled to accommodate the previously reported MMIC. The successful demonstration of wireless data transmission at 300 GHz highlights the feasibility and potential of this compact THz receiver, achieving data rates of up to 27 Gbps.In addition to contactless distance and speed sensing, determining the direction to a target is a fundamental task of radar systems. A minimum of two receiving channels are necessary to gather information about the direction of signal reflection. The monolithically integrated radar includes a VCO, power amplifiers (PAs), low-noise amplifiers (LNAs), and sub-harmonic mixers (SHMs). The chip is implemented in a 130 nm SiGe-BiCMOS process with f_T /f_{max}= 289/329 GHz.

2. METHODOLOGY & EXPERIMENTAL DETAILS

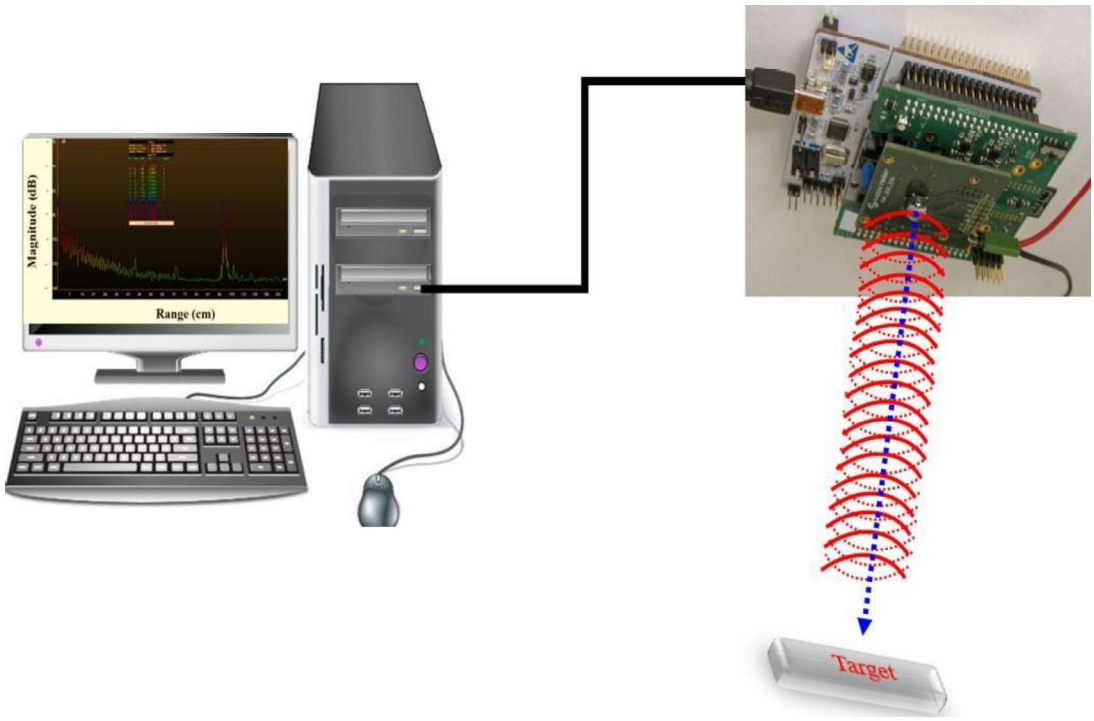

Fig.1 Experimental setup for 300 GHz radar Source

A miniaturized 0.3 THz (300 GHz) Industrial, Scientific, and Medical (ISM) band frequency-modulated continuous wave **(FMCW)** radar system is employed to achieve micrometer accuracy. This radar system comprises a Si single-chip radar sensor and Liquid Crystal Polymer (LCP) off-chip antennas. These antennas are integrated into a Quad Flat No-Lead (QFN) package. To enhance the radar gain, an additional dielectric lens is utilized. The experimental setup is illustrated in Figure 1. The radar sensor, known as the **'Evalkit SiRad Simple Easy 300 GHz,'** is a compact board measuring 40 x 40 mm, as shown in Fig. 1. The chip itself is visible as a black square, with dimensions of 2x2 mm. Notably, the T_X/R_X

antennas are already integrated into the chip. Each antenna features four patch elements and is manufactured on a separate ceramic substrate, which can be placed directly onto the silicon IC. This integration enables the creation of extremely fine structures down to a few microns in size. However, it's worth noting that the total antenna area is limited. These high-performance integrated antenna structures are suitable for frequencies up to the THz range. The antennas are directly connected to the IC structures, ensuring maximum efficiency and making them suitable for designs ranging from 60 GHz to THz, with high bandwidth capabilities. To achieve a narrow beam, a plastic dielectric black lens is used. The kit comes with a standard 32 mm diameter lens, which results in a 2-degree beam [9]. The evaluation kits come with an accessible graphical user interface **(WebGUI)** that provides a user-friendly platform for configuring the baseband board's parameters and visualizing radar data in various modes. This system's adaptability allows users to fine-tune parameter settings for specific applications, gain insights into radar data processing fundamentals, and make real-time adjustments to radar parameters. Our aim was to employ the radar in detecting materials. We collected samples of various materials to analyses with the evaluation kit. Namely, we collected samples of Acrylic, Aluminium, Composition Exploding (CE) , Copper, Glass, Stainless Steel, TEX (a Nitramine high Explosive), Wood, Titanium, Zinc, Lead and Nickel. We calculated the density of each sample using the mass and volume of the sample as

Density = Mass of Sample /Volume of the sample

The samples were then used as a target at a fixed mean distance of 52.2 cm from the radar system, and the reflected THz signals was collected (*Referred to as 'dataset' in later discussions*). A cardboard sheet of fixed dimensions (50 x 40 x 2 mm) was used to conceal samples and the same was repeated to get another set of datasets. A total of 822 distinct individual datasets of all materials in concealed and non-concealed conditions was obtained using the collected samples. The data was analyzed for a resulting patterns and distinguishable features across the materials. The conclusions drawn were used to construct a machine learning algorithm (K-Nearest-Neighbours or KNN) to make a prediction system that can predict the material's identity from its peak reflected signal from the THz radar and the value of density, which can be obtained using the routine formula to find density using mass and volume, or otherwise. A K-Nearest Neighbour algorithm [10] is a traditional machine learning tool routinely used to classify objects, materials, images, etc. using a formula based on Euclidean (or other) distance. It classifies a data point as belonging to the class of the data points closest to the given data point in question. Accuracy of the K-NN Algorithm's prediction is defined to be the following:

Accuracy = Number of Samples Correctly Predicted/ Total Number of Samples Predicted. The accuracy of this model was thus used to quantify the efficacy of the above methodology to classify materials.

3. RESULT AND DISCUSSION

Peak Value for Materials Samples, when targeted with the radar source, produce a peak in the magnitude of reflected signal strength (measured in dB) at the distance where the sample is kept. The system was able to give reflected signals for all materials as discussed in Section 2 with a signature peak. One of such outputs from the radar using a metal sample is as in Fig.2. The average of peak values for each sample was calculated and plotted with density of samples to study the relationship between the two, as shown in Fig. 3. It can be clearly inferred from Fig. 3 that each material gives a characteristic peak value for a given density of sample (Given that other samples are kept at the same distance as the one that needs to be identified). Such a signature peak suggests that reflected signals from the THz radar and density of the material can give reasonable prediction about the identity of the material, such as explosive, drug, metal or other articles. This aspect of the radar makes it an ideal candidate for real time and quick detection of materials in situations when it is unfeasible to do a chemical analysis. We show proof of concept further by creating a machine learning system (a standard K-Nearest Neighbor Classification Algorithm) which was trained on 657 individual data points, that could successfully predict 165 untrained samples from the collected datasets with an accuracy of 90.31% correctly. Predictions of various materials through the KNN system is as shown in Fig. 3 (b)

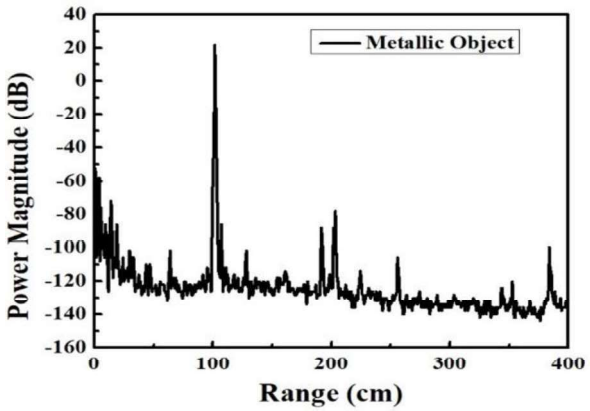

Fig.2: Direct response of metal detection using prototype 300 GHz radar.

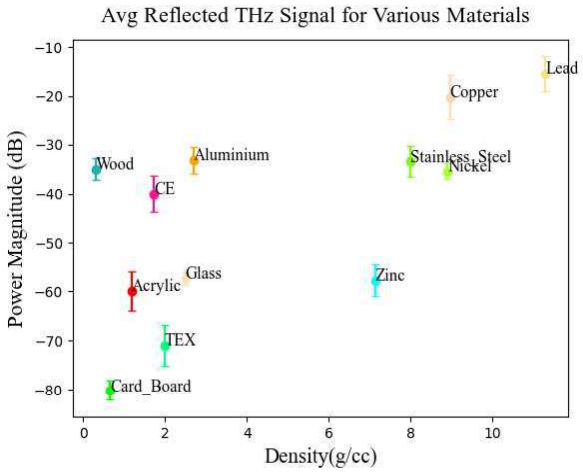

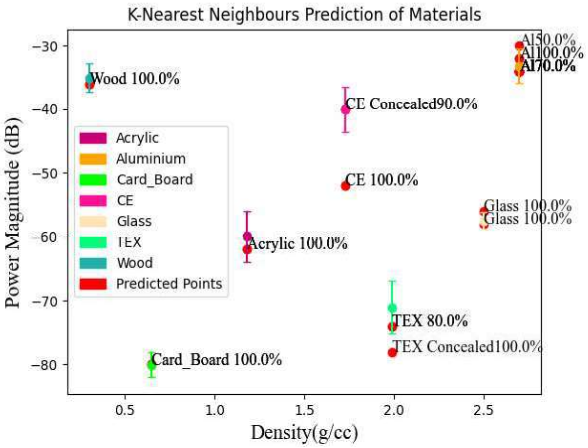

Fig 3. (a) **Fig 3. (b)**

Fig. 3 (a): Average reflected signals plotted with the Density of the materials. One can observe signature peaks from the THz system. The error bars show variation in the signal strength over samples. TEX and CE are explosive materials. Fig. 3 (b): Predictions from KNN algorithm using the THz radar. Predicted points are shown in red.

Concealed/Hidden Materials:

Terahertz waves can effectively penetrate through different types of mediums such as clothing and packaging materials and provides valuable information about the composition of hidden objects. Moreover, it is a noncontact nonionizing physical technique. As a result, the THz RADAR system is a powerful tool in the realm of security, particularly in scenarios where the concealed objects may pose a threat to public safety. Fig.4 exhibits the concealed metallic object detection at 1.0 m target distance using 300 GHz silicon radar source. Data collected under concealed conditions reveals that the signal strength reduces non uniformly when any object is concealed with a penetrable obstruction. THz waves could penetrate the cardboard obstruction as reported by others [11]. The average of signal strength under concealed conditions is compared to previous condition (direct measurement) in Fig. 5. It may be noted that the KNN Model described in the previous sub-section could also predict material in both concealed and non-concealed conditions, rendering it useful for defense or surveillance related activities.

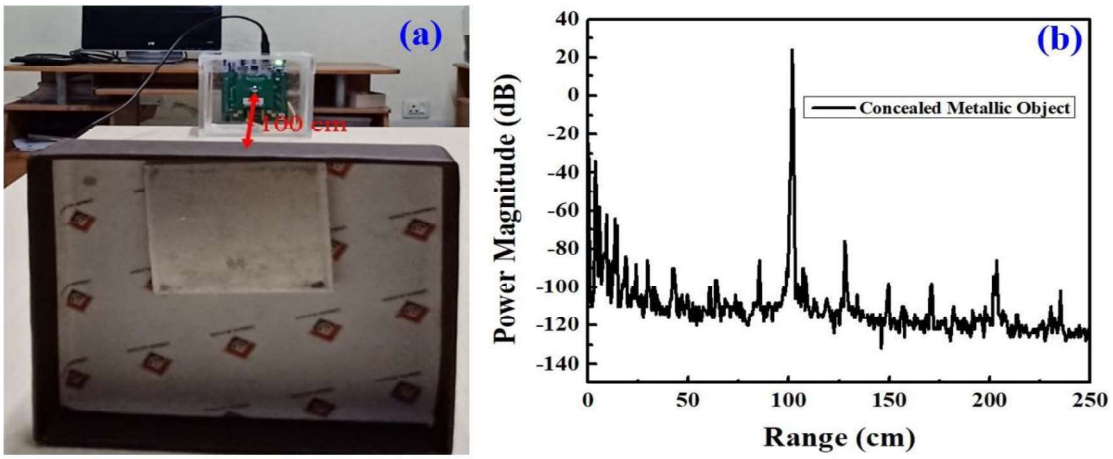

Fig.4 (a) Concealed Metallic object detection at 1.0 m distance using 300 GHz Si radar source (b) Reflected signal from metallic object

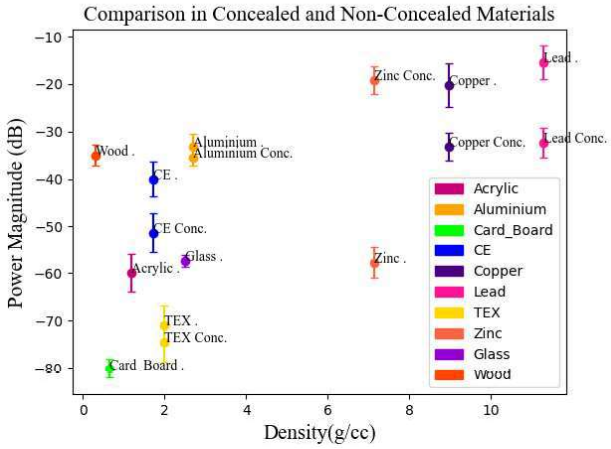

Fig. 5 Change in average signal strength under concealed conditions.

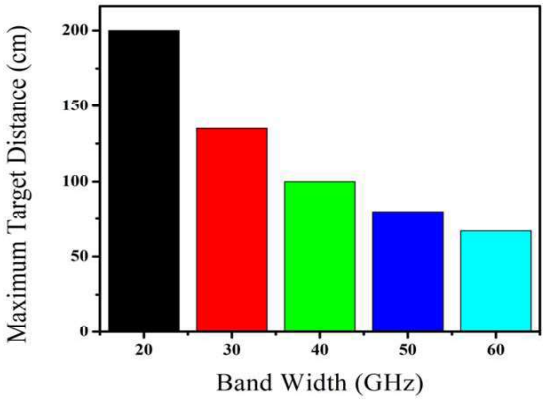

Fig.6. Response of Bandwidth to achieved maximum target distance using 300 GHz radar source

Fig 6. detailed analysis 300 GHz SiGe radar source capabilities, with respect to the maximum target distance 2.0 m for a 20 GHz bandwidth, 1.46 m for 30 GHz, 100 cm for 40 GHz, 80 cm for 50 GHz, and 63 cm for 60 GHz.

4. CONCLUSION

We have successfully demonstrated the system's operational capacity, achieving remarkable precision up to 2.0 m distance. It is realized using a miniaturized 300 GHz Industrial, Scientific, and Medical (ISM) band frequency-modulated continuous wave (FMCW) radar system. The reflected signal strength exhibits a second-order polynomial nature intricately correlated with the signal bandwidth and the target's distance. The system's showing of maximum and minimum peak power at 289 and 329 GHz, respectively. The signal-to-noise ratio (SNR) of the order of 0.79 at a detection distance of 2.0 m. A detailed analysis underscores the system's capabilities, revealing a maximum target distance spanning 2.0 m for a 20 GHz bandwidth, 1.46 m for 30 GHz, 100 cm for 40 GHz, 80 cm for 50 GHz, and 63 cm for 60 GHz. This comprehensive investigation contributes valuable insights into the potential applications and performance parameters of TRCS measurements in the THz frequency range. We have demonstrated that materials such as explosives, metals and even nonmetals such as wood and acrylic, have signature peaks in reflected signals from the THz source. We further showed using the K-Nearest Neighbors algorithm that this can be exploited to quickly identify materials by measuring their reflected signals from a fixed distance at which the expected peak is experimentally known, combined with a quick calculation of density using the routine formula. It is useful in situations such as a bomb diffusion site or a sudden emergency wherein chemicals or other means to identify materials is not available. Owing to its non-harmful nature and small form-factor, this system can be deployed in practically any situation where such classification of materials is deemed necessary. One may also see its use in a commercial setting such as in Malls, Metros, Railways, Airports, etc. where real time testing of potentially dangerous/illegal material may be required.

5. ACKNOWLEDGEMENTS

The authors would like to express thanks to Defense Research and Development Organization (DRDO), Ministry of Defence Govt. of India for financial support under grant No. DRDO/18/1801/2016/01038: ACRHEM- Phase-III and the Director of ACRHEM for support. First author Chandan Ghorui expresses sincere thanks to the Prime Minister's Research Fellowship (PMRF) grant under the Govt.of India for maintence the fellowship. Authors also thank to Silicon Radar for close cooperation during development and optimization process of the radar sensor.

6. REFERENCES

[1]. H.-J. Song and T. Nagatsuma, "Present and future of terahertz communications," IEEE Trans. THz Sci. Technol., vol. 1, no. 1, pp. 256–263, Sep. 2011.
[2]. T. Kürner, "Towards future THz communications systems," Int. J. THz Sci. Technol., vol. 5, no. 1, pp. 11–17, Mar. 2012.
[3]. H.-J. Song, J.-Y. Kim, K. Ajito, M. Yaita, and N. Kukutsu, "Fully integrated ASK receiver MMIC for terahertz communications at 300 GHz," IEEE Trans. THz Sci. Technol., vol. 3, no. 4, pp. 445–452, Jul. 2013.
[4]. H.-J. Song, J.-Y. Kim, K. Ajito, N. Kukutsu, and M. Yaita, "50-Gb/s direct conversion QPSK modulator and demodulator MMICs for terahertz communications at 300 GHz," IEEE Trans. Microw. Theory Techn., vol. 62, no. 3, pp. 600–609, Mar. 2014.
[5]. Y. P. Zhang, M. Sun, K. M. Chua, L. L. Wai, and L. Duixian, "Antenna in package design for wire bond interconnection to highly integrated 60-GHz radios," IEEE Trans. Antennas Propag., vol. 57, no. 10, pp. 2842–2852, Oct. 2009.
[6]. T. Tajima, H.-J. Song, K. Ajito, M. Yaita, and N. Kukutsu, "300-GHz step-profiled corrugated horn antennas integrated in LTCC," IEEE Trans.Antennas Propag., vol. 62, no. 11, pp. 5437–5444, Nov. 2014.
[7]. S. E. Gunnarsson, N. Wadefalk, J. Svedin, S. Cherednichenko, I. Angelov, H. Zirath, I. Kallfass, and P. Leuther, "A 220 GHz single-chip receiver MMIC with integrated antenna," IEEE Microw. Wireless Compon. Lett., vol. 18, no. 4, pp. 284–286, Apr. 2008.
[8]. J. Grzyb, Y. Zhao, and U. R. Pfeiffer, "A 288-GHz lens-integrated balanced triple-push source in a 65 nm CMOS technology," IEEE J. Solid-State Circuits, vol. 48, no. 7, pp. 1751–1761, Jul. 2013.
[9]. Silicon Radar. http://www.siliconradar.com.
[10]. Guo, Gongde & Wang, Hui & Bell, David & Bi, Yaxin. (2004). KNN Model-Based Approach in Classification.
[11]. V. Wallace, E. MacPherson, J. Zeitler, and C. Reid, "Three-dimensional imaging of optically opaque materials using nonionizing terahertz radiation," J. Opt. Soc. Am. A 25, 3120-3133 (2008).

Spectrochimica Acta Part A: Molecular and Biomolecular Spectroscopy 321 (2024) 124697

Contents lists available at ScienceDirect

Spectrochimica Acta Part A:
Molecular and Biomolecular Spectroscopy

journal homepage: www.journals.elsevier.com/spectrochimica-acta-part-a-molecular-and-biomolecular-spectroscopy

Terahertz-based optoelectronic properties of ZnS quantum dot-polymer composites: For device applications

Chandan Ghorui [a], Partha Kumbhakar [b,c], Arjun Vs Kidavu [a], Pathik Kumbhakar [b], A.K. Chaudhary [a,*]

[a] Advanced Centre for Research in High Energy Materials (ACRHEM, DIA-CoE), School of Physics, University of Hyderabad, Telangana 500046, India
[b] Nanoscience Laboratory, Dept. of Physics, National Institute of Technology Durgapur, West Bengal 713209, India
[c] Department of Physics and Electronics, CHRIST (Deemed to be University), Bengaluru, Karnataka, 560029, India

HIGHLIGHTS

- THz based optical characterization of ZnS QD of different concentrations.
- Fluorescence and Decay Life time measurement of Zinc Sulfide QDs.
- Measurement of Kirchhoff surface scattering Property of ZnS QD in THz domain.
- Optical impedance, surface roughness, and reflection coefficients of ZnS QDs in TE and TM mode in THz frequency range.
- Evaluation of ZnS QDs for the development of low-cost CMOS camera in THz domain.

GRAPHICAL ABSTRACT

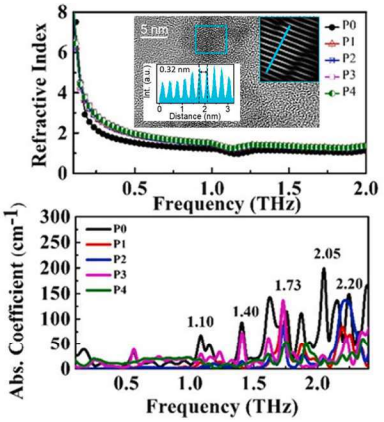

ARTICLE INFO

Keywords:
ZnS
THz
Refractive Index
Optical impedance
Fluorescence

ABSTRACT

Terahertz (THz) technology integration with nanomaterials is receiving excellent attention for next-generation applications, including enhanced imaging and communication. The excellent optical properties in THz domain can lead to preparation of low-cost CMOS camera which can convert THz radiation into optical signal in very efficient manner. In the present study, we have studied the properties of Zinc Sulfide quantum dots (ZnS QDs) embedded with Polyvinyl Alcohol (PVA) composites films using THz Signal at room temperature. The optical characterizations such as refractive index, absorption coefficients and dielectric constants of these samples were measured in the 0.1–2.0 THz range. Additionally, optical impedance, surface roughness, and reflection coefficient in TE and TM mode between 0.1 and 2.0 THz range were determined for these samples based on surface roughness-based reflection and scattering properties. The surface roughness factor was used to measure the optical impedance of the ZnS QDs based polymer films. The measured values of the absorption coefficient at 266 nm are compared with THz radiation, and the refractive indices of these samples range from 1.75 to 2.0. Finally, these samples were subjected to UV light excitation (λ_{exe} = 266 nm) of 0.15 ns duration and 400 nm for the

* Corresponding author.
E-mail addresses: pkumbhakar.phy@nitdgp.ac.in (P. Kumbhakar), akcphys@gmail.com, akcsp@uohyd.ac.in, anilphys@yahoo.com (A.K. Chaudhary).

https://doi.org/10.1016/j.saa.2024.124697
Received 19 December 2023; Received in revised form 7 June 2024; Accepted 19 June 2024
Available online 24 June 2024
1386-1425/© 2024 Published by Elsevier B.V.

Study of THz time-domain spectroscopy based optical properties and detection of minerals and explosives from soil samples of different origins

Chandan Ghorui
Advanced Centre of Research in High Energy Materials
University of Hyderabad
Hyderabad, India
chandanghorui1994@gmail.com

P.Naveen Kumar
Advanced Centre of Research in High Energy Materials
University of Hyderabad
Hyderabad, India
naveenperiketi@gmail.com

Koalla Rajesh
Advanced Centre of Research in High Energy Materials
University of Hyderabad
Hyderabad, India
rraj.0448.rr@gmail.com

Anil Kumar Chaudhary
Advanced Centre of Research in High Energy Materials
University of Hyderabad
Hyderabad, India
akcphys@gmail.com

***Abstract*— We report the time domain THz-based optical evaluation of different sized soil samples obtained from the jungle and defense test range of the country. The soil samples testing exercise using reflection mode time-domain terahertz (THz) spectroscopy technique is related to the development of a small range THz radar system. The study helps us to understand the role of soil particles in terms of identifying the presence of minerals /ores including organic and explosives contaminants. The E-M waves between 0.1- 4.0 THz range provide significant information of the soil of different origins in terms of refractive index and absorption coefficients etc.**

Keywords—THz, Soil, R.I.

I. INTRODUCTION

Soil is a fundamental resource of the earth's ecosystem & human life. Understanding of soil status and function is highly relevant because it contributes to the recycling, filtering, transformation & buffering of the substance and the production of food & biogenic raw materials. The sustainability of agriculture soils in nature must be analyzed regularly to assess their fertility. THz radiation acts as verstile means for the measurement of organic material density, water content & other parameters of soil samples collected from different depths. The collected information plays very important role towards the development of fractional soil sensors [1-2]. We have received soil samples from two sites i.e. jungle and defense test range of the country for identification and detection of ores, organic and explosive molecules .

II. EXPERIMENTAL DETAILS

- We used fiber optical coupled 1560 nm wavelength obtained from typically 50-60 femtosecond laser pulses at 100 MHz repetition rate to pump the In GaAs photoconductive antennas for THz generation and detection (TOPTICA Tera flash system, Germany made) [3]. The system provides a bandwidth greater than 4 THz. In this system, a 50:50 fiber splitter divides the output beam into two emitter and detector branches. The soil samples were placed in a specially designed sample holder which has a Quartz window of dimension 2.5 cm x 2.5 cm x 1 mm and a Teflon-made cube holder.

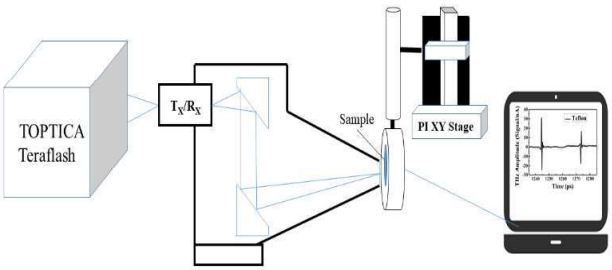

Fig. 1 Schematic experimental set up of THz reflection geometry

III. THEORETICAL CONSIDERATION

THz short pulses are reflected from different surfaces such as quartz plate, combination of quartz plate and soil the sample etc. The resulting reflected signal carry information from the front of the quartz window & delay pulse reflected quartz & soil interface (Sample pulse). Measurement of the frequency-dependent change in phase & amplitude of the pulse train was obtained from a single scan. The ratio of Fourier transforms of the reference pulse $\widehat{E_R}(\nu)$ and sample pulse $\widehat{E_S}(\nu)$ is given by

$$\frac{\widehat{E_S}(\nu)}{\widehat{E_R}(\nu)} = \frac{t_{Air-Quartz}\hat{r}_{Quartz-Soil}t_{Quartz-Air}}{r_{Air-Quartz}} \exp\left(\frac{i4\pi\nu n_{Quartz}d_{Quartz}}{c}\right) (1)$$

where $t_{\text{Air-Quartz}}$, $t_{\text{Quartz-Air}}$, $r_{\text{Air-Quartz}}$, and $\hat{r}_{\text{Quartz-soil}}$ are the Fresnel coefficients at normal incidence for the amplitude transmission t, and reflection r. The exponential factor represents the phase shift (delay) due to propagation in the window material, where n_{Quartz} is the index of refraction of quartz and d_{Quartz} is the thickness of the quartz window.

We have calculated the refractive index and absorption coefficient using formulas (2) & (3) (self-reference method) [4]. Since the soil samples are not homogeneous in nature .Therefore, we get the different refractive index and absorption cofficients of test soil sample.

$$n_{Soil} = \frac{n_{ref}(1-R^2)}{1+R^2-2R\cos\theta} \quad \text{---- (2)}$$

$$\alpha_{Soil} = \frac{4\pi\nu n_{ref}}{c}\frac{2R\sin\theta}{1+R^2-2R\cos\theta} \quad ---(3)$$

978-1-6654-0702-1/22/$31.00 © 2022 IEEE

2022 Workshop on Recent Advances in Photonics (WRAP) | 978-1-6654-0702-1/22/$31.00 ©2022 IEEE | DOI: 10.1109/WRAP54064.2022.9758310

Authorized licensed use limited to: University of Hyderabad IG Memorial Library. Downloaded on August 25,2022 at 16:56:59 UTC from IEEE Xplore. Restrictions apply.

J Mater Sci: Mater Electron (2024) 35:76

Investigation of the dielectric and optoelectronic properties of Nd^{3+}-substituted bismuth ferrite ceramics in THz/far-infrared region

Subhadeep Saha[1], Chandan Ghorui[2], Gomasu Sreenu[1], Anil Kumar Chaudhary[2,*], and Dibakar Das[1,*]

[1] *School of Engineering Sciences and Technology, University of Hyderabad, Hyderabad, Telangana 500046, India*
[2] *Advanced Centre of Research in High Energy Materials (ACRHEM), DRDO Industry Academia – Centre of Excellence (DIA-COE), University of Hyderabad, Hyderabad, Telangana 500046, India*

Received: 26 September 2023
Accepted: 25 December 2023
Published online: 9 January 2024

© The Author(s), under exclusive licence to Springer Science+Business Media, LLC, part of Springer Nature, 2024

ABSTRACT

The real part of the dielectric permittivity of bulk ceramic ferroelectric of composition $Bi_{1-x}Nd_xFeO_3$ ($x = 0, 0.15, 0.2$), synthesized by solid-state route, was characterized in the frequency range 0.1–3.5 THz using time-domain Tera-Hertz spectroscopy, and the effect of Nd^{3+} concentration on the Terahertz (THz) properties of polycrystalline $BiFeO_3$ (BFO) was investigated and is being reported for the first time. A partial transformation in the rhombohedral structural symmetry of $BiFeO_3$ was noticed with increasing Nd^{3+} % concentration. With increasing Nd^{3+} concentration, a gradual increase in the THz signal strength has been observed indicating a reduction in losses. For the first time, the refractive index and absorption coefficients of $Bi_{1-x}Nd_xFeO_3$ ($x = 0.0, 0.15, 0.20$) samples were measured in the THz reflection mode, and the sample with higher Nd concentration was found to be more stable in terms of refractive index and absorption coefficient. The sample with $x = 0.2$ has the highest dielectric value (~ 4.5) at 3.5 THz radiation, which could have potential for THz applications. The detected temporal and spectral THz profiles of $Bi_{1-x}Nd_xFeO_3$ ($x = 0, 0.15, 0.2$) bulk ceramic have shown exceptional stability in the frequency range studied.

1 Introduction

With an increase in the need for global communication, wireless telecommunication technologies have made significant strides. The unprecedented growth in wireless telecommunication technologies over the past few decades is accompanied mainly by the need for higher bandwidth and data rates in wireless communication systems [1, 2]. Wireless communications with frequencies as high as 300 GHz have already been established [3, 4]. It is predicted that data rates of around 5–10 Gb/s will be indispensable in near future

Chandan Ghorui and Gomasu Sreenu have contributed equally to this work.

Address correspondence to E-mail: akcsp@uohyd.ac.in; dibakardas@uohyd.ac.in

https://doi.org/10.1007/s10854-023-11896-4

J Mater Sci: Mater Electron (2024) 35:477

Structural, microstructural and optical characteristics of lead-free $(1-x)(BiFeO_3)-x(CaTiO_3)$ ceramics in submillimeter region

Sreenu Gomasu[1], Chandan Ghorui[2], Subhadeep Saha[1], Anil Kumar Chaudhary[2,*] and Dibakar Das[1,*]

[1] *School of Engineering Sciences and Technology, University of Hyderabad, Hyderabad 500046, India*
[2] *Advanced Centre of Research in High Energy Materials (ACRHEM-DIE-CoE), University of Hyderabad, Hyderabad, Telangana 500046, India*

Received: 23 January 2024
Accepted: 25 February 2024
Published online: 29 February 2024

© The Author(s), under exclusive licence to Springer Science+Business Media, LLC, part of Springer Nature, 2024

ABSTRACT

Lead-free ceramic, $(1-x)(BiFeO_3)-x(CaTiO_3)$ with x values of 0, 0.6, 0.7, 0.8 and 1.0 ($0 \le x \ge 1$) were synthesized from $BiFeO_3$ (BFO) and $CaTiO_3$ (CTO) powders prepared by the chemical solution combustion method. Powder X-ray diffractogram revealed the structural features of the samples. FESEM results were analyzed to examine the microstructure of the samples. Terahertz (THz) region characteristics of polycrystalline BFO-CTO samples were investigated and reported in 0.2–3.5 THz range. Submillimeter spectroscopy (on a THz time-domain spectrometer) and Fourier transform infrared spectroscopy in the frequency range of 0.2 to 3.5 THz have been used to study the reflection infrared spectra of $BiFeO_3$ ceramic samples. In the 30 to 60 cm^{-1} range, an additional absorption with a significant dielectric contribution has been found. It has been shown that the matching oscillators couple with both phonon modes with the lowest frequencies.

1 Introduction

Ferroelectrics have diverse applications including dielectric capacitors, pyroelectric detectors, medical ultrasound equipment, and ferroelectric memories for data storage. These materials also find utility in sensors, actuators, transducers, photonics, telecommunications, and optical data storage [1–7]. As wireless communication technologies continue to advance to increasingly higher frequencies, the development of dielectrics and other functional materials will become crucial for the design of passive and potentially active devices. Appropriate knowledge of dielectric properties at sub-THz and THz frequencies will be essential to achieve this. The characteristics of ferroelectric ceramics are often influenced by their structural, microstructural, and density attributes [8–10]. As such, comprehension of the crystal structure and surface morphology of these materials will be pivotal for their design and advancement. The present investigation primarily

Chandan Ghorui and Subhadeep Saha have contributed equally to this work.

Address correspondence to E-mail: akcsp@uohyd.ac.in; dibakardas@uohyd.ac.in

https://doi.org/10.1007/s10854-024-12272-6

J Mater Sci: Mater Electron (2023) 34:2301

Optoelectronic property correlation with structure and valence band spectra for Fe-doped Zn_2SnO_4-nanostructured films

Isha Arora[1,2], Chandan Ghorui[3], Vanasundaram Natarajan[1], Harkawal Singh[1], Praveen Kumar Sharma[1,4,*], Anil Kumar Chaudhary[3,*], and T. Stephen Sathiaraj[5]

[1] *Department of Physics, Semiconductors Laboratory, DAV University, Sarmastpur, Jalandhar 144012, India*
[2] *School of Natural Sciences, GNA University, Phagwara, Punjab 144401, India*
[3] *Advanced Centre of Research in High Energy Materials (ACRHEM), DRDO Industry Academia–Centre of Excellence (DIA-COE), University of Hyderabad, Hyderabad, Telangana 500046, India*
[4] *Department of Nano Science and Materials, Central University of Jammu, Bagla Suchani, Samba, Jammu 181143, India*
[5] *Department of Physics and Computer Science, Wilfrid Laurier University (WLU), Waterloo, ON N2L 3C5, Canada*

Received: 31 August 2023
Accepted: 29 November 2023
Published online: 13 December 2023

© The Author(s), under exclusive licence to Springer Science+Business Media, LLC, part of Springer Nature, 2023

ABSTRACT

A high Figure of merit (*FOM*) is expected to justify the role of any TCO material as Transparent conducting electrode in the state-of-the-art devices. Here, we are reporting the superior value of Haacke's *FOM* of the order of $0.4 \times 10^{-3}\ \Omega^{-1}$ for Fe-doped ZTO nanostructured films. Optical properties reveal higher optical transparency of 86% ($x = 0.08$) along with band gap curtailing by about 0.3 eV for Fe-doped samples. Electrical measurements give high carrier concentration (10^{20} cm^{-3}) and low resistivity (10^{-3} Ω cm) along with improved mobility that demonstrate electron-cloaking effect at highest dopant concentrations. A significant broadening of the T_{2g} Raman characteristic mode indicates increased degeneracy along with phonon confinement effect. The valence band spectra reveal an upshift in VBM and CBM with Valence band offset value varying from 3.08 to 1.98 eV. Time domain terahertz measurements reveal an appreciable decrease in absorption coefficient (4000 cm^{-1} to 5 cm^{-1} at 0.7 THz) and the refractive index dispersion change to nearly constant value of 1.8 between 0.8 and 2.5 THz with Fe doping in ZTO films. These results are very important for the development of transparent electronics and active materials for the components for manipulating THz spectrum.

Address correspondence to E-mail: prafiziks@gmail.com; akcphys@gmail.com

https://doi.org/10.1007/s10854-023-11736-5

Optical Materials 148 (2024) 114968

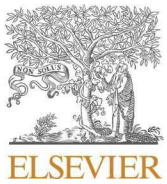

Contents lists available at ScienceDirect

Optical Materials

journal homepage: www.elsevier.com/locate/optmat

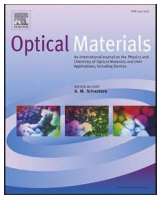

Short Communication

Growth and characterization of piperazinium bis(trifluoroacetate) (PTFA) single crystal for terahertz (THz) optoelectronic applications

B. Sahaya Infant Lasalle [a], Senthil Pandian Muthu [a,*], Chandan Ghorui [b], A.K. Chaudhary [b,**], P. Karuppasamy [a], P. Ramasamy [a]

[a] Department of Physics, SSN Research Centre, Sri Sivasubramaniya Nadar College of Engineering, Chennai, 603110, Tamil Nadu, India
[b] Advanced Centre of Research in High Energy Materials (ACRHEM), University of Hyderabad, Hyderabad 500046, Telangana, India

ARTICLE INFO

Keywords:
Nonlinear optics
X-ray diffraction
THz
HR-XRD
Crystal morphology

ABSTRACT

Piperazinium bis (trifluoroacetate) organic single crystal has been successfully grown by slow evaporation solution technique (SEST). The Piperazinium bis (trifluoroacetate) crystal structural parameters (unit cell & space group) were confirmed by single crystal X-ray diffraction (SXRD). Various crystal planes were identified by powder X-ray diffraction (PXRD) analysis. The crystalline perfection of PTFA crystal was investigated by High Resolution X-ray diffraction (HR-XRD) analysis. The optical characterizations such as photoconductivity and photoluminescence properties of this PTFA crystal were investigated. The electrical property of PTFA crystal was identified by the piezoelectric analysis. The piezoelectric charge coefficient (d_{33} = 13 pC/N) has been measured, which shows it a suitable material for piezoelectric devices. A saturated loop with values of coercive field of remnant polarisation of 0.66 μC/cm^2 and 2.45 kV/cm, respectively, was discovered in ferroelectric investigations. Laser Damage Threshold value of SEST grown PTFA crystal has been determined at 532 nm by using a ns second harmonic of Nd: YAG laser. Finally, we have evaluated the optical properties such as refractive index (R.I.), absorption coefficients (α) and real part of dielectric constant of PTFA using reflection mode time/frequency domain terahertz (THz) spectroscopy between 0.2 and 3.2 THz range. We have measured the conversion efficiency of the PTFA single crystal is 2.4 × 10^{-4} % at 110 μ W incident laser pump power.

1. Introduction

In the recent years, there has been lot of research happening on the NLO crystals, which is mostly used in various areas such as optical signal processing [1], remote sensing [2], telecommunication [3] and so on. The synthesis and assessment of polar organic compounds have significance due to their various physical and chemical characteristics. Organic compounds typically have a π-electron conjugated structure. Under the influence of an external electric field, the conjugation of the π-electron moiety provides an option for the entire length of the conjugation. The functionalisation of both ends of the π-bond systems utilising suitable electron donor and acceptor groups may enhance the asymmetric electronic distribution in both the ground and excited states, hence contribute to the boosting of NLO characteristics [4]. Organic NLO crystals, in general, have strong nonlinearity and good physicochemical characteristics such as optical, thermal, electrical, chemical, mechanical, and laser damage threshold, essential to various uses. For practical device applications, a high laser damage threshold value is preferred for NLO crystal that can be used in the device. As a result, from a device-making standpoint, every researcher has put outstanding efforts on the development of innovative organic materials that work at a high level in real-time NLO devices. The large NLO coefficients and ultra-fast responses for their inherent structures, such as donor-acceptor (D-π-A), π-delocalization length, the structure of each molecule, distinct hydrogen bond interactions, and strong NLO chromophores, are among the finest characteristics of organic materials [5,6]. The organic NLO crystal can be utilised for various applications because of its unique structure, including frequency conversion, laser devices, optical data storage, electro-optical modulation, third harmonic generation, and detection [7]. Organic NLO single crystals are being studied widely due to their high nonlinearity and synthetic flexibility in an attempt to meet all of the technical requirements specified. An additional piece of

* Corresponding author. Department of Physics, SSN College of Engineering, Chennai, 603110, Tamil Nadu, India.
** Corresponding author. School of Physics, ACRHEM (DIA-COE), University of Hyderabad, Hyderabad, 500046, Telangana, India.
E-mail addresses: senthilpandianm@ssn.edu.in (S.P. Muthu), akcsp@uohyd.ac.in (A.K. Chaudhary).

https://doi.org/10.1016/j.optmat.2024.114968
Received 13 December 2023; Received in revised form 21 January 2024; Accepted 22 January 2024
Available online 25 January 2024
0925-3467/© 2024 Elsevier B.V. All rights reserved.

Journal of Molecular Structure 1265 (2022) 133449

Contents lists available at ScienceDirect

Journal of Molecular Structure

journal homepage: www.elsevier.com/locate/molstr

Terahertz time-domain spectroscopy, imaging and density functional theory based studies of 3, 4, 5 Trinitro 1 H Pyrazole

Rajesh Koalla, Naveen Periketi, Chandan Ghorui, Shivanand Mangali, A.K. Chaudhary*

Advanced Centre of Research in High Energy Materials (ACRHEM), University of Hyderabad, Hyderabad Telangana 500046, India

ARTICLE INFO

Article history:
Received 21 February 2022
Revised 2 June 2022
Accepted 3 June 2022
Available online 5 June 2022

Keywords:
Terahertz
Spectroscopy
Reflection mode
FTIR
DFT
Imaging

ABSTRACT

The paper reports the terahertz time-domain spectroscopy (THz-TDS) and imaging on 3, 4, 5 -Trinitro 1-H Pyrazole (explosive) in solid form between 0.1 and 3.5 THz range, including Density Functional Theory was implemented in this study. We have employed a commercially available fiber-coupled THz reflection mode system. We have experimentally ascertained the optical and dielectric properties such as refractive index, absorption coefficients, and dielectric constants in the THz domain. The refractive index values varies between 1.5 and 2.0 range, and absorption coefficients varies between 10 and 400 cm^{-1} in the stated THz range. In addition, Density Functional Theory was used to assign some important vibrational modes obtained experimentally. In the next step, the Dimer and Trimer configurations of the molecule were also incorporated in the existing theoretical model for developing a clear-cut understanding the role of the intermolecular vibrational modes in the molecule. The simulated results were compared in the IR region (4000–400 cm^{-1}) and the THz region (0.1–3.5 THz). Finally, an improvised version of the imaging system was used to record the THz time and frequency domain images of pure pyrazole and mixed in a teflon matrix with different concentrations. The spatial distributions of pyrazole in the pure and teflon matrix at different absorption frequencies have been analysed.

© 2022 Published by Elsevier B.V.

1. Introduction

THz TDS is an attractive and unique nonionizing and non-destructing spectroscopic technique in the far-IR range [1,2]. THz-TDS can provide information in terms of the refractive index and absorption coefficient of a sample with a high signal-to-noise ratio (SNR) without using Kramers-Kronig analysis. During the past two decades, it has been used in a wide range of research applications such as detecting explosives, drugs, biological molecules, pharmaceuticals, and identifying concealed objects [3–7]. Megan et al. demonstrated the capabilities of THz-TDS to identify and detect trace/bulk amounts of the most common types of explosive composition, Such as RDX, HMX, PETN, and TNT [3]. Kyujin Choi group reported the THz TDS in reflection mode of the most commonly used plastic explosives RDX and HMX [8]. Previously, our group reported the temperature-dependent studies of premium aqua-soluble and plastic explosives such as Ammonium nitrate, TNT, and RDX between 30 °C and 200 °C range. Also, it explained the temperature-dependent variation in the refractive index and absorption coefficients of these molecules between 0.1 and 2.0 THz range. We also reported the study of THz- TDS and DFT on centrosymmetric energetic nitrogen-rich aryl-tetrazole high-energy molecules [9,10]. Damian et al. compared the experimental THz (THz) spectrum of the explosive HMX in β-crystal form using the solid-state density functional theory calculations. An excellent agreement between density functional theory results and experiment has been achieved [11]. Similarly, Y. C. Shen et al. group studied the spatial distribution of individual chemical substances lactose, sucrose, and RDX mapped out using reflection THz spectroscopic imaging combined with component spatial pattern analysis [12]. A Cuisset et al. group has reported the first successful rovibrational study of gas phase mononitrotoluene, and dinitrotoluene in the THz spectral domain. Showed that the THz domain spectroscopy would be very useful to identify and discriminate unambiguously different compounds in a complex mixture [13]. A Roucou et al. group studied the conformational landscape of 3-Methoxyphenol using the room temperature millimeter-wave (70–330 GHz) rotational spectroscopy supported by high level of quantum chemical calculations. They measured the 70–330 GHz rotational signatures of the four stable conformations theoretically predicted. In addition to that, rotational transitions in the vibrationally excited states have been assigned for two conformers of 3-Methoxyphenol [14]. The study of explosives and drugs is particularly important due to the ability of THz radiation to penetrate

* Corresponding author.
E-mail addresses: akcphys@gmail.com, anilphys@yahoo.com, akcsp@uohyd.ac.in (A.K. Chaudhary).

https://doi.org/10.1016/j.molstruc.2022.133449
0022-2860/© 2022 Published by Elsevier B.V.

Nonlinear Crystal Based Efficient Terahertz Generation and Development of Prototype RADAR System for Defense & Food Processing Applications

by Chandan Ghorui

20.08.2024

Dr. Anil Kr. Chaudhary
Professor (Physics)
Advanced Centre of Research in
High Energy Materials (ACRHEM),
UNIVERSITY OF HYDERABAD
HYDERABAD-500 046. T.S. INDIA.

Submission date: 20-Aug-2024 10:54AM (UTC+0530)
Submission ID: 2434869597
File name: Chandan_Ghorui.pdf (51.96M)
Word count: 6843
Character count: 36888

Nonlinear Crystal Based Efficient Terahertz Generation and Development of Prototype RADAR System for Defense & Food Processing Applications

ORIGINALITY REPORT

6%	1%	3%	2%
SIMILARITY INDEX	INTERNET SOURCES	PUBLICATIONS	STUDENT PAPERS

PRIMARY SOURCES

1	Submitted to University of Hyderabad, Hyderabad Student Paper	1%
2	eprints.nottingham.ac.uk Internet Source	1%
3	A. K. Haghi, Sabu Thomas, Sukanchan Palit, Priyanka Main. "Methodologies and Applications for Analytical and Physical Chemistry", Apple Academic Press, 2019 Publication	1%
4	Koustuban Ravi, W. Ronny Huang, Sergio Carbajo, Xiaojun Wu, Franz Kärtner. "Limitations to THz generation by optical rectification using tilted pulse fronts", Optics Express, 2014 Publication	1%
5	Submitted to University of New Mexico System Student Paper	<1%

Dr. Anil Kr. Chaudhary
Professor (Physics)
Advanced Centre of Research in High Energy Materials (ACRHEM)
UNIVERSITY OF HYDERABAD
HYDERABAD-500 046. T.S. INDIA.
20-08-2024

6	Koustuban Ravi, Wenqian Ronny Huang, Sergio Carbajo, Emilio A. Nanni, Damian N. Schimpf, Erich P. Ippen, Franz. X. Kärtner. "Theory of terahertz generation by optical rectification using tilted-pulse-fronts", Optics Express, 2015 Publication	<1 %
7	Submitted to Manipal University Student Paper	<1 %
8	Klaus D. Sattler. "Silicon Nanomaterials Sourcebook - Arrays, Functional Materials, and Industrial Nanosilicon", CRC Press, 2017 Publication	<1 %
9	repository.rudn.ru Internet Source	<1 %
10	Rahul Kumar, Neeraj Goel, Monu Mishra, Govind Gupta, Mattia Fanetti, Matjaz Valant, Mahesh Kumar. " Growth of MoS -MoO Hybrid Microflowers via Controlled Vapor Transport Process for Efficient Gas Sensing at Room Temperature ", Advanced Materials Interfaces, 2018 Publication	<1 %
11	Chandan Ghorui, Kidavu V Arjun, P Naveen Kumar, Subhasis Das, Anil K Chaudhary, Yuri Andreev. "Comparative studies of terahertz-based optical properties in transmission/	<1 %

20.08.2019

Dr. Anil Kr. Chaudhary
Professor (Physics)
Advanced Centre of Research in
High Energy Materials (ACRHEM),
UNIVERSITY OF HYDERABAD
HYDERABAD-500 046. T.S. INDIA.

reflection modes of GaSe: S and measurement of its scattering losses due to surface roughness for efficient terahertz generation", Physica Scripta, 2022
Publication

20.08.2024

Dr. Anil Kr. Chaudhary
Professor (Physics)
Advanced Centre of Research in High Energy Materials (ACRHEM),
UNIVERSITY OF HYDERABAD
HYDERABAD-500 046. T.S. INDIA.

Exclude quotes	On	Exclude matches	< 14 words
Exclude bibliography	On		

This is to certify that Similarity Index of thesis of Sri. Chandan Ghosh excluding his own articles is 6% - 1% = 5%, which is less than 10% according to the university guidelines.

20.08.2024

Dr. Anil Kr. Chaudhary
Professor (Physics)
Advanced Centre of Research in High Energy Materials (ACRHEM),
UNIVERSITY OF HYDERABAD
HYDERABAD-500 046. T.S. INDIA.

Plagiarism-free Statement

This is to certify that the thesis titled "Nonlinear Crystal Based Efficient Terahertz Generation and Development of Prototype RADAR System for Defense & Food Processing Applications" has been screened by the Turnitin software at the Indira Gandhi Memorial Library of the University of Hyderabad. The software shows a 6% similarity index, of which 1% came from the candidate's own research articles related to the thesis, which are published and available online. Thus, effective similarity index excluding his own article is 6%-1%=5%, which is lower than 10% according to the rule specified by the university guidelines. Therefore, this may be considered free from plagiarism as per guidelines.

20.08.2024

Prof. Anil Kumar Chaudhary

(Professor in Physics)

(PhD Supervisor)

DIA CoE, ACRHEM, School of Physics,

University of Hyderabad

Dr. Anil Kr. Chaudhary
Professor (Physics)
Advanced Centre of Research in
High Energy Materials (ACRHEM),
UNIVERSITY OF HYDERABAD
HYDERABAD-500 046. T.S. INDIA.